



POLITECNICO DI TORINO
Repository ISTITUZIONALE

Dynamic tailoring of beam-like structures. Application to High Aspect Ratio unitized box-beam and internal resonant structures

Original

Dynamic tailoring of beam-like structures. Application to High Aspect Ratio unitized box-beam and internal resonant structures / Danzi, Francesco. - (2018 Aug 07).

Availability:

This version is available at: 11583/2712259 since: 2018-09-04T16:07:12Z

Publisher:

Politecnico di Torino

Published

DOI:10.6092/polito/porto/2712259

Terms of use:

Altro tipo di accesso

This article is made available under terms and conditions as specified in the corresponding bibliographic description in the repository

Publisher copyright

(Article begins on next page)



ScuDo

Scuola di Dottorato ~ Doctoral School

WHAT YOU ARE, TAKES YOU FAR

Doctoral Dissertation

Doctoral Program in Aerospace Engineering (30th cycle)

Dynamic tailoring of beam-like structures

Application to High Aspect Ratio unitized box-beam and internal resonant structures

By

Francesco Danzi

Supervisor(s):

Prof. G. Frulla, Supervisor

Prof. E. Cestino, Supervisor

Prof. J. M. Gibert , Supervisor

Doctoral Examination Committee:

Prof. A.F. Arrieta Diaz, Referee, Purdue University

Prof. A. Erturk , Referee, Georgia Institute of Technology

Prof. D.J. Inman, University of Michigan

Prof. M. Karpel, Technion - Israel Institute of Technology

Prof. S. Preidikman, University of Maryland - College Park

Politecnico di Torino
2018

Declaration

This thesis is licensed under a Creative Commons License, Attribution- Noncommercial-NoDerivative Works 4.0 International: see www.creativecommons.org. The text may be reproduced for non-commercial purposes, provided that credit is given to the original author.

I hereby declare that, the contents and organization of this dissertation constitute my own original work and does not compromise in any way the rights of third parties, including those relating to the security of personal data.

Francesco Danzi
2018

* This dissertation is presented in partial fulfillment of the requirements for **Ph.D. degree** in the Graduate School of Politecnico di Torino (ScuDo).

Acknowledgements

First and foremost I would like to express my gratitude to my advisors Prof. Giacomo Frulla, Prof. Enrico Cestino and Prof. James M. Gibert, they did me feel like a colleague, rather than a student, and gave me the freedom to express myself and develop my own style, which I believe, is what really matter for a young researcher. I owe a particular thank to Prof Frulla and Prof. Cestino for giving me the possibility of pursuing the PhD.

I would like to thank Dr Gibert for giving me the possibility to join the Advanced Dynamics and Mechanics Lab at Purdue University. It was a great pleasure work under his guidance, his kindness and committment to his students are invaluable. I owe him a lot. I wish I can extended my acknowledgments to my colleagues at the Advanced Dynamics and Mechanics Lab, Amin, Dennis and Hongcheng.

I truly enjoyed sharing the same office with Alberto, Andrea, Caterina, Giovanni, Giuseppe, Francesco and Mario in the Departement of Mechanical and Aerospace Engineering at Turin Polytechnic and, with Davide and Medhi at Ray W. Herrick Lab during my staying at Purdue University.

I would extended my gratitude to Prof. Arrieta and Prof. Erturk for serving as reviewers for my PhD Thesis providing invaluable comments. I owe a special thank also to Prof. Stephen W. Tsai form Stanford University, his passion for knowledge and his dedication are for me a source of inspiration.

Words are not enough to express my gratitude to my beloved parents and family for having encouraged me to pursue my goals even at hardship, for their patience and wholehearted support.

Ever since I was a kid I have always been curious but I wish I should spend few words for the guy that brought me here, somehow and unintentionally. I still remember that day, I was laying over a mulberry tree's branch at my grandparents' farm, a Panavia Tornado flewby, few meters above my head, and the tree started trembling. Arguably, that was the beginning...

Abstract

This work is a journey into the dynamic tailoring of beam-like structures which aims to exploit unconventional couplings and nonlinearities to enlarge the design space and improving the performances of engineering systems. Particularly, two examples pertaining dynamic tailoring of aerospace and mechanical systems are investigated in depth.

In the first case, the work aims to attain a desired structural performance exploiting typical nonlinear structural phenomena and unconventional couplings offered by the unitized structures. As for the unitized structures, the present work, derives two equivalent plate models of curvilinear stiffened panels namely, constant (or homogenized) stiffness model and variable stiffness model. The models are assessed through finite element analysis. In the spirit of CAS (Circumferentially Asymmetric Stiffness), the equivalent plate stiffness's are used to determine the cross-sectional beam stiffness's. The governing equations for the Euler-Bernoulli, anisotropic beam with variable stiffness are derived and then used to address the optimization problem. The objective of the optimization is to attain a desired static or dynamic performance of the unitized beam exploiting the enlarged design space which arises from the stiffness variability and the unconventional couplings.

In the second type of system analyzed, the aim is synthesize meaningful topologies for planar resonators. The topology optimization is addressed using as initial guess a ground structure. Motivated by the results of the optimization, a generalized reduced order model is derived for multi-members beam structures. The generalized model have been then specialized for three cases namely, V- Y- and Z-shaped resonators. The analytical solution for the V-shaped resonator is also derived along with the electro-mechanical equations of motion. Different solutions are studied aiming at investigating the effect of the folding angle on to the performances of a V-shaped harvester.

Beside the study of the static and dynamic behavior of the systems, the thesis presents two novel optimization algorithms namely, the Stud^P GA and the GERM. The Stud^P GA, is a population based algorithm conceived to enhance the exploration capabilities, and hence the convergence rate, of classical GA. The Stud^P GA has been preliminary assessed through benchmark problems for composite layered structure and then used for the optimization of the stiffeners' path aiming at attaining a desired static or dynamic performances. The GERM (Graph-based Element Removal Method), is a double filtering technique conceived for the topology synthesis of planar ground structures. The GERM has been used, in combination with a standard GA, to address the topology optimization problem of the two types of system namely, planar resonator and compliant structures.

The work introduces also the concept of trace-based scaling for predicting the behavior of anisotropic structures. The effectiveness of the trace-based scaling is assessed through comparison between scaled and analytical performances of anisotropic structures.

Sommario

Questo lavoro si pone l'obiettivo di sfruttare accoppiamenti non convenzionali e non linearità per ampliare lo spazio di progettazione e migliorare le prestazioni di elementi strutturali ad elevato allungamento di tipo trave. In particolare, due esempi riguardanti l'ottimizzazione dinamica di sistemi aerospaziali e meccanici sono presi in considerazione.

Nel primo caso, il lavoro si propone di posticipare il verificarsi di instabilità sfruttando i tipici fenomeni strutturali non lineari e gli accoppiamenti non convenzionali offerti dalle strutture integrali. In primo luogo vengono derivati due modelli di piastra equivalente di pannelli irrigiditi con irrigidimenti curvi. I modelli equivalenti vengono quindi utilizzati per determinare le rigidità di elementi trave composti da pannelli irrigiditi.

Nel secondo tipo di sistema analizzato nel presente studio, l'obiettivo è invece quello di sfruttare gli accoppiamenti strutturali per migliorare il comportamento di risonatori planari. A tal fine, la tesi affronta prima l'ottimizzazione della topologia dei risonatori planari utilizzando il metodo "*Ground Structure*". Motivati dai risultati dell'ottimizzazione, viene derivato un modello di ordine ridotto generalizzato per strutture planari a più membri. Il modello generalizzato è stato quindi specializzato per tre casi, cioè risonatori a forma di V, Y e Z rispettivamente. Per il risonatore a forma di V vengono derivate anche le equazioni esatte del moto e il modello elettro-meccanico.

I due progetti utilizzano lo stesso modello fondamentale di trave. In entrambi i casi il problema di ottimizzazione è riscritto sotto forma di ottimizzazione combinatoria vincolata.

Per i due tipi di sistemi presentati, le soluzioni semi-analitiche derivate sono confrontate con analisi ad elementi finiti.

Oltre allo studio del comportamento dinamico strutturale, la tesi presenta due nuovi algoritmi di ottimizzazione, ovvero lo Stud^P GA e GERM. Lo Stud^P GA viene in primo luogo testato su problemi di benchmark e successivamente utilizzato per l'ottimizzazione della topologia degli irrigidimenti al fine di ottenere una data prestazione strutturale, statica o dinamica. Il GERM (metodo di rimozione degli elementi basato su grafi), è una tecnica di filtraggio concepita per la sintesi topologica delle *Ground Structure*.

Il lavoro introduce il concetto di "scalatura" al fine di predire l'effetto dell'impegno di differenti materiali anisotropici sul comportamento strutturale. L'efficacia della procedura di "scalatura" viene mostrata attraverso diversi esempi concernenti strutture anisotrope.

Contents

List of Figures	xv
List of Tables	xxii
1 Structural Tailoring	1
1.1 Introduction and Significance	1
1.2 Structural Tailoring: a short overview	4
1.2.1 Idealized beam models	6
1.2.2 Material selection	9
1.3 Design and optimization of electro-mechanical system	10
1.4 Objectives of the work	12
1.5 Layout of the thesis	13
1.6 Contribution of the thesis	14
1.6.1 Major contribution	16
1.6.2 Minor contribution	17
1.7 Others contribution	18
2 Equivalent models of straight and curved reinforced structures	19
2.1 Overview of equivalent plate models for reinforced structures	20
2.2 Structural model	23
2.3 Direct compatibility	25

2.3.1	Statical equivalence	25
2.3.2	Kinematical equivalence	28
2.4	Energy equivalence method	31
2.4.1	Preliminary consideration on the rank of the stiffness matrices	39
2.4.2	Considerations on the equivalent thickness	44
2.4.3	Derivation of the effective engineering constants	46
2.5	Kinematic Equations for First Order Shear Deformation curved beam	51
2.5.1	Implications of the kinematics of curved beam	54
2.5.2	Equivalent panel density	57
2.6	Assessment of the equivalent models	58
2.6.1	Effect of the curvature	58
2.6.2	Effect of the torsional stiffness	64
2.6.3	Effect of the number of subcells	64
2.6.4	Effect of the transverse shear	66
2.6.5	Effect of the panel density	71
2.7	Case studies	72
2.7.1	Concentric panel with one family of stiffeners	72
2.7.2	Buckling and free-vibrations of concentric grid stiffened panel	73
2.8	Summary and conclusions	76
3	Beam model	77
3.1	Motivation	77
3.2	Assumptions on the cross sectional properties	78
3.2.1	Effect of the stiffeners orientation on to the effective beam properties	81
3.3	Basic assumptions for the beam model	85
3.4	Derivation of the equations of motion of variable stiffness beam . .	91

3.4.1	Variation of the potential energy	91
3.4.2	Linear terms	92
3.4.3	Second order terms	93
3.4.4	Equations of motion	94
3.4.5	Second order linearized equations	95
3.4.6	Solution methodology	95
3.5	Summary and conclusions	96
4	Trace-based scaling of anisotropic structures	97
4.1	Motivation	97
4.2	Trace-based scaling: theoretical framework	98
4.2.1	Definition of the material sample	99
4.2.2	Definition of the Master Ply	100
4.2.3	Scaling	104
4.3	Application of trace based scaling for anisotropic structures	106
4.3.1	Scaling of buckling loads	106
4.3.2	Scaling of post-buckling deflections	108
4.3.3	Scaling for divergence speed	109
4.3.4	Scaling for normal frequencies	111
4.3.5	Scaling for buckling loads of curvilinear stiffened panels	111
4.4	Summary and conclusions	114
5	Optimization of anisotropic plates and beams	115
5.1	Introduction	115
5.2	Stud ^P GA	116
5.2.1	Implementation of the breeding farm paradigm	118
5.2.2	Effect of η and \mathcal{P}_{ext} on the algorithm's reliability and efficiency	122

5.2.3	Selection strategy	125
5.2.4	Reproduction and genetic operators	126
5.2.5	Termination criteria	127
5.3	Buckling load maximization of composite panels	127
5.3.1	Objective function	131
5.3.2	Results	133
5.4	Linear static optimization of unitized beam	138
5.4.1	Problem formulation	140
5.4.2	Results and discussion	143
5.5	Dynamic tailoring of HAR box-beam with curvilinear stiffeners	152
5.5.1	Identification of the benchmark model	154
5.6	Formulation of the optimization problem	158
5.6.1	Optimization with two control points	159
5.6.2	Optimization with three control points	160
5.7	Conclusions	165
6	Topology synthesis of planar ground structures	169
6.1	Introduction and motivation	169
6.2	Topology optimization	170
6.3	Ground structure	171
6.3.1	Parameterization of the design domain	172
6.4	Graph Based Element Removal Method	173
6.4.1	Threshold Limit Removal	175
6.4.2	Graph Based Search and Cut	178
6.5	Case Study: Optimization of planar resonators	180
6.6	Summary and conclusions	184

7	Analytical and semi-analytical model for multi-member structures	187
7.1	Introduction	187
7.2	Formulation of the Governing Equations	188
7.2.1	Equation of motion of angle-shaped resonator having two members adjoined at an angle φ	188
7.2.2	Characteristic equation	192
7.2.3	Validation of the analytical model	195
7.3	Generalized Reduced Order Model	196
7.3.1	Determining the Admissible Functions	196
7.3.2	Case $N = 2$: V-shaped resonator	201
7.3.3	Case $N = 3$: Y-shaped resonator	205
7.3.4	Case $N = 3$: Z-shaped resonator	208
7.4	Design charts for the V-shaped resonator	210
7.5	Summary and conclusion	213
8	Electro-mechanical model for the V-shaped resonators	215
8.1	Introduction	215
8.2	Resonator Design	217
8.3	Electro-mechanical equation of motion	220
8.4	Analysis of the performances	224
8.4.1	Identification of the optimal resistance	224
8.4.2	Performances of the resonator of the inner envelope	225
8.5	Conclusions	230
9	Summary and outlook	233
9.1	Contribution to knowledge	233
9.2	Outlook	237

References	239
Appendix A Typical HAR HALE wing box	254
A.1 Lay-up of the composite wing box used for scaling	254
Appendix B Non-dimensional Euler-Bernoulli beam element	256
B.1 Derivation of the non-dimensional form of the Euler Bernoulli beam model	256
Appendix C Coefficients of the stiffness and mass matrices	258
C.1 Case $p = 3$, Y-shaped resonator	258
C.2 Case $p = 3$, Z-shaped resonator	260
Appendix D Optimization of compliant mechanisms	263
D.1 Preliminary Numerical Results	264

List of Figures

2.1	Example of (a) stiffened plate and (b) equivalent continuum structure	23
2.2	Flowchart of the numerical implementation of the equivalent models.	24
2.3	Example of steering stiffened panel	25
2.4	Reference systems for the plate xyz and stiffeners XYZ respectively.	26
2.5	Stress resultants acting on the generic stiffeners.	28
2.6	Plate stress resultants onto the equivalent continuum layer.	29
2.7	Exemplification of the basic cell and subcell	31
2.8	Non-dimensional membrane matrix coefficients for a stiffened panel with $\vartheta_1 = 16.75^\circ$, $\vartheta_2 = 45^\circ$	36
2.9	Non-dimensional bending matrix coefficients for a stiffened panel with $\vartheta_1 = 16.75^\circ$, $\vartheta_2 = 45^\circ$	36
2.10	Non-dimensional shear matrix coefficients for a stiffened panel with $\vartheta_1 = 16.75^\circ$, $\vartheta_2 = 45^\circ$	37
2.11	Non-dimensional membrane matrix coefficients for a stiffened panel with $\vartheta_1 = 10^\circ$, $\vartheta_2 = -10^\circ$	38
2.12	Non-dimensional bending matrix coefficients for a stiffened panel with $\vartheta_1 = 10^\circ$, $\vartheta_2 = -10^\circ$	38
2.13	Non-dimensional shear matrix coefficients for a stiffened panel with $\vartheta_1 = 10^\circ$, $\vartheta_2 = -10^\circ$	39
2.14	Comparison of the D_{66} coefficient obtained using different models .	43

2.15	Comparison of the D_{ij} coefficients for a rectangular stiffened plate with straight stiffeners oriented at $\vartheta = 20^\circ$	44
2.16	Input for the MAT2 card of MSC [®] Patran	46
2.17	Contour plots of the equivalent membrane properties for stiffened panels	49
2.18	Contour plots of the mutual influence coefficients for stiffened panels	50
2.19	Contour plots of the equivalent transverse shear properties for stiffened panels	50
2.20	Chentsov's (shear-shear coupling) coefficient	51
2.21	Contour plots of the equivalent bending properties for stiffened panels	52
2.22	Kineamtics of a planar curved beam	53
2.23	Geometrical interpretation of the design's envelope limit	56
2.24	Design envelope limits for the model derived	57
2.25	Example of topologies lying over the boundary curve depicted in Figure 2.24	59
2.26	Comparison of the buckling modes of a stiffened panel with $\vartheta_1 = -40^\circ$ and $\vartheta_2 = -14^\circ$	61
2.27	Comparison of the first buckling mode for different stiffeners topologies	62
2.28	Comparison of the first vibration mode for different stiffeners topologies	62
2.29	Comparison of the buckling modes of a substiffened panel with $\vartheta_1 = 45^\circ$ and $\vartheta_2 = -45^\circ$	65
2.30	Effect of the number of sub-cells on the normalized bending coefficients \hat{d}_{ij}	67
2.31	Contour plot of the relative percentage error between the buckling loads obtained retaining and neglecting the effect of the transverse shear.	69
2.32	First buckling mode of a steering stiffened panel with $\vartheta_1 = 0^\circ$, $\vartheta_2 = 10^\circ$	73

2.33	Comparison of the bending modes of a stiffened panel with $\vartheta_1 = 0^\circ$ and $\vartheta_2 = 10^\circ$	74
2.34	Example of the orientation angles for a grid stiffened panel	75
3.1	Exemplification of the generic cross section for the CAS configu- ration and its reference system (a) and example of the beam cross section considered in this work	80
3.2	Exemplification of the box-beam cross section.	82
3.3	Normalized envelope for the torsional stiffness \overline{GJ}_t	83
3.4	Normalized envelope for the flexural-torsional coupling coefficient \overline{K}	84
3.5	Normalized envelope for the bending stiffness \overline{EI}_2	85
3.6	Normalized envelope for the bending stiffness \overline{EI}_3 (flap-wise stiffness). 86	
3.7	Effective beam properties with respect to the stiffeners' orientation ϑ_2 at fixed ϑ_1	87
3.8	Effective beam stiffnesses with respect to the beam abscissa x for the case of curvilinear stiffeners $\vartheta_1 = 0^\circ, \vartheta_2 = 25^\circ$	88
3.9	Coordinate systems used in the present derivation.	88
3.10	Exemplification of the three successive counterclockwise rotations defined to align the inertial system to the deformed system.	89
4.1	Trace-normalized reduced stiffened components and Trace for dif- ferent angle of orientation ϑ	99
5.1	Schematic representation of linebreeding and outcrossing.	118
5.2	Flowchart of the mating's pool structure for implementing the in- breeding (or line breeding) and outcrossing.	119
5.3	Mean Hamming distance (μ) and standard deviation of Hamming distance (σ) between the Stud and others offspring	121
5.4	Example of the stacking sequence of laminate plates.	132
5.5	Example panel subjected to combined loads.	134

5.6	Exemplification of the beam's cross section considered in [125]. . .	138
5.7	Flowchart for the evaluation of the beam's stiffnesses.	139
5.8	Exemplification of a clamped free beam with control-points distributed span-wise.	142
5.9	Comparison of the stiffnesses obtained with the presented model and the model adopted in [125] considering straight stiffeners $\vartheta_1 = \vartheta_2$. .	145
5.10	Comparison of the mean tip displacement and tip rotation obtained with different models and experiments.	146
5.11	Experimental setup for the first load case with straight stiffeners oriented at 25°	147
5.12	Optimized stiffeners topology obtained with Altair OptiStruct. . . .	147
5.13	Detailed view of the stiffeners cross section as obtained in [160] . .	148
5.14	Normalized optimum beam stiffness for the case of uniformly distributed load.	150
5.15	Normalized optimum beam stiffness for the case of triangular load. .	151
5.16	Isometric view of the High Aspect Ratio wing considered herein for the analysis.	153
5.17	Static assessment of the edgewise stiffness for the benchmark wing-box.	154
5.18	Static assessment of the flat-wise stiffness for the benchmark wing-box.	155
5.19	Static assessment of the torsional stiffness for the benchmark wing-box.	155
5.20	Nonlinear static deformation of the benchmark box-beam	156
5.21	First nonlinear mode shape of the wing box.	157
5.22	Second nonlinear mode shape of the wing box.	157
5.23	Third nonlinear mode shape of the wing box.	157
5.24	Nonlinear static deformation for the optimized wing box with two control points ($\vartheta_1 = 0^\circ$, $\vartheta_2 = 10^\circ$).	160
5.25	First nonlinear mode shape of the optimized wing box with two control points ($\vartheta_1 = 0^\circ$, $\vartheta_2 = 10^\circ$).	161

5.26	Second nonlinear mode shape of the wing box with two control points($\vartheta_1 = 0^\circ$, $\vartheta_2 = 10^\circ$).	161
5.27	Third nonlinear mode shape of the wing box with two control points ($\vartheta_1 = 0^\circ$, $\vartheta_2 = 10^\circ$).	162
5.28	Nonlinear static deformation for the optimized wing box with three control points ($\vartheta_1 = -2.5^\circ$, $\vartheta_2 = 5^\circ$, $\vartheta_3 = 12.5^\circ$).	163
5.29	First nonlinear mode shape of the optimized wing box with three control points ($\vartheta_1 = -2.5^\circ$, $\vartheta_2 = 5^\circ$, $\vartheta_3 = 12.5^\circ$).	163
5.30	Second nonlinear mode shape of the wing box with three control points ($\vartheta_1 = -2.5^\circ$, $\vartheta_2 = 5^\circ$, $\vartheta_3 = 12.5^\circ$).	163
5.31	Third nonlinear mode shape of the wing box with three control points ($\vartheta_1 = -2.5^\circ$, $\vartheta_2 = 5^\circ$, $\vartheta_3 = 12.5^\circ$).	164
5.32	Exemplification of the stiffeners geometries synthesized with (a) 2 and (b) 3 control points.	164
5.33	Comparison of the torsional stiffness distribution with respect to the normalized abscissa for the case of 2 and 3 control points.	166
5.34	Comparison of the coupling stiffness distribution with respect to the normalized abscissa for the case of 2 and 3 control points.	166
5.35	Comparison of the edge-wise stiffness distribution with respect to the normalized abscissa for the case of 2 and 3 control points.	167
5.36	Comparison of the flat-wise stiffness distribution with respect to the normalized abscissa for the case of 2 and 3 control points.	167
6.1	Example of a Ground Structure with 7×7 and 3×3 nodes.	173
6.2	Exemplification of the doubly linked list implemented in the optimization algorithm	175
6.3	Effect of GERM on the ground structure	176
6.4	Examples of resonators synthesized to have 1:2 frequency ratio.	178
6.5	Number of active members of the optimum solution during the optimization.	181

6.6	Optimized topology for planar resonators	183
6.7	Example of optimized topologies for different frequency ratios.	185
7.1	Schematic of Angle-shaped resonator composed of two prismatic beams having a folding angle φ	189
7.2	Generalized model representing a 4-DOF structure with $N = 4$ elements, $F = 2$ free nodes, and $\theta = 2$ internal nodes.	197
7.3	Detail of an internal node β of the structure.	198
7.4	V-shaped resonator with a 2-DOF structure with $N = 2$ elements, $F = 1$ free nodes, and $\theta = 1$ internal nodes.	201
7.5	Bifurcation envelopes obtained through FEA and with the present semi-analytical model for $\omega_2/\omega_1 = 2$ as a function of φ	204
7.6	Contour plots for (a) $\hat{l} < 1$ and (b) $\hat{l} > 1$ with $\omega_2/\omega_1 = 2$ as a function of φ	205
7.7	Nondimensional distance of the center of gravity, \hat{d} , from the fixed end	206
7.8	Polar surface plot of FRFs at $u_2(L_2)$ due to a base excitation for a V-shaped resonator with respect to folding angle φ for $\hat{h} = 0.5$ that have 1:2 commensurate frequencies	207
7.9	Topology of Y and Z shaped resonators	207
7.10	Design chart for $\omega_2/\omega_1 = 2$ resonator with square cross sections from the outer envelope	211
7.11	Design chart for $\omega_2/\omega_1 = 2$ resonator with a square cross section from the outer envelope	212
7.12	Exemplification of the usage of the universal chart to design a resonator in a ratio one-to two.	213
8.1	Accelerometer measurements from a Ward Leonard DC generator: (a) x-axis, (b) y-axis, and (c) z-axis. Data was downloaded from the EH Network Data Repository (http://eh-network.org/data).	216
8.2	Polar representation of the solution having 1:2 frequency ratio as a function of the folding angle φ , $\hat{h} = 0.5$	218

8.3	First and second mode shape of the five resonators under study, drawn to scale	221
8.4	Experimental setup: a) the V_{80} resonator mounted on the rigid support and connected to the base of the APS Dynamics ELECTRO-SEIS Shaker, b) the data acquisition system.	222
8.5	Optimum resistance for the three angled resonators.	224
8.6	FRF of Voltage(left) and of Power Density (right) for the three resonators under study, respectively from top to bottom V_{80} , L and V_{120}	226
8.7	Power harvested as a function of time over one cycle of oscillation: a) V_{80} resonator, b) L resonator, and c) V_{120} resonator.	227
8.8	Effect of the phase shifting angle on the instantaneous voltage and instantaneous power for the V_{120}^i harvester.	229
8.9	[Effect of the phase shifting angle on the instantaneous voltage and instantaneous power for the L^i harvester.	230
8.10	[Effect of the phase shifting angle on the instantaneous voltage and instantaneous power for the V_{80}^i harvester.	231
B.1.1	Exemplification of the two node, 6 degree of freedom finite element adopted in the present analysis	257
D.1.1	Starting structure and optimized topology for the compliant mechanisms	264

List of Tables

2.1	First buckling load [N/mm] of simply supported curvilinearly stiffened panels subjected to uniaxial compression N_x	60
2.2	First frequencies [Hz] of a simply supported curvilinearly stiffened panels.	60
2.3	Buckling loads [N/mm] of a simply supported flat panel with concentric substiffeners.	64
2.4	Comparison of the first buckling loads of simply supported curvilinearly stiffened panels with and without higher order terms for the torsional stiffness	66
2.5	Effect of the density's model adopted for free vibrations of simply supported plates.	72
2.6	Buckling loads for a simply supported, square panel, reinforced with concentric curvilinear stiffened $\vartheta_1 = 0^\circ$, $\vartheta_2 = 10^\circ$	73
2.7	Natural frequencies for a simply supported, square panel, reinforced with concentric curvilinear stiffened $\vartheta_1 = 0^\circ$, $\vartheta_2 = 10^\circ$	73
2.8	First buckling load and first natural frequencies for a simply supported, square panel, reinforced with grid stiffeners.	75
3.1	Geometric features of the wing box under study.	82
4.1	Engineering properties of the materials' sample considered.	100
4.2	Trace-normalized reduced stiffness components.	101
4.3	Engineering properties of the Master Ply.	102

4.4	Trace normalized in-plane components $A_{ij}^* = (A_{ij})/(h Tr)$ for $[0/\pm 45/90]_S$ laminates.	102
4.5	Trace normalized bending components $D_{ij}^* = (12D_{ij})/(h^3 Tr)$ for the family $[0/\pm 45/90]_S$	103
4.6	Trace normalized bending components $D_{ij}^* = (12D_{ij})/(h^3 Tr)$ components for $[0_5/45_2/90]_S$ laminates.	103
4.7	Engineering properties of the materials' sample considered.	107
4.8	Analytical (a) and scaled (s) buckling loads for simply supported (SSSS) and fully clamped (CCCC) panels.	107
4.9	Membrane and bending stiffness normalized components for E-glass composite laminate $[0/\pm 45/90]_S$	108
4.10	Analytical (a) and scaled (s) buckling loads for simply supported (SSSS) GFRP composite panels.	109
4.11	Analytical (a) and scaled (s) post buckling deflection w for simply supported (SSSS) and fully clamped (CCCC) panels. The load increment with respect to the buckling load is fixed at 1.5.	110
4.12	Comparison of the trace based scaled and numerical computed divergence speed of an HAR wing.	110
4.13	Comparison of the trace based scaled and numerical flap/coupled frequencies of an HAR wing under moderate deformations.	111
4.14	Comparison of the trace-based scaled and numerical flap/coupled frequencies of an HAR wing under moderate deformations.	112
4.15	Comparison of the trace-based scaled and numerical torsional/coupled frequencies of an HAR wing under moderate deformations.	112
4.16	Scaled buckling loads for flat panles with cured stiffeners.	113
4.17	Scaled buckling loads for flat panels with cured stiffeners.	113
5.1	Loads applied and optimal plies numbers for composite laminate panels under study	123
5.2	Physical properties of the composite material (graphite/epoxy) used for the optimization	123

5.3	Effect of probability of extinction and stress parameter on the number of evaluations and reliability of the Stud ^P GA	123
5.4	Effect of probability of extinction and stress parameter on the cost-effectiveness of the Stud ^P GA.	124
5.5	Optimized stacking sequence from GA	135
5.6	Comparison of computational efficiency between Stud ^P GA, PS and other three GAs without contiguity constraint.	136
5.7	Comparison of computational efficiency between Stud ^P GA, PS and other three GA with contiguity constraint.	137
5.8	Comparison of the cost-effectiveness between Stud ^P GA, PS and other three GA with contiguity constraint.	137
5.9	Geometric features of the wing box under study.	138
5.10	Results of the topology optimization for the static cases.	148
5.11	Comparison of the tip deflection and tip rotation obtained with the different models for different topologies for the case of uniformly distributed load.	149
5.12	Comparison of the tip deflection and tip rotation obtained with the different models for different topologies for the case of traingular load.	151
5.13	Comparison of the wing box stiffnesses between the benchmark model established herein and that given in Cestino <i>et al</i> in [64].	155
5.14	Linear and nonlinear frequencies [Hz] of the benchmark problem ($\vartheta_1 = 0^\circ, \vartheta_2 = 0^\circ$).	156
5.15	Linear and nonlinear frequencies [Hz] of the otpimized wing box ($\vartheta_1 = 0^\circ, \vartheta_2 = 10^\circ$).	159
5.16	Linear and nonlinear frequencies [Hz] of the otpimized wing box ($\vartheta_1 = -2.5^\circ, \vartheta_2 = 5^\circ, \vartheta_3 = 12.5^\circ$).	162
7.1	Parameters for the two validation structures.	196
7.2	Bending frequencies [rad/s] for the straight and <i>L</i> -shaped structures.	196
7.3	Geometric and Material Properties for N-DOF Resonators	200

7.4	Non-dimensional ratios for <i>Y</i> -shaped resonators with $\omega_2/\omega_1 = 2$ and $\omega_3/\omega_1 = 3$ resonances.	209
7.5	Non-dimensional ratios for <i>Z</i> -shaped resonators with $\omega_2/\omega_1 = 2$ and $\omega_3/\omega_1 = 3$	210
8.1	Non-dimensional ratios for the different resonators and first bending frequency [Hz]. The solutions are obtained using a root finding algorithm to have commensurable frequencies in a ratio 1:2 using the reduced order model. [194]	218
8.2	Configuration parameters for the angled resonators.	219
8.3	Scaled design: first beam length, and first two modal frequencies. . .	220
8.4	Natural frequencies [Hz] of the angle-shaped resonators under study.	220
8.5	Geometric and Material Properties of the PVDF	222
A.1.1	Number of plies for the wing box used for scaling.	255

Chapter 1

Structural Tailoring

1.1 Introduction and Significance

The last few decades have seen the exploitation of nonlinear dynamic phenomena utilized to improve the performance of engineering systems. This new design paradigm is known as Nonlinear Dynamics for Design. The introduction of this paradigm is ascribed to Prof. Ali H. Nayfeh [1]. It has provided: a) the fundamental understanding of various nonlinear phenomena, for example to provide insights into the physics of how small insects get aloft [2, 3] and b) innovative design solutions such as the antenna of the Hubble telescope [4]. Moreover, nonlinearities were proved to be effective in: a) enhancing the performances of energy harvesters [5–9], b) exhibiting conformal shape adaptation (or morphing) capabilities [10–13], c) developing feedback controllers for aeroelastic systems [14–17] and so forth. Despite the achievements obtained so far, there is still a need to develop a systematic approach to optimize engineering systems and obtain full advantage of nonlinear behavior.

Automated design optimization is rapidly being adopted by engineers in nearly all major industries. This adoption is made possible by advances in high-performance computing, material characterization methods and enabling technologies, such as additive manufacturing, have led towards multi-scale and/or multi-field modeling, and simulation-based design of materials and systems in the aerospace industry [18].

To date, Integrated Computational Materials Engineering¹ (ICME) has been the catalyst for multi-scale design, decreasing the gap between the materials development cycle and product development cycle [19, 20]. Despite significant progress in the development of aerospace components and systems have been achieved, that progress has been limited by persistent technology and infrastructure challenges.

In a technical recent report [18], NASA envisages the use of computational materials tools and techniques, combined with structural engineering tools, to be the enabling factor for cost-effective, rapid, and revolutionary design of fit-for purpose materials, components and systems. The NASA's Vision 2014 emphasizes the role of optimization to achieve such goals. Particularly, the report underlined the importance of properly formulating the optimization problem such that the solutions are manufacturable designs². The need for advanced design and optimization tools and methods, as well as the developing of advanced materials and manufacturing technologies, is also underlined in the Fixed Wing project of NASA's Fundamental Aeronautics program. The new design paradigm exemplified in the Subsonic Fixed Wing project of NASA's Fundamental Aeronautics program aims to: a) develop revolutionary tools and methods enabling practical design, analysis and optimization, and (b) explore concepts and technologies to reduce the environmental impact of next generation transport aircraft. Particularly, gains in fuel efficiency can be achieved by means of structural weight reduction and higher aspect ratio. However, the resulting slender, lighter and highly flexible structures are prone to exhibit aeroelastic instabilities. In order to postpone the occurrence of such instabilities, aeroelastic tailoring plays a crucial role due to the extensive use of anisotropic structures. The importance of having a set spacing between the bending and torsional frequencies is clear if one considers that the onset of flutter instability is given by the coalescence of coupled bending and torsional mode [21]. This phenomenon can be anticipated due to the large deformations that High Aspect Ratio (HAR) wing undergoes during normal flight operations [22, 23].

The importance of the development of optimization methods for smart structures is discussed by Frecker [24], and emphasized in a review paper by Zhu and co-workers [25], where the challenges of conventional design and optimization methods

¹Integrated Computational Materials Engineering (ICME) is an approach to design products, the materials that comprise them, and their associated materials processing methods by linking materials models at multiple length scales (Source: Wikipedia).

²It is worth noting that the plural form is intentionally used to recognize that engineering design problems are likely to have multiple solutions, thereby permitting a range of design options.

for Micro Electro-Mechanical Systems (MEMS) are pointed out. A particular emphasis is posed onto the design of resonators. Resonators in fact, have a broad range of applications, including Atomic Force Microscopy (AFM), signal filtering, mass sensing, biological sensing, motion sensing, and other diverse applications. In [26], Tripathi and Bajaj they wrote “*Identifying or designing structures that will lead to 1:2 internal resonance between the different modes of vibration is not a trivial task. Most of the examples of such physical systems in the literature are based on prior experiences of the investigators.*”. To date, despite the huge effort undertaken there is not a systematic method to design resonators, as will be discussed in a dedicate section in the following.

In broad terms, the design of engineering systems is an optimization problem in nature. Looking at the work-flow during structural design, engineers modify the design variables such as material properties, node locations, cross-sectional geometries and topology to achieve a desired performance while respecting a set of given constraints. Thereby the entire structural design process may be seen as the problem of seeking for the set of design variables x_i which minimize/maximize a certain merit function $f(\vec{x})$ under given set of inequality and equality constraints, $g_j(\vec{x})$ and $h_k(\vec{x})$ respectively. Mathematically, the definition given above, can be written as in Gerhard [27], that is

$$\begin{aligned}
 & \underset{\vec{x} \in \mathbb{R}^n}{\text{minimize}} && f(\vec{x}) \\
 & \text{subject to} && g_j(\vec{x}) \leq b_j, \quad j = 1, \dots, m \\
 & && h_k(\vec{x}) = c_k, \quad k = 1, \dots, p \\
 & && x_{iL} \leq x_i \leq x_{iU} \quad i = 1, \dots, n
 \end{aligned}$$

being x_{iL} and x_{iU} the side constraints, i.e. the upper and lower bounds of any of the i – th design variables.

During the last decades several numerical methods have been proposed to handle optimization problems; those methods, according to Gandom *et al.* [28], can be classified as either deterministic or probabilistic. Mathematical programming methods are mostly gradient-based algorithms and are deterministic. Conversely, meta-heuristics and heuristics are mainly bio-inspired algorithms which have been developed on the basis of observed evolutionary behaviors; these methods belong to the class of probabilistic methods. Despite their slow convergence rate when com-

pared against the deterministic counterpart, heuristics offer the advantage of being more robust in terms of converge to the global solutions when multiple objectives have to be handled at once.

The distinctive features of heuristics are intensification/exploitation and diversification/exploration. Exploration ensure that the algorithm searches within the entire domain while exploitation is mostly related to the search of best candidates within a particular area. A fine balance of the two features significantly influences the performance of the optimization algorithm [29]. As a result of the above mentioned distinctive features and capabilities, and by virtue of the concurrently advancing in high performance computing, heuristics methods have been widely adopted to handle engineering problems. Countless algorithm have been proposed to handle optimization problems however, as discussed by Wolpert and Macready, there is not an *optimum* optimization algorithm [30]. The choice of the most suitable algorithm for a given problem is not trivial and usually leads to "the chicken and egg" dilemma. Indeed, the latter choice depends upon the characteristics of the design space that has been defined. Paradoxically, the characteristics of the design space are typically not known until the design space has been explored, which is the primary role of the search method. In view that some algorithms may perform better on a given class of problem, researchers, if not proposing novel optimization algorithm, rely on previous experiences and/or works to select a proper optimization technique.

This work is aimed at using optimization techniques to efficiently navigate the design space for structural systems. Particularly, the two design problems considered are the optimization of high aspect ratio anisotropic wings and the synthesis of resonators for scavenging purposes. Despite the main goal of the present work remains the design and optimization of engineering structures, the work provides insights also onto the algorithmic aspects.

1.2 Structural Tailoring: a short overview

According to the definition given by Shrik *et al.* [31],

“structural tailoring is the embodiment of directional stiffness into a structural design to control static or dynamic deformation in such a fashion as to affect structural performance in a beneficial way”

The first documented work related with aeroelastic tailoring is due to Munk [32], who optimized the orientation of the grains of a wooden propeller to achieve the best deformation couplings. Two pioneering projects related with the aeroelastic tailoring, which is worth mentioning, are the forward swept wings of the X-29 and the Active Aeroelastic Wing [33]. A comprehensive review of the aeroelastic tailoring for transport aircraft wings is given by Jutte and Stanford [34].

According to the definition given in [34], structural tailoring can be classified as: global (or uniform) tailoring and local tailoring. Global tailoring techniques seek at modifying the wing's primary stiffness direction, for example the wing's bending and torsional stiffness, as well as the degree of coupling between the two, to achieve a desirable performance. The primary stiffness direction is defined by Weisshaar as "*the locus of points where the structure exhibits the most resistance to bending deformation*" [35]. When global tailoring approach is used, structural properties such as bending and torsional stiffness are the design variables. For global tailoring, simplified structural models, such as beam-like and plate-like structures are generally adopted. Gasbarri *et al.* [36] pointed out that the approach is shortsighted in that, bending and torsional stiffnesses are treated as independent quantities and, as a consequence, there is no guarantees that a manufacturable design can be identified. However, the idealized models are particularly useful during preliminary design stages to help navigate the search space aiming at identify areas of feasible designs. While overlooked in most research effort, the idealized models have a prominent effect on the final aircraft; outcomes they provide may influence considerably the entire life-cycle costs [37].

On the other hand, local tailoring is applied when separate sections of the wing becomes design areas. This is a common choice for composite wings, where plies' orientations and/or the stacking sequence of each of the panel composing the wing are optimized separately to achieve desired cross sectional properties. However, the use of local variables, generally requires a large number of design's parameters which, in turn, render the optimization problem computationally expensive.

While it is true that high-fidelity models for aeroelastic tailoring have been developed, as mentioned in [34], the survey presented in the next section is mostly focused on to beam models. However, some interesting works are covered to motivate the lack of analytical/theoretical low fidelity models capable of representing the state of art of aerospace technologies.

1.2.1 Idealized beam models

Librescu and his co-workers were among the first to use a box-beam model, made of composite laminates, to model a wing [38, 39]. The focus of their work was on seeking potential advantages of using the bending-torsion coupling to postpone static aeroelastic instabilities. Weissnar and co-workers [35] investigated the effect of the aeroelastic tailoring on a wing modeled as a beam. On the basis of their analysis they concluded that, for Unmanned Air Vehicle UAV, aeroelastic tailoring may not yields a drastic weight reduction compared against the untailored structure but can offer improved aeroelastic performances with nearly the same weight.

Chattopadhyay *et al.* [40] performed a parametric analysis of box beams with thick walls employing higher-order laminate theory to model each wall of the box beam and concluded that : a) the flutter speed is affected by transverse shear deformations, b) the existence of various coupling modes, for different ply angles, strongly influence the wing aeroelastic behavior.

Cesnik *et al.* [41] performed an aeroelastic stability analysis for high-aspect ratio composite wings. The structural model they adopted is based on an asymptotically correct cross sectional formulation and a nonlinear geometric exact beam analysis. The work emphasize the importance of using the right stiffness formulation in order to model material couplings, the variations of divergence and flutter speeds with the changes in the lamination angle of a box-beam model of a wing cross section, and some of the effects of a nonlinear structural model on the aeroelastic stability of a slender wing.

Patil [42] analyzed a swept composite box beam, using a linear structural model and Theodorsen's theory to get unsteady aerodynamic forces. The wing was modeled as a thin-walled composite box beam of rectangular cross section. Patil has showed that the possibility of using material couplings in the structural tailoring process opens new frontiers to the design of a composite wing. Static and dynamic aeroelastic stability can be altered by those couplings.

Patil and co-workers [43] developed an aeroelastic analysis tool capable to model the complete aircraft as a set of beams. They used a geometrically exact mixed formulation for the structural dynamics analysis coupled to a finite-state air loads model. The results they obtained indicate the necessity of including higher-order nonlinear effects for accurate aeroelastic analysis. Patil [44] wrote: "*by efficiently*

designing the structural cross section one could provide some level of structural coupling which lead to shift of the nonlinear flutter speed/frequency”.

Gasbarri *et al.* [36] used a plate-like structure to address the integrated aerodynamic, dynamic and structural optimization problem for a composite wing-box design. They employed a hybrid multilevel decomposition procedure, which comprises an aeroelastic optimization of a composite wing based on the Sequential Quadratic Programming (SQP) and, a composite optimization using Genetic Algorithm (GA).

Koohi *et al.* [45] developed a 1D structural dynamics model for aeroelastic analysis of a composite wing under large deformations. The structural model was coupled with a semi-experimental unsteady aerodynamic (ONERA dynamic stall) model. They adopted a Finite Element formulation to discretize the aeroelastic equations. The cross-sectional properties of the wing were determined through the Variational Asymptotical Beam Sectional Analysis (VABS). The perturbed dynamic equations, about the nonlinear static equilibrium, were established to capture the flutter boundaries when the wing undergoes large deformations.

Wan *et al.* [46] presented an aeroelastic two-level optimization methodology for preliminary design of wing structures. In the first-level optimization, the parameters for structural layout and sizes were taken as design variables while aeroelastic constraints were considered in the second-level optimization. They used a simplified 2D finite element model where spars and stringers were modeled as bars, while skins and inter-space between upper and lower skins are treated as a multi-layer composites structure.

Continued research into advanced materials and structures is enlarging the aeroelasticity designs space. Examining at the most recent works in the field of aeroelastic tailoring, clearly illustrates how new technologies such as Variable Angle Tow (or Automated Fiber Placement) and 3D printing are paving the way to a myriad of potential manner of designing fit for purpose materials and structures. An example which is worth mention is given in Locatelli *et al* [47], where they used curved spar and ribs to enhance the performance of a civil aircraft. A comprehensive overview of the curvilinear placement fiber technology is given in Lozano [48]. A review of the mathematical modeling of tow steering fiber is given in Ribeiro *et al* [49]. AFP allows to place the fiber along a desired path giving rise to a laminate which has variable stiffness. Allowing the layup of curvilinear fibers has different benefit from

a structural perspective. Indeed it results in a better stress distribution and expands the design space compared to the conventional stacking sequence [50–54].

A comprehensive and detailed work on the potential enabling technologies for the aeroelastic tailoring is presented in Jutte *et al* [55]. They explored the use of tow steered composite laminates, functionally graded metals (FGM), thickness distributions, and curvilinear rib/spar/stringer topologies for aeroelastic tailoring. In their analysis they used a parametrized model of the NASA's Common Research Model as a reference model. They performed their analysis employing a finite element model. However, they pointed out that during the first stages, *"...formal optimization should be used to further locate the capabilities and trade-offs of the tailoring schemes..."*. They also wrote *"...the tradeoffs between straight and curvilinear members are significant enough that formal design optimization should expose new topological insights..."* and they concluded that *"The addition of spars increases the flutter resistance of the wing with a corresponding weight penalty. When spars are located toward the leading edge, the flutter point increases, such that a wing design with spars (and 4 stringers) can have the same flutter resistance as a wing design with 8 spars (and 0 stringers). This follows a well-known trend of pushing the CG forward for better flutter resistance"*.

Doyle *et al* [56], performed the optimization of the NASA ATW2 and ATW4 configuration aiming at postponing the onset of flutter instability. They obtained up to 6% increment of the flutter speed by using curvilinear spar and ribs. Stanford *et al* [57], performed a comparative study of curvilinear stiffeners and tow steered composite for aeroelastic tailoring of transport aircraft. They wrote that *"High local curvature is noted at the side-of-body and the aileron attachment locations, but gradual stiffener curvature spanning multiple panels is noted as well"*.

In view of the enlarged design space introduced by innovative technologies and reviewing the state of art of idealized beam model, emerges the lack of analytical/theoretical 1D model which considers variable stiffness. The latter is envisaged to be useful to identify promising design areas within the framework of earliest design stages, as pointed out in Jutte *et al* [55].

1.2.2 Material selection

Within the preliminary design stages, material and functional requirements have to be considered with great care since, erroneous assumptions and/or improper material choices can lead to unrealistic responses and ultimately waste of resources. In order to select the material on the basis of the performances enhancement, Material Selection Optimization (MSO) method have been proposed since the early '80s [58–62]. In spite of the huge effort undertaken, Material Selection Optimization (MSO), requires cumbersome and time-consuming computations. On the other hand, two alternative approaches are possible namely, performances indices or scaling and self-similarity methods [63, 64]. Performances indices are usually derived for a particular applications and lack to be generalized in order to provide guidelines for material selection [65–67]. To this end, within the preliminary design framework, scaling and self-similarities methods seem to be the most promising methods to predict the structural responses and perform a broadband investigation. These concepts have been only partially exploited for aeroelastic applications [64, 68, 69].

Bisplinghoff *et al* [68] presented the classical approach to aeroelastic scaling, based on the use of dimensional analysis and the fundamentals of the Buckingham's (π) theorem.

Bond *et al* [70] presented an aeroelastic scaling procedure that accounts for geometric nonlinearity by scaling the eigenvalue associated with the buckling load. They wrote *"The Goland wing model was used as a case study to demonstrate that both the natural frequencies and mode shapes must be matched to properly scale the aeroelastic response. A variant of the Goland wing joined with a strut was developed as the case study for scaling geometric nonlinearity. Scaling its first buckling eigenvalue together with the natural frequencies and mode shapes resulted in accurate aeroelastically scaled response in the initial nonlinear range. The fully nonlinear response of the scaled model decreased in accuracy as the critical load predicted by the buckling eigenanalysis was approached."*

Wan and Cesnik [69] proposed a methodology for geometrically nonlinear aeroelastic scaling of high aspect ratio aircraft. They extended the linear scaling factors and similarity rules to address geometrically nonlinear aeroelastic scaling. They noted the following: *"The analysis results indicate that the current existing aeroelastic scaling law for linear structure is also suitable for geometrically nonlinear*

structure with large deformation. It was shown that the scaling factors for the linear and nonlinear parts of the stiffness matrix follow the same similarity rule. Moreover, it is imperative that the Froude number similarity be met. The Froude number determines the ratio of the deflection under gravitational load to deflection due to aerodynamic and inertial loads. Satisfying the Froude number similarity guarantees that the large static wing deflection under initial trim condition is met, and therefore the nonlinear stiffness properties between models is satisfied as well. The stiffness has a direct impact into the static and dynamic aeroelastic response of the system. Reynolds-number similarity is also important particularly when its value is low enough for laminar/turbulence transition. In practice, however, matching the Reynolds number criterion may present a challenge in view of the other scaling factors.”

Cestino *et al* [64] applied the Buckingham’s theorem to design a small scale wing model of an High Aspect Ratio wing. On the basis of the set of 12 nondimensional parameters they identified, they built the small scale wing and conducted experimental tests. They concluded that the scale model’s reduced flutter frequency match closely the reduced frequency of the full scale model.

It is worth noting that for the works previously mentioned, the scaling was used to resize the structure in order to build a model suitable for wind tunnel tests. Contrary, in the framework of material selection, the scaling is limited to the elastic properties of the anisotropic material while all the other geometric parameters remain unchanged.

1.3 Design and optimization of electro-mechanical system

Tailoring the dynamic response of a structure based on its shape or topology can be a daunting task. However, this has been of particular interest to the design of resonators for kinetic energy harvesters and MEMS based resonators. MEMS design efforts is dated back to the late 1960s with the microscale resonant structure developed by Nathanson *et al* [71] for filtering purpose. Efforts in this area are: 1) ad hoc relying on structures with geometries that historically have been observed to exhibit certain dynamic behavior [72, 73] , 2) rely on shape optimization routines

that have restrictions on the geometry of the resonator [74–79], or 3) use techniques from topology optimization where the optimal distribution of material is determined computationally [80–84].

To the author’s knowledge, the first author showing that Multi Objective Genetic Algorithm (MOGA) combined with the open source SUGAR, yields meandering resonators was Zhou *et al* [74]. Kamalian *et al* [75] extended the work of Zhou. They discussed about the limitations of symmetry constraints previously used in MEMS design and on the role of human interaction in a computer-aided MEMS design. In their multi-objective optimization, Kamalian *et al.* relaxed the geometric constraints and noted that, the algorithm leads to unsymmetrical rather than meandering structure with the same frequencies and smaller occupied area.

Mukherjee *et al* [85] focused on parametric optimization of a MEMS accelerometer with predefined topology. They concluded that *”synthesis algorithms have been successfully applied to automatic layout of surface-micromachined accelerometers”*; however, because the configuration they selected had a fixed topology, it did not allow to identify radical and innovative designs. Agarwal *et al* [86] developed a grammar language to synthesize resonator topology. They noted that MEMS designs having small differences can have a substantially different behavior.

Kamalian and Agogino [87] proposed some modifications to the objectives and constraint settings of the GA formulation to synthesize designs that match more closely to the desired performance of MEMS when fabricated. Particularly, they imposed angle limitations to the synthesis procedure to avoid intersection of the beams composing the resonator.

In designing resonators that have 1:2 modal frequency ratio, the first approach has a long history in the research community. A common geometric configuration of resonators exhibiting this behavior are *L*-shaped structures. *L*-shaped resonators have been of interest to the dynamics community for several decades [88–91]. This structure can behave effectively as 2-DOF system with commensurate frequencies [89]. If the resonator is excited so that the response is nonlinear, it exhibits rich dynamic behavior by having: 1) strong modal interactions resulting in an energy exchange between the modes when the system is excited, i.e., an internal resonance, 2) both saddle-node and Hopf bifurcations, and 3) saturation, i.e., the amplitude of a mode being directly excited becomes independent of the level of excitation. In designing vibration energy harvesters (VEHs) the *L* shaped structure’s internally

resonant behavior has been exploited to improve the range of frequencies that energy can be extracted, [8, 92]. Harne *et. al* [9] exploited the saturation phenomena present in the L -shaped structure to enhanced the average power scavenged by the device.

Concurrently, VEHs have been designed with orthogonally oriented members essentially a collection of L -shaped resonators. These designs either: 1) maximize the power response [93], 2) in a fixed volume ensures a lower bending stiffness, an increase in mass or both [94–96]. The latter makes the devices suitable for harvesting energy at low frequencies.

Reviewing the research that uses techniques from structural optimization, several studies are noteworthy. Tripathi and Bajaj [79] presented a computational synthesis based on FEA to achieve natural frequencies of a structure in some desired ratio, notably 1:2 and 1:3. These planar, orthogonally connected multi-member structures are intended for MEMS applications. Deng *et al.* [97] used topology optimization to maximize the frequency response in the design of vibration energy harvesting electro-magnetic device. Furthermore Dou *et. al.* [84] presented a formulation based on shaped optimization to tailor the nonlinear response of a resonator that considers multiple modes in the response.

1.4 Objectives of the work

The primary objective of this work is to advantageously exploit dynamic phenomena to enlarge the design envelope and to improve performances of engineering systems. Two classes of problems are addressed, namely: optimization of unitized structures and synthesis of planar resonators. The two problems are connected in that the mathematical formulation fall within the same class of optimization problems, i.e. topology optimization. Moreover, provided some simplifications adopted for the planar resonator, the same beam model, i.e. Euler-Bernoulli beam, is adopted for the two problem in hand.

Beside the aforementioned objective, and closely related to the design of unitized structures, the work aim at derive an homogenization model of curvilinear stiffened structures. The latter being useful to bring the complex topology optimization problem, to a constrained combinatorial problem, where the design variables become the orientations of the stiffeners at prescribed control points.

Moreover, the work aims at exploiting the invariants' objective property to introduce a systematic method, as opposite to Material Selection Optimization, to select a proper material for a targeted application. The methodology can be cast within the scaling or self-similarity methods.

1.5 Layout of the thesis

The remainder of the thesis is organized as follow. Chapter 2 presents the derivation of the equivalent engineering properties of curvilinear stiffened panels. The derivation is two folds: the homogenized properties, i.e. panel-wise constant, and the variable stiffness properties are derived. The derivation is extended to concentric panels with one and two families of stiffeners. It is shown that the model presented is suitable for both stiffened and sub-stiffened panels.

Motivated by the results of the equivalent model, in chapter 3, we derive the non-linear equations of motion of an anisotropic, thin-walled box-beam. The equations of motion are derived by means of the Hamiltonian principle. Nonlinearities up to order two have been retained. Only geometric nonlinearities are considered. The beam is made by an arrangement of stiffened/unstiffened panels. Once the equivalent properties are derived as indicated in chapter 2, the Circumferentially Asymmetric Stiffness (CAS) model is used to evaluate the section-wise properties of the beam.

Chapter 4 introduces the Invariant-based scaling of anisotropic structures. Several examples pertaining scaling of composite structures are presented.

In chapter 5, we briefly introduce a novel optimization algorithm developed within the framework of this thesis to handle constrained combinatorial problems. Then we formulate and hence solve the optimization of the stiffeners topology in order to attain a prescribed structural behavior.

Chapter 6 presents the optimization of a multi-member truss structure. The objective of the optimization is the ratio between the bending frequencies; particularly structures that exhibit commensurate frequencies are sought. The design problem is formulated as topology optimization problem and solved using the Ground Structure Method. To handle the design complexity the topology optimization problem is formulated and hence solved by means of an in-house developed Genetic Algorithm

coupled with a double filtering strategy, namely the Graph-based Element Removal Method (GERM), originally developed in the framework of this work.

In view of the results obtained by the topology synthesis, in chapter 7 we derive the equations of motion of a cantilever, multi-member structure. The equations of motion are then parametrically solved in order to identify structures that exhibit commensurable frequencies in a ratio one-to-two and one-to-three. The analytical solution for the case of a two-members structure is also derived. Universal design chart for the one-to-two resonator are presented.

In chapter 8, the electro-mechanical equations of motion are derived for the case of a two members structure. The detailed analysis of the linear dynamic behavior of the angle-shaped resonator is presented.

Chapter 9 summarizes the results obtained in this work and draws some concluding remarks.

1.6 Contribution of the thesis

The main contributions of the present work are summarized hereto:

- The formulation two equivalent plate models of unitized panel with straight and curved stiffeners have been derived, respectively constant stiffness model and variable stiffness model. The limit of validity of the homogenized model have been identified. It is shown that the variable stiffness model is more accurate than the constant stiffness model in predicting buckling loads and frequencies of the stiffened structure.
- The development a second order nonlinear, flexural-flexural-torsional beam model which includes span-wise stiffness' variability. It has been shown that the stiffness variability enlarges significantly the design space for anisotropic structures.
- The introduction of a novel scaling procedure for anisotropic structure. The procedure relies on the objective properties of the stiffness' invariant. The procedure is effective in predicting the behavior of different anisotropic materials using linear scaling laws, irrespective of geometric nonlinearities. The scaling procedure is applicable to a variety of structural performances including:

deflection, mode of vibrations, divergence speed, buckling and post-buckling of anisotropic structures. The author envisages the use of such procedure within the framework of preliminary design to select the most promising anisotropic material on the basis of structural performance rather than other indexes unrelated to the structural behavior.

- The development of a novel optimization algorithm to deal with constrained combinatorial optimization has been presented. It has been shown that the algorithm outperforms other heuristics in terms of convergence rate and reliability when benchmark problems are considered.
- A Graph-based filtering scheme has been conceived to synthesize meaningful structures starting from Ground Structures with high cardinality. The filtering scheme, coupled with an in-house developed GA, has been used to design planar resonators and compliant structures. The GERM (Graph-based Element Removal Method) has led to unconventional topologies for planar resonators.
- Motivated by the results of the topology synthesis, a reduced order model (ROM) for multi-members resonators have been developed. The ROM was useful to establish a rule of thumb, i.e. a planar structure can be designed to have exactly N -commensurate frequencies, where N is the number of members constituting the resonator. Particularly, three class of resonators were introduced, namely: V- shaped (or angle shaped) resonator, Y-shaped and Z-shaped resonators. The reduced order model was used also to establish a systematic way to design resonators, i.e. the universal design charts. The electro-mechanical equations of motion for the V-shaped resonator have also been derived. It has been shown that the V-shaped resonator outperforms the L-shaped resonator in term of energy harvested.

The above mentioned contributions has led to the publications listed below. In the interest of clarity, the publications list is divided in two parts, namely publications with a major contribution of the author (developing the model, performing analysis and simulations, writing the main body of the article) and publications with minor contribution. The lists have been further divided in to: Journal publications and conference publications. Papers which are in preparation and/or under review, even if those paper are directly related to the Doctorate activities, have not been included.

1.6.1 Major contribution

Journal papers

1. Danzi, F., Gibert, J. M., Frulla, G. and Cestino, E. "*Generalized topology for resonators having N commensurate harmonics*". JOURNAL OF SOUND AND VIBRATION. Volume 419, 2018, pp 585-603, ISSN 0022-460X, <https://doi.org/10.1016/j.jsv.2017.10.001>.
2. Danzi, F., Frulla, G. and Romeo, G. "*An Invariant-based Performance-Oriented Procedure for Preliminary Design of Composite Structures*". AIR-CRAFT ENGINEERING AND AEROSPACE TECHNOLOGY, Volume 90, Issue 3, pp.532-541, <https://doi.org/10.1108/AEAT-11-2016-0228>.
3. Danzi, F., Frulla, G. and Cestino, E. "*Constrained combinatorial optimization of multi-layered composite structures by means of Stud GA with proportionate selection and extinction*". STRUCTURAL AND MULTIDISCIPLINARY OPTIMIZATION. Volume 55, Issue 6, pp. 2239–2257, ISSN 1615-1488, <https://doi.org/10.1007/s00158-016-1638-4>.
4. Danzi, F., Gibert, J. M., Frulla, G. and Cestino, E. "*Graph-based element removal method for topology synthesis of beam based ground structures*". STRUCTURAL AND MULTIDISCIPLINARY OPTIMIZATION. Volume 57, Issue 4, pp. 1809–1813, ISSN 1615-1488, <https://doi.org/10.1007/s00158-017-1818-x>.
5. Romeo, G., Danzi, F. and Tsai, S.W. "*Using Trace to Scale the Properties of Composite Materials*". JEC COMPOSITES, Volume 88, pp. 42-45, ISSN 1639-965X.

Conference papers

1. Danzi, F., Cestino, E., Frulla, G. and Gibert, J. M. "*Numerical and experimental validation of unitized beam model*". Proc. of 31st Congress of the International Council of the Aeronautical Sciences, Belo Horizonte (Brasil), 9-14 September, 2018.

2. Danzi, F. and Gibert, J. M. "*Exact dynamics of an angle-shaped resonator for energy scavenging applications*". Proc. of SPIE Smart Structures and Materials + Nondestructive Evaluation and Health Monitoring, 2018, Denver, Colorado (USA), 5-8 March 2018, <https://doi.org/10.1117/12.2296642>.
3. Danzi, F., Cestino, E., Frulla, G. and Gibert, J. M. "*Equivalent plate model of curvilinear stiffened panels*". Proc of 7th International Conference on Mechanics and Materials in Design, pp. 553-568, Albufeira (Portugal), 11-15 June 2017.
4. Danzi, F., Frulla, G., Cestino, E. and Gibert, J. M. "*MDO/MSO of Slender Thin Walled Box Beam Model*". Proc. of AIAA/ISSMO Multidisciplinary Analysis and Optimization Conference (2017). Denver, Colorado (USA), 5-9 June 2017, <https://doi.org/10.2514/6.2017-4323>.
5. Danzi, F., Gibert, J. M., Cestino, E. and Frulla, G. "*Topology Synthesis of Planar Ground Structures for Energy Harvesting Applications*". Proc. of SPIE Smart Structures+Nondestructive Evaluation and Health Monitoring (SS/NDE), Portland, Oregon (USA), 25-29 March 2017, <https://doi.org/10.1117/12.2257351>.
6. Romeo, G., Danzi F. and Cestino E. "*Multi-objective optimization of the composite wing box of solar powered HALE UAV*". Proc. of 29th Congress of the International Council of the Aeronautical Sciences, St. Petersburg (Russia), 7-12 September, 2014.

1.6.2 Minor contribution

1. Cestino, E.; Frulla, G., Duella, R., Piana, P., Pennella, F. and Danzi, F. "*Application of Structural Topology Optimization to Couple Thin-Walled Stiffened Box-Beams*". SAE Technical paper, SAE 2017 AeroTech Congress & Exhibition, Fort Worth, Texas (USA), 26-28 September 2017.
2. Frulla, G., Danzi, F. and Romeo, G. "*Preliminary design of anisotropic plate in critical and post-critical regime by extended Trace procedure*". Proc. of 11th International Aerospace Supply Fair (AIRTEC), Munich (Germany), 25-27 October 2016.

1.7 Others contribution

Here are listed some collateral works, unrelated to the work presented herein but performed during the PhD.

1. Cestino, E., Romeo, G., Piana, P. and Danzi, F. "*Numerical/experimental evaluation of buckling behaviour and residual tensile strength of composite aerospace structures after low velocity impact*". AEROSPACE SCIENCE AND TECHNOLOGY. Volume 54, 2016, pp 1-9, ISSN 1270-9638,<https://doi.org/10.1016/j.ast.2016.04.001>.
2. Romeo, G., Frulla, G., Cestino, E. and Danzi, F. "*Experimental buckling behavior of composite aerospace structures after low velocity impact*". JEC Europe 2015, Paris (France), 10-12 March 2015.

Chapter 2

Equivalent models of straight and curved reinforced structures

Some of the contents and derivations presented in this chapter have been previously published in the Proceedings of Mechanics and Materials in Design 2017

Danzi, F., Cestino, E., Frulla, G. and Gibert, J. M. "*Equivalent plate model of curvilinear stiffened panels*". Proc of 7th International Conference on Mechanics and Materials in Design, pp. 553-568, Albufeira (Portugal), 11-15 June 2017.

This chapter presents the derivation of two equivalent plate models of a curvilinear stiffened panel. The curved stiffeners are modeled as piecewise straight beams, neglecting the effect of the Jacobian of the curved beam on the strains and stresses. The effect of the curvature on the equivalent properties is investigated through a parametric analysis. Using a homogenization method, based on strain-energy density equivalence, the stiffnesses of the equivalent stiffener layer, in the following referred to as equivalent continuum layer, are derived. The derivation is further extended in order to identify the apparent engineering constants of the equivalent-stiffened layer. By virtue of the rank sub-additivity properties, it is demonstrated analytically that, for curved stiffeners, the homogenization give rise to full rank, i.e. invertible, matrices. This allows one to consider, according to the particular geometry of the stiffeners, whether it is possible or not neglect the effect of the transverse shear. The derivation presented herein is limited to one family of stiffeners in the symmetric, or concentric, configuration. However, it is shown in the chapter that, the equivalent

properties of lattice structures, i.e. structures with two stiffeners' families, can be obtained by superposition.

2.1 Overview of equivalent plate models for reinforced structures

In this section, we provide a short overview of the equivalent models for reinforced plate and shells with straight and curvilinear stiffeners. A comprehensive review of ortho-grids and braced panels is given in Nemeth [98].

Homogenization theories as well as surrogate models have been widely used in calculating effective properties of reinforced shells and plates. Homogenization is particularly useful in the early stages of building-block analysis for navigating the design space and identifying optimal preliminary configurations. The earliest works on equivalent stiffnesses of stiffened plates and shells date back to the beginning of last century, and are ascribed to Huber [99, 100] and Flugge [101], respectively.

Smith *et al.* [102] improved upon the formulation of Huber by accounting for the local interactions between the skin and the stiffeners. A more accurate treatment of shear stresses with respect to Huber's work was presented by Pfluger [103]. In Gomza *et al.* [104], they derived the effective plate thickness of stiffened plate. Benscoter and MacNeal [105], presented an equivalent plate theory, based on first-order difference equations, that includes transverse-shear deformations to study a straight multicell wing. Dow *et al.* [106], identified the fundamental repeating element of the stiffened plate with integral stiffeners and replaced each stiffener in the repeating element with a homogeneous orthotropic plate. They enforced a direct compatibility between the stiffeners and the equivalent repetitive element, that is the strains in the repeating-element stiffeners were related to the corresponding plate strains. Finally, they applied an energy equivalence method to calculate the expressions for twelve independent elastic constants. Crawford and Libove [107] presented a study that focused on the torsional stiffness of orthogonally stiffened plates. Hoppmann, in a series of successive works prevalently related to experimental measures, derived the effective stiffness moduli to describe accurately the bending behavior [108] and the elastic compliances [109] of orthogonally stiffened plates.

Huffington [110] introduced a method based on the strain energy equivalence between an infinitely long stiffened plate and an orthotropic plate to calculate the expressions of concentric orthogonally stiffened panels. Heki and Saka [111] derived the closed form expressions for the stiffnesses associated with the homogeneous isotropic stiffeners with negligible in-plane shear stiffnesses. Won [112] presented a set of equations for homogeneous isotropic beam stiffeners with rectangular cross-sections. The expressions given by Won are for a pair of oblique stiffener families and include higher-order effects associated with the interaction of the plate wall with the stiffeners while neglecting the transverse shear stiffnesses.

Pshenichnov [113] derived the expression of the stiffness for an equivalent single-layer plate-like and shell-like ortho-grid structures. The equivalent stiffnesses presented are based on a classical shell theory and are obtained by using tensor transformations to equate beam strains with corresponding shell strains and by equating shell stress resultants with transformed beam forces. The latter were presumed uniformly distributed across the equivalent shell wall. Although the analysis is based on a classical shell theory, the effects of stiffener bending in the tangent plane is included expressing the beam shearing forces that acts in the tangent plane in terms of the derivatives of the corresponding beam moments. The beam bending strain is obtained in terms of the shell tangential displacements and strains by considering deformation associated with rotation about the unit vector normal to the middle surface. Although this approach captures tangential stiffener bending effects, the effects cannot be represented directly in terms of the shell strains and, as a result, are not accounted into the equivalent stiffness expressions.

Jaunky *et al.* [114] introduced a refined smeared-stiffener theory for grid-stiffened laminated-composite accounting for the variation of the neutral surface caused by interactions between the skin and the stiffeners. In Chen and Tsai [115], they presented the equivalent stiffnesses for laminated composite grid plates and circular cylindrical shells. In their study, generally laminated walls stiffened with ribs, stringers, and a pair of identical diagonal stiffeners with an arbitrary orientation angle were considered. Grid-stiffness expressions are given that include out-of-plane (transverse) and in-plane shear flexibility of the stiffeners and in-plane stiffener bending. Slinchenko [116] derived the equivalent stiffnesses for homogeneous isotropic stiffeners with negligible in-plane shear and torsional stiffnesses.

Kapania and co-workers [117] were the first introducing the concept of curvilinear stiffened panel. In the earliest work they performed numerical studies to investigate the effects of orientation, spacing, location, and curvature of the stiffeners on the optimal designs. They noted that a curvilinear stiffeners, in some circumstance, resulted in a better design than straight stiffeners in terms of buckling load resistance. Moreover, they found that gradient-based optimization techniques are inadequate to optimize panels with curvilinear stiffeners. Joshi *et al.* [118] presented a surrogate model based on Response Surface (RS) to optimize curvilinear stiffened panels in terms of end point design and curvature.

Locatelli *et al.* [47] introduced a design/optimization framework SpaRibs to optimize unitized wing-box structures. Tamijani and Kapania [119] adopted an Element Free Galerkin method to study the effect of stiffeners' number and size onto the natural frequencies of curvilinear stiffened panels. The formulation they implemented is based on first order shear deformation theory. Wang *et al* [120] used a double-scale scheme to derive the equivalent properties of a curvilinear stiffened panel. At the macroscopic level the panel is treated as a continuum plate, the equivalent properties were derived imposing the strain energy equivalence between the stiffened structure and a small cell. At the microscopic level they used periodic boundary conditions to correlate the behavior of adjacent cells. They used the Block's wave theory to study local instability of the plate and the homogenization method to derive global instability.

Although curvilinear stiffeners have been already proven to be effective in enhancing the structural performances, most of the works already presented in the open literature are performed using finite element models [34, 47, 57, 117, 118, 121]. Equivalent model have the advantage of simplifying the physics to gain insights into the problem and identifying promising solutions. Moreover, to achieve one the objectives of this work, i.e., to derive an equivalent 1D model of unitized structure, homogenization is an essential step to reduce the complexity of the problem. Indeed, once an equivalent model is established, the circumferentially asymmetric structure model can be used to derive the equivalent beam stiffnesses. The derivation of the equivalent beam stiffnesses is addressed in the subsequent chapter. This chapter is aimed at deriving a systematic set of equations for equivalent continuum model of straight and curved stiffened panels. The model is meant to shade light into the attainable performances. The apparent engineering properties of the resulting 2D anisotropic material are derived. To assess the validity of the proposed method, a

comparative study of the buckling loads and frequencies of simply supported panels is carried out. Results for the stiffened structures are compared against those of the equivalent models. In Figure 2.1 is reported an exemplification of the stiffened structure and the equivalent model that we aim to derive.

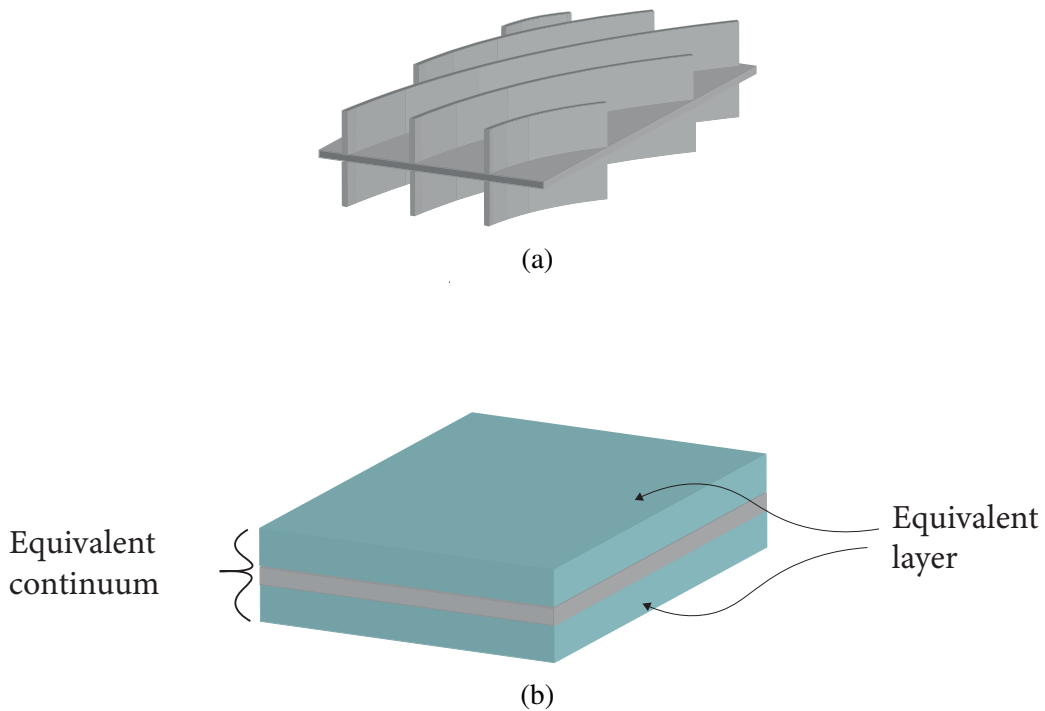


Fig. 2.1 Example of (a) stiffened plate and (b) equivalent continuum structure

2.2 Structural model

The structural model is derived on the basis of first-order transverse-shear deformation theory for anisotropic plates (Reissner-Mindlin type). The stiffeners are modeled consistently using the FSDT beam theory (Timoshenko). Two basic repetitive elements useful respectively to enforce the direct compatibility and to impose the strain energy density equivalence are introduced. The direct compatibility is established relating the stress and strain resultants of the repeating element stiffeners to the corresponding plate strains, as in [98, 106]. Consistent with the work of Nemeth

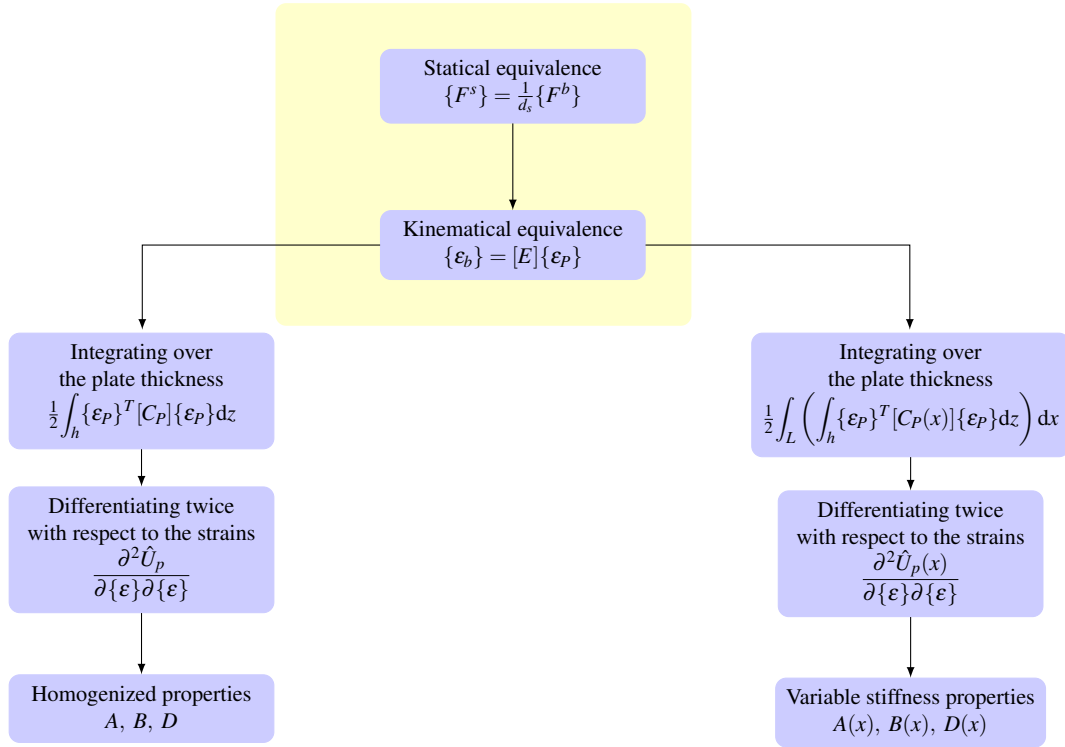


Fig. 2.2 Flowchart of the numerical implementation of the equivalent models.

[98] and Pshenichnov [113], the variation of the stress resultants across the width of the stiffeners is neglected. This assumption holds for thin stiffeners, as those considered in the present analysis. Contrary to Zhao [122] and Slinchenko [116] and, in accordance with the derivation presented by Crawford [107] and Nemeth [98], the torsional rigidity of the stringers is retained in the present derivation.

The local orientation of the stiffeners is presumed to vary linearly as in [51] for tow-placed fibers and [120] for curved stiffeners. The stiffeners' orientation $\vartheta(x)$ is given as

$$\vartheta(x) = \vartheta_1 + \frac{\vartheta_2 - \vartheta_1}{b}x \quad (2.1)$$

being b the panel length, as shown in Figure 2.3. The stiffeners path satisfies the following Equation

$$\frac{dy}{dx} = \tan \vartheta. \quad (2.2)$$

The derivation is based on the assumption that a curved beam can be faithfully represented by a collection of piece-wise rectilinear oriented beams. The aforemen-

tioned assumption will be justified later on in the chapter and it will be shown that gives rise to the limits of validity of the models presented herein.

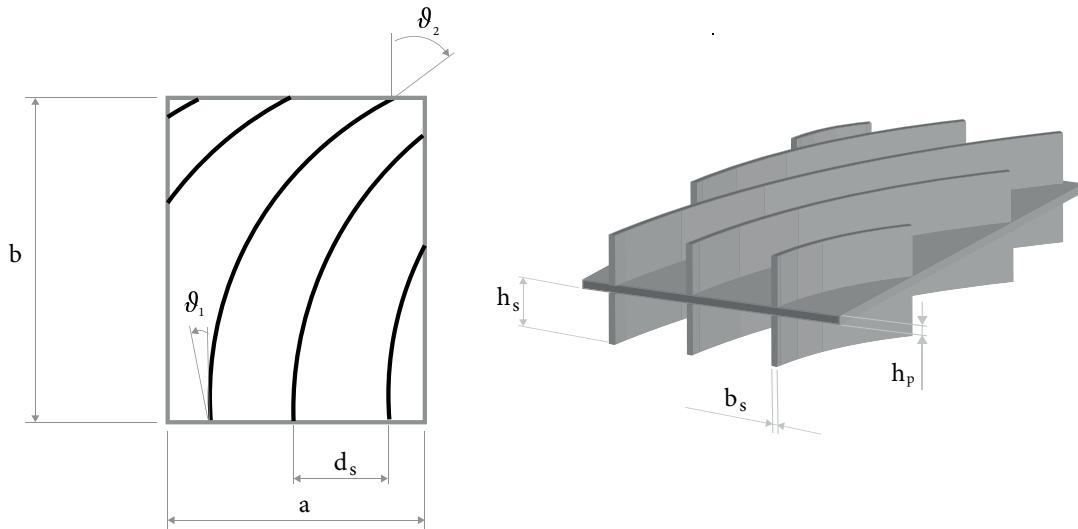


Fig. 2.3 Example of steering stiffened panel. The figure shows the main features of the stiffened panels considered in this work.

2.3 Direct compatibility

Following Dow [106] and Nemeth [98], the direct compatibility is derived for a family of rectilinear and equally spaced stiffeners. The stiffeners are presumed being oriented with an angle $\vartheta(x)$ with respect to the x -axis of the plate. The prismatic rectangular stiffeners are in the symmetric (or concentric) configuration and perfectly bonded to the skin panel. The material points of the beam are located on the local Cartesian coordinates XYZ , which follow the stiffeners orientation as shown in Figure 2.4.

2.3.1 Statical equivalence

In order to establish the statical equivalence, the stress resultants of the equivalent continuum layer, expressed in the XYZ coordinate system, must be equal to the beam's forces and moments. Denoting with the superscript "p" and "s" respectively

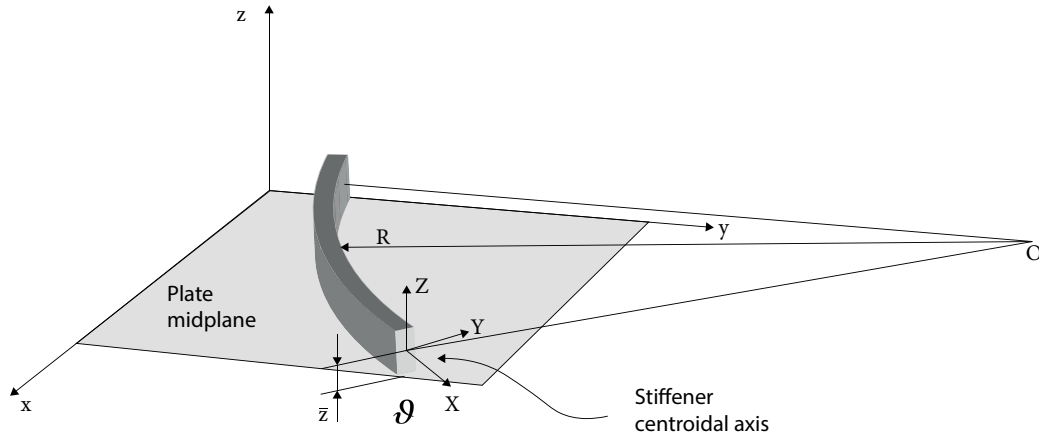


Fig. 2.4 Reference systems for the plate xyz and stiffeners XYZ respectively.

the contribution of the plate and stiffeners, the stress resultants of the stiffened plate are given by the following set of equations

$$N_{xx} = \int_{-h/2}^{h/2} \sigma_{xx} dz = N_{xx}^p + 2N_{xx}^s, \quad (2.3a)$$

$$N_{xy} = \int_{-h/2}^{h/2} \tau_{xy} dz = N_{xy}^p + 2N_{xy}^s, \quad (2.3b)$$

$$M_{xx} = \int_{-h/2}^{h/2} z \sigma_{xx} dz = M_{xx}^p + 2M_{xx}^s, \quad (2.3c)$$

$$M_{xy} = \int_{-h/2}^{h/2} z \tau_{xy} dz = M_{xy}^p + 2M_{xy}^s, \quad (2.3d)$$

$$Q_{xz} = \int_{-h/2}^{h/2} \tau_{xz} dz = Q_{xz}^p + 2Q_{xz}^s, \quad (2.3e)$$

where h is the total thickness of the stiffened plate, i.e. $h = h_p + 2h_s$ where h_p and h_s are respectively the plate and stiffeners thicknesses. Note that the definition above still holds for eccentric stiffeners except that the factor 2 should be dropped from the stress resultants. In this latter case, Equations 2.3 agree with those given by Nemeth for a family of equally spaced eccentric stiffeners. Focusing onto the stiffeners contribution, the stress resultants for the Timoshenko beam are given as follows:

$$N_x^b = \int_{A_s} \sigma_{xx} dA_s, \quad (2.4a)$$

$$T_y^b = \int_{A_s} \tau_{xy} dA_s, \quad (2.4b)$$

$$T_z^b = \int_{A_s} \tau_{xz} dA_s, \quad (2.4c)$$

$$M_{xy}^b = \int_{A_s} (y\sigma_{xx} - z\sigma_{xx}) dA_s, \quad (2.4d)$$

$$M_y^b = \int_{A_s} z\sigma_{xx} dA_s, \quad (2.4e)$$

$$M_z^b = \int_{A_s} y\sigma_{xx} dA_s = 0, \quad (2.4f)$$

where A_s is the stiffener cross sectional area and the apex b stands for beam. The positive signs for the axial N_x and shear forces T_y and T_z as well as those of the moments are depicted in Figure 2.5. Noting that the forces and moments given in the Eqns 2.3 are forces and moments per unit length, it follows that Eqns 2.4 can be equated to the Eqns 2.3 dividing by d_s , being d_s the stiffeners' spacing, as shown in Figure 2.3. It should be noted that the moment M_z vanishes because we neglected the variation of σ_{xx} along the stiffener width. This assumption is consistent with the plate continuum model and agrees also with the assumption made by Nemeth. Since we assumed that the stresses are constant along the beam width, one have that the Eqns 2.4 can be written as

$$N_x^b = d_s \int_{h_p/2}^{h/2} \sigma_{xx} dz, \quad (2.5a)$$

$$T_y^b = d_s \int_{h_p/2}^{h/2} \tau_{xy} dz, \quad (2.5b)$$

$$T_z^b = d_s \int_{h_p/2}^{h/2} \tau_{xz} dz, \quad (2.5c)$$

$$M_{xy}^b = d_s \int_{h_p/2}^{h/2} (y\sigma_{xx} - z\sigma_{xx}) dz, \quad (2.5d)$$

$$M_y^b = d_s \int_{h_p/2}^{h/2} z\sigma_{xx} dz. \quad (2.5e)$$

Finally, the beam's stress resultants on the equivalent continuum layer are given as

$$N_{xx}^s = \frac{N_x^b}{d_s}, \quad (2.6a)$$

$$N_{xy}^s = \frac{T_y^b}{d_s}, \quad (2.6b)$$

$$M_{xx}^s = \frac{M_y^b}{d_s}, \quad (2.6c)$$

$$M_{xy}^s = -\frac{M_{xy}^b}{d_s}, \quad (2.6d)$$

$$Q_{xz}^s = \frac{T_z^b}{d_s}, \quad (2.6e)$$

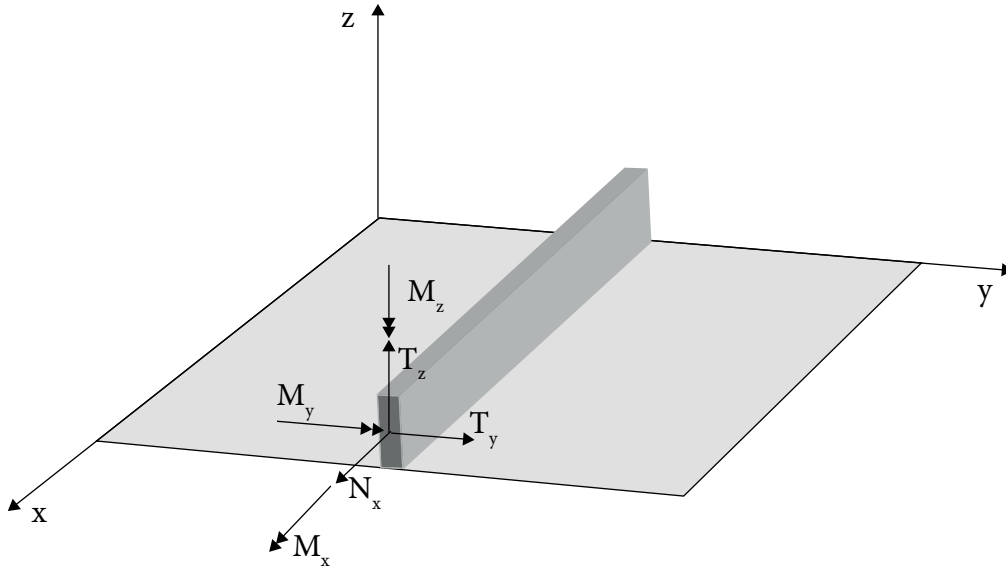


Fig. 2.5 Stress resultants acting on the generic stiffeners.

Notice that the terms on the left-end side of Eqns 2.6 are the stress resultants onto the stiffeners rewritten into the equivalent continuum layer, consistently with the plate theory. The negative sign in Eq. 2.6d is due to the different convention adopted for the twisting between the beam and plate model, as depicted in Figure 2.5 and Figure 2.6 respectively.

2.3.2 Kinematical equivalence

In order to enforce a full compatibility among the discrete stiffened structure and the equivalent continuum model, we need to establish the kinematical equivalence. The latter being established imposing that the strains in any point of the equivalent continuum layer are equal to the strains in any point of the stiffeners. Consistently

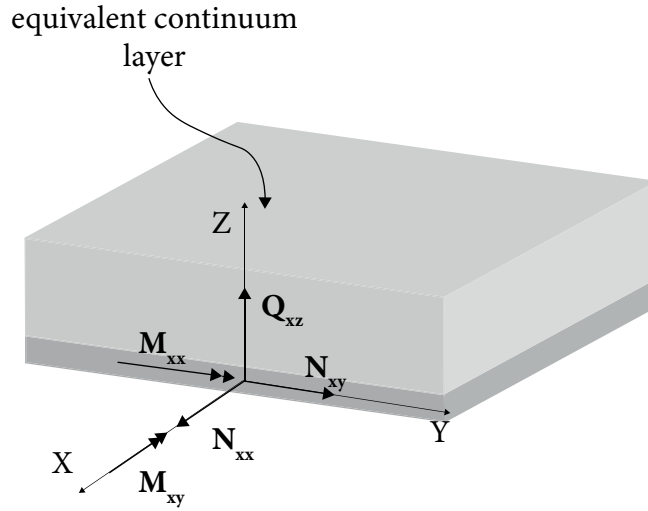


Fig. 2.6 Plate stress resultants onto the equivalent continuum layer.

with the assumption that yielded $M_z = 0$, the variation of the strain along the stiffeners width is neglected. Noting that the shear and twisting deformations act only on one face of the stiffeners while on both faces of the differential plate element, the stiffeners are presumed contributing only to half of the shear deformation. The resulting linear strains, according to the First Order Shear Deformation Theory, are given as in Reddy [123]

$$\varepsilon_{xx} = \frac{\partial u^{(0)}}{\partial x} + z \frac{\partial \psi_x}{\partial x} = \varepsilon_{xx}^{(0)} + z \kappa_{xx}, \quad (2.7a)$$

$$\varepsilon_{yy} = \frac{\partial v^{(0)}}{\partial y} + z \frac{\partial \psi_y}{\partial y} = \varepsilon_{yy}^{(0)} + z \kappa_{yy}, \quad (2.7b)$$

$$\gamma_{xy} = \left(\frac{\partial u^{(0)}}{\partial y} + \frac{\partial v^{(0)}}{\partial x} \right) + z \left(\frac{\partial \psi_x}{\partial y} + \frac{\partial \psi_y}{\partial x} \right) = \gamma_{xy}^{(0)} + z \kappa_{xy}, \quad (2.7c)$$

$$\gamma_{xz} = \frac{\partial w^{(0)}}{\partial x} + \psi_x \equiv \gamma_{xz}^{(0)}, \quad (2.7d)$$

$$\gamma_{yz} = \frac{\partial w^{(0)}}{\partial y} + \psi_y \equiv \gamma_{yz}^{(0)}, \quad (2.7e)$$

$$\varepsilon_{zz} = 0, \quad (2.7f)$$

where $\varepsilon_{xx}^{(0)}$ and $\varepsilon_{yy}^{(0)}$ are the extensional strains, $\gamma_{xy}^{(0)}$ is the in-plane shear strain, κ_{ij} are the bending curvatures, finally $\chi_{xz}^{(0)}$ and $\chi_{yz}^{(0)}$ are the transverse shear strains. Now, being $\varepsilon_b^T = \{e_x^{(0)}, \Gamma_{xy}^{(0)}, \Gamma_{xz}^{(0)}, \chi_z^{(0)}, \chi_y^{(0)}, \tau_{xz}^{(0)}\}$ the strains for the Timoshenko beam and, $\varepsilon_P^T = \{\varepsilon_{xx}^{(0)}, \varepsilon_{yy}^{(0)}, \gamma_{xy}^{(0)}, \kappa_{xx}^{(0)}, \kappa_{yy}^{(0)}, \kappa_{xy}^{(0)}, \gamma_{yz}^{(0)}, \gamma_{xz}^{(0)}\}$ the strains for the Reissner-Mindlin plate, one have

$$e_x = \varepsilon_{xx}^{(0)}, \quad (2.8a)$$

$$\Gamma_{xy}^{(0)} = \frac{1}{2} \chi_z^{(0)}, \quad (2.8b)$$

$$\Gamma_{xz}^{(0)} = \chi_y^{(0)}, \quad (2.8c)$$

$$\chi_z^{(0)} = 0, \quad (2.8d)$$

$$\chi_y^{(0)} = \kappa_{xx}^{(0)}, \quad (2.8e)$$

$$\tau_{xz}^{(0)} = -\frac{1}{2} \kappa_{xy}^{(0)}, \quad (2.8f)$$

where $\chi_z^{(0)}$ and $\chi_y^{(0)}$ are the strains due to the change of curvature of the beam, $\tau_{xz}^{(0)}$ is the strain due to the torsion of the beam and finally, $\Gamma_{xy}^{(0)}$ and $\Gamma_{xz}^{(0)}$ are the strains due to the shear forces T_y and T_z . Equations 2.8 in matrix form become

$$\{\varepsilon_b\} = [E]\{\varepsilon_P\} \quad (2.9)$$

being E given by

$$E = \begin{bmatrix} 1 & 0 & 0 & 0 & 0 & 0 & 0 & 0 \\ 0 & 0 & 1/2 & 0 & 0 & 0 & 0 & 0 \\ 0 & 0 & 0 & 0 & 0 & 0 & 0 & 1 \\ 0 & 0 & 0 & 0 & 0 & 0 & 0 & 0 \\ 0 & 0 & 0 & 1 & 0 & 0 & 0 & 0 \\ 0 & 0 & 0 & 0 & 0 & -1/2 & 0 & 0 \end{bmatrix}. \quad (2.10)$$

Equation 2.9 relates the generalized strains of the Timoshenko beam model to those of the Reissner-Mindlin plate model.

2.4 Energy equivalence method

In the previous section the direct compatibility equations are derived for a family of straight but oriented, concentric stiffeners. In this section a homogenization technique based on strain energy density equivalence is presented; the method is useful to derive the stiffnesses of a family of curved stiffeners. To establish the energy density equivalence it is worthwhile to define the basic cell, i.e. the simplest element that will generate the whole stiffened geometry by simple translation over the stiffeners centroidal plane. Aiming at approximating the curved stiffeners path, a set of sub-cells is defined. The basic cell is then given as the union of the sub-cells. The direct compatibility is enforced within the sub-cell, where the stiffener is presumed to be straight. An example of the basic cell and sub-cell is given in Figure 2.7.

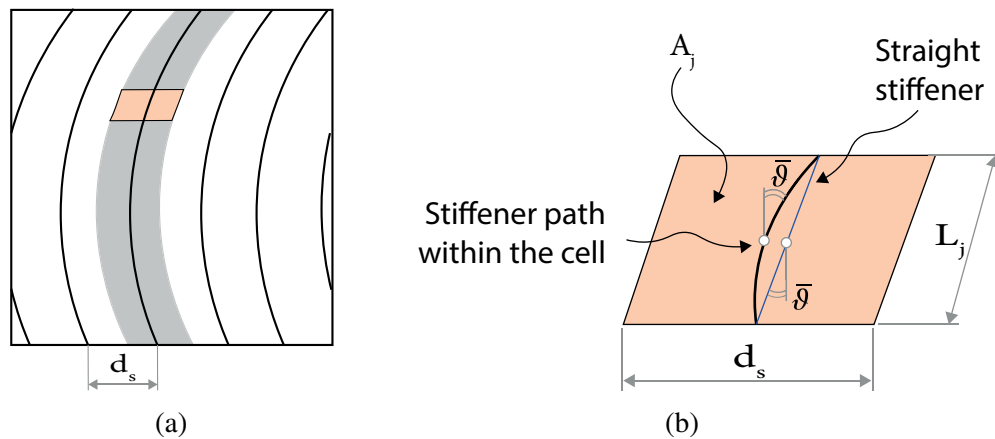


Fig. 2.7 Exemplification of the basic cell Fig. (a) (shaded gray area) and subcell (shaded red area). Fig. (b) shows a detailed view of the subcell area where the strain energy density is evaluated.

The idea behind this energy-based homogenization method is that the basic unit, i.e. the sub-cell, is small enough compared to the overall structural dimensions such that the strain-energy density within it can be approximately represented by a constant value. No overlapping of the sub-cells nor of the basic repetitive cell is premised.

The derivation starts by writing the expression of the strain energy for the Timoshenko beam as in Nemeth [98]. Being $[C_b]$ the constitutive matrix for the beam and denoting with L_j the length of the sub-cell, the strain energy for the beam is

given as

$$U_b = \frac{1}{2} \int_{L_j} \{\boldsymbol{\varepsilon}_b\}^T [C_b] \{\boldsymbol{\varepsilon}_b\} dX \quad (2.11)$$

where $[C_b]$ is given as follow

$$[C_b] = \begin{bmatrix} EA_s & 0 & 0 & EA_s \bar{y} & EA_s \bar{z} & 0 \\ 0 & k_y GA_s & 0 & 0 & 0 & -k_y GA_s \bar{z} \\ 0 & 0 & k_z GA_s & 0 & 0 & k_z GA_s \bar{y} \\ EA_s \bar{y} & 0 & 0 & EI_{zz} & EI_{yz} & 0 \\ EA_s \bar{z} & 0 & 0 & EI_{yz} & EI_{yy} & 0 \\ 0 & -k_y GA_s \bar{z} & k_z GA_s \bar{y} & 0 & 0 & GJ_t \end{bmatrix}. \quad (2.12)$$

being E, G the Young modulus and the shear modulus of the isotropic material (or equivalently the effective modulus for the case of a special orthotropic material), k_y and k_z are the shear correction factors, I_{yy} and I_{zz} are the second area moment of inertia with respect to the y and z axis respectively, I_{yz} is the product moment of area, $\bar{y} = 0$ having assumed the coordinate system XYZ to be centroidal, \bar{z} is the distance between the centroidal axis of the stringer and the plate midplane (see Figure 2.4) and, finally J_t is the torsional moment of inertia. In this work J_t is evaluated as in Wang [124]

$$J_t = \frac{1}{3} b^3 h \left[1 - \frac{192b}{\pi^5 h} \sum_{n=1}^5 \frac{1}{(2n+1)^5} \tanh \left(\frac{(2n+1)\pi h}{2b} \right) \right]. \quad (2.13)$$

Equivalently, recalling that $\boldsymbol{\varepsilon}_P^T = \{\boldsymbol{\varepsilon}_{xx}^{(0)}, \boldsymbol{\varepsilon}_{yy}^{(0)}, \boldsymbol{\gamma}_{xy}^{(0)}, \boldsymbol{\kappa}_{xx}^{(0)}, \boldsymbol{\kappa}_{yy}^{(0)}, \boldsymbol{\kappa}_{xy}^{(0)}, \boldsymbol{\gamma}_{yz}^{(0)}, \boldsymbol{\gamma}_{xz}^{(0)}\}$, the strain energy for the beam written in the equivalent plate-strains assumes the following form

$$U_P = \frac{1}{2} \int_{L_j} \{\boldsymbol{\varepsilon}_P\}^T [C_P] \{\boldsymbol{\varepsilon}_P\} dX \quad (2.14)$$

where $[C_p] \in \mathbb{R}^{8 \times 8}$ is given as

$$[C_p] = [E]^T [C_b] [E]$$

$$= \begin{bmatrix} EA_s & 0 & 0 & EA_s \bar{z} & 0 & 0 & 0 & 0 \\ 0 & 0 & 0 & 0 & 0 & 0 & 0 & 0 \\ 0 & 0 & \frac{1}{4} k_y GA_s & 0 & 0 & \frac{1}{4} k_y GA_s \bar{z} & 0 & 0 \\ EA_s \bar{z} & 0 & 0 & EI_{zz} & 0 & 0 & 0 & 0 \\ 0 & 0 & 0 & 0 & 0 & 0 & 0 & 0 \\ 0 & 0 & \frac{1}{4} k_y GA_s \bar{z} & 0 & 0 & GJ_t & 0 & -\frac{1}{2} k_z GA_s \bar{y} \\ 0 & 0 & 0 & 0 & 0 & 0 & 0 & 0 \\ 0 & 0 & 0 & 0 & 0 & -\frac{1}{2} k_z GA_s \bar{y} & 0 & k_z GA_s \bar{y} \end{bmatrix}. \quad (2.15)$$

It is worth noting that the stiffness matrix given in Eq. 2.15 is rank deficient therefore, in this form, is not invertible. The equations given above agree with those given in [98] and differ from that of the classic smeared stiffness approach for the presence of the transverse shear. The strain energy written as in Eqn. 2.14 is in the local reference frame, oriented within the sub-cell at an angle $\bar{\vartheta}$, being the latter the averaged orientation of the stiffeners within the subcell, as shown in Figure 2.7.

Next, the reference system XYZ must be rotated to align the beam to the plate global reference system xyz . It follows that

$$U_p = \frac{1}{2} \int_{L_j} \{\epsilon_p\}^T [C_p] \{\epsilon_p\} dx \quad (2.16)$$

where $[C_p] = [T]^T [C_p] [T]$.

The transformation $T \in \mathbb{R}^{8,8}$ matrix is given as

$$\begin{bmatrix} [T_\epsilon] & [0] & [0] \\ [0] & [T_\epsilon] & [0] \\ [0] & [0] & [T_t] \end{bmatrix}, \quad (2.17)$$

where

$$[T_\epsilon] = \begin{bmatrix} \cos^2 \bar{\vartheta} & \sin^2 \bar{\vartheta} & \cos \bar{\vartheta} \sin \bar{\vartheta} \\ \sin^2 \bar{\vartheta} & \cos^2 \bar{\vartheta} & \cos \bar{\vartheta} \sin \bar{\vartheta} \\ -2 \cos \bar{\vartheta} \sin \bar{\vartheta} & 2 \cos \bar{\vartheta} \sin \bar{\vartheta} & \cos^2 \bar{\vartheta} - \sin^2 \bar{\vartheta} \end{bmatrix}, \quad (2.18)$$

and

$$[T_t] = \begin{bmatrix} \cos \bar{\vartheta} & -\sin \bar{\vartheta} \\ \sin \bar{\vartheta} & \cos \bar{\vartheta} \end{bmatrix}, \quad (2.19)$$

being

$$\bar{\vartheta} = \frac{\vartheta|_{x_j=0} + \vartheta|_{x_j=L_j}}{2}. \quad (2.20)$$

So far, the beam's strain energy have been rewritten using the equivalent-plate strains and then transformed it to align the beam reference system to the plate reference system. It is worth noting that being $[C_p]$ a rank deficient matrix, and being the rotation an affine transformation, the rank is preserved thus, the rotated stiffness matrix $[C_p]$ is still rank deficient. Despite the constitutive matrix of the beam written in the plate reference $[C_p]$ is singular, the energy equivalence method leads to full rank, thus invertible, matrices, except for the case of straight stiffeners. This aspect deserves some more discussion that will be addressed in the next section.

Based on the presumption that the sub-cell is small enough, the strain energy can be approximated as follow

$$U_p = \frac{L_j}{2} \{\varepsilon_p\}^T [C_p] \{\varepsilon_p\}, \quad (2.21)$$

the strain energy density per unit area is given by

$$\hat{U}_p = \frac{U_p}{A_j} \quad (2.22)$$

where A_j is the area of the sub-cell. From Figure 2.7 follows that $A_j \approx L_j d_s \cos \hat{\vartheta}$. The strain energy density for the equivalent continuum layer is then given as

$$2\hat{U}_p = n_s \sum_{j=1}^{n_{sc}} \frac{\{\varepsilon_p\}^T [C_p] \{\varepsilon_p\}}{d_s \cos \hat{\vartheta}} = \int_0^{h_s} \{\varepsilon\}^T [Q] \{\varepsilon\} dz, \quad (2.23)$$

where n_s is the number of stiffeners, n_{sc} is the number of sub-cells, and $[Q]$ on the right-hand side of the eq. 2.23 is the reduced stiffness matrix of the equivalent-continuum layer. Likewise, in the limit for $n_{cell} \rightarrow \infty$ one have

$$\begin{aligned} \lim_{n_{cell} \rightarrow \infty} \bar{\vartheta} &\rightarrow \vartheta(x), \\ \lim_{n_{cell} \rightarrow \infty} 2\hat{U}_p &\Rightarrow \int_0^{h_s} \{\varepsilon\}^T [Q(x)] \{\varepsilon\} dz. \end{aligned} \quad (2.24)$$

Finally, taking the derivatives of the quadratic forms given in the Eqns. 2.23 and 2.24 respectively, gives the stiffness matrices of the equivalent continuum layer. The

resulting stiffness matrices are given as

$$[A^{stiff}] = \frac{L_s}{A_{cell}} \begin{bmatrix} C_p^{11} & C_p^{12} & C_p^{13} \\ C_p^{21} & C_p^{22} & C_p^{23} \\ C_p^{31} & C_p^{32} & C_p^{33} \end{bmatrix}, \quad (2.25a)$$

$$[B^{stiff}] = \frac{L_s}{A_{cell}} \begin{bmatrix} C_p^{14} & C_p^{15} & C_p^{16} \\ C_p^{51} & C_p^{24} & C_p^{26} \\ C_p^{61} & C_p^{62} & C_p^{36} \end{bmatrix}, \quad (2.25b)$$

$$[D^{stiff}] = \frac{L_s}{A_{cell}} \begin{bmatrix} C_p^{44} & C_p^{45} & C_p^{46} \\ C_p^{54} & C_p^{55} & C_p^{56} \\ C_p^{64} & C_p^{65} & C_p^{66} \end{bmatrix}, \quad (2.25c)$$

$$[A_T^{stiff}] = \frac{L_s}{A_{cell}} \begin{bmatrix} C_p^{77} & C_p^{78} \\ C_p^{87} & C_p^{88} \end{bmatrix}. \quad (2.25d)$$

In this case, the stiffeners in the concentric configurations the membrane-bending coupling matrix B is zero. Following the same procedure discussed above, one can obtain the stiffness matrices of the equivalent continuum plate adjoining to the strain energy density of the stiffeners, the strain energy of the skin plate. In this latter case the integral on the right-hand side of the Eqns. 2.23 and 2.24 should be extended to the whole plate thickness, $h = 2h_s + h_p$.

Figures 2.8, 2.9 and 2.10 depict the stiffness coefficients for the membrane, bending and shear matrices respectively derived with the present procedure. The stiffness coefficients reported in Figures 2.8-2.10 are relative to a rectangular flat panel in the concentric configuration, with $a = 500$ mm, $b = 800$ mm, $h_s = 20$ mm, $h_p = b_s = 3$ mm, $\vartheta_1 = 16.75^\circ$ and $\vartheta_2 = 45^\circ$. The plate and stiffeners dimensions are those of a typical aeronautical panel. The plate and stiffeners constituent material is Aluminum Alloy ($E = 73$ GPa, $\nu = 0.3$). The solid lines represent the variable properties obtained using Eq. 2.24 while, the dotted lines, are the constant coefficients calculated as in Eq. 2.23. As can be seen from Figures 2.8-2.10, despite the constituent material is isotropic, the stiffness matrices obtained are those of a complete 2D anisotropic material. This regardless if one looks at the constant stiffness coefficients (dotted lines) or at the variable stiffness coefficients (solid lines). Both, the variable stiffness coefficients and the constant stiffness coefficients were obtained using 1000 sub-cells.

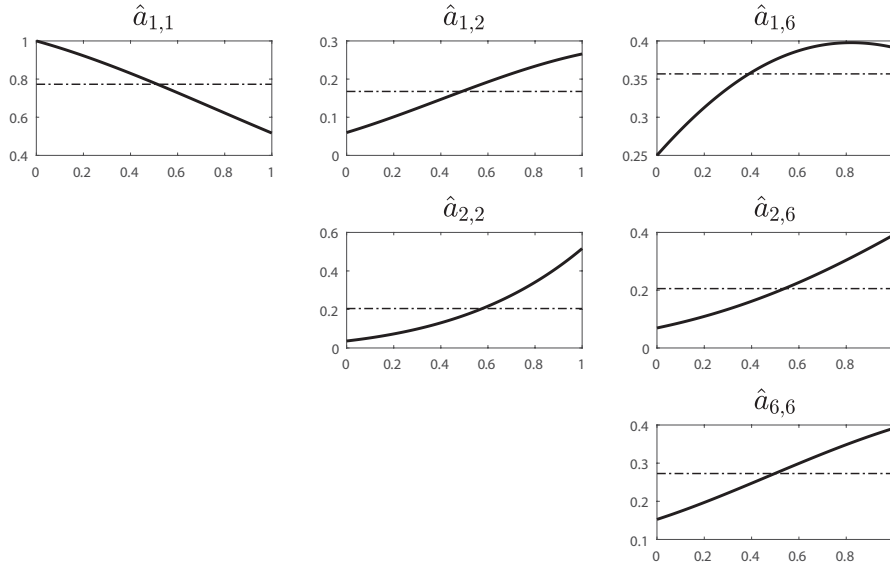


Fig. 2.8 Non-dimensional membrane matrix coefficients for a stiffened panel with $\vartheta_1 = 16.75^\circ$, $\vartheta_2 = 45^\circ$ with respect to the non-dimensional abscissa $\hat{x} = x/b$. The coefficients are normalized with respect to the maximum of A_{11} . Solid lines are the variable coefficients while dotted lines represent the homogenized coefficients.

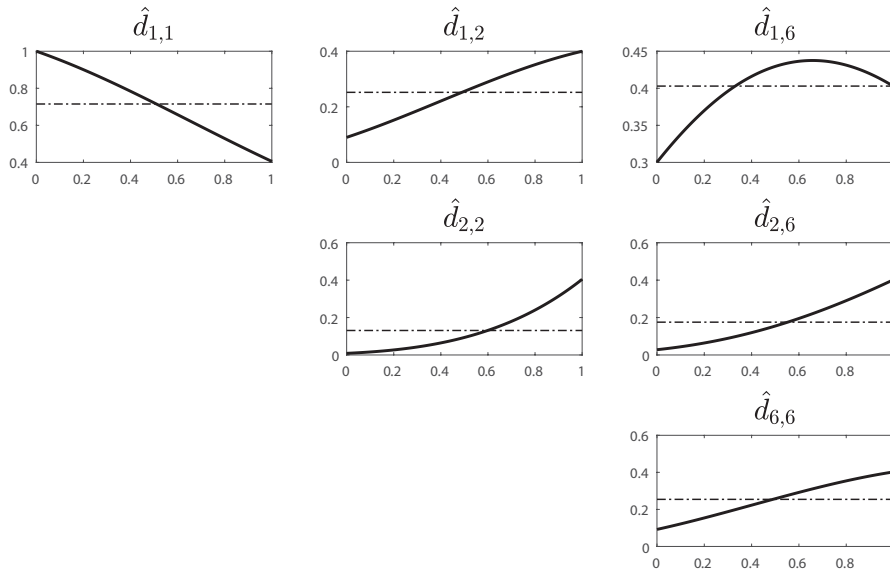


Fig. 2.9 Non-dimensional bending matrix coefficients for a stiffened panel with $\vartheta_1 = 16.75^\circ$, $\vartheta_2 = 45^\circ$ with respect to the non-dimensional abscissa $\hat{x} = x/b$. The coefficients are normalized with respect to the maximum of D_{11} . Solid lines are the variable coefficients while dotted lines represent the homogenized coefficients.

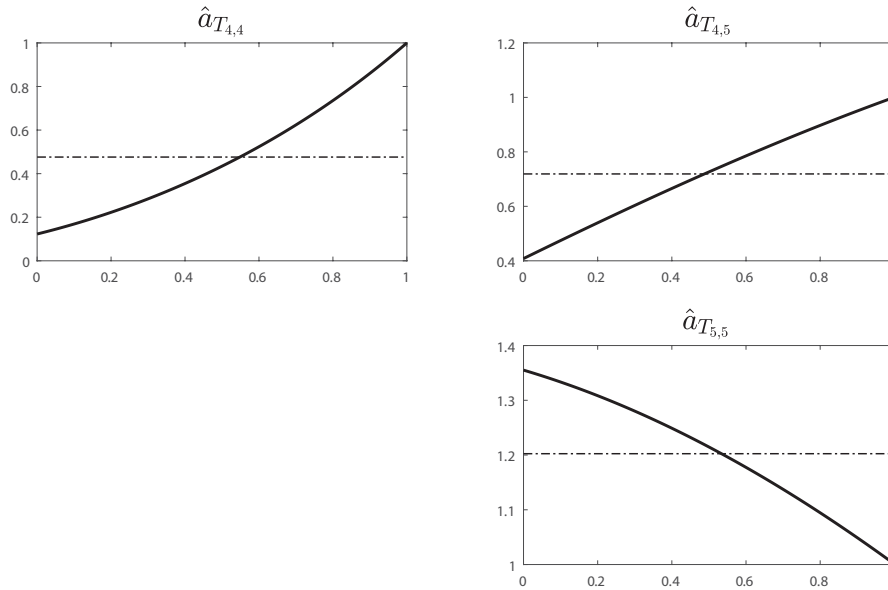


Fig. 2.10 Non-dimensional shear matrix coefficients for a stiffened panel with $\vartheta_1 = 16.75^\circ$, $\vartheta_2 = 45^\circ$ with respect to the non-dimensional abscissa $\hat{x} = x/b$. The coefficients are normalized with respect to the maximum of $A_{T_{44}}$. Solid lines are the variable coefficients while dotted lines represent the homogenized coefficients.

By varying the angle of orientation $\vartheta(x)$ of the stiffeners and retaining all the other parameters, one can obtain a completely different structural behavior. One example that is worth mentioning is the case in which $\vartheta_1 = -\vartheta_2$. Let us consider a concentric stiffened panel having $\vartheta_1 = 10^\circ$, $\vartheta_2 = -10^\circ$ while all the other dimensions remain unchanged with respect to the panel studied above. As can be seen from Figure 2.11-2.13, looking at the constant coefficients the resulting structural behavior is that of a 2D orthotropic material. Indeed, the coefficients A_{16} , A_{26} , D_{16} , D_{26} and $A_{T_{45}}$ are all zero. It is important notice that, despite the averaged stiffness coefficients (dotted lines) are $A_{16} = A_{26} = D_{16} = D_{26} = A_{T_{45}} = 0$, there is still a local anisotropy if one considers the variable coefficients (solid lines). This latter observation is crucial to explain the differences of the two equivalent models, as we will see in the next sections.

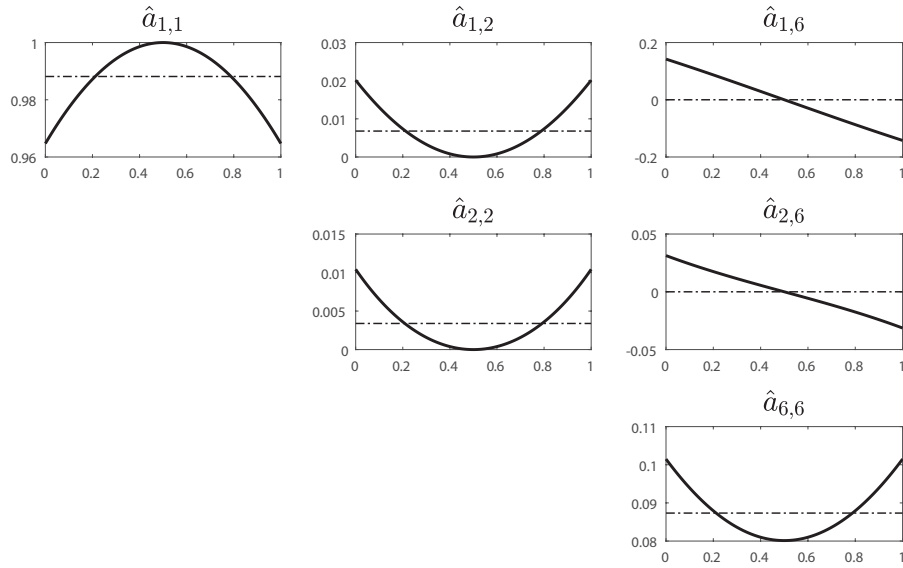


Fig. 2.11 Non-dimensional membrane matrix coefficients for a stiffened panel with $\vartheta_1 = 10^\circ$, $\vartheta_2 = -10^\circ$ with respect to the non-dimensional abscissa $\hat{x} = x/b$. The coefficients are normalized with respect to the maximum of A_{11} . Solid lines are the variable coefficients while dotted lines represent the homogenized coefficients.

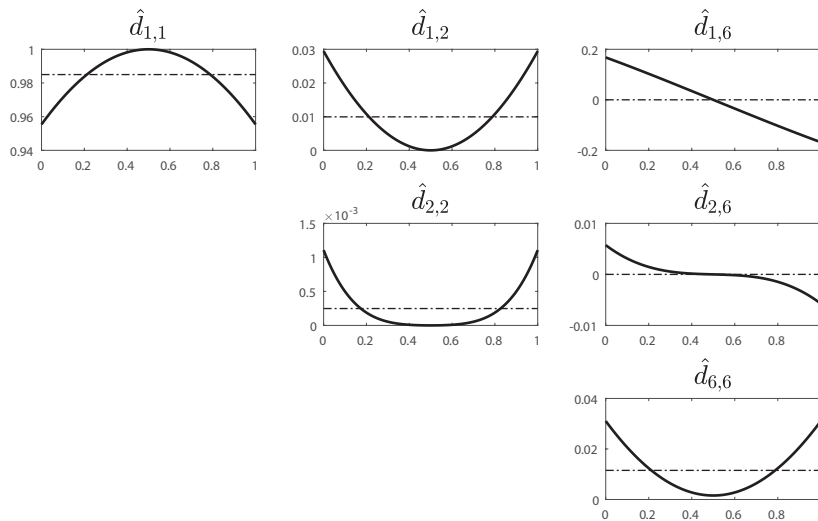


Fig. 2.12 Non-dimensional bending matrix coefficients for a stiffened panel with $\vartheta_1 = 10^\circ$, $\vartheta_2 = -10^\circ$ with respect to the non-dimensional abscissa $\hat{x} = x/b$. The coefficients are normalized with respect to the maximum of D_{11} . Solid lines are the variable coefficients while dotted lines represent the homogenized coefficients.

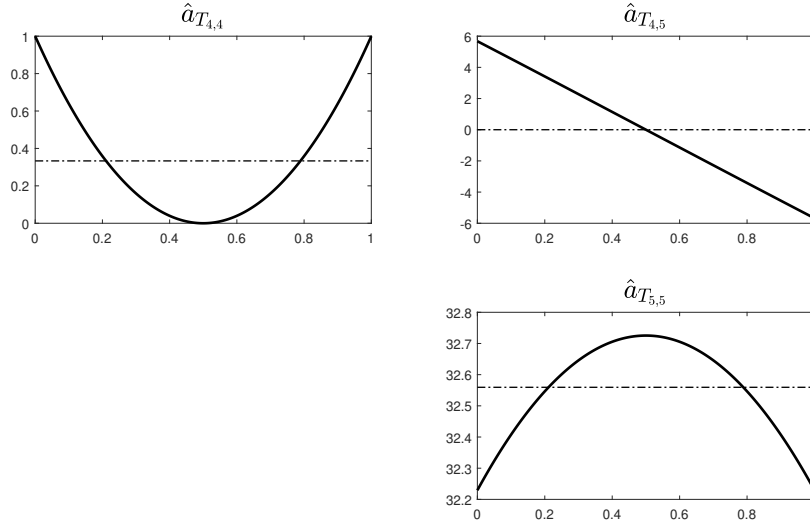


Fig. 2.13 Non-dimensional shear matrix coefficients for a stiffened panel with $\vartheta_1 = 10^\circ$, $\vartheta_2 = -10^\circ$ with respect to the non-dimensional absciss $\hat{x} = x/b$. The coefficients are normalized with respect to the maximum of $A_{T_{44}}$. Solid lines are the variable coefficients while dotted lines represent the homogenized coefficients.

2.4.1 Preliminary consideration on the rank of the stiffness matrices

In the previous section we wrote that the energy equivalence method leads to an equivalent continuum layer with full rank, therefore invertible, matrices. In this section we seek a formal explanation for the latter observation.

Let $A \in \mathbb{K}^{n \times n}$, and T_A a linear map $T_A : \mathbb{K}^n \rightarrow \mathbb{K}^n$, then the following two statements are equivalent:

1. $\text{rank}(A) = n$
2. $\det(A) \neq 0$

Recalling the rank sub-additivity properties, i.e.

$$\text{rank}\left(\sum_i a_i\right) \leq \sum \text{rank}(a_i) \quad (2.26)$$

being $a_i \in \mathbb{K}^{n \times n}$. By definition of rank

$$\text{rank}\left(\sum_i a_i\right) \leq \sum \text{rank}(a_i) \leq n \quad (2.27)$$

Here, we aim to prove the following

Lemma 1. *If the stiffeners are curvilinear, the rank of the matrix is maximum, i.e. $\text{rank}(A) = n$, where A denotes the sum of the matrices a_i .*

Proof. Let us suppose that exists an angle of orientation $\vartheta_2 \neq \vartheta_1$ with $\vartheta_2, \vartheta_1 \in \mathbb{R}$, such that $\dim(\mathbf{A}) = \dim(a_1 + a_2) < n$, i.e. $\det(A) = 0$. Recalling that

$$a_i = r_{\vartheta_i}^t \tilde{a} r_{\vartheta_i} \quad (2.28)$$

where r_{ϑ} is the rotation matrix of the stiffness tensor \tilde{a} expressed in the local reference system. Summing the two matrices $a_1 = r_{\vartheta_1}^t \tilde{a} r_{\vartheta_1}$ and $a_2 = r_{\vartheta_2}^t \tilde{a} r_{\vartheta_2}$ we obtain the matrix A . From statement 2 follows that the determinant should be equal to zero for A to be singular. Imposing the latter condition to the matrix A give rise to a transcendental equation $f(\vartheta_1, \vartheta_2)$ which admits only one real solution, i.e.

$$\sin \vartheta_1 = \sin \vartheta_2 \cos \vartheta_1 / \cos \vartheta_2. \quad (2.29)$$

This solution can be reworded as $\tan \vartheta_1 = \tan \vartheta_2$, i.e. $\vartheta_1 = \vartheta_2$ that is the contrapositive of our initial hypothesis. \square

Observation 1.1. *Let us consider the case of curved stiffeners were $\vartheta_2 = \vartheta_1 + \delta\vartheta$, with $0 < \delta\vartheta \ll 1$. According to the Lemma 1, the rank of the stiffness matrices would be maximum and hence the apparent engineering constants would be single valued functions.*

A close inspection of the Lemma 1 and subsequent observation leads to the following

Observation 1.2.

$$\lim_{\vartheta \rightarrow \vartheta_0^-} Y = c \quad \lim_{\vartheta \rightarrow \vartheta_0^+} Y = c \quad (2.30)$$

being Y the generic engineering constant of a family of straight stiffeners, then, despite the singularity, the engineering constant of the equivalent layer can be

determined also for a straight stiffener by letting the orientation in one point varies of a small perturbation $\delta\vartheta$.

It is worth noting that the singularity of the stiffness matrices when straight stiffeners are concerned, can be fixed by adjoining to the stiffeners matrices the contribution of the skin plate. Despite the equivalent continuum structure, can be modeled as a three layers anisotropic structure, in the following we will consider the equivalent engineering properties of the entire stiffened structure, i.e. the one obtained adjoining the contribution of the skin plate to the stiffness obtained as in Eqns. 2.25a-2.25d. In other words, we will consider the structure as a thick monolithic layer exhibiting three different structural behavior, i.e.: membrane, bending and shear. The equivalent thickness models generally adopted for homogenized models, along with a discussion of the model adopted in the present work, is presented in the next section.

Before going further with the model, is worthwhile comparing the model derived herein with that given in [125]. Cestino and Frulla [125] calculated the apparent engineering properties (E_{11} , E_{22} , ν_{12} and G_{12}) of the equivalent continuum layer for a family of straight stiffeners. The apparent engineering properties were calculated by dividing the expression of the membrane matrix, given as in Equation 24a of Nemeth [98], by the stiffeners height h_s . The equivalent properties were determined in the local reference system XYZ and the rotation were performed *a posteriori*. The method adopted in [125] gives rise to an inconsistency, i.e. the bending matrix of the equivalent layer differs from that of the stiffened structure. According to the model presented in [125], the reduced stiffness matrix of the equivalent layer is given as follow

$$Q = \begin{bmatrix} \frac{Eb_s}{d_s} & 0 & 0 \\ 0 & 0 & 0 \\ 0 & 0 & \frac{k_y G_s b_s}{4d_s} \end{bmatrix} \quad (2.31)$$

Neglecting the effect of the bending curvature, and retaining only the planar components, the direct compatibility for the stiffeners expressed in the plate form can be expressed as follow

$$N_{xx}^s = \frac{EA_s}{d_s} \varepsilon_{xx}^{(0)}, \quad (2.32a)$$

$$N_{xy}^s = \frac{K_y GA_s}{4d_s} \gamma_{xy}^{(0)}. \quad (2.32b)$$

Dividing Eqns. 2.32 by the stiffeners height h_s recalling that $A_s = b_s h_s$ and rewriting in matrix form, one obtain the Eq. 2.31. It is worth mentioning that this is consistent with the model of Nemeth and the model presented herein for what concerns the in-plane behavior. The inconsistency arises since they assumed that

$$D = \int_{h_p/2}^{h/2} Qz^2 dz. \quad (2.33)$$

which is not necessarily true for a stiffened structure. Looking at the coefficient D_{66} obtained with the two formulations one have

$$\begin{aligned} D_{66}^{(m)} &= \int_{h_p/2}^{h/2} z^2 \frac{K_y G b_s}{4d_s} dz = \frac{1}{3} \frac{K_y G b_s}{4d_s} \left(\frac{h_p^3}{8} + \frac{3h_p^2 h_s}{4} + \frac{3h_p h_s^2}{2} + h_s^3 - \frac{h_p^3}{8} \right) \\ &= \frac{1}{3} \frac{K_y G b_s}{4d_s} h_s^3 \left(1 + \frac{3}{4} \frac{h_p^2}{h_s^2} + \frac{3}{2} \frac{h_p}{h_s} \right), \end{aligned} \quad (2.34)$$

where m stands for membrane, to recall that is the equivalent bending stiffness obtained imposing the statical equivalence for the membrane stress resultants as in [125]. Contrary, in this work we have

$$D_{66_{present}} = \frac{G J_t}{4d_s}, \quad (2.35)$$

where J_t is given as in Eq. 2.13. Neglecting higher order terms for the torsional rigidity J_t we have

$$\frac{D_{66}^{(m)}}{D_{66_{present}}} = \frac{\frac{1}{3} \frac{K_y G b_s}{4d_s} h_s^3 \left(1 + \frac{3}{4} \frac{h_p^2}{h_s^2} + \frac{3}{2} \frac{h_p}{h_s} \right)}{G \frac{1}{3} \frac{b_s^3 h_s}{d_s}} \quad (2.36)$$

by letting $h_p/h_s \rightarrow 0$, i.e. for stiffened structures

$$\frac{D_{66}^{(m)}}{D_{66_{present}}} = \frac{K_y}{4} \left(\frac{h_s}{b_s} \right)^2. \quad (2.37)$$

Figure 2.14 shows a comparison of the D_{66} coefficient obtained using the model presented herein (red line) against that obtained with the model given in [125] (black line). A rectangular flat plate $a = 500$ mm, $b = 800$ mm, $h_s = 20$ mm, $b_s = h_s = 3$ mm, made by an Aluminum alloy $E = 58000$ Mpa, $\nu = 0.33$ was considered for the

purpose of this comparison. The plate has 5 straight stiffeners oriented at zero. From Figure 2.14 follows that the model given in [125] overestimates the D_{66} coefficient. It is worth mentioning that for straight stiffeners oriented at zero, the D_{66} coefficient is the only coefficient that differs among the two models. Recalling that

$$\int_{h_p/2}^{h/2} b_s z^2 dz = I_{yy}$$

follows that the coefficient D_{11} calculated as in Cestino [125], coincides with that given as in Nemeth [98]. Considering now the case of a straight stiffeners oriented at an angle ϑ , and recalling that $[C_p] = [T]^T [C_p] [T]$, one have that the discrepancy originally presented only in the D_{66} coefficient is now spread to all the coefficients of the bending matrix, as shown in Figure 2.15.

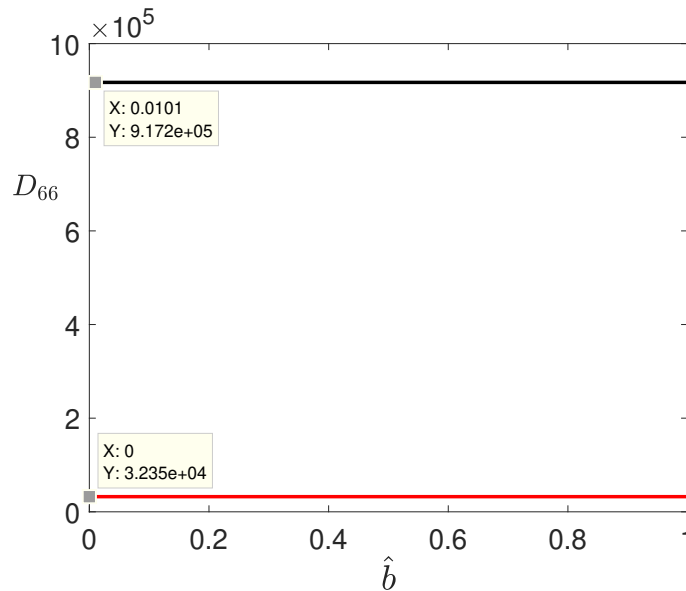


Fig. 2.14 Comparison of the D_{66} coefficient for a rectangular stiffened plate with straight stiffeners oriented at $\vartheta = 0^\circ$. The solid black line is the D_{66} coefficient calculated as in [125] while the solid red line is the coefficient calculated using the present model.

It is worth mention that, for sub-stiffened structures ($h_s \approx h_p$), the approach given in [125] can led to a first order approximation of the bending matrix. The present approach is in agreement with the model given by Nemeth [98] and yields, in general, different bending matrices with respect to those calculated as in [125]. The three models agree if one compares the membrane matrices.

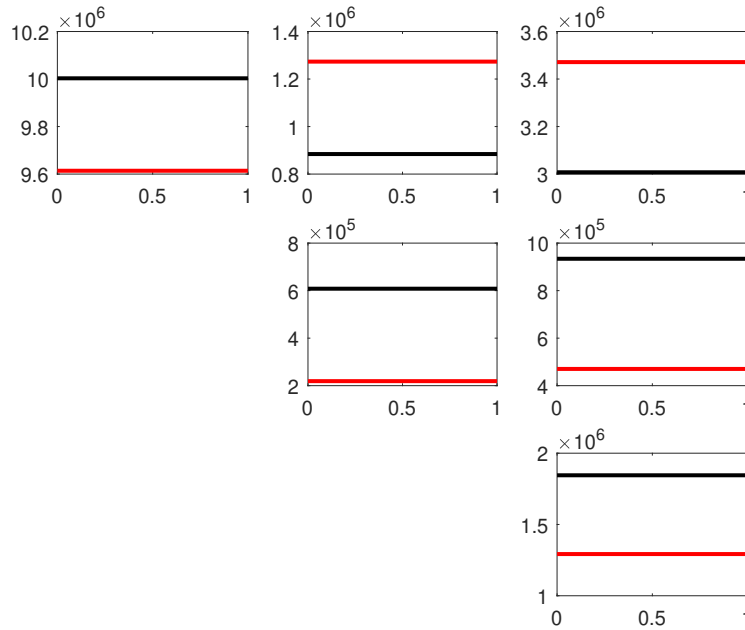


Fig. 2.15 Comparison of the D_{ij} coefficients for a rectangular stiffened plate with straight stiffeners oriented at $\vartheta = 20^\circ$. The solid black lines are the D_{ij} coefficients calculated as in [125] while the solid red lines are the coefficients calculated using the present model.

2.4.2 Considerations on the equivalent thickness

In his treatise on equivalent plate model of stiffened plates, Nemeth pointed out that the equivalent plate thickness of a lattice structures is not defined uniquely and that the adequate formulation should be selected according to the dominant phenomena that one aims to describe [98]. Nemeth proposes four methods to calculate the equivalent thickness $h_s^{(e)}$ hereafter summarized as follows

1. *Equivalent area* by imposing the equivalence between the area of the stiffener and the area of the equivalent layer

$$h_s^{(e)} = \frac{A_s}{d_s}.$$

2. *Equivalent first moment of area* by writing the equivalence between the stiffener weighted first moment and the first moment of the equivalent layer. For the case of homogeneous orthotropic material with the principal axes aligned

to the beam axes ($E_s \equiv E_x$), the expression of the equivalent layer thickness is given as

$$\begin{aligned} A_s \bar{z}_s &= \frac{1}{E_s} \int_A E_x z dA \quad \text{being } dA = dydz \\ A_s \bar{z}_s &= \int_A E_x z dA = \frac{d_s}{2} \left(h_s^{(e)2} + h_s^{(e)} h_p \right) \\ \frac{2A_s \bar{z}_s}{d_s} &= h_s^{(e)} \left(h_s^{(e)} + h_p \right). \end{aligned}$$

3. *Equivalent second moment of area* by requiring that the second moment of area of the equivalent layer equals the second weighted moment of area of the stiffeners

$$\begin{aligned} I_{yy}^s &= \frac{1}{E_s} \int_A E_x z^2 dA \\ I_{yy}^s &= \frac{d_s}{3} \left[\left(h_s^{(e)} + \frac{h_p}{2} \right)^3 - \left(\frac{h_p}{2} \right)^3 \right] \\ \frac{3}{d_s} I_{yy}^s &= h_s^{(e)3} + \frac{3}{2} h_s^{(e)2} h_p + \frac{3}{4} h_s^{(e)} h_p^2. \end{aligned}$$

4. *Equivalent torsional rigidity* by imposing the equivalence of the torsional rigidity among the equivalent layer and the stiffener.

For the purpose of this work, it is preferred to not discern *a priori* which among membrane, bending or shear behavior is dominant. Therefore, an alternative method to identify the equivalent thickness is defined which, in turns, allows

- to represent consistently all the aforementioned structural behaviors, and
- that is suitable for implementation on commercial Finite Element codes.

The method chosen in this work considers the equivalent continuum model having the same thickness of the real structure, i.e. $h = h_p + 2h_s$ and derives the equivalent anisotropic material for each of the aforementioned structural behavior. In other words, one will have three equivalent materials, namely membrane material, bending material and shear material, the latter being calculated as follow

$$C_{ijM} = \frac{A_{ij}}{h}, \quad C_{ijB} = \frac{12D_{ij}}{h^3}, \quad C_{ijT} = \frac{A_{Tij}}{h}, \quad (2.38)$$

where A_{ij} , D_{ij} and A_{Tij} are respectively the membrane, bending and shear matrices of the equivalent continuum model. Finite Element codes, such as, MSC Patran allows to model an anisotropic thick structure by means of MAT2 card. Using MAT2 one can have up to four different structural behaviors, namely: membrane, bending, shear and membrane-bending coupling. In the successive analysis, we will extensively adopt the MAT2 to model the equivalent continuum structure.

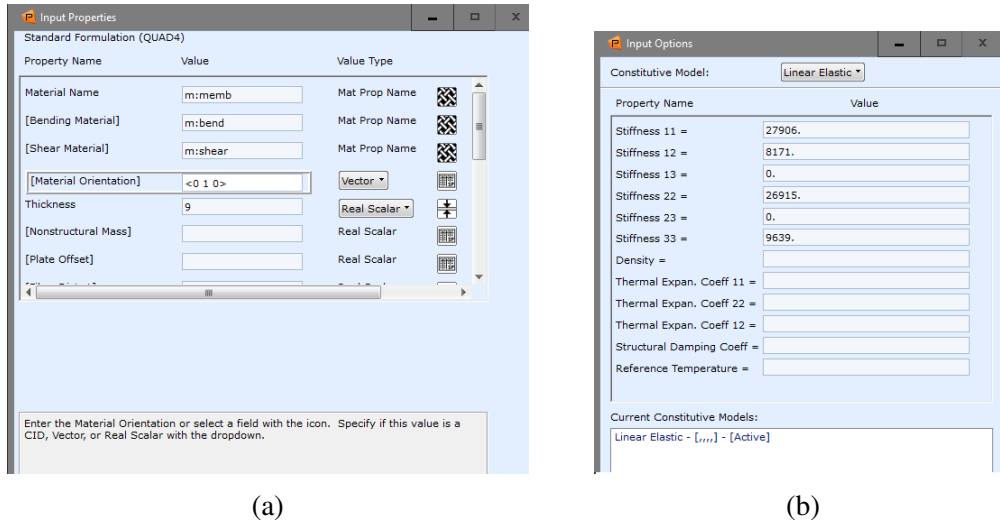


Fig. 2.16 Input for the MAT2 card of MSC[®] Patran (a) and (b) example of input properties for a 2D anisotropic structure.

2.4.3 Derivation of the effective engineering constants

The equivalent engineering properties of the continuum structure can be evaluated by direct comparison with the flexibility matrix $[S]$ of a 2D anisotropic structure given as in [126]. The flexibility matrix is given as follow

$$\begin{bmatrix} \epsilon_x \\ \epsilon_y \\ \gamma_{xy} \end{bmatrix} = \begin{bmatrix} S_{11} & S_{12} & S_{16} \\ S_{12} & S_{22} & S_{26} \\ S_{16} & S_{26} & S_{66} \end{bmatrix} \begin{bmatrix} \sigma_x \\ \sigma_y \\ \tau_{xy} \end{bmatrix}, \quad (2.39)$$

that is

$$\begin{aligned}
\varepsilon_1 &= S_{11}\sigma_x + S_{12}\sigma_y + S_{16}\tau_{xy} = \frac{1}{E_1}\sigma_x - \frac{\nu_{21}}{E_2}\sigma_y + \frac{\eta_{61}}{E_6}\tau_{xy}, \\
\varepsilon_2 &= S_{12}\sigma_x + S_{22}\sigma_y + S_{26}\tau_{xy} = -\frac{\nu_{12}}{E_1}\sigma_x - \frac{1}{E_2}\sigma_y + \frac{\eta_{62}}{E_6}\tau_{xy}, \\
\gamma_{12} &= S_{16}\sigma_x + S_{26}\sigma_y + S_{66}\tau_{xy} = \frac{\eta_{16}}{E_1}\sigma_x + \frac{\eta_{26}}{E_2}\sigma_y + \frac{1}{E_6}\tau_{xy}.
\end{aligned} \tag{2.40}$$

Recalling that the flexibility matrix can be written as $[S] = [Q]^{-1}$ and applying the definition of inverse, one has that the component S_{ij} is the ratio between the determinant of the minor obtained by eliminating the i^{th} row and the j^{th} columns of Q . It follows that

$$\begin{aligned}
\varepsilon_x &= \frac{Q_{26}^2 - Q_{22}Q_{66}}{\Delta}\sigma_x + \frac{Q_{12}Q_{66} - Q_{16}Q_{26}}{\Delta}\sigma_y + \frac{Q_{16}Q_{22} - Q_{12}Q_{26}}{\Delta}\tau_{xy}, \\
\varepsilon_y &= \frac{Q_{12}Q_{66} - Q_{16}Q_{26}}{\Delta}\sigma_x + \frac{Q_{16}^2 - Q_{11}Q_{66}}{\Delta}\sigma_y + \frac{Q_{11}Q_{26} - Q_{12}Q_{16}}{\Delta}\tau_{xy}, \\
\gamma_{xy} &= \frac{Q_{16}Q_{22} - Q_{12}Q_{26}}{\Delta}\sigma_x + \frac{Q_{11}Q_{26} - Q_{12}Q_{16}}{\Delta}\sigma_y + \frac{Q_{12}^2 - Q_{11}Q_{22}}{\Delta}\tau_{xy},
\end{aligned} \tag{2.41}$$

where

$$\Delta = -(Q_{66}Q_{12}^2 - 2Q_{12}Q_{16}Q_{26} + Q_{22}Q_{16}^2 + Q_{11}Q_{26}^2 - Q_{11}Q_{22}Q_{66}).$$

It can be shown that

$$E_1 = \frac{1}{S_{11}} = \frac{\Delta}{Q_{26}^2 - Q_{22}Q_{66}} \equiv E_x^{equiv}, \tag{2.42}$$

$$E_2 = \frac{1}{S_{22}} = \frac{\Delta}{Q_{16}^2 - Q_{11}Q_{66}} \equiv E_y^{equiv}, \tag{2.43}$$

$$G_{12} = \frac{1}{S_{11}} = \frac{\Delta}{Q_{12}^2 - Q_{11}Q_{22}} \equiv G_{xy}^{equiv}, \tag{2.44}$$

$$\nu_{21} = -E_2 S_{12} = \frac{\Delta}{Q_{16}^2 - Q_{11}Q_{66}} \frac{Q_{12}Q_{66} - Q_{16}Q_{26}}{\Delta} = \frac{Q_{12}Q_{66} - Q_{16}Q_{26}}{Q_{16}^2 - Q_{11}Q_{66}} \equiv \nu_{yx}^{equiv}, \tag{2.45}$$

$$\nu_{12} = -E_1 S_{21} = \frac{\Delta}{Q_{26}^2 - Q_{22}Q_{66}} \frac{Q_{12}Q_{66} - Q_{16}Q_{26}}{\Delta} = \frac{Q_{12}Q_{66} - Q_{16}Q_{26}}{Q_{26}^2 - Q_{22}Q_{66}} \equiv \nu_{xy}^{equiv}, \tag{2.46}$$

$$\eta_{61} = G_{12}S_{16} = \frac{\Delta}{Q_{12}^2 - Q_{11}Q_{22}} \frac{Q_{16}Q_{22} - Q_{12}Q_{26}}{\Delta} = \frac{Q_{16}Q_{22} - Q_{12}Q_{26}}{Q_{12}^2 - Q_{11}Q_{22}} \equiv \eta_{zx}^{equiv}, \quad (2.47)$$

$$\eta_{62} = G_{12}S_{26} = \frac{\Delta}{Q_{12}^2 - Q_{11}Q_{22}} \frac{Q_{11}Q_{26} - Q_{12}Q_{16}}{\Delta} = \frac{Q_{11}Q_{26} - Q_{12}Q_{16}}{Q_{12}^2 - Q_{11}Q_{22}} \equiv \eta_{zy}^{equiv}. \quad (2.48)$$

Likewise, the apparent engineering properties for the shear matrix, can be evaluated as

$$G_{13} = \frac{1}{S_{44}} = \frac{\Delta_T}{Q_{T22}} \equiv G_{xz}^{equiv}, \quad (2.49)$$

$$G_{23} = \frac{1}{S_{55}} = \frac{\Delta_T}{Q_{T11}} \equiv G_{yz}^{equiv}, \quad (2.50)$$

$$\mu_{13,23} = -G_{13}S_{45} = \frac{Q_{T22}}{Q_{T11}}, \quad (2.51)$$

$$\text{and} \quad (2.52)$$

$$\Delta_T = Q_{T11}Q_{T22} - Q_{T12}^2, \quad (2.53)$$

where E_x and E_y are the extensional moduli, G_{xy} , G_{xz} and G_{yz} are the shear moduli, ν_{xy} and ν_{yx} the Poisson's ratios, $\eta_{xy,x}$ and $\eta_{xy,y}$ are coefficients of mutual influence of the first and second kind, also known as shear-extension coupling coefficients and finally $\mu_{13,23}$ is the Chentsov's coefficient, also referred to as shear-shear coupling. In Figure 2.17 are reported the equivalent engineering properties of the continuum layer, in the form of contour plots, for the membrane behavior. The properties are those of the homogenized model to get rid of the spatial dependency. It can be noted that the maximum of E_x is given for straight stiffeners oriented at zero while, E_y and G_{xy} achieve their maximum for straight stiffeners oriented at $\vartheta = \pm 45^\circ$. It is worth mentioning that the function $E_y(\vartheta_1, \vartheta_2)$ would increase monotonically till $\vartheta = \pm 90^\circ$, that is with the stiffeners aligned to the y -axis. However, since the stiffeners' orientations are bounded, $-45^\circ \leq \vartheta \leq 45^\circ$, E_y exhibits a local maximum. A superscript "m" is used to recall that those equivalent engineering properties are those of the membrane behavior.

In Figure 2.18 are reported the coefficients of mutual influence obtained considering the membrane behavior of the stiffened plate. It can be noted that both $\eta_{xy_1}^m$ and $\eta_{xy_2}^m$ are zero when $\vartheta_1 = -\vartheta_2$, that is the global behavior of the equivalent model resembles that of an equivalent orthotropic continuum ($Q_{16} = Q_{26} = 0$). It is also

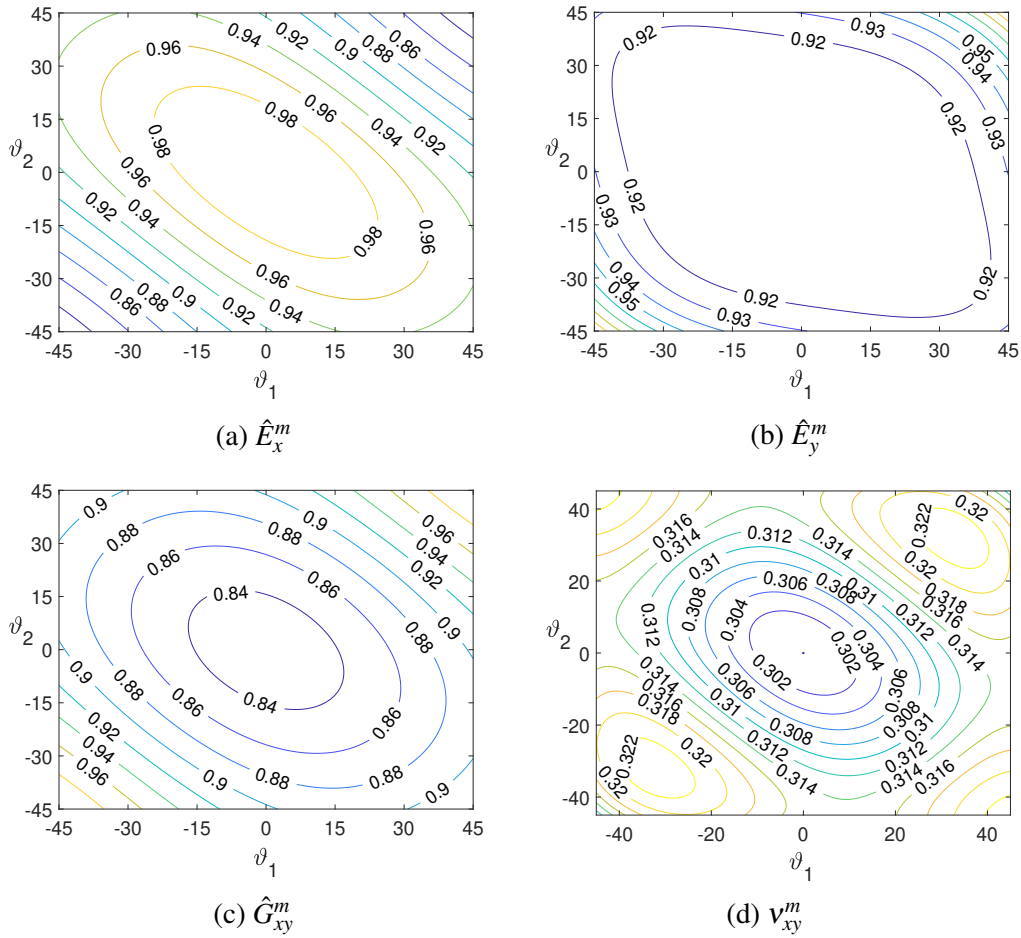


Fig. 2.17 Normalized engineering properties of the equivalent-continuum-plate with respect to the angles of orientation of the stiffeners ϑ . The figures show the equivalent membrane properties of the stiffened plate. Notice that the equivalent E_x , E_y and G_{xy} have been normalized respectively with their maximum value.

worth pointing out that $\eta_{xy_2}^m$ presents a sort of ellipse centered around zero in which the coefficient is null. In this case is the averaged (homogenized) coefficient that is zero, meaning that $\eta_{xy_2}^m(x, \vartheta_1, \vartheta_2)$ exhibits an anti-symmetry over the plate's domain.

In Figure 2.19 are depicted the normalized shear coefficients G_{xz} and G_{yz} . It is worth noting that in either cases the maximum is attained for straight stiffeners oriented at $\vartheta = \pm 45^\circ$. A local maximum is obtained for curved stiffeners with $\vartheta_1 = -\vartheta_2 = \pm 45^\circ$.

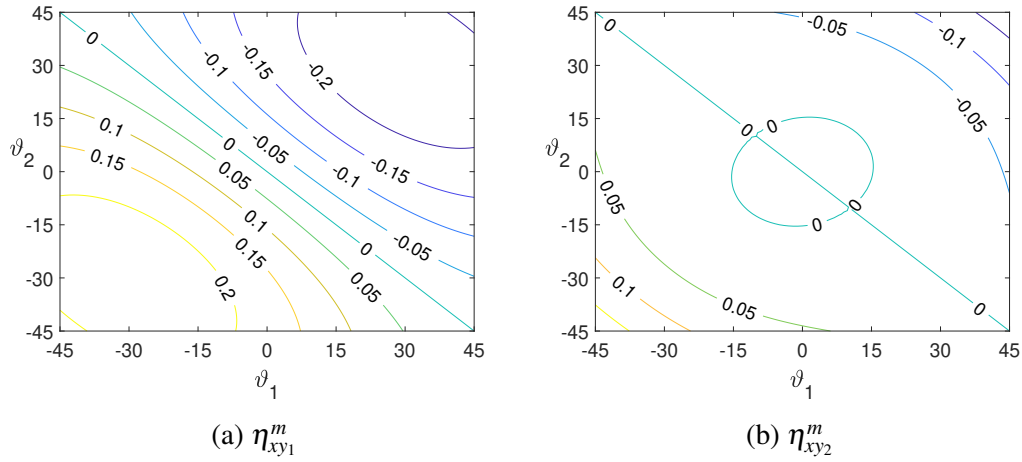


Fig. 2.18 Coefficients of mutual influence η_{xy1} and η_{xy2} of the equivalent-continuum-plate with respect to the angles of orientation of the stiffeners ϑ .

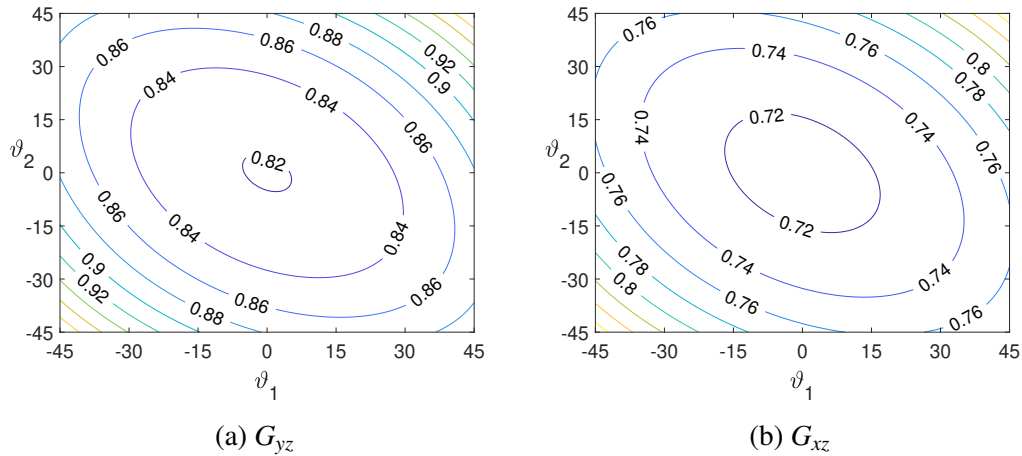


Fig. 2.19 Normalized engineering properties of the equivalent-continuum-plate with respect to the angles of orientation of the stiffeners ϑ . The figures show the equivalent shear properties of the stiffened plate. Notice that the equivalent G_{yz} and G_{xz} have been normalized respectively with their maximum value.

Figure 2.20 illustrates the Chentsov's coefficient (or shear-shear coupling coefficient) with respect to the angles of orientation of the stiffeners. In this case, as for the mutual coefficients, the coefficient is zero for equivalent orthotropic behavior.

In Figure 2.21 are reported the equivalent engineering properties obtained considering the bending behavior. It is worth noting that the contour plots reported herein differs with respect to the contour plots reported for the case of membrane behavior (see Fig. 2.17). The difference is due to the the fact that $D_{66} \neq \int Q_{66} z^2 dz$,

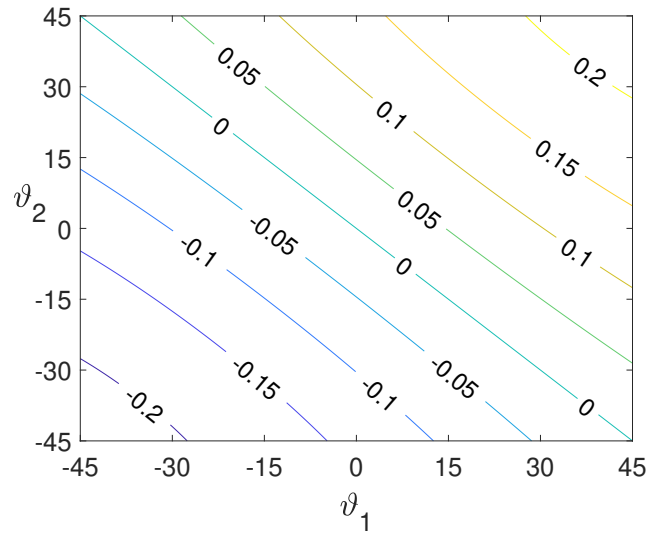


Fig. 2.20 Chentsov's (shear-shear coupling) coefficient

as explained above and hence also the equivalent properties are remarkably different not only in terms of values but also in terms of shapes of the contour.

2.5 Kinematic Equations for First Order Shear Deformation curved beam

This section aims at identifying the limit of validity of the model presented above. In view of geometry of the stiffeners considered, which have the mid-line lying on a plane, herein it is considered a planar curved beam. A more accurate description of the physics of the problem should consider a 3D curved beam. Nonetheless, the planar model is yet useful to show that, for a curved beam, the deformations are coupled and hence writing the kinematic compatibility as in Eq. 2.8 leads to an inconsistency.

The following kinematic equations are presumed on the basis of the Timoshenko beam theory (FSDT). The displacement field in the local reference frame is given as

$$\begin{aligned} u_2^* &= v^*(s), \\ u_3^* &= w_0^*(s) + y^* \varphi(s), \end{aligned} \quad (2.54)$$

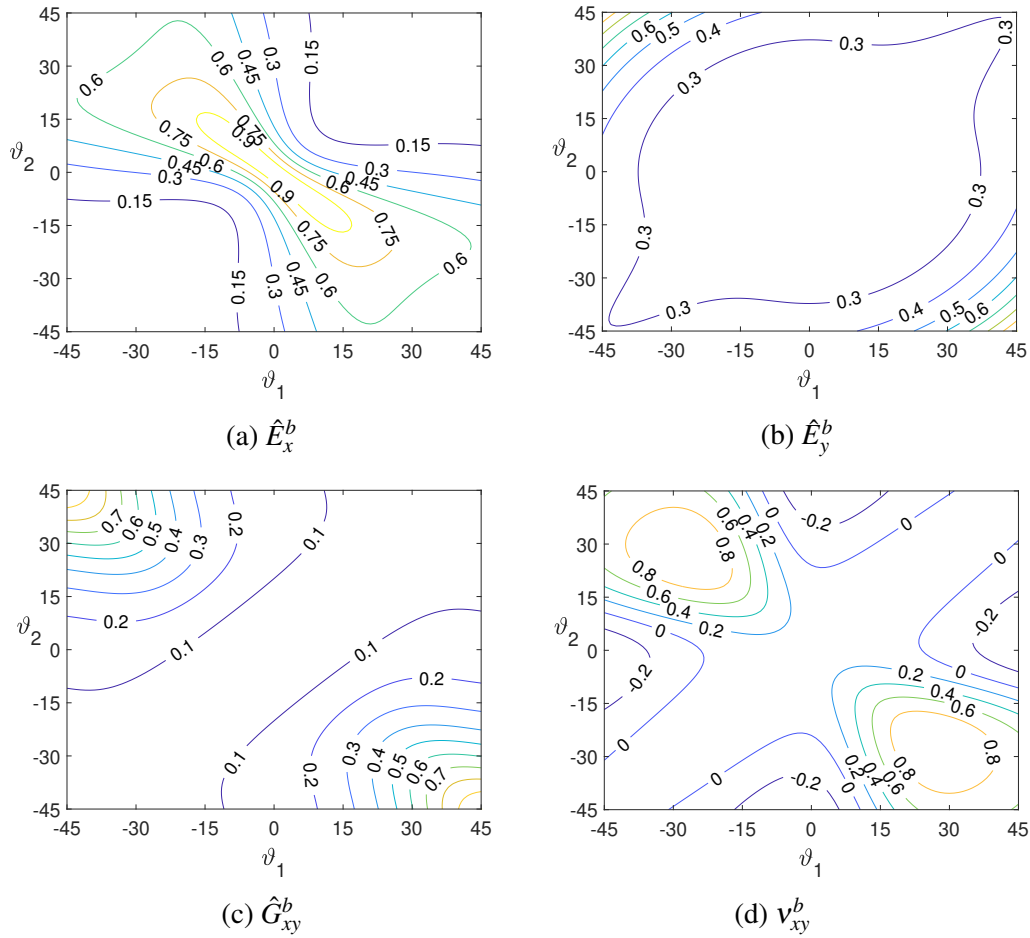


Fig. 2.21 Normalized engineering properties of the equivalent-continuum-plate with respect to the angles of orientation of the stiffeners ϑ . The figures show the equivalent bending properties of the stiffened plate. Notice that the equivalent E_x , E_y and G_{xy} have been normalized respectively with their maximum value.

where v is the transverse displacement, w is the axial displacement and φ is the rotation about the beam axis. The displacement u can be written as

$$\mathbf{u}^* = v^*(s)\mathbf{n}(s) + [w_0^*(s) + y\varphi(s)]\mathbf{t}(s) \quad (2.55)$$

where \mathbf{n} and \mathbf{t} the normal and tangent unit vector in s , where s is the curvilinear abscissa. The derivative of the displacement field with respect to the curvilinear abscissa s' is

$$u_{,ss'}^* = v_{,s'}^* \mathbf{n} + v^* n_{,s'} + [w_0^* + y\varphi]_{,s'} \mathbf{t} + [w_0^* + y\varphi]_{,s'} \mathbf{t}_{,s'} \quad (2.56)$$

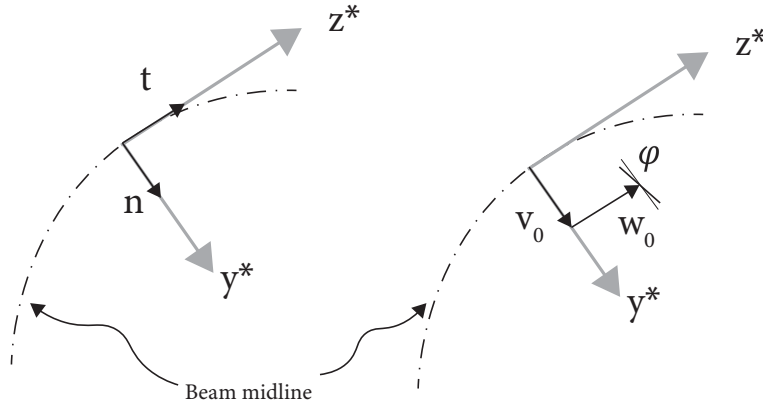


Fig. 2.22 Kinematics of a planar curved beam

Recalling Frenet-Serret formulas

$$n_{,s'} = -\frac{1}{R-y^*}t, \quad \text{and} \quad t_{,s'} = -\frac{1}{R-y^*}n. \quad (2.57)$$

Eqn. 2.56 becomes

$$u_{,s'}^* = \left\{ v_{s'}^* + \frac{1}{R-y^*} [w_0^* + y^* \varphi] \right\} \mathbf{n} + \left\{ -\frac{1}{R-y^*} v^* + [w_0^* + y^* \varphi]_{,s'} \right\} \mathbf{t}. \quad (2.58)$$

The deformations are given by

$$\begin{aligned} \varepsilon &= \frac{\partial u_3^*}{\partial s'} = -\frac{1}{R-y^*} v^* + w_{0,s'}^* + y^* \varphi_{,s'}, \\ \gamma &= \frac{\partial u_2^*}{\partial s'} + \frac{\partial u_3^*}{\partial y^*} = v_{s'}^* + \frac{1}{R-y^*} [w_0^* + y^* \varphi] + \varphi, \end{aligned} \quad (2.59)$$

since

$$\frac{\partial}{\partial s'} = \frac{R}{R-y^*} \frac{\partial}{\partial s}, \quad (2.60)$$

$$\begin{aligned} \varepsilon &= -\frac{1}{R-y^*} v^* + \frac{R}{R-y^*} [w_{0,s}^* + y^* \varphi_{,s}], \\ \gamma &= \frac{R}{R-y^*} v_s^* + \frac{1}{R-y^*} [w_0^* + y^* \varphi] + \varphi. \end{aligned} \quad (2.61)$$

If the width of the stiffeners is negligible with respect to the radius of curvature R , i.e. $R \gg y^*$ then the compatibility eqns. become

$$\begin{aligned}\varepsilon &= -\frac{v^*}{R} + w_{0,s}^* + y^* \varphi_{,s}, \\ \gamma &= v_s^* + \frac{w_0^*}{R} + \varphi.\end{aligned}\tag{2.62}$$

In the limit for $R \rightarrow \infty$,

$$\begin{aligned}\varepsilon &= w_{0,s}^* + y^* \varphi_{,s}, \\ \gamma &= v_s^* + \varphi,\end{aligned}\tag{2.63}$$

the compatibility equations become in turn those of the straight beam.

As can be seen, for a curved beam, the in plane deformations in Eqns. 2.61 are coupled. Hence, the direct replacement of the generalized deformations of a straight beam with those of a curved beam leads to an inconsistency, as discussed by Yang and Kuo [127]. Moreover, Yang and Kuo noted that also the out of plane deformations are coupled. It follows that the kinematic compatibility as in Eqns. 2.8 cannot be enforced. One should proceed, for example, equating the work done by a system of external forces on to the curved beam to the work done by the same system of external forces onto a straight beam and finally deriving the stiffness of the equivalent continuum layer by imposing the equality among the two systems. However, Yang and Kuo [127] noted that, for relatively small angle subtended by the curved beam, the approximation with piece-wise straight but oriented beam leads to a good approximation. In the next section, based on the work of Yang and Kuo, we will discuss the validity of having considered the curved stiffeners as piecewise rectilinear.

2.5.1 Implications of the kinematics of curved beam

In section 2.3 we have conjectured that the curvature of the beam can be neglected and, based on this assumption, we have enforced the direct compatibility within the subcell. Here the aim is to ascertain that this assumption holds for the particular geometry of the stiffeners we have chosen and eventually identify the limit of validity of the present theory. Substituting Eqn. 2.1 and integrating one have the reference

stiffeners path is given as

$$y = \begin{cases} x \tan \vartheta_1 & \text{if } \vartheta_1 = \vartheta_2 \\ \frac{b}{\vartheta_1 - \vartheta_2} \ln \left| \frac{\cos \vartheta}{\cos \vartheta_1} \right| & \text{if } \vartheta_1 \neq \vartheta_2 \end{cases}. \quad (2.64)$$

In the following only the of the second equation will be considered 2.64, i.e. the case $\vartheta_1 \neq \vartheta_2$. Indeed in the first case the beam would be straight and the radius of curvature R infinite. For a steering stiffener, the curve path is given by

$$f(x) = \frac{b}{\vartheta_1 - \vartheta_2} \ln \left\| \frac{\cos \vartheta(x)}{\cos \vartheta_1} \right\|. \quad (2.65)$$

The curvature of a planar curve given in the implicit form $y = f(x)$ is given as:

$$\kappa = \frac{\|f''\|}{(1 + f'^2)^{(3/2)}} \quad (2.66)$$

and since

$$f' = -\tan(\vartheta(x)), \quad f'' = -\frac{(\vartheta_2 - \vartheta_1) \sec^2(\vartheta(x))}{b}$$

with some algebraic manipulations one have

$$\kappa = \frac{\frac{\vartheta_2 - \vartheta_1}{b} (1 + \tan^2 \vartheta(x))}{(1 + \tan^2 \vartheta(x))^{3/2}}. \quad (2.67)$$

Noting the the radius of curvature $R = 1/\kappa$, it follows that:

$$R = \frac{b \sqrt{1 + \tan^2 \vartheta(y)}}{\vartheta_2 - \vartheta_1}. \quad (2.68)$$

Eq. 2.68 can be used to establish whether effect of the radius of curvature onto the strains and stresses can be neglected or not.

Yang and Kuo [127] noted that, if the angle subtended by the curved beam β is less than twenty degree ($\beta < 20^\circ$), the effect of the Jacobian $R/(R - y)$ and of the radial contribution onto the strains can be neglected and hence, the curved beam can be approximated by straight but oriented beams. For the particular geometry of the stiffeners considered herein, following straightforward geometric considerations exemplified in Figure 2.23, and being c the arc length subtended by the curved

stiffeners $c = \beta R$, the constraint $\beta < 20^\circ$ is equivalent to

$$\frac{b}{c} = \frac{|\vartheta_2 - \vartheta_1|}{\sqrt{1 + \tan^2 \vartheta(y)}} < \beta \quad (2.69)$$

where β is expressed in radians. Notice that it has been presumed that b approx-

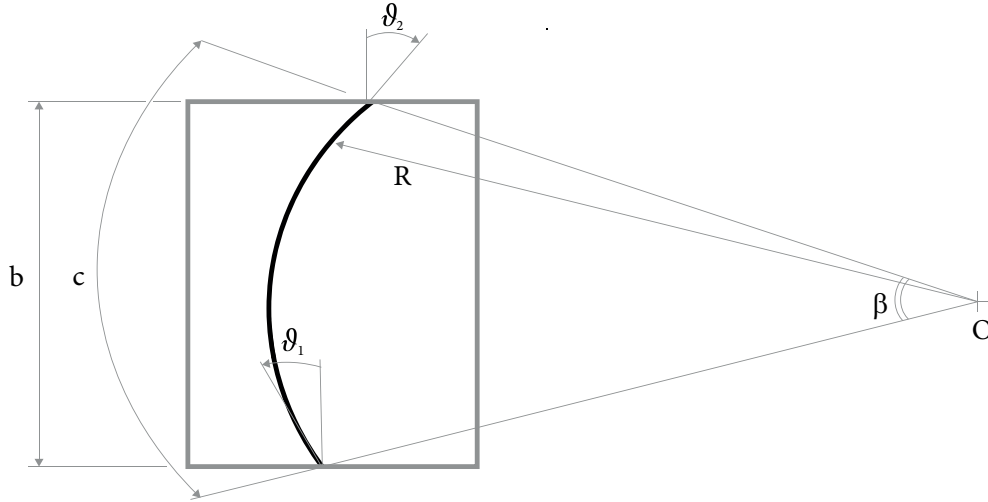


Fig. 2.23 Geometrical interpretation of the design's envelope limit

imates the chord subtended by the curve. Based on the observation of Yang and Kuo [127], Eqn. 2.69 gives in turn the limit of validity of the model derived herein. Geometrically, the limit can be interpreted as the ratio between the arc length and the chord subtended by the curved beam. This limit will be evaluated *a posteriori* in a dedicated section in this chapter. Eqn. 2.69 leads to the limit envelope reported in Figure 2.24, where the shaded gray areas represent the region where the geometric limit is violated and hence, according to the limit identified by Yang and Kuo, the model error would increase. Looking at the limit envelope reported in Figure 2.24 follows that moderately curved stiffeners, as those synthesized in the work of Jutte and Stanford [55], can faithfully be described by the model presented herein. Notwithstanding the above identified envelope, it is also worth mentioning that, in the following we will consider stiffened plates with a radius of curvature typical of aeronautic panels ($R \approx 5 \cdot 10^3 \text{ mm}$ or more). Indeed, if the radius of curvature is smaller, the terms $-\frac{v^*}{R}$ and $\frac{w_0^*}{R}$ become of the same order of magnitude as the other terms in Eqns. 2.62 and cannot be neglected. In that case, the limit envelope identified previously shrinks.

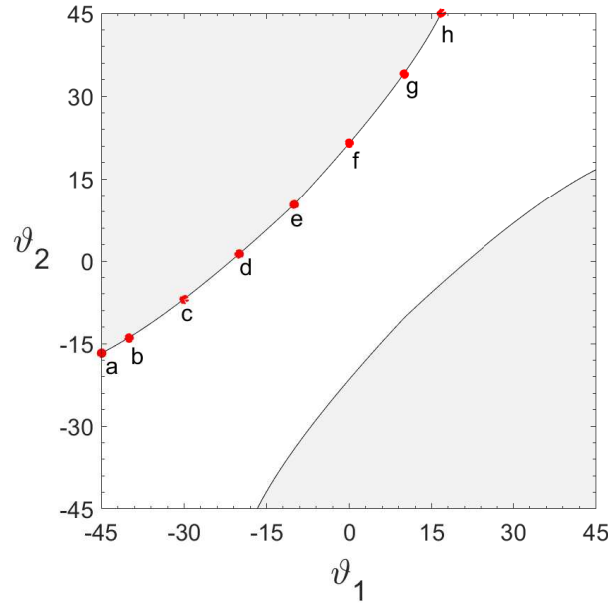


Fig. 2.24 Design envelope's limits for curvilinear beam modeled as a piece-wise straight but oriented beam. The gray shaded area represent the design zones which violates the geometric constraint, thus require the stiffeners modeled as curved beam. The red circles represent the topologies studied for the purpose of verification of the limit envelope.

2.5.2 Equivalent panel density

The equivalent panel density is calculated based on the presumption that the mass is uniformly distributed within the subcell. The expression of the equivalent density is then given as

$$\rho_{equiv} = \frac{2n_s \rho_s A_s L_s + \rho_p a b h_p}{a b h}, \quad (2.70)$$

where L_s is the stiffener's length and can be written as

$$L_s = \begin{cases} \frac{b}{\cos \vartheta} & \text{if } \vartheta_1 = \vartheta_2 \\ \frac{b}{\vartheta_2 - \vartheta_1} \log \left(\frac{\sec(\vartheta_2) + \tan(\vartheta_2)}{\sec(\vartheta_1) + \tan(\vartheta_1)} \right) & \text{if } \vartheta_1 \neq \vartheta_2 \end{cases}$$

substituting L_s with L_j one can obtain the equivalent density within the subcell. It is worth noting that, in thi first case, the panel density is constant over the entire plate's

domain while, in the second case, the model yields a variable density over the plate's domain.

2.6 Assessment of the equivalent models

In this section, parametric studies are performed to investigate the effect of prominent parameters onto the equivalent models derived as above. The nature of parametric analysis requires that some parameters be held constant while the remaining parameters are varied. The results were obtained considering a rectangular flat plate $a = 500$ mm, $b = 800$ mm having 5 equally-spaced stiffeners. The plate is simply supported along the edges, made by Aluminum alloy ($E = 73\text{GPa}$, $\nu = 0.3$, $\rho = 2780 \text{ kg/m}^3$). The skin plate thickness is $h_p = 3\text{mm}$, the stiffeners dimensions are respectively $h_s = 20\text{mm}$ and $b_s = 3\text{mm}$ and finally the stiffeners' spacing d_s is $d_s = 100$ mm. The error between the real structural behavior and the predicted behavior is calculate as follow

$$E_{R\%} = \frac{X_p - X_c}{X_c} \times 100, \quad (2.71)$$

where X_p is the generic performance obtained with the equivalent model while X_c is the performance calculated modeling the real stiffened structure. In the following all the analysis were performed using MSC Patran/Nastran. The equivalent model where meshed using C-Quad4 elements with a mesh having 5000 elements. The stiffened structure was instead meshed with a global edge length of 5 mm using C-Quad 4 elements.

2.6.1 Effect of the curvature

In section 2.5.1, based on the work of Yang and Kuo [127], we conjectured that the effect of the curvature is negligible when the angle subtended by the curved beam is less than 20° . Here the aim is to ascertain such assumption by comparing the stiffness of the equivalent models against that of the stiffened structure. Particularly, the assessment is performed comparing the first buckling load and the first frequency for 8 panels laying over the boundary curves, i.e. on the curves that define the limit of validity of the present model. All the configurations used herein for the sake of

comparison are indicated onto the design map (Figure 2.24) and are also depicted for the interest of clarity (Figure 2.25).

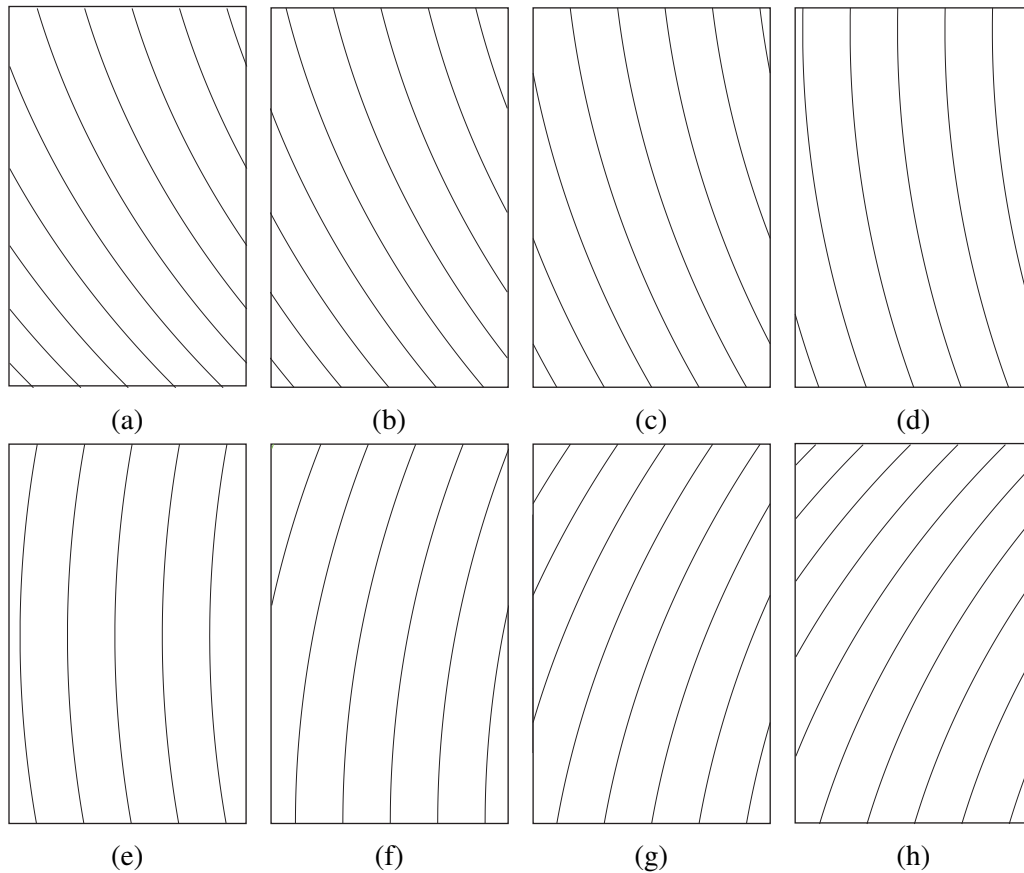


Fig. 2.25 Example of topologies lying over the boundary curve depicted in Figure 2.24. The panels are labelled consistently with their representation in the ϑ_1 - ϑ_2 plane in Figure 2.24.

The results pertaining the first buckling load and the first eigenfrequency, for each of the panels analyzed, are reported respectively in Table 2.1 and Table 2.2. For the sake of completeness, the results obtained for the real stiffened structures against those of the two equivalent continuum models, i.e. variable stiffness continuum model (Eq. V.S.) and constant stiffness constitutive model (Eq. H.), are compared. The latter comparison being useful to verify whether one can neglect or not the variability of the properties. It is observed that the mode shapes, either for the buckling analysis and the modal analysis, assume a particular form which resemble the orientation of the stiffeners. The variable stiffness continuum model is capable to represent faithfully such mode asymmetry as shown in Figure 2.26 and in turn gives a closer estimation of the eigenvalue. On the other hand, the equivalent constant

Table 2.1 First buckling load [N/mm] of simply supported curvilinearly stiffened panels subjected to uniaxial compression N_x .

	Topology		Stiffened	Eq. V.S.	$Err_{R\%}$	Eq. H.	$Err_{R\%}$
	θ_1	θ_2					
a	-45°	-16.75°	291.3	294.8	1.2	355.85	22.2
b	-40°	-14°	293.2	300.0	2.3	338.19	15.3
c	-30°	-7°	301.9	286.6	-5.1	314.2	3.9
d	-20°	1.25°	278.1	275.2	-1.0	300.84	8.18
e	-10°	10.25°	267.1	270.6	1.3	293.47	9.8
f	0°	21.5°	272.5	276.5	1.5	302.5	17.6
g	10°	34°	292.7	293.2	0.2	313.5	7.1
h	16.75°	45°	296.93	294.9	0.7	355.85	19.8

Table 2.2 First frequencies [Hz] of a simply supported curvilinearly stiffened panels.

	Topology		Stiffened	Eq. V.S.	$Err_{R\%}$	Eq. H.	$Err_{R\%}$
	θ_1	θ_2					
a	-45°	-16.75°	120.6	120.6	-	126.5	4.7
b	-40°	-14°	114.25	115.01	0.7	118.65	3.8
c	-30°	-7°	105.7	105.1	-0.5	108.6	2.7
d	-20°	1.25°	101.1	98.0	-3.0	101.7	0.5
e	-10°	10.25°	99.89	95.4	-4.4	98.9	-1
f	0°	21.5°	101.59	98.8	-2.7	102.5	0.9
g	10°	34°	103.91	108.78	4.7	112.46	7.6
h	16.75°	45°	119.98	120.6	0.5	126.5	5.4

model gives rise to an approximation of the eigenvalue and eigenmode which results in an higher error with respect to the variable stiffness model, as follows looking at Tables 2.1-2.2 and Figure 2.26. To the author knowledge, the need for modeling a variable stiffness laminate was already pointed out for AFP composites [50] but not for curvilinear stiffened structure because of the lack of equivalent continuum model. It is also worth noting that the two models, in general, overestimate the rigidity of the structure. The equivalent constant model underestimate the frequencies of the structure while the variable stiffness model yields, in most of the cases, an higher frequencies. However, the variable stiffness model in either cases yields a maximum error within 5% while the EqH model yields a maximum error of 7.6%.

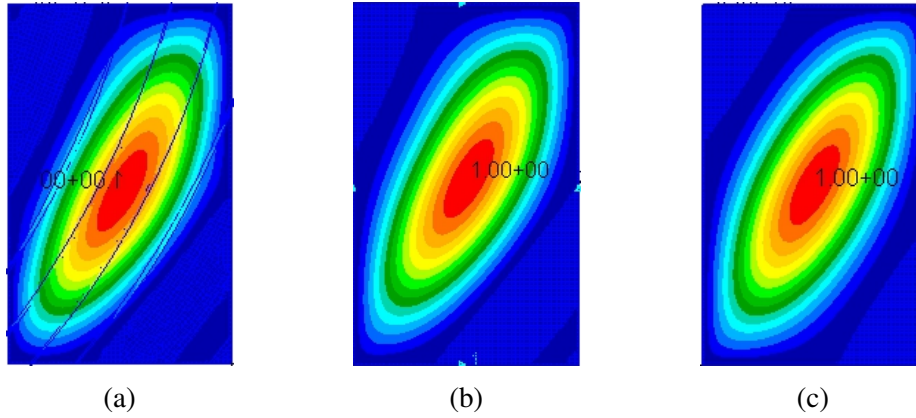


Fig. 2.26 Comparison of the buckling modes of a stiffened panel with $\vartheta_1 = -40^\circ$ and $\vartheta_2 = -14^\circ$. Fig. (a) is the first buckling mode of the stiffened structure, while Fig. (b) and Fig. (c) are the first buckling mode for the case of variable (*EqVS*) and constant (*EqH*) stiffness respectively.

Figures 2.27 and 2.28 report the eigenvectors obtained with the models adopted herein for three among the configurations analyzed, for the case of buckling loads and free vibrations. The eigenvectors reported in Figures 2.27 and 2.28 were obtained using the *EqVS* model with 100 subcells. It is worth noting that the eigenvectors resemble the geometry of the stiffeners and that for the case of $\vartheta_1 = -10^\circ$, $\vartheta_2 = 10.25^\circ$ in either cases, i.e. buckling and free vibrations, the mode shape resemble that of an orthotropic panel. This serves as further confirmation that when $\vartheta_1 = -\vartheta_2$, the global behavior of the plate is that of an orthotropic plate.

Despite the limit envelope for curved beam is valid regardless of the thicknesses of the skin plate and stiffeners, it is worth noting that for sub-stiffeners, i.e. for those stiffeners having $h_s \approx h_p$ is it possible to extend the present procedure to entire set of orientations, i.e. $-45^\circ \leq \vartheta_i \leq 45^\circ$. For the sake of clarity, let us consider the first of eqns. 2.38

$$\begin{aligned}
 C_{ijM} &= \frac{2A_{ij}^s + A_{ij}^p}{2h_s + h_p} \\
 &= \frac{2Q_{ij}^s h_s + Q_{ij}^p h_p}{2h_s + h_p} \\
 &= \frac{2Q_{ij}^s h_s}{h_s \left(2 + \frac{h_p}{h_s}\right)} + \frac{Q_{ij}^p h_p}{h_s \left(2 + \frac{h_p}{h_s}\right)}
 \end{aligned}$$

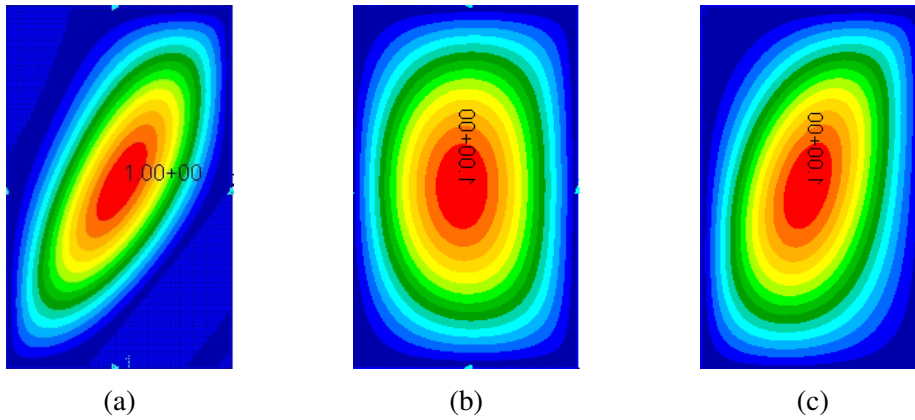


Fig. 2.27 Comparison of the first buckling mode for different stiffeners topologies, respectively Figure 2.28a $\vartheta_1 = -40^\circ$, $\vartheta_2 = -14^\circ$, Figure 2.28b $\vartheta_1 = -10^\circ$, $\vartheta_2 = -10.25^\circ$ and Figure 2.28c $\vartheta_1 = 0^\circ$, $\vartheta_2 = 21^\circ$. The figures are obtained considering the variable stiffness model with 100 subcells. It can be noted that the mode shapes resemble the stiffeners geometry. For the case reported in Figure 2.28b it can be noted that the mode shape resemble that of an orthotropic plate.

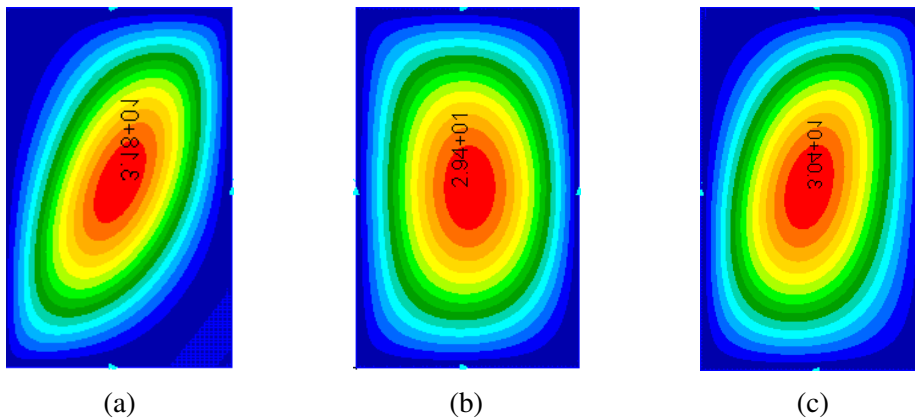


Fig. 2.28 Comparison of the first vibration mode for different stiffeners topologies, respectively Figure 2.28a $\vartheta_1 = -40^\circ$, $\vartheta_2 = -14^\circ$, Figure 2.28b $\vartheta_1 = -10^\circ$, $\vartheta_2 = -10.25^\circ$ and Figure 2.28c $\vartheta_1 = 0^\circ$, $\vartheta_2 = 21^\circ$. The figures are obtained considering the variable stiffness model with 100 subcells. It can be noted that the mode shapes resemble the stiffeners geometry. For the case reported in Figure 2.28b it can be noted that the mode shape resemble that of an orthotropic plate.

$$= \frac{2Q_{ij}^s}{\left(2 + \frac{h_p}{h_s}\right)} + \frac{Q_{ij}^p \frac{h_p}{h_s}}{\left(2 + \frac{h_p}{h_s}\right)}$$

Considering two distinct cases, i.e. $h_s \gg h_p$ and $h_s \approx h_p$, one has

$$C_{ijM} = \begin{cases} \frac{2Q_{ij}^s}{3} + \frac{Q_{ij}^p}{3} & \text{for } h_s \approx h_p \\ \frac{Q_{ij}^s}{2} + \frac{Q_{ij}^p \frac{h_p}{h_s}}{2} & \text{for } h_s \gg h_p \end{cases}. \quad (2.72)$$

For the case of straight stiffeners oriented at $\vartheta_1 = 0$, and considering an isotropic material for the stiffeners and skin plate, $Q_{11}^s = \frac{Eb_s}{d_s} \ll \frac{E}{1-\nu} = Q_{11}^p$ it follows that for the case of $h_s \approx h_p$ the dominant component is due to the skin plate. On the other hand, when $h_s \gg h_p$, Q_{11}^s is the dominant component hence the effect of having neglected the beam curvature into the direct compatibility becomes predominant. The same conclusion can be drawn considering the expression of C_{ijD} and C_{ijT} . Indeed, the effect is even more relevant if one considers the bending component because the latter goes with the thickness ratio h_p/h_s raised to the cube.

Let us consider a rectangular flat plate having the same dimensions of the panels analyzed previously ($a = 500$ mm, $b = 100$ mm, $h_p = b_s = 3$ mm) except for the stiffeners height. In this case we considered the stiffener height $h_s = 3$ mm, i.e. the same as the skin panel thickness. The topology of the stiffeners is taken such that the radius of curvature is minimum, i.e. $\vartheta_1 = 45$, $\vartheta_2 = -45$. We compare the buckling loads of the real structure against those of the variable stiffness model. The result pertaining this analysis are reported in Table 2.3. For the sake of comparison we considered the first three buckling loads. The results reported in Table 2.3 demonstrate the following:

- If we consider sub-stiffened structures the equivalent models presented herein and in Cestino *et al* [125] are in good agreement and agree also with the results of the stiffened structure.
- If we consider sub-stiffened structures the limit envelope reported in Figure 2.24 is no longer valid therefore the topology of the stiffeners can span all over the design domain.

Table 2.3 Buckling loads [N/mm] of a simply supported flat panel with concentric substiffeners.

Mode	Stiffened	Eq. V.S.	$E_{R\%}$	Eq. H.	$E_{R\%}$	Eq. H. [125]	$E_{R\%}$
I	40.28	40.11	-0.42	40.77	1.24	40.77	1.24
II	41.76	41.74	-0.05	42.41	1.54	42.77	2.43
III	59.11	58.72	-0.65	59.48	0.63	59.48	0.63

It is worth mentioning that, for the case of stiffened structure with $h_s = 20$ mm and $\vartheta_1 = 45$, $\vartheta_2 = -45$, the variable stiffness model yields an error up to 30%.

2.6.2 Effect of the torsional stiffness

Herein are reported the buckling loads for simply supported panels respectively neglecting and retaining higher order terms for the torsional stiffness. The two cases are labelled as (*f.o.*) for first order approximation, i.e. $J_t = 1/3b_s h_s^3$ and *h.o.* for higher order approximation, i.e. with 10 terms in the series given in Equation 2.13. The buckling loads retaining and neglecting the torsional stiffness are reported in Table 2.4. The panel considered herein for comparison is the same as in section 2.6.1. Without loss in generality, the case of constant stiffness is considered. As can be seen from Table 2.4, the effect of the higher order terms on the torsional stiffness is negligible as discussed by [122] and the results obtained with the two methods are found in good agreement.

2.6.3 Effect of the number of subcells

A parametric study has been performed in order to evaluate the convergence of the stiffness coefficients to their asymptotic values. We defined the latter as the value of the stiffness coefficients obtained using 1000 sub-cells. The analysis is limited to stiffened panels however the same conclusion can be drawn for sub-stiffened panels. Without loss of generality, the comparison are made considering the bending coefficients D_{ij} for the case of constant stiffened model.

In Figure 2.30 are reported the non-dimensional bending coefficients \hat{d}_{ij} for two stiffened panels. The curve are drawn with respect to the number of sub-cells,

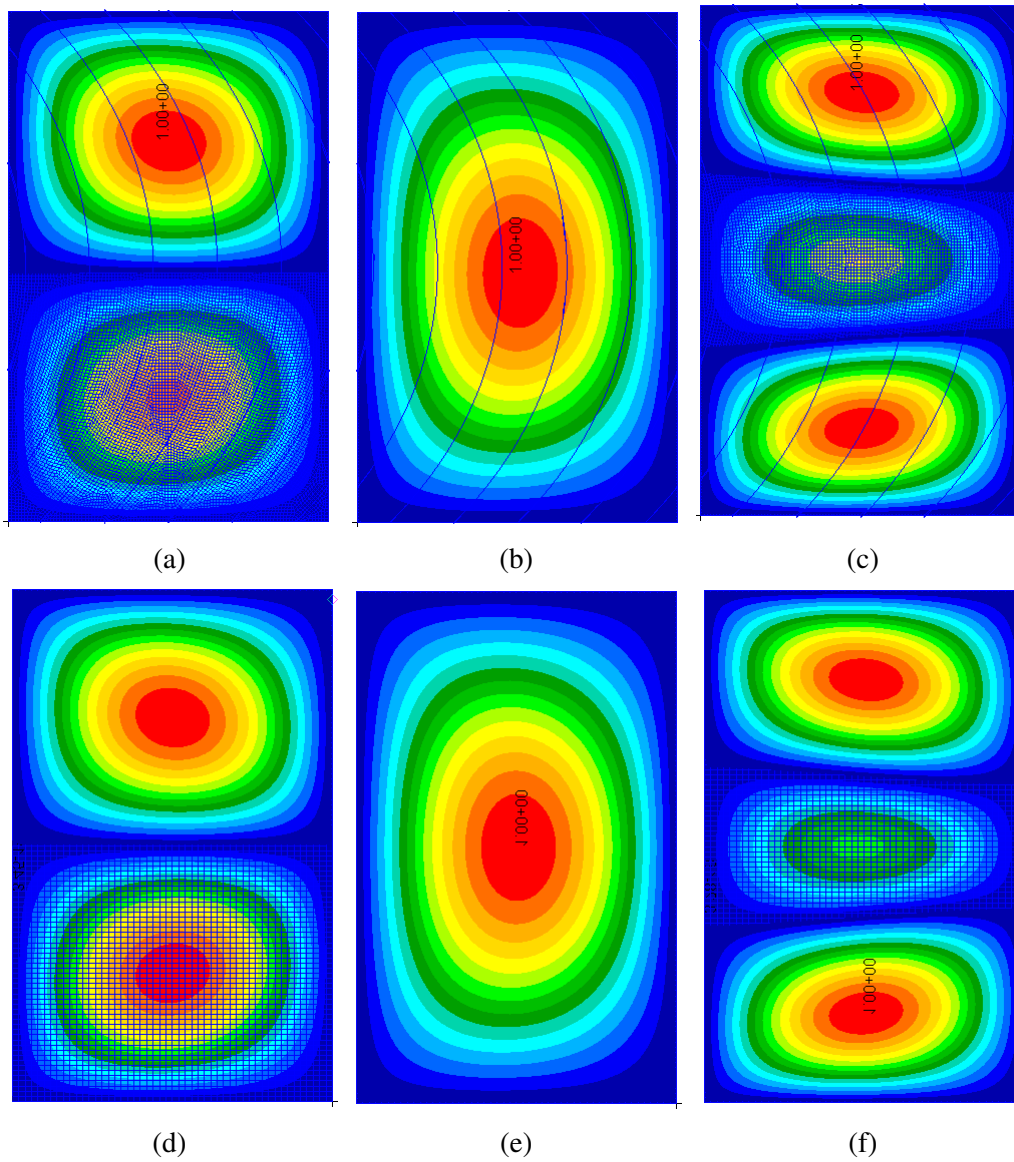


Fig. 2.29 Comparison of the buckling modes of a substiffened panel with $\vartheta_1 = 45^\circ$ and $\vartheta_2 = -45^\circ$. Figures 2.29a-2.29c are the first three buckling modes for the stiffened structure. Figures 2.29d-2.29f are the buckling modes for the case of variable stiffened properties derived using 100 sub-cells.

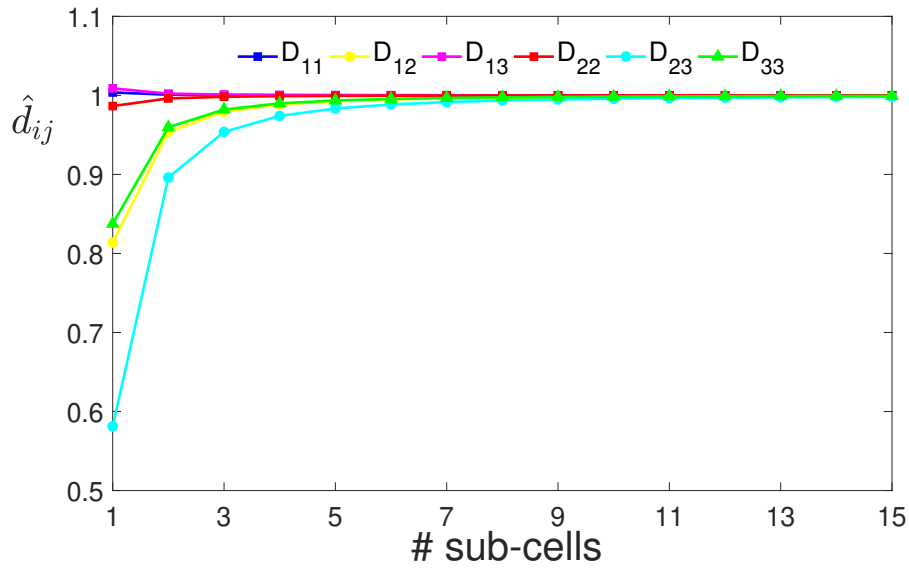
Table 2.4 Comparison of the first buckling loads of simply supported curvilinearly stiffened panels with and without higher order terms for the torsional stiffness

	Topology		Buckling	
	θ_1	θ_2	f.o.	h.o.
a	-45°	-16.75°	371.0	355.85
b	-40°	-14°	341.6	338.19
c	-30°	-7°	311.5	314.2
d	-20°	1.25°	294.5	300.84
e	-10°	10.25°	286.5	293.47
f	0°	21.5°	295.8	302.5
g	10°	34°	325.5	313.5
h	16.75°	45°	371.0	355.85

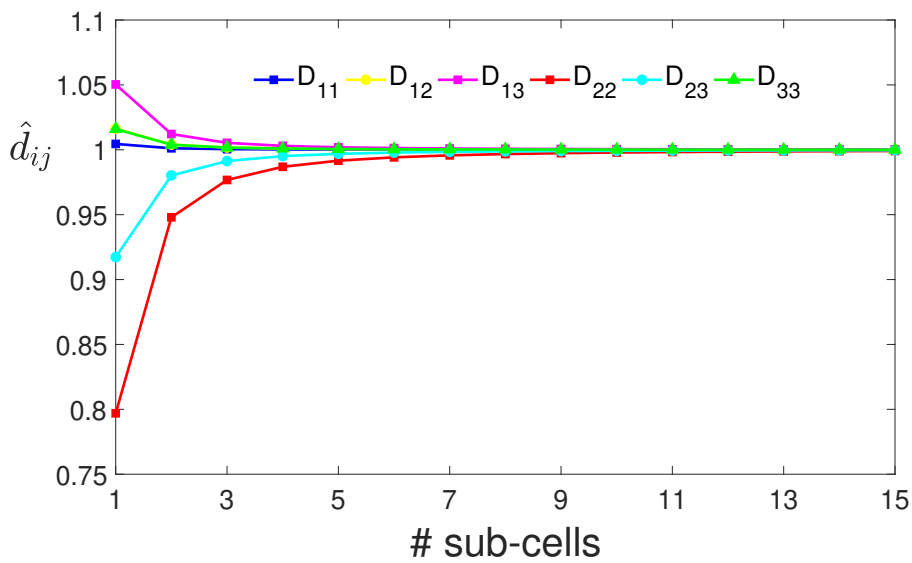
aiming at showing the number of sub-cells necessary to reach the convergence of the stiffness coefficients. The normalized coefficients are obtained by dividing each of the coefficients with its own asymptotic value, i.e. $\hat{d}_{ij} = D_{ij}(n_{cell})/D_{ij}^{asy}$. As shown in Figure 2.30, the stiffness coefficients require few sub-divisions to converge to the asymptotic value. Depending on the topology of the stiffeners, some of the stiffness coefficients may converge faster than the other. In general, is not possible to draw an rule of thumb except for D_{11} , which indeed converges faster. However, despite the fast convergence it is advisable to increase the number of subcells to get an accurate estimation of the variable stiffness properties.

2.6.4 Effect of the transverse shear

In the previous section we have seen that the energy equivalence method gives rise to the stiffness matrices of the equivalent continuum plate. In particular, being the stiffeners in the concentric configuration, the membrane-bending coupling matrix $[B]$ is zero. Moreover, it has been shown that the properties of the equivalent continuum material may differ to a great extend according to the particular topology of the stiffeners considered. Here the aim is to investigate whether the effect of the transverse shear can be neglected or not according to the topology of the stiffeners that one have. The investigation presented herein is limited to rectangular panels having the same dimension as discussed above, i.e. $a = 500$ mm, $b = 800$ mm, $h_s = 20$, $h_p = b_s = 3$ mm and $n_s = 5$. Both the panel and the stiffeners are made by



(a)



(b)

Fig. 2.30 Effect of the number of subcell on the normalized bending coefficients \hat{d}_{ij} for two stiffened panels having (a) $\vartheta_1 = 0^\circ$, $\vartheta_2 = 10^\circ$ and, (b) $\vartheta_1 = -45^\circ$, $\vartheta_2 = -20^\circ$.

Aluminum alloy. As a rule of thumb, is known that for plates with span-to-thickness ratio below 15 the effect of the transverse shear increase and cannot be neglected. However, this rule of thumb may differ according to the nondimensional ratio of the material's moduli. Herein we aim at verify whether the effect of the transverse shear is negligible or not according to the topology of the stiffeners, or equivalently according to the effective engineering properties of the equivalent material.

The effect of the transverse shear onto the buckling loads is considered through a parametric study. Particularly, the buckling loads obtained accounting for the transverse shear are compared against those obtained neglecting the effect of the latter. The parametric analysis is performed by varying the orientation of the stiffeners within the design space ϑ_1, ϑ_2 and allows the representation of an error map, being the latter the contour plot of the relative percentage error. The buckling loads were computed by means of FEA.

Despite limited to one plate with fixed aspect ratio $b/a = 1.6$ and with span-to-thickness ratio $b/h \approx 19$ and $a/h \approx 12$ respectively, the analysis shows some interesting trends that is worth to discuss. As expected, the error committed neglecting the shear stress depends on the topology of the stiffeners and to the relative equivalent properties. Particularly it is seen that, in the region $-15^\circ \leq (\vartheta_1, \vartheta_2) \leq 15^\circ$ the error is minimum. This can be explained looking at the shear-shear coupling (or Chentsov's) coefficient and at the mutual coefficients (Figure 2.18). Contrary, when the Chentsov's coefficient reaches its maximum, the maximum error is obtained when the effect of the transverse shear is neglected. However the maximum error obtained is of the order of 1% as shown in Figure 2.31. In Figure 2.31 is indeed reported the contour plots of the error between the model with shear matrix retained and omitted. The contour plots are drawn over the design envelope obtained as in section 2.5.1. The shaded gray areas are the design zone which violates the assumption for the Jacobian $R/(R - y)$ to be neglected (see Figure 2.24).

In order to explain why the transverse shear can be neglected is worth deriving the non-dimensional form of the equations for the Reissner-Mindlin plate. Let us consider the constitutive equations for the Reissner-Mindlin plate

$$N_x = A_{11}\varepsilon_{xx} + A_{12}\varepsilon_{yy} + A_{16}\gamma_{xy}, \quad (2.73a)$$

$$N_y = A_{21}\varepsilon_{xx} + A_{22}\varepsilon_{yy} + A_{26}\gamma_{xy}, \quad (2.73b)$$

$$N_{xy} = A_{61}\varepsilon_{xx} + A_{62}\varepsilon_{yy} + A_{66}\gamma_{xy}, \quad (2.73c)$$

$$Q_x = A_{44}\gamma_{xz} + A_{45}\gamma_{yz}, \quad (2.73d)$$

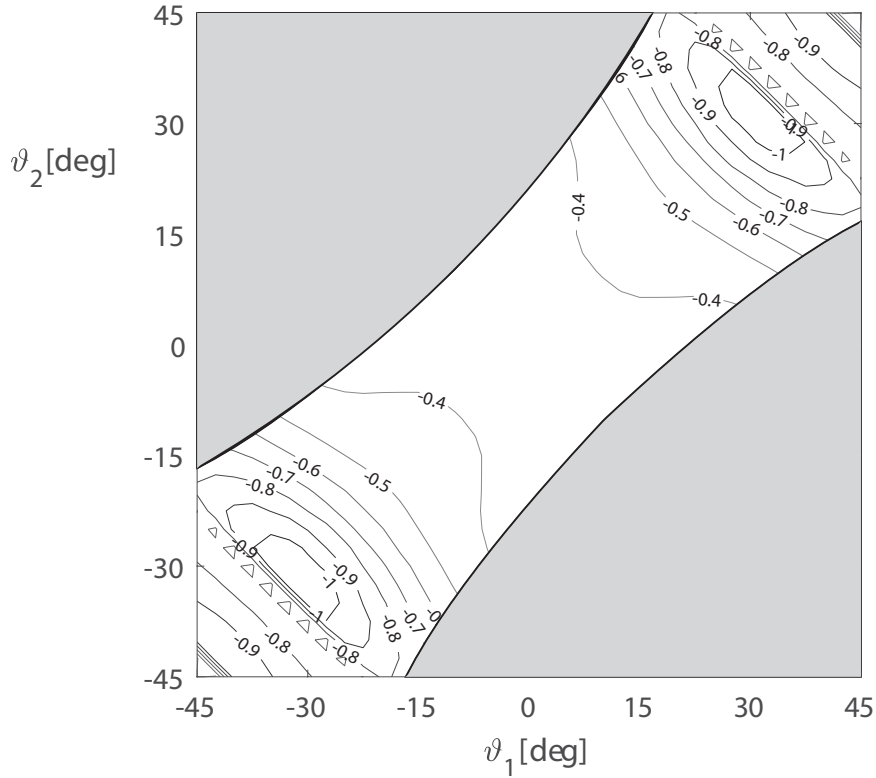


Fig. 2.31 Contour plot of the relative percentage error between the buckling loads obtained retaining and neglecting the effect of the transverse shear.

$$Q_y = A_{54}\gamma_{xz} + A_{55}\gamma_{yz}, \quad (2.73e)$$

$$M_x = D_{11}\kappa_{xx} + D_{12}\kappa_{yy} + D_{16}\kappa_{xy}, \quad (2.73f)$$

$$M_y = D_{21}\kappa_{xx} + D_{22}\kappa_{yy} + D_{26}\kappa_{xy}, \quad (2.73g)$$

$$M_{xy} = D_{61}\kappa_{xx} + D_{62}\kappa_{yy} + D_{66}\kappa_{xy}. \quad (2.73h)$$

The equilibrium eqns. can be written as

$$N_{x,x} + N_{xy,y} = 0, \quad (2.74a)$$

$$N_{xy,x} + N_{y,y} = 0, \quad (2.74b)$$

$$Q_{x,x} + Q_{y,y} + \bar{q}_z = 0, \quad (2.74c)$$

$$M_{x,x} + M_{xy,y} - Q_x = 0, \quad (2.74d)$$

$$M_{xy,x} + M_{y,y} - Q_y = 0. \quad (2.74e)$$

Now replacing eqns. in 2.73 in eqns. in 2.74 one have:

$$(A_{11}\epsilon_{xx} + A_{12}\epsilon_{yy} + A_{16}\gamma_{xy})_{,x} + (A_{61}\epsilon_{xx} + A_{62}\epsilon_{yy} + A_{66}\gamma_{xy})_{,y} = 0, \quad (2.75a)$$

$$(A_{61}\epsilon_{xx} + A_{62}\epsilon_{yy} + A_{66}\gamma_{xy})_{,x} + (A_{21}\epsilon_{xx} + A_{22}\epsilon_{yy} + A_{26}\gamma_{xy})_{,x} = 0, \quad (2.75b)$$

$$(A_{44}\gamma_{xz} + A_{45}\gamma_{yz})_{,x} + (A_{54}\gamma_{xz} + A_{55}\gamma_{yz})_{,y} + \bar{q}_z = 0, \quad (2.75c)$$

$$(D_{11}\kappa_{xx} + D_{12}\kappa_{yy} + D_{16}\kappa_{xy})_{,x} + (D_{61}\kappa_{xx} + D_{62}\kappa_{yy} + D_{66}\kappa_{xy})_{,y} - [A_{44}\gamma_{xz} + A_{45}\gamma_{yz}] = 0, \quad (2.75d)$$

$$(D_{61}\kappa_{xx} + D_{62}\kappa_{yy} + D_{66}\kappa_{xy})_{,x} + (D_{21}\kappa_{xx} + D_{22}\kappa_{yy} + D_{26}\kappa_{xy})_{,y} - [A_{54}\gamma_{xz} + A_{55}\gamma_{yz}] = 0. \quad (2.75e)$$

Rewriting the expression in terms of the displacements, taking the derivatives, and defining:

$$u = \bar{u}h, \quad v = \bar{v}h, \quad w = \bar{w}h, \quad (\cdot)_{,x} = \frac{1}{a}(\cdot)_{,\xi}, \quad (\cdot)_{,y} = \frac{1}{b}(\cdot)_{,\eta},$$

$$A_{11}u_{,xx}^{(0)} + A_{12}v_{,yx}^{(0)} + A_{16} \left(u_{,yx}^{(0)} + v_{,xx}^{(0)} \right) + A_{61}u_{,xy}^{(0)} + A_{62}v_{,yy}^{(0)} + A_{66} \left(u_{,yy}^{(0)} + v_{,xy}^{(0)} \right) = 0, \quad (2.76a)$$

$$A_{61}u_{,xx}^{(0)} + A_{62}v_{,yx}^{(0)} + A_{66} \left(u_{,yx}^{(0)} + v_{,xx}^{(0)} \right) + A_{21}u_{,xy}^{(0)} + A_{22}v_{,yy}^{(0)} + A_{26} \left(u_{,yy}^{(0)} + v_{,xy}^{(0)} \right) = 0l \quad (2.76b)$$

$$A_{44} \left(\psi_{x,x} + w_{,xx}^{(0)} \right) + A_{45} \left(\psi_{y,x} + w_{,yx}^{(0)} \right) + A_{54} \left(\psi_{x,x} + w_{,xy}^{(0)} \right) + A_{55} \left(\psi_{y,y} + w_{,yy}^{(0)} \right) + \bar{q}_z = 0, \quad (2.76c)$$

$$D_{11}\psi_{x,xx} + D_{12}\psi_{y,yx} + D_{16} \left(\psi_{x,yx} + \psi_{y,xx} \right) + D_{61}\psi_{x,xy} + D_{62}\psi_{y,yy} + D_{66} \left(\psi_{x,yy} + \psi_{y,xy} \right) - A_{44} \left(\psi_x + w_{,x}^{(0)} \right) - A_{45} \left(\psi_y + w_{,y}^{(0)} \right) = 0, \quad (2.76d)$$

$$D_{61}\psi_{x,xx} + D_{62}\psi_{y,yx} + D_{66} \left(\psi_{x,yx} + \psi_{y,xx} \right) + D_{21}\psi_{x,xy} + D_{22}\psi_{y,yy} + D_{26} \left(\psi_{x,yy} + \psi_{y,xy} \right) - A_{54} \left(\psi_x + w_{,x}^{(0)} \right) - A_{55} \left(\psi_y + w_{,y}^{(0)} \right) = 0. \quad (2.76e)$$

Defining:

$$u = \bar{u}h, \quad v = \bar{v}h, \quad w = \bar{w}h, \quad (\cdot)_{,x} = \frac{1}{a}(\cdot)_{,\xi}, \quad (\cdot)_{,y} = \frac{1}{b}(\cdot)_{,\eta}.$$

The set of Eqns 2.74 can be finally written in the non-dimensional form as follow

$$\bar{u}_{,\xi\xi}^{(0)} \frac{h}{a^2} + \frac{A_{12}}{A_{11}} \bar{v}_{,\eta\xi}^{(0)} \frac{h}{ab} + \frac{A_{16}}{A_{11}} \left(\bar{u}_{,\eta\xi}^{(0)} \frac{h}{ab} + \bar{v}_{,\xi\xi}^{(0)} \frac{h}{a^2} \right) + \frac{A_{61}}{A_{11}} \bar{u}_{,\xi\eta}^{(0)} \frac{h}{ab} + \frac{A_{62}}{A_{11}} \bar{v}_{,\eta\eta}^{(0)} \frac{h}{b^2} + \frac{A_{66}}{A_{11}} \left(\bar{u}_{,\eta\eta}^{(0)} \frac{h}{a^2} + \bar{v}_{,\xi\eta}^{(0)} \frac{h}{ab} \right) = 0, \quad (2.77a)$$

$$\frac{A_{61}}{A_{11}} \bar{u}_{,\xi\xi}^{(0)} \frac{h}{a^2} + \frac{A_{62}}{A_{11}} \bar{v}_{,\eta\xi}^{(0)} \frac{h}{ab} + \frac{A_{66}}{A_{11}} \left(\bar{u}_{,\eta\xi}^{(0)} \frac{h}{ab} + \bar{v}_{,\xi\xi}^{(0)} \frac{h}{a^2} \right) + \frac{A_{21}}{A_{11}} \bar{u}_{,\xi\eta}^{(0)} \frac{h}{ab} + \frac{A_{22}}{A_{11}} \bar{v}_{,\eta\eta}^{(0)} \frac{h}{b^2} + \frac{A_{26}}{A_{11}} \left(\bar{u}_{,\eta\eta}^{(0)} \frac{h}{b^2} + \bar{v}_{,\xi\eta}^{(0)} \frac{h}{ab} \right) = 0, \quad (2.77b)$$

$$\left(\psi_{\xi,\xi} \frac{1}{a} + \bar{w}_{,\xi\xi}^{(0)} \frac{h}{a^2} \right) + \frac{A_{45}}{A_{44}} \left(\psi_{\eta,\xi} \frac{1}{a} + \bar{w}_{,\eta\xi}^{(0)} \frac{h}{ab} \right) + \frac{A_{45}}{A_{44}} \left(\psi_{\xi,\xi} \frac{1}{a} + \bar{w}_{,\xi\eta}^{(0)} \frac{h}{ab} \right) + \frac{A_{55}}{A_{44}} \left(\psi_{\eta,\eta} \frac{1}{b} + \bar{w}_{,\eta\eta}^{(0)} \frac{h}{b^2} \right) + \bar{q}_z = 0, \quad (2.77c)$$

$$\begin{aligned}
& \psi_{\xi,\xi\xi} \frac{1}{a^2} + \frac{D_{12}}{D_{11}} \psi_{\eta,\eta\xi} \frac{1}{ab} + \frac{D_{16}}{D_{11}} \left(\psi_{\xi,\eta\xi} \frac{1}{ab} + \psi_{\eta,\xi\xi} \frac{1}{a^2} \right) + \frac{D_{61}}{D_{11}} \psi_{\xi,\xi\eta} \frac{1}{ab} \\
& + \frac{D_{62}}{D_{11}} \psi_{\eta,\eta\eta} \frac{1}{b^2} + \frac{D_{66}}{D_{11}} \left(\psi_{\xi,\eta\eta} \frac{1}{b^2} + \psi_{\eta,\xi\eta} \frac{1}{ab} \right) - \frac{A_{44}}{D_{11}} \left(\psi_{\xi} + \bar{w}_{,\xi}^{(0)} \frac{h}{a} \right) \\
& - \frac{A_{45}}{D_{11}} \left(\psi_{\eta} + \bar{w}_{,\eta}^{(0)} \frac{1}{b} \right) = 0,
\end{aligned} \tag{2.77d}$$

$$\begin{aligned}
& \frac{D_{61}}{D_{11}} \psi_{\xi,\xi\xi} \frac{1}{a^2} + \frac{D_{62}}{D_{11}} \psi_{\eta,\eta\xi} \frac{1}{ab} + \frac{D_{66}}{D_{11}} \left(\psi_{\xi,\eta\xi} \frac{1}{ab} + \psi_{\eta,\xi\xi} \frac{1}{a^2} \right) + \frac{D_{21}}{D_{11}} \psi_{\xi,\xi\eta} \frac{1}{ab} \\
& + \frac{D_{22}}{D_{11}} \psi_{\eta,\eta\eta} \frac{1}{b^2} + \frac{D_{26}}{D_{11}} \left(\psi_{\xi,\eta\eta} \frac{1}{b^2} + \psi_{\eta,\xi\eta} \frac{1}{ab} \right) - \frac{A_{45}}{D_{11}} \left(\psi_{\xi} + \bar{w}_{,\xi}^{(0)} \frac{h}{a} \right) \\
& - \frac{A_{55}}{D_{11}} \left(\psi_{\eta} + \bar{w}_{,\eta}^{(0)} \frac{1}{b} \right) = 0.
\end{aligned} \tag{2.77e}$$

From the Eqns. 2.77, follows that the effect of the transverse shear for the cases analyzed herein can be neglected. Indeed, the apparent engineering properties of the bending material, and thus the bending stiffness coefficients, are at least one order of magnitude smaller than that of the shear matrix. Under these circumstances, γ_{xz} and γ_z are small compared with the other strains and can be neglected. After some algebraic manipulation, omitted for the sake of brevity, is possible recover, from Eqns. 2.77 those of the Kirchhoff-Love plate theory.

2.6.5 Effect of the panel density

In section 2.5.2 we have defined two equivalent density models namely, constant density and variable density. Herein we aim at showing the difference between the two models comparing the first natural frequency of the panels with variable density against those obtained with the constant density. The panels selected for the present analysis are the same considered in section 2.5. It is worth mentioning that the results reported in Table 2.2 were obtained considering the variable density model. Moreover, in either cases herein considered, we use the variable stiffness model. From Table 2.5 follows that the two models are in good agreement and hence the effect of the density variability can be neglected.

Table 2.5 Effect of the density's model adopted for free vibrations of simply supported plates.

	Topology		Frequency [Hz]	
	θ_1	θ_2	Variable density	Constant density
a	-45°	-16.75°	120.6	122.05
b	-40°	-14°	115.01	116.49
c	-30°	-7°	105.1	106.47
d	-20°	1.25°	98.0	99.40
e	-10°	10.25°	95.4	96.82
f	0°	21.5°	98.8	100.18
g	10°	34°	108.78	110.27
h	16.75°	45°	120.6	122.6

2.7 Case studies

In this section are evaluated the buckling loads and frequencies of simply supported square panels $a = b = 500$ mm. In all the cases investigated herein, the constituent material for the panel and the stiffeners is an Aluminum alloy with Young modulus $E = 73$ GPa, Poisson's ratio $\nu = 0.3$ and density $\rho = 2780$ kg/m³. In all the cases analyzed in this section the effect of the transverse shear is retained.

2.7.1 Concentric panel with one family of stiffeners

Consider a stiffened panel having $h_s = 21.5$ mm, $h_p = b_s = 3$ mm subjected to uniaxial compression. The number of stiffeners is $n_s = 8$. The orientation of the stiffener are: $\vartheta_1 = 0^\circ$, $\vartheta_2 = 10^\circ$. The first three buckling loads are given in Table 2.6 while the frequencies are listed in Table 2.7. The buckling loads and frequencies of the stiffened structure are compared against those of the variable stiffness equivalent continuum (*Eq.V.S.*) model and the constant stiffness model (*Eq.H.*). In Figure 2.32 is illustrated a 3D view of the first buckling mode of the stiffened structure obtained from the FEA. In Figure 2.33 are reported the modes relative to the first three eigenvalues for the case of the stiffened structure and the equivalent model with variable stiffness. It can be seen that the mode shapes between the two models agree and thus also the eigenvalue are found in good agreement.

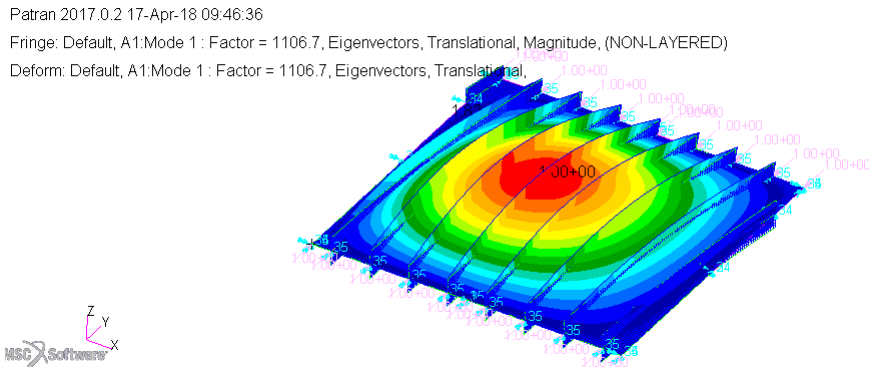


Fig. 2.32 First buckling mode of a steering stiffened panel with $\vartheta_1 = 0^\circ$, $\vartheta_2 = 10^\circ$.

Table 2.6 Buckling loads for a simply supported, square panel, reinforced with concentric curvilinear stiffened $\vartheta_1 = 0^\circ$, $\vartheta_2 = 10^\circ$.

# Mode	Stiffened	Eq V.S.	$Err_R\%$	EqH	$Err_R\%$
1	1106.7	1117.3	0.96	947.8	-14.3
2	1264.2	1273.6	0.74	1156.5	-8.53
3	1773.6	1795.4	1.23	1568.0	-11.59

Table 2.7 Natural frequencies for a simply supported, square panel, reinforced with concentric curvilinear stiffened $\vartheta_1 = 0^\circ$, $\vartheta_2 = 10^\circ$.

# Mode	Stiffened	Eq V.S.	$Err_R\%$	EqH	$Err_R\%$
1	300.9	302.1	0.4	292.5	-2.8
2	350.2	350.7	0.14	430.7	23
3	507.8	509.3	0.3	614.4	21

2.7.2 Buckling and free-vibrations of concentric grid stiffened panel

Let us consider a grid stiffened panel having the following dimensions $a = b = 500\text{mm}$, $h_s = 21.5\text{mm}$, $h_p = b_s = 3\text{mm}$. The panel is made with an Aluminum Alloy having the same properties listed above. The panel is simply supported along the edges and it is subjected to uniaxial compression. The orientation of the stiffener are: $\vartheta_1 = 0^\circ$, $\vartheta_2 = 10^\circ$ and $\vartheta_3 = \vartheta_4 = 0^\circ$. An exemplification of the panel is depicted in

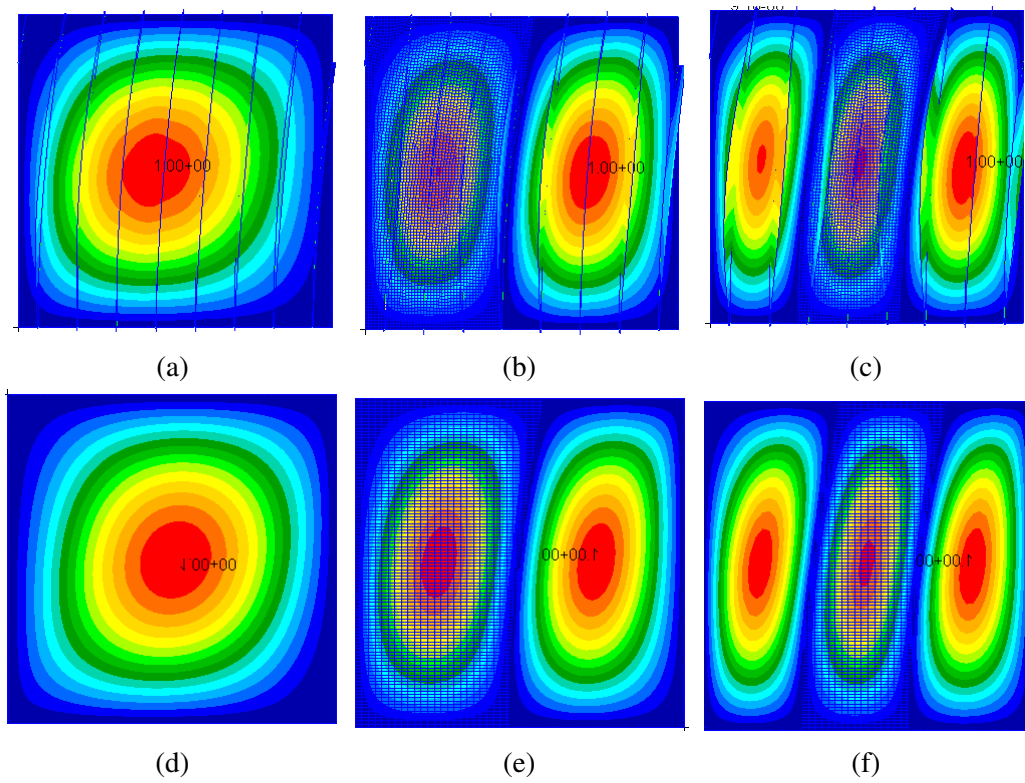


Fig. 2.33 Comparison of the bending modes of a stiffened panel with $\vartheta_1 = 0^\circ$ and $\vartheta_2 = 10^\circ$. Figures 2.33a-2.33c are the first three modes for the stiffened structure. Figures 2.33d-2.33f are the modes for the case of variable stiffened properties derived using 100 sub-cells.

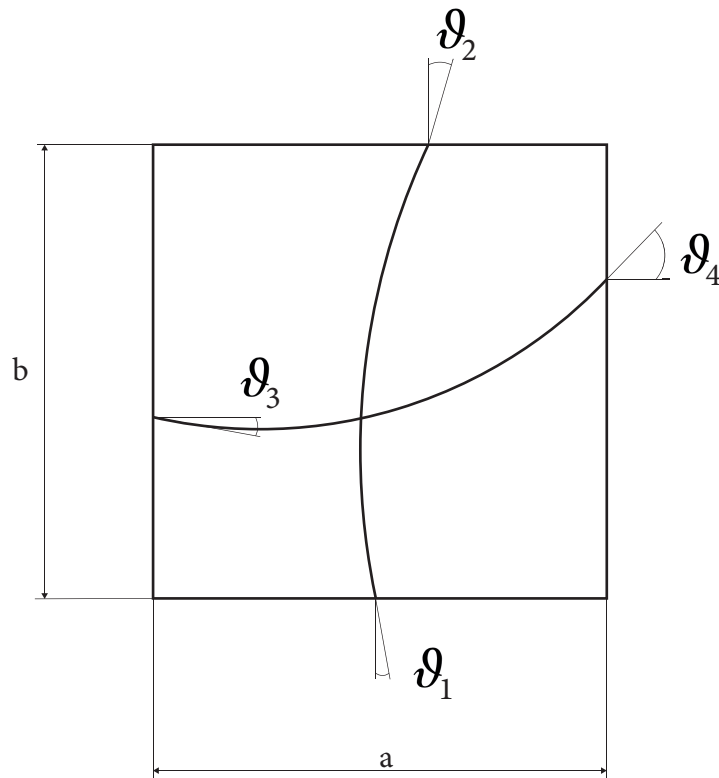


Fig. 2.34 Example of the orientation angles for a grid stiffened panel

Figure 2.34 The panels has 8 equally spaced stiffeners along the x direction, with $d_s = 62.5\text{mm}$ and 4 along the y direction with $d_s = 125\text{mm}$. The first buckling load and natural frequencies are given in Table 2.8. The buckling loads and frequencies of the stiffened structure are compared against those of the variable stiffness equivalent continuum model and the constant stiffness model. In this case the stiffnesses of the equivalent layers are obtained separately for each families of the stiffeners and then summed to give rise to the stiffness of the equivalent layer.

Table 2.8 First buckling load and first natural frequencies for a simply supported, square panel, reinforced with grid stiffeners.

# Mode	Stiffened	Eq V.S.	$Err_{R\%}$	EqH	$Err_{R\%}$
Buckling	1716.0	1715.9	-	292.5	-2.8
Frequency	304.6	307.9	1.1	430.7	23

2.8 Summary and conclusions

In this chapter the equivalent continuum properties of curvilinear stiffened panel were derived. The equivalent models were derived enforcing the direct compatibility in the sub-cell and smearing the strain energy density into the repetitive element. The two models have been assessed through comparative studies via FEA. It is shown that the two models derived are in good agreement with the results obtained via FEA. Particularly, the variable stiffness model is more accurate to represent a curvilinear stiffened structure. The derivation has been extended to derive the apparent engineering properties of the equivalent layer. The effect of the prominent parameters has been studied; it is discussed that the curvature give rise to a limit of validity of the present model. For the case of substiffeners, the limit can be ignored and model is valid to represent all the design space $45^\circ \leq \vartheta_{1,2} \leq 45^\circ$. It has been investigated the effect of the torsional stiffness onto the buckling loads of the panels. The results shows that the higher order terms in the expression of the torsional stiffness can be neglected, as discussed by [122]. It is demonstrated that the effect of transverse shear can be neglected since the equivalent transverse shear moduli are, in general, an order of magnitude larger that that of the bending. It is shown that the model converge to the asymptotic values of the stiffnesses with few subdivisions. However, having noted that the variable stiffness model is more reliable, it is advisable have an higher number of subdivision to obtain a good approximation of such stiffness variability. It has been shown that the stiffness matrices for a grid structure can be obtained by superposition. Namely, summing the contribution of the two families of stiffeners after a proper rotation, necessary to dispose the stiffeners as they are in the grid structure.

Chapter 3

Beam model

3.1 Motivation

This chapter is devoted to the derivation of the equations of motion of a box-beam made by an arrangement of stiffened and unstiffened panels. As already highlighted in Chapter 1, the idealized models used during preliminary design have a prominent effect on the final system. Indeed, outcomes they provide may influence considerably the entire life-cycle costs [37]. These models represent the physics of the problem, using a minimum number of degrees of freedom and number of design variables, rendering the models to have low fidelity that can qualitatively predict the system's behavior. Material and functional requirements have to be considered with great care within the preliminary design stages since, erroneous assumptions and/or improper material choices can lead to unrealistic responses and ultimately waste of resources.

The model derived in this chapter expand the current body of research in that it introduces variable stiffness beam and certain couplings which arise from the particular arrangement of the panels that one can have. The derivation is extended up to second order nonlinear terms for non-planar, flexural-flexural-torsional motion.

While the need of having a variable stiffness beam has been already pointed-out in the previous chapter, where the equivalent properties of generally stiffened flat panels were derived to a different extend, it is worthwhile to emphasize the need of nonlinearities. According to the definition given in [128], linear structural mechanics relies on the following ansatz:

1. The displacements/rotations are small with respect to a characteristic length of the structure.
2. The strains are infinitesimal.
3. The equilibrium equations are given in the undeformed configuration,
4. The prescribed boundary conditions are linear in the generalized displacement and/or stress resultant.
5. The material is Hookean, i.e. the strain-stress relation is linear.

When one or more of the hypothesis listed above contravene, the linear theory would give erroneous qualitative and quantitative predictions. A suitable example is given by the reduction of modal frequencies of beam members when subjected to large displacements/rotations. In this case, to get an accurate estimation of the frequencies, the equations of motion should be written in the deformed configuration and the frequencies determined for example solving the associated linear eigenvalue problem, i.e. linearized around the deformed state [22, 23, 43, 45]. The related structural problem is referred to as geometrically nonlinear problem. Structures may suffer of other limit states usually referred to as physical or material nonlinearity.

Provided that real engineering structures rarely exhibit a nonlinearity of one type uncoupled from the nonlinearity of the other type, it is undoubtedly true that, for a variety of problems of technical interest, material behavior is well described by linear elastic constitutive laws. The derivation presented in this chapter falls within this class of nonlinear problems, i.e. geometrically nonlinear problems where linear elastic constitutive laws hold.

The nonlinear equations of motion presented in the following are derived by means of the extended Hamiltonian principle and are amenable for perturbation and numerical methods. A comparison of the present set of equations against those already presented in the open literature is provided.

3.2 Assumptions on the cross sectional properties

The beam cross sectional properties are derived according to the model presented by Berdichevsky and Armanios [129, 130], and consistently with the assumptions

considered by Cestino *et al.* [64]. For the sake of simplicity, a single cell, closed cross section anisotropic structure is considered. In the interest of clarity the assumptions to derive the cross sectional properties are herein summarized below:

1. The transverse shear effects are neglected consistent with the assumption of modeling high aspect ratio wing.
2. Assume free warping, the bimoment effect and resultant hoop stresses are neglected.
3. The shear flow N_{xs} is considered constant according to the Batho-Bredt theory.
4. The strains are presumed small and hence the linear elasticity theory is applied.

Being the box beam made by an arrangement of stiffened and unstiffened panels, as shown in Figure 3.1, the derivation of the cross sectional properties starts by writing the reduced stiffness matrix, as in [129, 130], namely

$$\begin{Bmatrix} N_{xx} \\ N_{xs} \\ M_{xx} \\ M_{xs} \end{Bmatrix} = \begin{bmatrix} A_{11}^* & A_{16}^* & B_{11}^* & B_{16}^* \\ A_{16}^* & A_{66}^* & B_{16}^* & B_{66}^* \\ B_{11}^* & B_{16}^* & D_{11}^* & D_{16}^* \\ B_{16}^* & B_{66}^* & D_{16}^* & D_{66}^* \end{bmatrix}, \quad (3.1)$$

where the expression of the reduced matrix are given as follow

$$A_{11}^* = A_{11} - \frac{A_{12}^2}{A_{22}}, \quad A_{16}^* = A_{16} - \frac{A_{12}A_{26}}{A_{22}}, \quad A_{66}^* = A_{66} - \frac{A_{26}^2}{A_{22}}, \quad (3.2a)$$

$$B_{11}^* = B_{11} - \frac{B_{12}^2}{B_{22}}, \quad B_{16}^* = B_{16} - \frac{B_{12}B_{26}}{B_{22}}, \quad B_{66}^* = B_{66} - \frac{B_{26}^2}{B_{22}}, \quad (3.2b)$$

$$D_{11}^* = D_{11} - \frac{D_{12}^2}{D_{22}}, \quad D_{16}^* = D_{16} - \frac{D_{12}D_{26}}{D_{22}}, \quad D_{66}^* = D_{66} - \frac{D_{26}^2}{D_{22}}. \quad (3.2c)$$

It is worth noting that in the following analysis the effect of membrane-bending coupling will be neglected. The latter is a direct consequence of having considered concentric stiffened panels. Next, relating the axial and shear stresses to the constitutive equations it is possible to derive the beam stiffnesses in the global

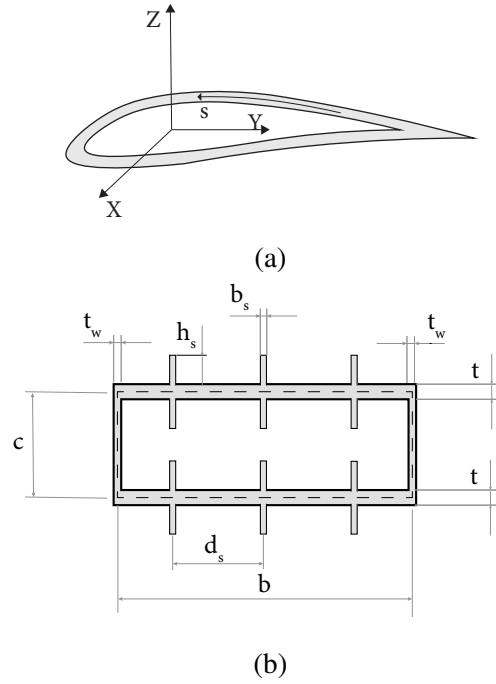


Fig. 3.1 Exemplification of the generic cross section for the CAS configuration and its reference system (a) and example of the beam cross section considered in this work

reference

$$\begin{Bmatrix} F_x \\ M_x \\ M_y \\ M_z \end{Bmatrix} = \begin{bmatrix} C_{00} & C_{01} & C_{02} & C_{03} \\ C_{10} & C_{11} & C_{12} & C_{13} \\ C_{20} & C_{21} & C_{22} & C_{23} \\ C_{30} & C_{31} & C_{32} & C_{33} \end{bmatrix} \begin{Bmatrix} e_x \\ \rho_x \\ \rho_y \\ \rho_z \end{Bmatrix} \quad (3.3)$$

where e_x is the elongation of the beam and ρ_i are the curvatures.

In the following analysis the effect of the elongation of the beam as well as the lag-torsion coupling C_{13} and the flap-lag coupling C_{23} are neglected. Only the flap-torsion coupling C_{12} is retained. This assumption derives from the particular arrangement of the panels chosen. Indeed it has been chosen to have upper and lower panel stiffened while the aft and fore panels are unstiffened, which is a common configuration for aeronautical box-beam. In view of this assumption, the Eqn. 3.3 assumes the following form

$$\begin{Bmatrix} M_x \\ M_y \\ M_z \end{Bmatrix} = \begin{bmatrix} C_{11} & C_{12} & 0 \\ C_{21} & C_{22} & 0 \\ 0 & 0 & C_{33} \end{bmatrix} \begin{Bmatrix} \rho_x \\ \rho_y \\ \rho_z \end{Bmatrix}. \quad (3.4)$$

By letting $C_{11} = GJ_t$, $C_{12} = k_{w\varphi}$, $C_{22} = EI_2$ and $C_{33} = EI_3$, one has

$$\begin{Bmatrix} M_1 \\ M_2 \\ M_3 \end{Bmatrix} = \begin{bmatrix} GJ_t & K_{\varphi w} & 0 \\ K_{w\varphi} & EI_2 & 0 \\ 0 & 0 & EI_3 \end{bmatrix} \begin{Bmatrix} \rho_x \\ \rho_y \\ \rho_z \end{Bmatrix} \quad (3.5)$$

where $K_{\varphi w} = K_{w\varphi}$ and for the isotropic case $K_{\varphi w} = K_{w\varphi} = 0$. Being $K_{\varphi w}$ the only coupling term hereafter considered, we will refer to it as K .

The circumferentially asymmetric stiffness coefficients are given as follow

$$GJ_t = \oint \frac{4\Omega^2}{1/A_{66}^*} ds + 4 \oint D_{66}^* ds, \quad (3.6a)$$

$$K = 2\Omega \frac{\oint (A_{16}^*/A_{66}^*) z ds}{\oint 1/A_{66}^* ds} - 2 \oint D_{16}^* \left(\frac{dy}{ds} \right) ds, \quad (3.6b)$$

$$EI_2 = \oint z^2 \left(A_{11}^* - \frac{A_{16}^{*2}}{A_{66}^*} \right) ds + \frac{[\oint A_{16}^*/A_{66}^* z ds]^2}{\oint 1/A_{66}^* ds} + \oint D_{11}^* \left(\frac{dy}{ds} \right)^2 ds, \quad (3.6c)$$

$$EI_3 = \oint y^2 \left(A_{11}^* - \frac{A_{16}^{*2}}{A_{66}^*} \right) ds + \frac{[\oint A_{16}^*/A_{66}^* y ds]^2}{\oint 1/A_{66}^* ds} + \oint D_{11}^* \left(\frac{dz}{ds} \right)^2 ds. \quad (3.6d)$$

The expressions in Eqn. 3.3 can be written in matrix form as

$$\{M\} = ([C] + [\tilde{C}]) \{\rho\} \quad (3.7)$$

where $[C]$ is the CAS matrix consistent with the membrane approach as in [131–133], while $[\tilde{C}]$ considers the bending stiffness effect as in [125].

3.2.1 Effect of the stiffeners orientation on to the effective beam properties

Let us consider the stiffened box-beam represented in Figure 3.2. In the interest of clarity all the geometry parameters are listed in Table 3.1. For the sake of simplicity, herein are reported the effective beam properties for the case in which the stiffeners orientation are assigned at the root and the tip of the beam. Therefore, the orientation in any point of the beam can be determined using the Eqn. 2.1.

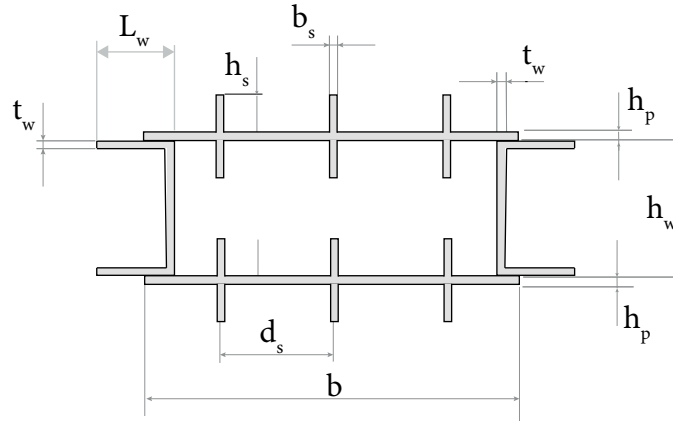


Fig. 3.2 Exemplification of the box-beam cross section.

Table 3.1 Geometric features of the wing box under study.

Stiffeners' width	b_s	3 mm
Stiffeners' spacing	d_s	10 mm
Stiffeners' height	h_s	4 mm
Number of stiffeners	n_s	6
Plate's skin thickness	h_p	2 mm
Beam's length	L	1100 mm
Spar caps length	L_w	20 mm
Spar height	h_w	40 mm
Spar's thickness	t_w	2 mm

In Figures 3.3-3.6 are reported the effective beam properties GJ_t, K, EI_2, EI_3 with respect to the angles of orientation of the stiffeners ϑ_1, ϑ_2 . It is worth noticing that the equivalent beam properties can be expressed, in general, as $C_{ij} = C_{ij}(\vartheta_1, \vartheta_2, x)$. In the following, for the sake of simplicity, we will consider the case of the homogenized properties \bar{C}_{ij} therefore eliminating the spatial dependency. The aim here is to give an estimate of the possible values that the equivalent beam stiffnesses can assume at different angles. It is also worth mentioning that, in this case, we considered sub-stiffened panels ($h_s \approx h_p$) therefore, the allowable orientations for the stiffeners span the entire domain $-45^\circ \leq \vartheta_i \leq 45^\circ$. All the stiffnesses reported in the following have been nondimensionalized with respect to their maximum value.

Figure 3.3 reports the normalized torsional stiffness with respect to the angle of orientations of the stiffeners. It can be noted that, the maximum torsional stiffness corresponds to the case of straight stiffeners oriented at $\vartheta_1 = \vartheta_2 = \pm 45^\circ$. The beam exhibits a local maximum when $\vartheta_1 = -\vartheta_2 = 45^\circ$ (or equivalently $\vartheta_1 = -\vartheta_2 = -45^\circ$), in this case $\overline{GJ}_t \approx 0.974$, that is 2.6% reduction with respect to the maximum attainable value. The minimum of the torsional stiffness ($\overline{GJ}_t \approx 0.836$) is obtained in the case of straight stiffeners oriented at zero.

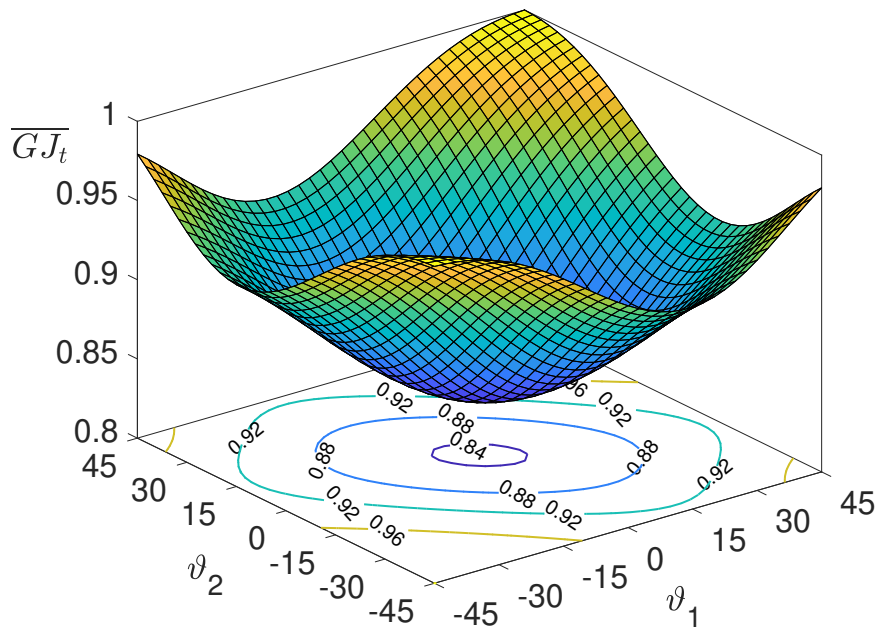


Fig. 3.3 Normalized envelope for the torsional stiffness \overline{GJ}_t . The stiffness is normalized with the maximum attainable value.

Figure 3.4 illustrates the normalized coupling coefficient \overline{K} with respect to the stiffeners' orientations. The maximum coupling coefficient is given when $\vartheta_1 = \vartheta_2 = \pm 27.5^\circ$. It is worth noticing that, for the case of equivalent orthotropic plate, i.e. when $\vartheta_1 = -\vartheta_2$, the coupling coefficient is zero. Indeed, from a cursory inspection of the second of eqns 3.6 one has $K \propto (A_{16}^*, D_{16}^*)$ which are both zero for the case of equivalent orthotropic plate (see Eqns. 3.2).

In Fig. 3.5 is depicted the normalized envelope for the bending stiffness \overline{EI}_2 with respect to the stiffeners' orientations. In this case the maximum is achieved for $\vartheta_1 =$

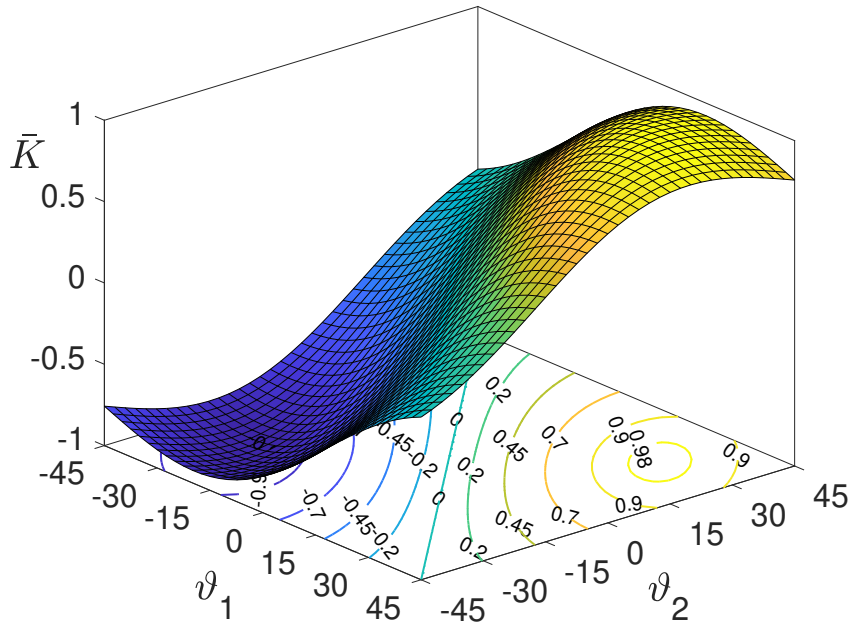


Fig. 3.4 Normalized envelope for the flexural-torsional coupling coefficient \bar{K} . The stiffness is normalized with the maximum attainable value.

$\vartheta_2 = 0^\circ$. The minimum bending coefficient is reached for straight stiffeners oriented at $\vartheta_1 = \vartheta_2 = \pm 45^\circ$, $\bar{EI}_2 \approx 0.712$. Another minimum is observed for the orthotropic solution when $\vartheta_1 = -\vartheta_2 = \pm 45^\circ$, here the normalized bending coefficient is $\bar{EI}_2 \approx 0.893$.

In Fig. 3.6 is depicted the normalized envelope for the bending stiffness \bar{EI}_2 with respect to the stiffeners' orientations. In this case the maximum is achieved for $\vartheta_1 = \vartheta_2 = 0^\circ$. The minimum bending coefficient is reached for straight stiffeners oriented at $\vartheta_1 = \vartheta_2 = \pm 45^\circ$, $\bar{EI}_2 \approx 0.712$. Another minimum is observed for the orthotropic solution when $\vartheta_1 = -\vartheta_2 = \pm 45^\circ$, here the normalized bending coefficient is $\bar{EI}_2 \approx 0.893$.

Figure 3.7 shows the attainable effective beam stiffnesses when ϑ_2 varies within the entire range of possible orientations while ϑ_1 is changed parametrically.

Figure 3.8 illustrates the variation of the effective beam stiffnesses with respect to the beam abscissa x when the upper and lower panels have curved stiffeners with $\vartheta_1 = 0^\circ$, $\vartheta_2 = 25^\circ$; all the others geometric parameters for the unitized beam are

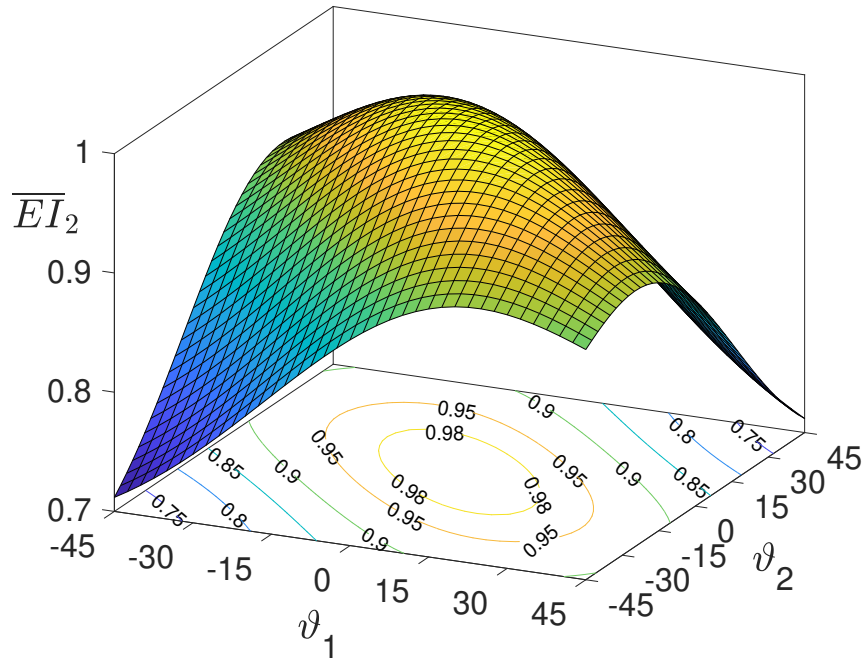


Fig. 3.5 Normalized envelope for the bending stiffness \overline{EI}_2 (edge-wise stiffness). The stiffness is normalized with the maximum attainable value.

listed in Table 5.9. The solid lines are the variable stiffness properties while the dashed lines are for the homogenized beam stiffnesses.

Aiming at deriving the closed form equations for the cross sectional stiffnesses, an interpolation method is used. Denoting with C_{ij} the generic stiffness coefficient, the interpolant is given as follow

$$C_{ij} = \sum_{k=0}^n a_{k_{ij}} x^k \quad (3.8)$$

Matlab[®] *polyfit* and *polyval* functions were used to find the coefficients $a_{k_{ij}}$.

3.3 Basic assumptions for the beam model

Let us consider an initially straight beam and define two coordinate systems, the Cartesian coordinate system xyz , which is used to represent the undeformed configu-

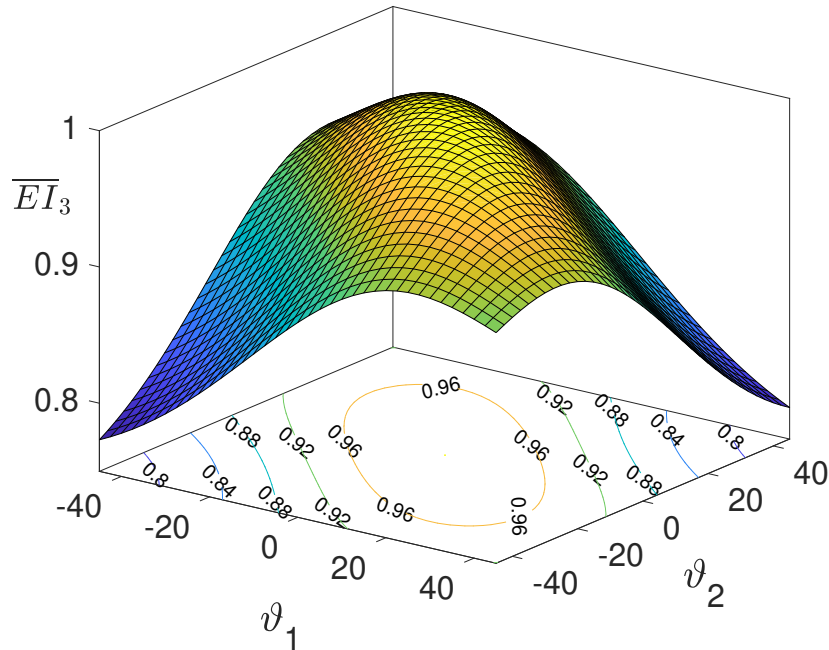
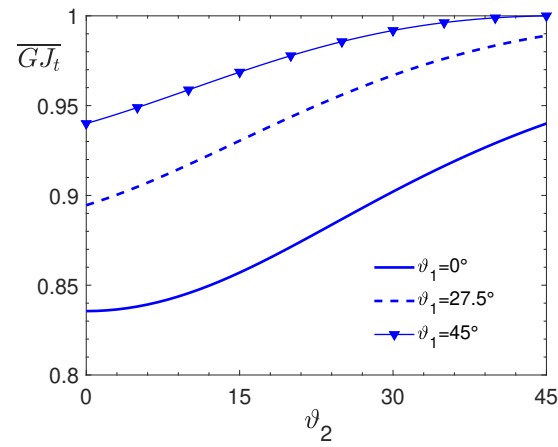
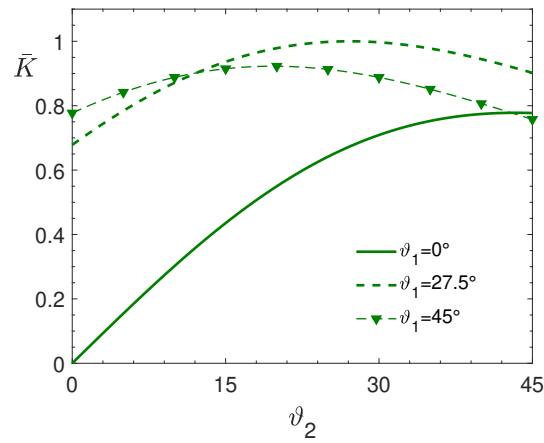


Fig. 3.6 Normalized envelope for the bending stiffness \overline{EI}_3 (flap-wise stiffness).

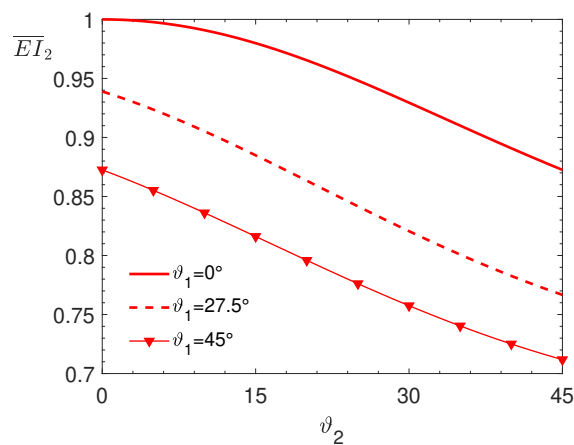
ration, and the orthogonal curvilinear coordinate system 123 which represents the deformed configuration. The latter is taken to be principal axes of the beam's cross section at the curvilinear abscissa s . Let $\mathbf{i}_x, \mathbf{i}_y, \mathbf{i}_z$ and $\mathbf{i}_1, \mathbf{i}_2, \mathbf{i}_3$ denote respectively the unit vectors of the two coordinate systems mentioned above. Moreover, let $u(s, t), v(s, t), w(s, t)$ be the component of the elastic displacements, with respect to the centroid C at an arbitrary abscissa s , as shown in Figure 3.9. In absence of warping, it is reasonable to assume that the motion of the differential beam element can be described using three translations and three rotations. Three consecutive Euler angle rotations can be used to describe the orientations of the centroidal axes 123 with respect to the inertial axis xyz . Crespo Da Silva and Glynn [134], showed that the sequence $\psi(s, t)$ about \mathbf{i}_z , $\vartheta(s, t)$ about \mathbf{i}_{y_1} , $\varphi(s, t)$ about \mathbf{i}_1 leads to a set of differential equations suitable to a perturbation method. For the sake of clarity, the sequence of rotations is shown in Figure 3.10.



(a)



(b)



(c)

Fig. 3.7 Effective beam properties with respect to the stiffeners' orientation ϑ_2 at fixed ϑ_1 . Solid lines are for $\vartheta_1 = 0^\circ$, dashed lines are for $\vartheta_1 = 27.5^\circ$ and the marker are for $\vartheta_1 = 45^\circ$. The envelopes are obtained considering the homogenized properties.

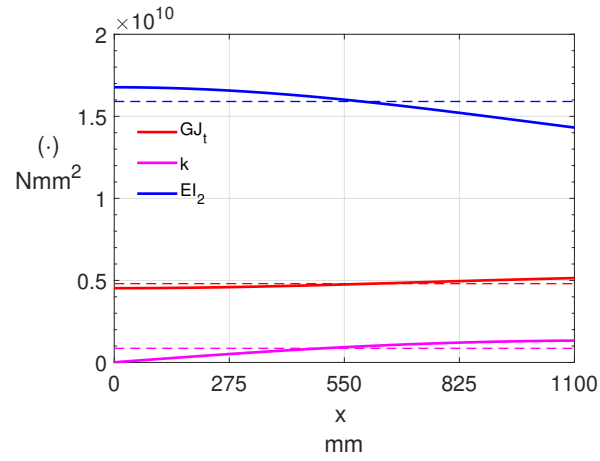


Fig. 3.8 Effective beam stiffnesses with respect to the beam abscissa x for the case of curvilinear stiffeners $\vartheta_1 = 0^\circ$, $\vartheta_2 = 25^\circ$. Solid lines represent the variable stiffnesses while the dashed lines are the homogenized stiffnesses.

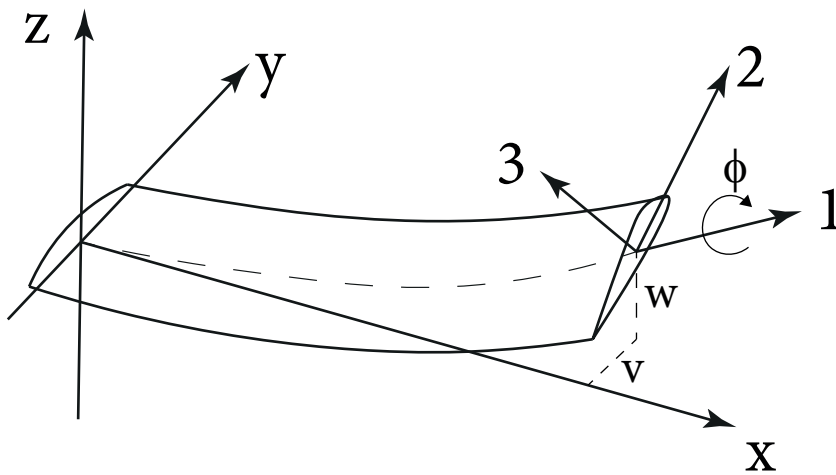


Fig. 3.9 Coordinate systems used in the present derivation.

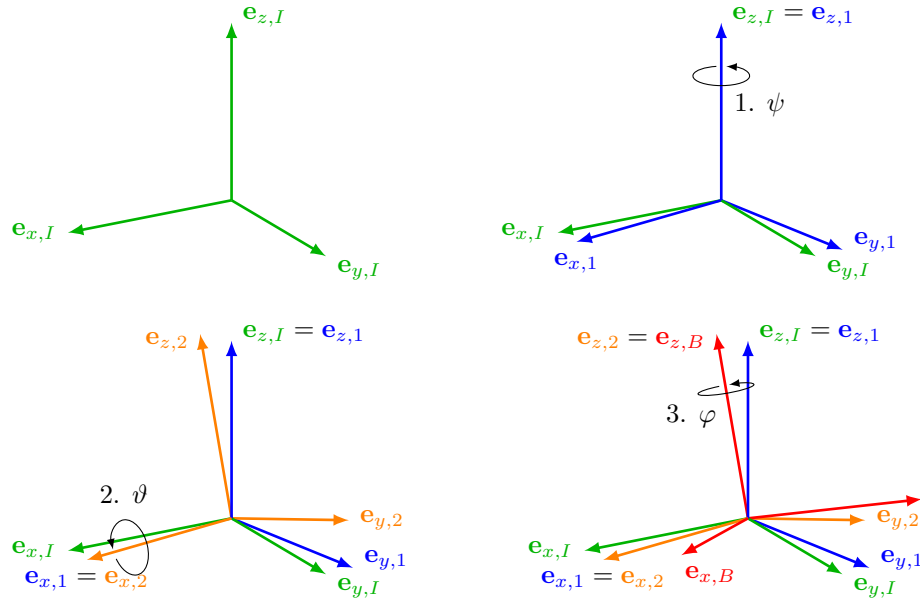


Fig. 3.10 Exemplification of the three successive counterclockwise rotations defined to align the inertial system to the deformed system.

The undeformed and deformed reference system are interrelated by the following transformation matrix

$$[T] = \begin{bmatrix} \cos \vartheta \cos \psi & \cos \vartheta \sin \psi \cos \varphi + \sin \vartheta \sin \varphi & \cos \vartheta \sin \psi \sin \varphi - \sin \vartheta \cos \varphi \\ -\sin \psi & \cos \psi \cos \varphi & \cos \psi \sin \varphi \\ \sin \vartheta \cos \psi & \sin \vartheta \sin \psi \cos \varphi - \cos \vartheta \sin \varphi & \sin \vartheta \sin \psi \sin \varphi + \cos \vartheta \cos \varphi \end{bmatrix}. \quad (3.9)$$

By letting dots denote the time derivative, the angular velocity ω of the centroidal frame with respect to the inertial frame can be written as

$$\begin{aligned} \omega(s, t) &= \dot{\psi} \mathbf{i}_z + \dot{\vartheta} \mathbf{i}_{y_1} + \dot{\varphi} \mathbf{i}_1 \\ &= (\dot{\varphi} - \dot{\psi} \sin \vartheta) \mathbf{i}_1 + (\dot{\psi} \cos \vartheta \sin \varphi + \dot{\vartheta} \cos \varphi) \mathbf{i}_2 \\ &\quad + (\dot{\psi} \cos \vartheta \cos \varphi - \dot{\vartheta} \sin \varphi) \mathbf{i}_3. \end{aligned} \quad (3.10)$$

By virtue of the Love's kinetic analogy, the components of the curvature ρ_1 , ρ_2 and ρ_3 can be readily obtained replacing the time derivatives with spatial derivatives in

equation 3.10. The component of the curvature's vector are given as follow

$$\begin{aligned}
\rho(s,t) &= \psi' \mathbf{i}_z + \vartheta' \mathbf{i}_{y_1} + \varphi' \mathbf{i}_1 \\
&= (\varphi' - \psi' \sin \vartheta) \mathbf{i}_1 + (\psi' \cos \vartheta \sin \varphi + \vartheta' \cos \varphi) \mathbf{i}_2 \\
&\quad + (\psi' \cos \vartheta \cos \varphi - \vartheta' \sin \varphi) \mathbf{i}_3 = \\
&= \rho_1 \mathbf{i}_1 + \rho_2 \mathbf{i}_2 + \rho_3 \mathbf{i}_3
\end{aligned} \tag{3.11}$$

where prime denotes the partial derivative with respect to the curvilinear abscissa s .

A total of six generalized displacements have been introduced namely, three traslations (u, v, w) and three rotations $(\psi, \vartheta, \varphi)$. In the successive derivation, the extension of the neutral axis, the shear deformation and the warping of the cross section are neglected. If the above assumptions hold, only three of the six generalized displacements are independent, since three equations of constraint are introduced. The inextensibility constraint can be written as:

$$(1 + u')^2 + v'^2 + w'^2 = 1. \tag{3.12}$$

From Figure 3.10 follows that the angles $\psi(s, t)$ and $\vartheta(s, t)$ can be rewritten as a function of the derivatives of $u(s, t)$, $v(s, t)$, $w(s, t)$ as

$$\tan \psi = \frac{v'}{1 + u'}, \tag{3.13a}$$

$$\tan \vartheta = -\frac{w'}{\sqrt{(1 + u')^2 + v'^2}}. \tag{3.13b}$$

The differential equation of motion derived in the following will involve only three independent variables, namely the flap-wise displacement $w(s, t)$, the lag displacement $v(s, t)$ and rotation about the curvilinear abscissa $\varphi(s, t)$.

In order to derive the equations of motion in terms of $u(s, t)$, $v(s, t)$, $w(s, t)$, taking into account the equations of constraint, it is proven being convenient eliminate the virtual variation $\delta\psi(s, t)$ and $\delta\vartheta(s, t)$ from the Lagrangian, as in [134]. Taking the variation of $\psi(s, t)$ and $\vartheta(s, t)$ one has

$$\delta\psi = \frac{\partial\psi}{\partial u'} \delta u' + \frac{\partial\psi}{\partial v'} \delta v' = -\frac{v' \delta u' + (1 + u') \delta v'}{(1 + u')^2 + v'^2}, \tag{3.14a}$$

$$\delta\vartheta = \frac{\partial\vartheta}{\partial u'} \delta u' + \frac{\partial\vartheta}{\partial v'} \delta v' + \frac{\partial\vartheta}{\partial w'} \delta w' = \frac{w' [(1 + u') \delta u' + v' \delta v'] - ((1 + u')^2 + v'^2) \delta w'}{((1 + u')^2 + v'^2)^{1/2}}. \tag{3.14b}$$

The variation of the curvatures are given as in Pai [135]. Applying a Taylor series expansion up to order two to the coefficients of the transformation matrix $[T]$ yields

$$T_{31} = -w', \quad T_{21} = -v', \quad (3.15a)$$

$$T_{32} = -\varphi, \quad T_{22} = 1, \quad (3.15b)$$

$$T_{33} = 1, \quad T_{23} = \varphi. \quad (3.15c)$$

where only those terms useful in the following steps of the derivation are retained. The expression of the curvature components, retaining only second order terms, are given by the following expression

$$\rho_1 = \varphi' + v''w', \quad (3.16a)$$

$$\rho_2 = -w'' + v''\varphi, \quad (3.16b)$$

$$\rho_3 = v'' + w''\varphi. \quad (3.16c)$$

3.4 Derivation of the equations of motion of variable stiffness beam

This section presents the derivation of the equation of motion of the beam model. The equation of motion are derived by means of the extended Hamiltonian principle

$$\mathcal{L} = \int_{t_1}^{t_2} (\delta T - \delta \Pi + \delta W_{nc}) dt \quad (3.17)$$

where δT is the variation of the kinetic energy, $\delta \Pi$ is the variation of the potential energy and finally δW_{nc} is the work done by the non-conservative forces. Particular emphasis is posed onto the stiffness contribution since the latter are presumed varying continuously span-wise.

3.4.1 Variation of the potential energy

The variation of the potential energy is given by

$$\delta \Pi = \int_0^L (M_1 \delta \rho_1 + M_2 \delta \rho_2 + M_3 \delta \rho_3) ds. \quad (3.18)$$

Expliciting terms the expression of the potential energy can be written as follow

$$\delta\Pi = \int_0^L [(-M'_1\delta\rho_1 - M_1\rho_3\delta\rho_2 + M_1\rho_2\delta\rho_3) + (M_2\rho_3\delta\rho_1 + -M'_2\delta\rho_2 - M_2\rho_1\delta\rho_3) + (-M_3\rho_2\delta\rho_1 + M_3\rho_1\delta\rho_2 - M'_3\delta\rho_3)] ds + (M_1\delta\rho_1 + M_2\delta\rho_2 + M_3\delta\rho_3)|_0^L. \quad (3.19)$$

Gathering like variations leads to the following equation

$$\delta\Pi = \int_0^L [(-M'_1 + M_2\rho_3 - M_3\rho_2)\delta\rho_1 + (-M_1\rho_3 - M'_2 + M_3\rho_1)\delta\rho_2 + (M_1\rho_2 - M_2\rho_1 - M'_3)\delta\rho_3] ds + (M_1\delta\rho_1 + M_2\delta\rho_2 + M_3\delta\rho_3)|_0^L. \quad (3.20)$$

The variation of the curvature are given as follows

$$\delta\rho_1 = \delta\varphi + w'\delta v', \quad (3.21a)$$

$$\delta\rho_2 = -T_{32}\delta v' - T_{33}\delta w', \quad (3.21b)$$

$$\delta\rho_3 = T_{22}\delta v' + T_{23}\delta w'. \quad (3.21c)$$

Substituting the Eqn. 3.21 into Eqn. 3.20 yields

$$\delta\Pi = \int_0^L [(-M'_1 + M_2\rho_3 - M_3\rho_2)(\delta\varphi + w'\delta v') + (-M_1\rho_3 - M'_2 + M_3\rho_1)(-T_{32}\delta v' - T_{33}\delta w') + (M_1\rho_2 - M_2\rho_1 - M'_3)(T_{22}\delta v' + T_{23}\delta w')] ds + (M_1(\delta\varphi + w'\delta v') + M_2(T_{32}\delta v' - T_{33}\delta w') + M_3(T_{22}\delta v' + T_{23}\delta w'))|_0^L \quad (3.22)$$

Finally, gathering like the variations of the generalized displacement $\delta\varphi$, δv and δw , one have

$$\delta\Pi = \int_0^L \left\{ (-M'_1 + M_2\rho_3 - M_3\rho_2)\delta\varphi + [(-M'_1 + M_2\rho_3 - M_3\rho_2)w']'\delta v + [(M_1\rho_3 + M'_2 - M_3\rho_1)T_{32}]'\delta v + [(M_1\rho_2 - M_2\rho_1 - M'_3)T_{22}]'\delta v + [(M_1\rho_3 + M'_2 - M_3\rho_1)T_{33}]'\delta w + [(M_1\rho_2 - M_2\rho_1 - M'_3)T_{23}]'\delta w \right\} ds. \quad (3.23)$$

3.4.2 Linear terms

Herein are reported the first order term of the case of variable stiffness anisotropic beam

$$\delta\varphi: \quad -(GJ)'\varphi' - GJ\varphi'' + k'w'' + kw''', \quad (3.24a)$$

$$\delta w : -k''\varphi' - 2k'\varphi'' - k\varphi''' + (EI_2)''w'' + 2(EI_2)'w''' + EI_2w^{IV}, \quad (3.24b)$$

$$\delta v : (EI_3)''v'' + 2(EI_3)'v''' + EI_3v^{IV}. \quad (3.24c)$$

It can be noted that with respect to the case of constant stiffness there are two additional terms in the equation of $\delta\varphi$, four terms more for the case of δw and two terms more for the case of the variation δv . The case of isotropic structure can be easily recovered by assuming the coupling term k equal to zero.

3.4.3 Second order terms

The nonlinear second order terms are reported below, higher order nonlinearities that arises substituting eqns 3.21 in to eq. 3.23 have been neglected.

$$\delta\varphi : -(GJ)'v''w' - GJ(v''w')' + k'v''\varphi + kv''' \varphi + (EI_3 - EI_2)v''w''. \quad (3.25)$$

In this case there are two additional terms in the variation $\delta\varphi$ with respect of the case of constant stiffness.

$$\begin{aligned} \delta w : & -(GJ)' \varphi' v'' - GJ(\varphi' v'')' - k'' v'' w' + k' v'' w'' - 2k' v'' w' - k(v'' w')' + \\ & + (EI_3 - EI_2)''(v'' \varphi) + 2(EI_3 - EI_2)'(v'' \varphi)' + (EI_3 - EI_2)(v'' \varphi)'' . \end{aligned} \quad (3.26)$$

The second order expression in the variation δw presents six terms more with respect to the case of constant stiffness. Likewise the equation of the variation δv has six additional terms with respect to the case of constant stiffness.

$$\begin{aligned} \delta v : & -(GJ)' \varphi' w'' - GJ(\varphi' w'')' + k''(\varphi' \varphi) + 2k'(\varphi' \varphi)' - k'w''w'' + k[(\varphi'' \varphi)' + (\varphi' \varphi)'] - \\ & - k(w''w'')' + (EI_3 - EI_2)''(w'' \varphi) + 2(EI_3 - EI_2)'(w'' \varphi)' \\ & + (EI_3 - EI_2)(w'' \varphi)'' . \end{aligned} \quad (3.27)$$

In summary, the system of governing equations obtained presents 22 additional terms with respect to the case of constant stiffness. Particularly, those terms, are the slope (first derivatives) and the curvature (second derivatives) of the beam's stiffness. It is presumed that those additional terms can enlarge the design space for tailoring.

3.4.4 Equations of motion

In the following, motivated by the results of the previous chapter, we speculate that the mass and the moment of inertia of the structure, are constant, meaning that the effect of the variation of the mass is assumed a higher order effect, i.e. neglected herein. Moreover, we speculated that the center of gravity of the structure lays on the x – axis. Denoting with j the mass moment of inertia about the beam's axis, m the wing mass, x_α the position of the center of mass and q_φ, q_w, q_v the generalized forces. The governing equations of the flexural-flexural-torsional beam with variable stiffness are given as follows

$$\begin{aligned} j\ddot{\varphi} + mx_\alpha\ddot{w} - (GJ)' \varphi' - GJ\varphi'' + k'w'' + kw''' - (GJ)' v''w' \\ - GJ(v''w')' + k'v''\varphi + kv''' \varphi + (EI_3 - EI_2)v''w'' = q_\varphi, \end{aligned} \quad (3.28a)$$

$$\begin{aligned} m\ddot{w} + mx_\alpha\ddot{\varphi} - (GJ)' \varphi'v'' - GJ(\varphi'v'')' - k''v''w' + k'v''w'' - 2k'v''w' - k(v''w')' \\ + (EI_3 - EI_2)''(v''\varphi) + 2(EI_3 - EI_2)'(v''\varphi)' + (EI_3 - EI_2)(v''\varphi)'' \\ - k''\varphi' - 2k'\varphi'' - k\varphi''' + (EI_2)''w'' + 2(EI_2)'w''' + EI_2w^{IV} = q_w, \end{aligned} \quad (3.28b)$$

$$\begin{aligned} m\ddot{v} + (EI_3)''v'' + 2(EI_3)'v''' + EI_3v^{IV} - (GJ)' \varphi'w'' - GJ(\varphi'w'')' + k''(\varphi'\varphi) \\ + 2k'(\varphi'\varphi)' - k'w''w'' + k[(\varphi''\varphi)' + (\varphi'\varphi)'] - k(w''w'')' \\ + (EI_3 - EI_2)''(w''\varphi) + 2(EI_3 - EI_2)'(w''\varphi)' + (EI_3 - EI_2)(w''\varphi)'' = q_v. \end{aligned} \quad (3.28c)$$

Neglecting the first and second derivatives of the stiffnesses, the set of equations derived agree with the equations derived in [64, 134, 136, 137]. The following set of boundary conditions for a clamped-free beam is considered

$$\begin{aligned} v = w = 0, \quad \varphi = 0, \quad w_{,x} = v_{,x} \quad \text{at } x = 0 \\ M_1 = M_2 = M_3 = 0, \quad V_2 = V_3 = 0 \quad \text{at } x = 0. \end{aligned}$$

3.4.5 Second order linearized equations

In the following it is reported the linearization of one of the equations reported above. Being understood that also the inertia terms should be linearized consistently here we limit our interest to the structural part since it represents the novelty with respect to the models already available in the open literature. Let $\bar{\varphi}, \bar{w}, \bar{v}$ be small perturbations around the deformed states φ_0, w_0, v_0 , i.e.

$$\varphi = \varphi_0 + \bar{\varphi}, \quad w = w_0 + \bar{w}, \quad \text{and} \quad v = v_0 + \bar{v}. \quad (3.29)$$

The linearized equations can be written as follows

$$\begin{aligned} & - (GJ)' \bar{\varphi}' - GJ \bar{\varphi}'' - (GJ)' (v_0'' \bar{w}' + \bar{v}'' w_0') - GJ (v_0'' \bar{w}' + \bar{v}'' w_0')' + k' \bar{w}'' + k' (v_0'' \bar{\varphi} + \bar{v}'' \varphi_0) \\ & + k \bar{w}''' + k (v_0''' \bar{\varphi} + \bar{v}''' \varphi_0) + (EI_3 - EI_2) (v_0'' \bar{w}'' + \bar{v}'' w_0''). \end{aligned} \quad (3.30)$$

The same procedure briefly summarized herein can be applied to the other equations to obtain a set of second-order linearized equations. The latter being useful to calculate the eigenvalues of the linearized system or, in other words, the natural frequencies of the system perturbed around the deformed configuration.

3.4.6 Solution methodology

In order to solve the set of the governing differential equations, the displacements' functions are approximated by modal analysis technique, i.e. assuming that the generic displacement p can be written as in [64]

$$p(x, t) = p_0(x) + \sum_{i=1}^{\infty} f_i(x) p(t) \quad (3.31)$$

where $f_i(x)$ are the mode shapes derived from a vibrating, non-rotating, uniform cantilever beam while $p(t)$ are the generalized coefficients. Particularly

$$f_{w,v} = \cosh(\alpha_i L \hat{x}) - \cos(\alpha_i L \hat{x}) - \beta_i [\sinh(\alpha_i L \hat{x}) - \sin(\alpha_i L \hat{x})] \quad (3.32a)$$

$$f_{\varphi} = \sqrt{2} \sin(\gamma_i L \hat{x}) \quad (3.32b)$$

where α_i, β_i and γ_i depend on the number of modes considered.

3.5 Summary and conclusions

In this chapter are derived the equation of motion of a second order flexural-flexural-torsional beam. The nonlinear equation of motion are derived considering that the beam has variable stiffnesses properties span-wise. The variation of the mass and inertial term is neglected. Particular emphasis is posed on the structural terms. The complete equation of motion are provided.

The chapter provides also a parametric study on to the attainable beam stiffnesses with respect to the stiffeners orientations. Particularly it is shown that varying the stiffeners path result in remarkably different stiffness and hence structural behavior which open up a variety of opportunity for tailoring.

Chapter 4

Trace-based scaling of anisotropic structures

Some of the contents and derivations presented in this chapter have been previously published, below are provided the references

Danzi, F., Frulla, G. and Romeo, G. "*An Invariant-based Performance-Oriented Procedure for Preliminary Design of Composite Structures*". AIRCRAFT ENGINEERING AND AEROSPACE TECHNOLOGY, Volume 90, Issue 3, pp.532-541, <https://doi.org/10.1108/AEAT-11-2016-0228>.

Danzi, F., Frulla, G., Cestino, E. and Gibert, J. M. "*MDO/MSO of Slender Thin Walled Box Beam Model*". Proc. of AIAA/ISSMO Multidisciplinary Analysis and Optimization Conference (2017). Denver, Colorado (USA), 5-9 June 2017, <https://doi.org/10.2514/6.2017-4323>.

4.1 Motivation

The chapter presents an introduction and some examples pertaining trace-based scaling of anisotropic structures with application to static and dynamic structural performances. For the sake of simplicity, in the examples presented in this chapter, is considered the case of a second order nonlinear beam with constant stiffness. Examples pertaining variable stiffness model are reported in the next chapter.

4.2 Trace-based scaling: theoretical framework

Stiffness and compliance for composite materials are second order tensors and, as such, they possess three quantities that are invariants with respect to the ply's orientation [138]. Particularly, in the following we consider the hydro-static component of the stiffness tensor, i.e., the stiffness trace (first invariant). Physically, when a material is selected, the invariant imposes limits on the total stiffness potential of the multi-directional laminate made with this material. Moreover, it is easy to verify that the following identities hold

$$Tr(\mathbf{Q}) = Tr\left(\frac{\mathbf{A}}{h}\right) = Tr\left(\frac{12\mathbf{D}}{h^3}\right) \quad (4.1)$$

hence, for a given material: (a) Trace is constant whether we are considering plate and laminates and (b) Trace is the same irrespective of the ply orientation (see Figure 4.1). Indeed it follows from the definition of the reduced stiffness matrix that the stiffness trace can also be written as

$$Tr = \frac{E_x + E_y}{1 - \nu_{xy}\nu_{yx}} + E_s \quad (4.2)$$

which shows that the stiffness trace is a material property, since it is a function of the unidirectional ply engineering constants.

The invariant-based procedure presented herein is envisaged to be useful, within preliminary design stages, to predict the performance of different anisotropic materials avoiding cumbersome material selection optimization. Particularly, the aim is to show that irrespective of the structural behavior being linear or nonlinear, a given performance of an anisotropic structure can be scaled. In other words, knowing the performance of a structure made by an anisotropic material, the effect of changing the material can be predicted using a scaling equation. This is because the second Piola-Kirchhoff tensor transforms like a scalar, therefore the prediction of how an anisotropic material behaves can be made by means of linear scaling, exactly as it happens with isotropic materials when one uses the Young's modulus. Denoting with χ the generic structural performance, the scaling equation will assume the following form

$$\chi = \chi_{MP} g(R) \quad (4.3)$$

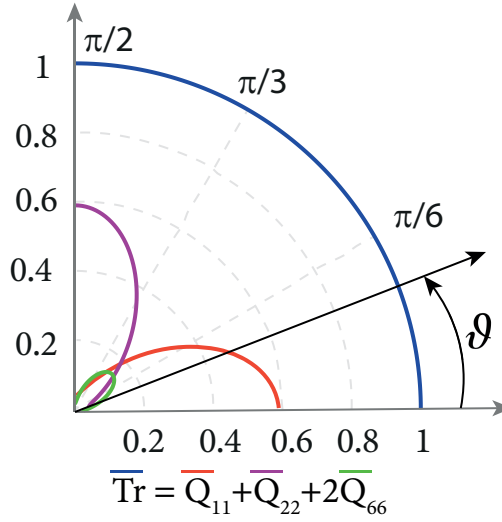


Fig. 4.1 Trace-normalized reduced stiffened components and Trace for different angle of orientation ϑ .

where MP is the Master Ply, R is the Trace ratio, i.e. the ratio of the stiffness traces of two different materials. We will see in the following how to select the function $g(R)$ accordingly to the particular structural response we aim to predict. Equation 4.3 holds if all the geometry parameters are retained and only geometric nonlinearities are considered. In the following only linear invariants will be considered. It is known that second order invariants exist [139].

The procedure consists of the following steps:

1. defining the material sample,
2. evaluating the Master Ply Elastic properties,
3. evaluating the structural performance(s) of interest,
4. scaling,
5. determining the rank of the material sample.

4.2.1 Definition of the material sample

The material sample definition is straightforward and it is up to factors like, for example, material availability and costs, and will be not discussed herein; there are

Table 4.1 Engineering properties of the materials' sample considered.

Material	E_{11} GPa	E_{22} GPa	G_{12} GPa	ν_{12} -	Tr GPa
T300/N5208	181.0	10.3	7.17	0.280	206.5
IM6/Epoxy	203.0	11.2	8.40	0.320	232.2
AS4/3501	138.0	8.96	7.10	0.300	162.0
M40/914V	209.3	6.89	4.26	0.305	225.4
M55J/Epoxy	270.0	5.80	4.10	0.300	284.5

no particular restrictions on this step, High Modulus (HM) or Intermediate Modulus (IM) CFRPs can be used as well as High Strength and so on, provided that the trace-normalized stiffness components of the different materials are comparable to each other. We will show later on that GFRP (Glass Fiber Reinforced Plastic) cannot be scaled on the basis of a Master Ply defined using CFRP. Let us consider the set of composite materials listed in Table 4.1. In the last column of the Table 4.1 is reported the Trace of each of the material considered herein. The aim is to show that the stiffness tensor can be written as a function of material properties and geometrical properties.

4.2.2 Definition of the Master Ply

The Master Ply is a fictitious material that is representative of the materials' sample under consideration. Particularly, the Mater Ply has the trace-normalized stiffness component that are the mean (or median) of those of the material sample¹. The elastic properties of the Master Ply are calculated based on the trace-normalized stiffness components defined on the basis of the material sample that one have. It is worth mentioning that the trace-normalized stiffness components are evaluated as follow

$$Q_{ij}^* = \frac{Q_{ij}}{Tr} \quad A_{ij}^* = \frac{A_{ij}}{hTr} \quad D_{ij}^* = \frac{12D_{ij}}{h^3Tr} \quad (4.4)$$

being h the laminate thickness. Once the normalized trace stiffness component are obtained, it is possible to calculate the engineering constants of the Master

¹There is an ongoing discussion about using the mean or median. However, since the trace normalized components of different CFRPs match closely, the choice of mean or median is just a matter of style. The accuracy of the predictions will remain of the same.

Table 4.2 Trace-normalized reduced stiffness components.

Material	Q_{xx}^* MPa	Q_{xy}^* MPa	Q_{yy}^* MPa	Q_{ss}^* MPa	Tr MPa
T300/N5208	0.8805	0.0140	0.0501	0.0347	206
IM6/Epoxy	0.8790	0.0155	0.0485	0.0362	232
AS4/3501	0.8567	0.0167	0.0556	0.0438	162
M40/914V	0.9315	0.0094	0.0307	0.0189	225
M55J/Epoxy	0.9508	0.0061	0.0204	0.0144	285
Master Ply	0.8900	0.0148	0.0477	0.0311	222

Ply through the inversion of the compliance matrix [140–144]. The Master Ply is particularly useful if the material sample contains several materials. For the material sample under consideration, the reduced stiffness components Q_{ij}^* are reported in Table 4.2. It can be noted how the in-plane normalized stiffness components match closely for the different materials. The reduced stiffness matrix of the Master Ply is

$$Q = Tr Q^* = 10^5 \begin{bmatrix} 1.9758 & 0.0329 & 0 \\ 0.0329 & 0.1059 & 0 \\ 0 & 0 & 0.0690 \end{bmatrix} [N/mm^2] \quad (4.5a)$$

The compliance matrix is then given as

$$S = Q^{-1} = 10^{-3} \begin{bmatrix} 0.0051 & -0.0016 & 0 \\ -0.0016 & 0.0949 & 0 \\ 0 & 0 & 0.1448 \end{bmatrix} [mm^2/N] \quad (4.5b)$$

and recalling that the compliance matrix for an orthotropic layer is given as

$$S = \begin{bmatrix} \frac{1}{E_{11}} & -\frac{\nu_{12}}{E_{11}} & 0 \\ -\frac{\nu_{21}}{E_{22}} & \frac{1}{E_{22}} & 0 \\ 0 & 0 & \frac{1}{G_{ss}} \end{bmatrix} \quad (4.5c)$$

it is easy to calculate the MP elastic properties. The elastic properties of the MP are reported in Table 4.3

Tables 4.4 and 4.5 report the trace-normalized in-plane and bending components respectively for all the materials of the sample reported in Table 4.1. For the case

Table 4.3 Engineering properties of the Master Ply.

Material	E_{11} GPa	E_{22} GPa	G_{12} GPa	ν_{12} -	Trace GPa
MP	196.56	10.535	6.904	0.31	222

Table 4.4 Trace normalized in-plane components $A_{ij}^* = (A_{ij})/(h Tr)$ for $[0/\pm 45/90]_S$ laminates.

Material	A_{11}^*	A_{12}^*	A_{13}^*	A_{22}^*	A_{23}^*	A_{33}^*
T300/N5208	0.370	0.109	0	0.370	0	0.130
IM6/Epoxy	0.370	0.109	0	0.370	0	0.130
AS4/3501	0.368	0.105	0	0.368	0	0.132
M40/914V	0.373	0.118	0	0.373	0	0.128
M55J/Epoxy	0.373	0.119	0	0.373	0	0.127

of in-plane and bending trace-normalized components a quasi-isotropic laminate is selected. However, for the sake of completeness also the case of hard-laminate, i.e. a laminate with a higher degree of anisotropy, is considered. In this latter case the laminate layup is $[0_5/\pm 45_2/90]_S$. For the sake of brevity, in the case of hard laminate, only the trace-normalized bending components are reported. For all the cases reported in Tables 4.4, 4.5 and 4.6, the trace-normalized components for the different materials are comparable. If one compares the trace-normalized bending components reported in Table 4.5 and 4.6 respectively, follows that for different lay-up the components are different. In view of the above, it is reasonable to assume that if the lamination holds and all the geometry parameters (dimension of the structure, constraints, loads and lay-up) are fixed, the behavior of different anisotropic materials can be predicted using the stiffness trace. The reason will be highlighted in the next section. Aiming at unveiling the theory behind the universal master ply concept, Ha and Cimini [145] considered a materials' sample with 44 materials belonging to four different classes namely, high modulus carbon/epoxy, standard modulus carbon/epoxy, aramid/epoxy, and glass/epoxy. They noted that the master ply concept can be applied for high modulus carbon/epoxy, standard modulus carbon/epoxy, and aramid/epoxy material systems but not to glass/epoxy. They defined the theoretical trace normalized longitudinal modulus, i.e. $E_X^* = E_x/Tr$ and

Table 4.5 Trace normalized bending components $D_{ij}^* = (12D_{ij})/(h^3 Tr)$ for the family $[0/\pm 45/90]_S$.

Material	D_{11}^*	D_{12}^*	D_{13}^*	D_{22}^*	D_{23}^*	D_{33}^*
T300/N5208	0.621	0.092	0.039	0.154	0.039	0.112
IM6/Epoxy	0.621	0.092	0.039	0.154	0.039	0.112
AS4/3501	0.610	0.088	0.038	0.159	0.038	0.125
M40/914V	0.647	0.098	0.042	0.140	0.042	0.107
M55J/Epoxy	0.656	0.098	0.043	0.132	0.043	0.106

Table 4.6 Trace normalized bending components $D_{ij}^* = (12D_{ij})/(h^3 Tr)$ components for $[0_5/45_2/90]_S$ laminates.

Material	D_{11}^*	D_{12}^*	D_{13}^*	D_{22}^*	D_{23}^*	D_{33}^*
T300/N5208	0.804	0.038	0.008	0.079	0.008	0.059
IM6/Epoxy	0.804	0.038	0.008	0.078	0.008	0.059
AS4/3501	0.784	0.038	0.007	0.084	0.007	0.066
M40/914V	0.848	0.036	0.008	0.061	0.008	0.046
M55J/Epoxy	0.864	0.034	0.008	0.051	0.008	0.042

noted that by increasing E_x the trace normalized longitudinal modulus E_x^* presents a plateau and hence is less sensitive to the variation of E_x . Glass/epoxy are instead located in the region in which the curve $E_x^* - E_x$ is nonlinear therefore the concept of master ply cannot be applied because of the relative high variation of the trace normalized longitudinal modulus with respect to the longitudinal modulus. We will show later on in the chapter that although the concept of universal master ply does not apply for Eglass/epoxy the trace based scaling still works provided that the scaling is performed with the correct material.

4.2.3 Scaling

For isotropic materials the scaling is straightforward. Let us consider, for example, the tip deflection w of a beam made by steel, subjected to a concentrated load F applied at the beam tip, one have

$$w = \frac{FL^3}{3EI}$$

Suppose that we are wondering how much the deflection will be if all the geometry parameters holds and the load remains unchanged, but the beam is made by aluminum; the answer is simply

$$w_{Al} = w_{steel} \frac{E_{steel}}{E_{Al}}$$

Following the same idea, it is easy to show that the frequencies f of a beam can be scaled as follow

$$f_{Al} = f_{steel} \sqrt{\frac{E_{Al}}{E_{steel}}} \sqrt{\frac{\rho_{steel}}{\rho_{Al}}} \quad (4.6)$$

The same rule applies also for the case of the buckling of an isotropic panel, that is

$$N_{cr} = \frac{\pi^2 EK_c t}{12(1-\nu)^2} \left(\frac{t}{b}\right)^2 \quad (4.7)$$

and the scaled load will be

$$N_{crAl} = N_{crsteel} \left(\frac{E_{Al}}{E_{steel}}\right) \quad (4.8)$$

It is worth noting that the ratio of the Young's modulus for the case of buckling and bending frequency is the reciprocal for that of the beam deflection. The reason is due to the the buckling and frequency are directly proportional to the stiffness while for the tip deflection there is an inverse proportionality. For orthotropic plates one have

$$\lambda_{cr}^{(m,n)} = \frac{\pi^2 \left[D_{11} \left(\frac{m}{a} \right)^4 + 2(D_{12} + 2D_{66}) \left(\frac{n}{b} \right)^2 \left(\frac{m}{a} \right)^2 + D_{22} \left(\frac{n}{b} \right)^4 \right]}{N_x \left(\frac{m}{a} \right)^2 + N_y \left(\frac{n}{b} \right)^2} \quad (4.9)$$

In view of the results reported in section 4.2.2, we know that all the D_{ij} are proportional to a constant (i.e. invariant) quantity I , which is the stiffness Trace. The eq. 4.9 can be rewritten as

$$\lambda_{cr}^{(m,n)} = Tr \left\{ \frac{\pi^2 \left[D_{11}^* \left(\frac{m}{a} \right)^4 + 2(D_{12}^* + 2D_{66}^*) \left(\frac{n}{b} \right)^2 \left(\frac{m}{a} \right)^2 + D_{22}^* \left(\frac{n}{b} \right)^4 \right]}{N_x \left(\frac{m}{a} \right)^2 + N_y \left(\frac{n}{b} \right)^2} \right\} \quad (4.10)$$

where $D_{ij}^* = 12D_{ij}/(Tr H^3)$. We speculate that the stiffness Trace (Tr) retains all the information related to the stiffness, exactly as the Young's modulus does for isotropic structures. All the other information related to geometry of the panel and lay-up are retained in the reference solution. In this case, the expression between curly braces in the equation above is constant (or almost constant) and the scaling rule for the buckling load of an orthotropic material is hence given as

$$\lambda_{cr_{newmaterial}} = \lambda_{cr} \frac{Tr_{new material}}{Tr_{MP}} \quad (4.11)$$

It is worth mentioning that, since the term between curly braces is not exactly constant for different materials, the scaling procedure will introduce a discrepancy between the scaled performance and those obtained solving the structural problem for each of the material in the sample.

4.3 Application of trace based scaling for anisotropic structures

4.3.1 Scaling of buckling loads

A symmetric, square flat plate (100x100 mm) 1mm thick, with $[0/45/90/-45]_S$ lay-up is considered for the Trace-based scaling of buckling loads under uniaxial compression N_x . Two different boundary conditions were considered namely, simply supported (SSSS) and clamped (CCCC). The numerical analysis has been performed by means of FEA. Analytical and scaled loads along with the percentage relative errors resulting from the scaling procedure are reported in Table 4.8. The scaled loads are computed using the following scaling rule

$$N_{x_{new\ material}} = N_x \frac{Tr_{new\ material}}{Tr_{MP}} \quad (4.12)$$

In this case the material sample considered is given in Table 4.7. The trace-normalized components of the MP, computed as above, are: $Q_{11}^* = 0.8946$, $Q_{12}^* = 0.0147$, $Q_{22}^* = 0.0494$ and $Q_{66}^* = 0.0280$ while the stiffness trace is $Tr = 195\ GPa$. The procedure to obtain these values is the same that has been already discussed in the previous section, provided that here the material sample is larger.

The maximum scaling error is obtained for the M55J-Epoxy composite. In either cases, simply supported and clamped panels, the scaling error is bounded within few percentages. In this case where bending matrix is concerned, the scaling error is proportional to the discrepancy of the trace-normalized bending components of the different materials. In Table 4.5 we have seen that the trace-normalized stiffness components of T300-N5208 and IM6-Epoxy match closely. Suppose now that, instead of using the MP as a reference solution, we want predict the buckling load of the IM6 on the basis of the buckling load of the T300, we have

$$N_{x_{IM6}} = N_x \frac{Tr_{IM6}}{Tr_{T300}} = -21.646 \frac{232}{206} = -24.378 \quad (4.13)$$

and the scaling error in this case is $E_{R\%} = 0.21\%$, which is closer to the analytical value; indeed the scaling error obtained using the MP was $E_{R\%} = -0.533\%$. Previously we have mentioned that the trace-based scaling does not work consistently for GFRPs. Moreover, Ha and Cimini [145] noted that the concept of Master Ply

Table 4.7 Engineering properties of the materials' sample considered.

Material	E_{11} GPa	E_{22} GPa	G_{12} GPa	ν_{12} -	Tr GPa
M55J/Epoxy	270.0	5.80	4.10	0.300	285
M40/914V	209.3	6.89	4.26	0.305	225
T1000/UF332	186.0	7.30	4.10	0.280	202
IM6/Epoxy	203.0	11.2	8.40	0.320	232
T300/N5208	181.0	10.3	7.17	0.280	206
T800/Epoxy	160.0	9.20	5.00	0.350	180
AS43501	138.0	8.96	7.10	0.300	162
T700/EPOXY	121.0	8.00	4.70	0.300	139
Kevlar49/Epoxy	76.0	5.50	2.30	0.340	87
Boron	204.0	18.5	5.59	0.230	235
MP	173.9	9.60	5.47	0.298	195

Table 4.8 Analytical (a) and scaled (s) buckling loads for simply supported (SSSS) and fully clamped (CCCC) panels.

Material	SSSS			CCCC		
	N_x^n	N_x^s	$E_{R\%}$	N_x^n	N_x^s	$E_{R\%}$
M55J/Epoxy	-29.180	-29.776	2.044	-86.697	-86.964	0.308
M40/914V	-23.333	-23.588	1.093	-68.879	-68.891	0.018
T1000/UF332	-20.956	-21.149	0.923	-61.728	-61.768	0.066
IM6/Epoxy	-24.431	-24.301	-0.533	-70.701	-70.974	0.387
T300/N5208	-21.646	-21.610	-0.169	-62.871	-63.113	0.386
T800/Epoxy	-18.992	-18.879	-0.597	-55.312	-55.137	-0.316
AS43501	-17.139	-16.956	-1.069	-49.202	-49.521	0.647
T700/EPOXY	-14.692	-14.564	-0.873	-42.545	-42.536	-0.020
Kevlar49/Epoxy	-9.198	-9.082	1.262	-26.748	-26.526	-0.832
Boron	-24.847	-24.567	-1.130	-72.439	-71.749	-0.953
MP	-20.447			-59.717		

Table 4.9 Membrane and bending stiffness normalized components for E-glass composite laminate $[0/\pm 45/90]_S$.

Material	D_{11}^*	D_{12}^*	D_{16}^*	D_{22}^*	D_{26}^*	D_{66}^*	Tr [GPa]
E-glass/Epoxy	0.5325	0.0875	0.0258	0.2225	0.0258	0.1225	56.824
E-glass/MY750	0.4838	0.0932	0.0182	0.2655	0.0182	0.1254	77.916
E-glass/LY556	0.4965	0.0980	0.0198	0.2600	0.0198	0.1218	87.420

does not apply to E-glass materials. However, we have just seen that the prediction made by scaling can be improved selecting a proper material, i.e. a material with trace normalized stiffness components which are closer to that of the material we aim to consider. Let us consider the E-glass material having the following properties: $E_{11} = 38.6GPa$, $E_{22} = 8.27GPa$, $G_{12} = 4.14GPa$ and $\nu_{12} = 0.26$. The trace-normalized membrane and bending components are listed in Table 4.9. Comparing the data reported in the first row of Table 4.9 with those listed in Table 4.5 follows that the trace-normalized component are far away from that of the material sample considered herein. In this case, considering for the sake of brevity only the case of simply supported panels, the scaling prediction would give $N_x = 5.85N/mm$, the buckling load computed is instead 6.46 therefore the scaling error is approximately 10%. Let us consider three different E-glass/Epoxy with bending-normalized components reported in Table 4.9; performing the scaling for the buckling loads using as a reference material the E-glass Epoxy, follows that the trace-based scaling still works and the accuracy is bounded within 0.5%, as shown in Table 4.10. It follows that the accuracy of the prediction is given by the difference among the trace-normalized stiffness components, the closer the trace-normalized components the better the prediction. Moreover, it can be concluded that the concept of universal master ply cannot be applicable, as stated in [145], however different master plies can be defined on the basis of the material sample select, i.e. splitting the material in different classes. To this end, a good practice to discern whether one universal master ply or more have to be used is useful look at the trace-normalized components.

4.3.2 Scaling of post-buckling deflections

Let us consider the same plate analyzed in the previous section. In this case, we aim at scaling the plate deflection in the post critical regime when the load increment is

Table 4.10 Analytical (a) and scaled (s) buckling loads for simply supported (SSSS) GFRP composite panels.

Material	SSSS		
	N_x^a	N_x^s	$E_R\%$
E-glass/Epoxy	-6.46	-	-
E-glass/MY750	-8.90	-8.86	0.45
E-glass/LY556	-9.97	-9.94	0.30

fixed. The out-of-plane deflection for a plate in the post-critical regime is a quadratic function of the load level therefore the scaling requires a square root of specific ratios. The analytical and scaled post-buckling deflections along with the scaling error are reported in Table 4.11. The analytical solutions have been obtained using the POBUCK code, developed by Romeo and Frulla [146]. Also for the case of post-buckling, the scaled deflections agree with those computed. The maximum scaling error in this case is less than 1%.

4.3.3 Scaling for divergence speed

A typical HALE UAV is considered herein aiming at showing the effectiveness of the trace-based scaling procedure to predict the divergence speed. The layup and dimensions of the wing box are reported in Appendix A. In this case the material sample considered is the one reported in Table 4.1. The wing box is modeled as a cantilever beam with 20 elements with piece-wise constant stiffnesses evaluated on the basis of the eqns. 3.6. The divergence speed is calculated solving the eigenvalue problem given as

$$\det([K] - \lambda[A]) = 0 \quad (4.14)$$

where $[K]$ is the stiffness matrix and $[A]$ is the aerodynamic matrix. In Table 4.12 are listed the scaled and numerical divergence speed along with the scaling error. The scaled divergence speeds are evaluated using the following equation

$$V_{div}^s = V_{div}^a \sqrt{\frac{Tr_{new\ material}}{Tr_{MP}}} \quad (4.15)$$

The scaled and analytical divergence speeds are found in good agreement. The

Table 4.11 Analytical (a) and scaled (s) post buckling deflection w for simply supported (SSSS) and fully clamped (CCCC) panels. The load increment with respect to the buckling load is fixed at 1.5.

Material	SSSS			CCCC		
	w^a	w^s	$E_{R\%}$	w^a	w^s	$E_{R\%}$
M55J/Epoxy	1.569	1.571	0.100	1.760	1.746	0.783
M40/914V	1.576	1.577	0.057	1.750	1.748	0.131
T1000/UF332	1.578	1.579	0.080	1.753	1.748	0.267
IM6/Epoxy	1.587	1.591	0.235	1.740	1.746	0.316
T300/N5208	1.586	1.589	0.212	1.743	1.746	0.144
T800/Epoxy	1.592	1.591	0.051	1.754	1.752	0.134
AS43501	1.590	1.595	0.320	1.737	1.743	0.358
T700/EPOXY	1.592	1.593	0.092	1.746	1.749	0.176
Kevlar49/Epoxy	1.599	1.597	0.150	1.758	1.756	0.102
Boron	1.598	1.596	0.153	1.754	1.757	0.187
MP	1.587			1.750		

Table 4.12 Comparison of the trace based scaled and numerical computed divergence speed of an HAR wing.

Material	V_{div}^a	V_{div}^s	$E_{R\%}$
T300/N5208	173.87	170.48	1.95
IM6/Epoxy	184.94	182.25	1.45
AS4/3501	157.68	152.30	3.41
M40/914V	173.37	179.48	-3.52
M55J	192.25	202,00	-5.07
Master Ply	178.28		

maximum scaling error is obtained for the case of M55J as expected, indeed the M55J presents the higher discrepancy of the trace-normalized component with respect to the master ply.

Table 4.13 Comparison of the trace based scaled and numerical flap/coupled frequencies of an HAR wing under moderate deformations.

Material	f_{flap}^a	f_{flap}^s	$E_R\%$
T300/N5208	4.75	4.72	0.66
IM6/Epoxy	5.03	5.04	-0.25
AS4/3501	4.18	4.21	-0.89
M40/914V	5.03	4.97	1.20
M55J	5.68	5.59	1.56
Master Ply	4.93		

4.3.4 Scaling for normal frequencies

Considering the same wing box of the previous section, here we compare the analytical and scaled vibration frequencies. The frequencies are evaluated considering the complete set of second order nonlinear equations reported in eqns. 3.30, linearized around the deformed configuration. It is worth mentioning that the variability of the stiffness span-wise has been neglected, i.e. the case of constant stiffness is considered. For the sake of simplicity, a single mode per dof is used. The scaling will work consistently irrespective of the number of mode shapes per dof used in the approximation. The frequencies are proportional to the square root of the stiffness, the scaled frequencies and are computed as follows

$$f_{div}^s = f_{div}^a \sqrt{\frac{Tr_{new\ material}}{Tr_{MP}}} \quad (4.16)$$

The analytical and scaled frequencies are reported in Tables 4.13, 4.14 and 4.15. A good agreement between scaled and analytical frequencies is found.

4.3.5 Scaling for buckling loads of curvilinear stiffened panels

In Chapter 2 we have derived an equivalent model of unitized panels, here we aim at scaling the buckling loads of those panels calculating the stiffness traces. The traces are calculated on the basis of the homogenized model, particularly considering the trace-normalized bending components. Moreover, herein the scaling is performed using as a reference the panel with $\vartheta_1 = 45$, $\vartheta_2 = 16.75$, i.e. panel h. It is worth

Table 4.14 Comparison of the trace-based scaled and numerical flap/coupled frequencies of an HAR wing under moderate deformations.

Material	f_{flap}^a	f_{flap}^s	$E_{R\%}$
T300/N5208	22.14	21.99	0.66
IM6/Epoxy	23.48	23.51	-0.11
AS4/3501	19.46	19.64	-0.93
M40/914V	23.37	23.15	0.93
M55J	26.41	26.06	1.33
Master Ply	23.00		

Table 4.15 Comparison of the trace-based scaled and numerical torsional/coupled frequencies of an HAR wing under moderate deformations.

Material	f_{tors}^a	f_{tors}^s	$E_{R\%}$
T300/N5208	135.94	133.39	1.88
IM6/Epoxy	144.55	142.59	1.35
AS4/3501	123.10	119.16	3.20
M40/914V	136.10	140.43	-3.18
M55J	152.16	158.05	-3.87
Master Ply	139.49		

Table 4.16 Scaled buckling loads for flat panles with cured stiffeners.

Panel	D_{11}^*	D_{12}^*	D_{16}^*	D_{22}^*	D_{26}^*	D_{66}^*	Trace
a	0.5267	0.1856	-0.2950	-0.0989	-0.1284	0.1872	2086.8
b	0.6114	0.1606	-0.2955	0.0644	-0.0956	0.1621	2001.8
c	0.7840	0.0956	-0.2525	0.0217	-0.0402	0.0971	1872.7
d	0.9188	0.0358	-0.1471	0.0065	-0.0097	0.0374	1796.7
e	0.9705	0.0112	0.0021	0.0040	0.0001	0.0128	1771.4
f	0.9031	0.0431	0.1661	0.0077	0.0126	0.0446	1804.7
g	0.7165	0.1228	0.2774	0.0348	0.0599	0.1243	1917.9
v	0.5267	0.1856	-0.2950	-0.0989	-0.1284	0.1872	2086.8

Table 4.17 Scaled buckling loads for flat panels with cured stiffeners.

Panel	N_x^a	N_x^s	$E_R\%$
a	0.5267	296.9	-1.27
b	293.2	300	5.65
c	301.9	284.8	4.183
d	278.1	266.5	4.04
e	267.1	256.3	7.50
f	272.5	252.1	12.26
g	292.7	256.8	8.09
v	296.9	272.8	-

noting that the equivalent model gives rise to trace-normalized components which, differently for the case of CFRPs, shows an higher discrepancy among each other as shown in Table 4.16. The label reported in Table 4.16 are the same used in Table 2.1. Notwithstanding the discrepancy between the trace-normalized components for the different plates, which, as mentioned before, will yields an higher error between the scaled and the analytical buckling loads, the maximum scaling error is 12% as shown in Table 4.17. It can be concluded that the trace-based scaling in this case provide a first approximation of the attainable performance however it is not advisable because the trace-normalized components are sparse and therefore the prediction is not as accurate as it was for composite materials previously analyzed.

4.4 Summary and conclusions

The chapter is devoted to the introduction of a scaling procedure for anisotropic structures. The procedure relies on the objective properties of the stiffness invariants and is envisaged to be useful instead of Material Selection Optimization (MSO). It has been shown that the generic structural response of anisotropic structure can be seen as a combination of geometry parameters and stiffness trace. The stiffness trace is the only parameter that accounts for the material properties and plays the same role as the Young's modulus for isotropic materials. Buckling loads, post-buckling deflection, frequencies and divergence speeds are among the structural performances that can be scaled. Linear and nonlinear structural performances can be faithfully predicted as long as the nonlinearities are geometric. The scaling error, i.e. the discrepancy between the structural performance predicted through the scaling procedure and the analytical solution, is bounded between few percentages. The scaling procedure can be used to investigate the structural behavior of different materials and help gain insights for material selection. Indeed, once a materials' sample is chosen, the MP can be defined and perform all the design and optimization on the basis of the MP. Subsequently, the performance of all the materials of the sample can be evaluated with simple calculations. The advantage given by trace-based scaling is twofold: (a) the material can be chosen on the basis of structural performances rather than index, and (b) the procedure is computationally cost-less compared against material selection optimization.

Chapter 5

Optimization of anisotropic plates and beams

Some of the results presented in this chapter, pertaining the buckling load maximization of composite flat panels through the Stud^P GA have been already published in the Structural and Multidisciplinary Optimization Journal, the full citation is provided below.

Danzi, F., Frulla, G. and Cestino, E. "*Constrained combinatorial optimization of multi-layered composite structures by means of Stud GA with proportionate selection and extinction*". STRUCTURAL AND MULTIDISCIPLINARY OPTIMIZATION. Volume 55, Issue 6, pp. 2239–2257, ISSN 1615-1488, <https://doi.org/10.1007/s00158-016-1638-4>.

5.1 Introduction

In this chapter the aim is to optimize anisotropic thin-walled structures to achieve desired structural performances.

In section 5.2 is presented a novel optimization algorithm, namely the Stud^P GA, originally conceived in the framework of this PhD Thesis. The algorithm is a revised version of the Stud GA which implements the breeding farm paradigm, i.e. the linebreeding and outcrossing concepts. The section details the main features and capabilities of the algorithm.

Section 5.3 provides a short overview of the results obtained using the Stud^P GA to maximize the buckling load of composite flat panels along with the mathematical formulation of the problem.

Section 5.4 presents the optimization of a unitized box beam under static constraints. The optimization problem is formulated and hence solved using the Stud^P GA. The topology optimization problems are formulated as constrained combinatorial problem, i.e. seeking the orientations of the stiffeners at prescribed control points located span-wise. Three different load cases are considered. Where available, numerical results are compared against those obtained using a commercial FE code and experiment.

In section 5.5 is presented the optimization of an High Aspect Ratio wing. The objective of the optimization is to minimize the difference between the frequencies of the deformed and undeformed structure. The optimization problem is formulated and hence solved by means of the Stud^P GA.

It is worth mentioning that for the unitized beam problems, the beam tip deformation are limited to one-tenth of the beam length, consistently with the second order model derived in the previous chapter. Indeed, the case of large deformations cannot be described faithfully with second order nonlinear model and a third order nonlinear model should be adopted, see for example [147, 148].

5.2 Stud^P GA

The Stud GA is a relatively novel version of the GA, introduced by Khatib and Fleming in [149]. Although it was presented as a mini revolution in evolutionary computing, its applications to real engineering problems are limited. Herein a revised version of the Stud GA, suitable for constraint combinatorial problem, is introduced. The algorithm has been developed in the framework of this thesis.

The unique difference between the standard GA and the Stud GA is the mating pool structure. Contrary to the standard version of GA, the basic idea behind the Stud GA is to use the best individual in the population (the Stud) to mate with all others to produce new offspring. It follows that the original version of Stud GA does not include stochastic selection.

The author believes that the Stud GA can be used as a starting point to raise the selective pressure aiming at increasing the convergence rate of the algorithm. In fact, it is well known that retaining the best individual within the population is useful to improve the algorithm efficiency. To increase the selective pressure to the highest level, in contrast with what has been done in the Stud GA, which let the stud mating with all the individual of the population, here a stochastic selection strategy is used. In [150] they stated

Bonnet macaques demonstrate an example of increased reproductive success from high rank. High-ranking males have more access to fertile females and consequently partake in most of the mating within the group, demonstrated by one population in which only three males were responsible for over 75% of mating. In this population, males often vary in their rank, and as they gain rank, they gain more time spent exclusively with fertile females; the opposite relationship is seen as males drop in rank

Instead of having more than one stud, herein it is preferred to have only one. This preference is influenced by the work of Khatib and Fleming ([149]). This situation is similar to the breeding farm when the breeder want to establish some genetic traits in his own bloodline¹. The usage of only one stud has been conceived to accelerate the exploration capabilities (raising the selective pressure) of the algorithm and try to fix one of the issue related with GA, i.e. the low convergence rate.

In turn, the increase of the selective pressure leads to an increase in exploitation capabilities and several issues in the exploration potentialities. In this case, premature convergence may arise and the algorithm could get trapped in local optimum. To prevent convergence to local optimum a diversity-preservation technique is implemented. The diversity preservation technique is essentially an extinction that carries out the same function of the infusion of different bloodline carried out in the breeding farm. In other words, the diversity preservation technique spreads the differences among the offspring increasing the exploration capabilities of the algorithm. A pictorial view of the mating pool structure of the algorithm is depicted

¹The eighteenth century English breeder, Robert Bakewell, is recognized as the father of the Science of animal improving. His success as a breeder is attributed to his care in the detection of the recordings and the use of consanguinity to secure the desired type - from: Elements of Dog's Genetics, Roberto Leotta, Faculty of Medical Veterinary, University of Pisa

in Figure 5.1. The two novelties briefly discussed above, namely the proportional selection and the extinction, in conjunction with the use of the Stud, stems from the breeding farm paradigm. Indeed, the proportionate selection and the use of the Stud replicates the concept of inbreeding (or linebreeding) while the extinction and the subsequent infusion of new offspring simulates the outcrossing. The flowchart describing the mating's pool structure is depicted in Figure 5.2.

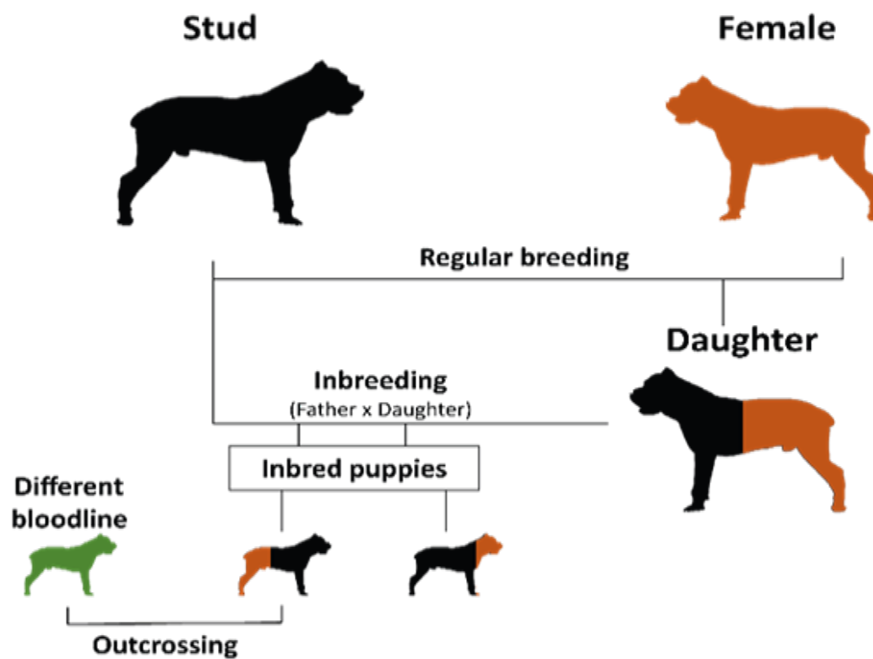


Fig. 5.1 Schematic representation of linebreeding and outcrossing.

5.2.1 Implementation of the breeding farm paradigm

Original Stud GA's genetic operators were diversity-dependent. Particularly, depending on the diversity between offspring, in terms of hamming distance, the operator

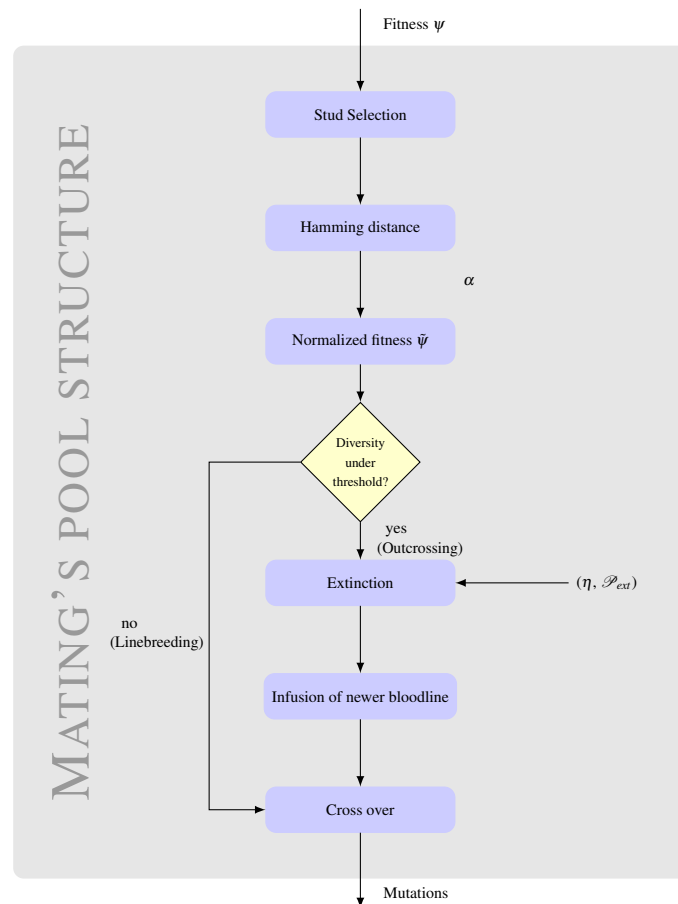


Fig. 5.2 Flowchart of the mating's pool structure for implementing the inbreeding (or line breeding) and outcrossing.

could be crossover or mutation. Furthermore, the mutation employed in [149], was a binary mutation with a low probability, that ranges from 0.001 to 0.003.

In the present work a modified Stud GA, namely Stud^P GA is introduced where "p" stands for proportionate. In fact, contrary to the original version of Stud GA, stochastic selection is used to select the elements that can mate with the Stud. Shuffle (or crossover) probability is set to 1 as well as the probability of mutation. The contemporary use of Stud and proportionate selection could increase the selective pressure in such a way that the algorithm might achieve premature convergence and hence lose in reliability. The reliability is a metric that gives the number of runs in which the algorithm, initialized at random, yields the same optimal solution. According to Liu *et al* [151], are considered being reliable all the runs that return

a fitness function which differs no more than 0.5% with respect to the optimum solution. In order to measure the reliability of the algorithm, a preliminary assessment is carried out. The results pertaining the assessment are reported in section 5.2.2.

Because the number of runs is limited to 100, if all the attempts return a reliable value then the reliability is 99% instead of 100%. To avoid the premature convergence that may arise due to the endogamic process, a diversity preservation technique is also included in the novel algorithm, as discussed above. Squillero and Tonda [152], noted that in absence of any domain-specific information on the problem, extinction is the preferable methodology to ensure diversity preservation.

The extinction was firstly introduced by Greenwood *et al* [153]. Contrary to Greenwood *et al* which used a probability of extinction equals to one [153] and, based on the assessment performed in the following, a probability of extinction of 40% is introduced. When activated, extinction concerns a certain number of individuals. All the offspring with a scaled fitness ($\tilde{\psi}_i$) lower than the stress factor (η) are eliminated. Follows that the extinction "filters" the population and let survive only those elements with $\tilde{\psi}_i \geq \eta$. The resulting empty slots are replaced with mutants of the Stud. The mutants are generated by applying a simple mutation, i.e. changing at random one gene of the genotype. The scaled fitness is given by the following equation

$$\tilde{\psi}_i = \alpha + (1 - \alpha) \frac{\Psi_{stud} - \Psi_i}{\Psi_{stud} - \min(\Psi)} \quad (5.1)$$

where ψ is the objective function while α is the strategy parameter. The strategy parameter is equal to the mean value of Hamming distance between offspring and the Stud of a given population divided by the number of plies of the laminate, thus $0 \leq \alpha \leq 1$. Let us consider the following strings

1 0 1 1 1 0 1	Stud
1 0 0 1 0 0 1	offspring a
1 1 0 1 1 0 1	offspring b

Defining the Hamming distance as the number of positions at which two strings of equal length are different, for the strings reported above the Hamming distance with respect to the Stud is: 2 for the offspring "a" and 1 for the offspring "b". In other words, it measures the minimum number of substitutions required to change one

string into the other, or the minimum number of errors that could have transformed one string into the other.

When the stress parameter η increases, increases also the selective pressure. This is because the number of individuals eliminated increases. In the limit for stress parameter equal to 1, the whole population, except the Stud, is replaced by mutants of the Stud. In fact, if $\eta = 1$, the only one individual that has a scaled fitness equal to 1 is the Stud; it follows that the remaining $n - 1$ empty slots are replaced with Stud's mutants. In this case premature convergence arises and hence having the extinction combined with an higher stress parameter has a detrimental effect.

It is important to point out that the stress parameter η acts on the scaled fitness. Thus, η does not give the information about the amount of individuals eliminated neither it means that individuals with fitness lower than $\eta\%$ with respect to the Stud are eliminated. The latter statement is true only if the strategy parameter α is zero.

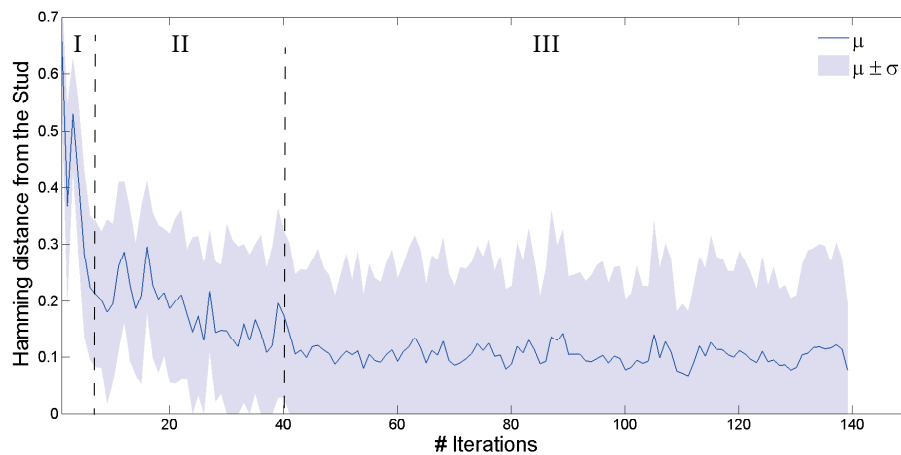


Fig. 5.3 Mean Hamming distance (μ) and standard deviation of Hamming distance (σ) between the Stud and others offspring with respect to number of iterations for load case 3. The figure shows the effect of the extinction in spreading the diversity among offspring when they tend to the best individual. The extinction causes the increasing of the standard deviation when the Hamming distance goes under 0.2.

The strategy parameter α is adaptive thus, varies during the computation accordingly to the hamming distance between the Stud and all other individuals. As shown in Figure 5.3, at early stages, the hamming distance is high (zone I); this means that the population is heterogeneous thus the extinction concerns a small percentage of the population with higher Hamming distance with respect to the best individual

(the Stud). When the diversity among individuals decreases (zone II), the second term of equation 5.1 gains more weight thus, the extinction strikes more and more individuals, even the ones similar to the Stud. That is, the extinction speeds up the exploration capability at early stages by removing the worst individuals (zone I) while, prevents the premature convergence by spreading the diversity when the offspring are more similar (zone II). Indeed, the standard deviation of the mean Hamming distance, which is represented by the shaded area in Figure 5.3, becomes higher when the mean Hamming distance decreases. In zone III the convergence has been already achieved but the algorithm is still running because of the first termination criteria defined below.

5.2.2 Effect of η and \mathcal{P}_{ext} on the algorithm's reliability and efficiency

The algorithm's performances depend on a great extent to the values of the stress parameter η and probability of extinction P_{ext} . A parametric study has been performed in order to find a suitable combination of η and P_{ext} . It is worth noting that the best combination of η and P_{ext} may varies according to the particular optimization problem considered. However, for all the optimizations reported in the following, the same probability of extinction and the same stress parameter will be used. In view to compare results, the following cost-effectiveness parameter is defined

$$\xi = \frac{\text{reliability}}{\text{number of iterations}}$$

In [153], in order to prevent premature convergence, it is suggested to eliminate a big amount of individuals; this is done, in this parametric study, by imposing that the stress parameter ranges from 0.7 to 0.9. Meanwhile the probability of extinction ranges from 30% up to 100%. Without loss of generality, the parametric analysis is done considering the problem of buckling load maximization of a composite square panel ($a = b = 609.6mm$). The panel is subjected to the following in-plane loads $N_x = -10000N/mm$, $N_y = -2000N/mm$ and $N_{xy} = 1000$. The allowable orientations are $0^\circ, \pm 45^\circ, 90^\circ$. The number of plies for each of the allowable orientation is fixed. The laminate is symmetric; particularly, for the optimization problem in hand one have: $n_0 = 7$, $n_{45} = 15$ and $n_{90} = 7$. The total number of plies is therefore 78, since the number of plies given in the fourth column of Table 5.1 refers to half the laminate

Table 5.1 Loads applied and optimal plies numbers for composite laminate panels under study

Load case	Applied Load (lb/in)			$N_{<0,45,90>}$	N_{Total}
	N_x	N_y	N_{xy}		
1	-20000	-2000	1000	(9, 18, 9)	36
2	-15000	-2000	1000	(8, 17, 8)	33
3	-10000	-2000	1000	(7, 15, 7)	29
4	-5000	-2000	1000	(6, 12, 6)	24
5	0	-2000	1000	(4, 8, 4)	16
6	0	-16000	8000	(8, 16, 8)	32
7	15980	-14764	10160	(9, 8, 13)	30
8	-16657	1963	828	(13, 7, 15)	35

Table 5.2 Physical properties of the composite material (graphite/epoxy) used for the optimization

Laminae's properties	
Longitudinal modulus	$E_{11}= 127.59$ GPa
Transverse modulus	$E_{22}= 13.03$ GPa
Shear modulus	$G_{12}= 6.40$ GPa
Poisson ratio	$\nu_{12}=0.3$
Ply thickness	$0.127mm$

and noting that the ± 45 are stacked in pairs. The mechanical properties along with the ply thickness for the composite material considered herein are reported in Table 5.2. Results reported in Table 5.3 are averaged over 50 attempts.

Table 5.3 Effect of probability of extinction and stress parameter on the number of evaluations and reliability of the Stud^P GA for a composite panel subjected to load case 3 Table 5.1.

Stress factor, η	Probability of extinction, P_{ext}							
	0.3	0.4	0.5	0.6	0.7	0.8	0.9	1
0.70	176(88)	198(90)	156(86)	193(84)	209(82)	227(82)	264(86)	229(84)
0.75	169(90)	195(96)	196(94)	214(90)	239(86)	253(86)	217(88)	253(84)
0.80	190(99)	186(99)	210(92)	240(90)	235(88)	274(86)	219(88)	274(98)
0.85	194(98)	202(94)	192(90)	247(88)	250(88)	269(90)	307(88)	387(82)
0.90	191(94)	254(82)	238(76)	299(76)	390(64)	444(64)	362(64)	471(54)

In Table 5.4 are reported the results in term of cost effectiveness parameter.

Table 5.4 Effect of probability of extinction and stress parameter on the cost-effectiveness of the Stud^P GA for load configuration 3 (see Table 5.1).

Stress factor, η	Probability of extinction, P_{ext}							
	0.3	0.4	0.5	0.6	0.7	0.8	0.9	1
0.70	0.500	0.454	0.544	0.435	0.339	0.361	0.326	0.367
0.75	0.532	0.492	0.447	0.420	0.360	0.339	0.406	0.332
0.80	0.521	0.532	0.438	0.375	0.374	0.314	0.402	0.358
0.85	0.505	0.465	0.468	0.356	0.352	0.335	0.287	0.212
0.90	0.492	0.322	0.319	0.352	0.164	0.144	0.177	0.115

As a general rule, at a given value of the stress parameter the number of iterations required to achieve the optimum value increases when the extinction probability's increases (Table 5.3). In other words the algorithm becomes less efficient when higher probability of extinction are set. When the probability of extinction is given, the algorithm reaches highest reliability for η that ranges from 0.75 to 0.85. At the extreme values for η the algorithm results less reliable. In particular, when η is 0.9, the selective pressure is too high since a large number of individual have to be eliminated. This affects the algorithm performances giving worst efficiency and reliability. At $P_{ext} = 1$ and stress parameter $\eta = 0.9$ is associated the minimum cost-effectiveness value, meaning that because of the higher selective pressure, notwithstanding an high level of infusion of new solutions, the algorithm get trapped in local optimum.

The best values of cost-effectiveness are far away from the highest value of probability of extinction for each value of η highlighting how a trend among the two exists (Table 5.4). In particular the highest cost-effectiveness are reached respectively for the following pairs of parameters ($\eta = 0.75, P_{ext} = 30\%$), ($\eta = 0.8, P_{ext} = 40\%$), ($\eta = 0.7, P_{ext} = 50\%$). Among these, it is chosen the pair ($\eta = 0.8, P_{ext} = 40\%$) since, even though ($\eta = 0.7, P_{ext} = 50\%$) ensure higher cost-effectiveness its reliability is lower than those of the other two pairs of values. The combination ($\eta = 0.75, P_{ext} = 30\%$) is a promising combination. To chose among the two we considered how many of the 50 attempts give exactly the same optimum value. The pair ($\eta = 0.8, P_{ext} = 40\%$) give the same optimum value 41 times against 37 of the pair ($\eta = 0.75, P_{ext} = 30\%$). For this reason, it has been chosen the pair ($\eta = 0.8, P_{ext} = 40\%$).

5.2.3 Selection strategy

The selection method chosen for the developed algorithm is the fitness proportionate selection, also known as roulette wheel selection. Fitness value is used to associate a probability of selection to each chromosome. Let φ_i is the fitness of the i^{th} individual, its probability of being selected \mathcal{P}_{rep_i} is given as:

$$\mathcal{P}_{rep_i} = \frac{\varphi_i}{\sum_{i=1}^n \varphi_i} \quad (5.2)$$

where φ_i is the value of the fitness function of the i^{th} chromosome and n is the population size.

Once the probability of reproduction of each chromosome is known, the algorithm computes the number of mating that each individual could make. According to the following equation, the higher the fitness the higher the number of offspring generated

$$n_{offspring_i} = \mathcal{P}_{rep_i} \cdot n \quad (5.3)$$

where $n_{offspring_i}$ is therefore rounded to the next integer.

The population size is fixed to 150 individuals. As appears clearly from equation 5.3, the number of offspring may vary through the iterations. The algorithm checks at each iteration the population size and, if the population's size tends to increase, the algorithm decreases the number of offspring that parents would generate starting from the worst individual. On the other hand, if the population size decreases the fittest element is promoted to the next generation (elitism).

It must be noted that in our algorithm the population size is 15 times larger than those used for SGA, PMX and GR in [151] as well as the one used in [154]. This is due to the fact that, since our algorithm is centered on the difference between offspring, to have a correct estimate of the diversity among offspring a larger population is required. Quite often, population size affects the efficiency of GA algorithm. In [155], they shown that increasing the population size increases the accuracy of the GA but also causes a loss in terms of rate of convergence. That is, our algorithm might benefit of the bigger population in term of accuracy but, at the same time, should lose in term of efficiency.

5.2.4 Reproduction and genetic operators

New offspring are generated by means of single point crossover and genetic modifications. The crossover point is randomly selected by the algorithm. The probability of crossover is set to 1. Three different genetic operators have been defined as follow

- mutation, randomly modification of one gene in the stacking sequence. The operator ensures that the new gene is different from the one that have been replaced;
- interchange, changes the position of two genes randomly selected in the stacking sequence, being the gene the orientation of a given ply for the case of buckling loads maximization or, for the case of unitized beam, the orientations of a pair of control points;
- swap, flips the stacking sequence of a sub-laminate or, in the case of unitized beams, inverts the vector of the stiffeners orientation. The initial and final point of swapping are randomly chosen.

The probability of undergoing genetic modifications is set to 1. Mutation and interchange have a probability of 10 % while, since the swap is the most effective operator due to the fact that strongly affects the bending stiffness, its probability is set to 80%. It is worth noting that, for the case of unitized beam with two control points, interchange and swap operators perform the same tasks.

Liu *et al* [151] defined a mutation operator that uses a partial repair operator. In addition they used an interchange mutation operator called stack-swap. The SGA used a standard two-point crossover meanwhile, since they observed that the permutation coding tend to produce infeasible children from feasible parents, they have introduced two different types of cross-over, the PMX ([156]) and the GR (Gene Rank). The GR, introduced by Liu and his colleagues ([151]), takes into account the fact that the outermost plies, hence leftmost genes, affect flexural stiffnesses more than the inner plies.

Both Liu *et al* [151] and Jing *et al* [154] have introduced a repair strategy to deal with contiguity constraint which has not be implemented in the Stud^P GA.

5.2.5 Termination criteria

Three termination criteria are defined as follow

1. limit number of iterations without any change of the fittest element;
2. maximum amount of individuals that can share the same fitness in each generation;
3. limit number of iterations.

5.3 Buckling load maximization of composite panels

Having detailed the main characteristics of the algorithm, here we aim at solving benchmark constrained combinatorial problems. Particularly, the focus is on to the buckling load maximization of composite flat panels. The panels are symmetric and balanced.

During normal flight conditions, aircraft panels are usually subjected to combined loads (tension/compression, bi-axial compression and shear), herein the effect of normal and shear loads are firstly considered separately. The combined effect is then included by means of the interaction equation reported in the following.

Because of symmetry there is no bending-extension coupling as well as, in view of the fact that the panel is balanced, the extension-shear coupling is zero. The governing equation for symmetric angle-ply laminate subjected to in-plane normal load is

$$\begin{aligned}
 D_{11} \frac{\partial^4 w}{\partial x^4} + 4D_{16} \frac{\partial^4 w}{\partial x^3 \partial y} + 2(D_{12} + 2D_{66}) \frac{\partial^4 w}{\partial x^2 \partial y^2} + \\
 4D_{26} \frac{\partial^4 w}{\partial x \partial y^3} + D_{22} \frac{\partial^4 w}{\partial y^4} = \lambda_n N_x \frac{\partial^2 w}{\partial x^2} + \lambda_n N_y \frac{\partial^2 w}{\partial y^2}
 \end{aligned} \tag{5.4}$$

where λ_n is the load multiplier and D_{ij} are the elements of bending stiffness matrix. Following [151, 154] we assumed that the plate is specially orthotropic, i.e. no bending-torsion coupling exists and hence D_{16} and D_{26} are zero. This is a common assumption for angle-ply laminate, as the ones analyzed in this work, where the bending-torsion terms are negligible with respect to the other terms of the stiffness

matrix. In this case the equation (5.4) assumes the form

$$D_{11} \frac{\partial^4 w}{\partial x^4} + 2(D_{12} + 2D_{66}) \frac{\partial^4 w}{\partial x^2 \partial y^2} + D_{22} \frac{\partial^4 w}{\partial y^4} = \lambda_n N_x \frac{\partial^2 w}{\partial x^2} + \lambda_n N_y \frac{\partial^2 w}{\partial y^2} \quad (5.5)$$

Solutions to the equation (5.5) can be obtained via direct approach assuming that the displacement w can be expressed as

$$w(x, y) = \sum_{m=1}^{\infty} \sum_{n=1}^{\infty} W_{m,n} \bar{X}(x) \bar{Y}(y) \quad (5.6)$$

where \bar{X} and \bar{Y} are sets of functions complete and orthogonal that satisfy the boundary conditions. Due to the uniform convergence, a finite number of functions is required to achieve the desired accuracy. For a simply supported plate along the edges, the boundary conditions are given as follow

$$\begin{aligned} \text{for } x = 0, a \quad w = M_x = -D_{11} \frac{\partial^2 w}{\partial x^2} - D_{12} \frac{\partial^2 w}{\partial y^2} &= 0 \\ \text{for } y = 0, b \quad w = M_y = -D_{12} \frac{\partial^2 w}{\partial x^2} - D_{22} \frac{\partial^2 w}{\partial y^2} &= 0 \end{aligned}$$

where a and b are respectively the dimensions along x and y directions of the plate. Given the boundary conditions, the equation (5.6) can be expressed as

$$w(x, y) = \sum_{m=1}^{\infty} \sum_{n=1}^{\infty} W_{m,n} \sin\left(\frac{m\pi x}{a}\right) \sin\left(\frac{n\pi y}{b}\right) \quad (5.7)$$

where m and n are the number of half-waves in which the panel buckles in x and y direction respectively. For a simply supported panel subjected to uni-axial compression N_x , the panel buckles for $n = 1$ and m to be determined in order to minimize the critical load \bar{N}_x ([157]). When the panel is subjected to combined load is it not possible to determine *a priori* the value of m and n which leads the minimum, thus critical, load. Therefore, we let m and n vary between 1 and 5 and then we take the minimum, thus critical, value. Substituting equation (7.17) in equation (5.5) one can

obtain the load multiplier λ_n as:

$$\lambda_n^{m,n} = \pi^2 \frac{D_{11}(\frac{m}{a})^4 + 2(D_{12} + 2D_{66})(\frac{m}{a})^2(\frac{n}{b})^2 + D_{22}(\frac{n}{b})^4}{N_x(\frac{m}{a})^2 + N_y(\frac{n}{b})^2} \quad (5.8)$$

A second buckling mechanism is shear buckling. Assuming that the panel has an infinite length along x, an estimation of the critical shear load amplitude is given as follow

$$\lambda_s = \begin{cases} \frac{4\beta_1(D_{11}D_{22}^3)^{1/4}}{b^2N_{xy}} & 1 \leq \Gamma \leq \infty \\ \frac{4\beta_1\sqrt{D_{22}(D_{12}+2D_{66})}}{b^2N_{xy}} & 0 \leq \Gamma \leq 1 \end{cases} \quad (5.9)$$

with

$$\Gamma = \frac{\sqrt{D_{11}D_{22}}}{D_{11} + 2D_{66}}$$

while β_1 is given in ([158]).

The effect of combined loads, both normal and shear, is taken into account by the following interaction equation

$$\frac{1}{\lambda_c^{(m,n)}} = \frac{1}{\lambda_n^{(m,n)}} + \frac{1}{\lambda_s^2} \quad (5.10)$$

where λ_n is the normal buckling load factor, λ_s is the shear buckling factor and λ_c is the combined buckling load factor. The combined buckling load factor $\lambda_c^{m,n}$ is always more critical than normal buckling factor $\lambda_n^{m,n}$. To prevent buckling both $\lambda_c^{m,n}$ and λ_s have to be greater than one. Overall buckling load factor λ is taken to be the minimum of the load factors:

$$\lambda = \min\{|\lambda_s|, \lambda_c^{m,n}\} \quad (5.11)$$

Therefore λ is the parameter to maximize. It appears clearly from equations (5.8) and (5.9) how λ depends on a great extent on the elements of flexural stiffness matrix. For a composite laminate panel made of a single fibrous material, the elements D_{ij} of the bending stiffness matrix can be computed as follow:

$$[D] = \frac{1}{3} \sum_{k=1}^N [\bar{Q}]^{(k)} (z_k^3 - z_{k-1}^3) \quad (5.12)$$

where N is the total number of plies, $[\bar{Q}]$ is the ply's transformed reduced stiffness matrix and z_k and z_{k-1} are respectively the outermost and innermost distances of the k^{th} ply from the mid-plane. The transformed reduced stiffness matrix is given by the following equation

$$\bar{Q}_t^{(k)} = [\Lambda^{(k)}]^{-1} [Q_p^{(k)}] [\Lambda^{(k)}]^{-T} \quad (5.13)$$

$$[\Lambda]^{(k)} = \begin{bmatrix} \cos^2 \vartheta & \sin^2 \vartheta & 2 \cos \vartheta \sin \vartheta \\ \sin^2 \vartheta & \cos^2 \vartheta & -2 \cos \vartheta \sin \vartheta \\ -\cos \vartheta \sin \vartheta & \cos \vartheta \sin \vartheta & \cos^2 \vartheta - \sin^2 \vartheta \end{bmatrix}^{(k)}$$

where $[Q_p^{(k)}]$ and ϑ are respectively the reduced stiffness matrix and the fiber angle of the k^{th} ply.

Following the approach given by Tsai [159], the first of the equations 5.13 can be rewritten introducing the trigonometric identities given below to rewrite the transformation eqns. from the fourth powers of trigonometric functions to those of multiple angles

$$\begin{aligned} \cos^4 \vartheta &= \frac{3 + 4 \cos 2\vartheta + \cos 4\vartheta}{8} \\ \cos^3 \vartheta \sin \vartheta &= \frac{2 \sin 2\vartheta + \sin 4\vartheta}{8} \\ \cos^2 \vartheta \sin^2 \vartheta &= \frac{1 - \cos 4\vartheta}{8} \\ \cos \vartheta \sin^3 \vartheta &= \frac{2 \sin 2\vartheta - \sin 4\vartheta}{8} \\ \sin^4 \vartheta &= \frac{3 - 4 \cos 2\vartheta + \cos 4\vartheta}{8} \end{aligned} \quad (5.14)$$

Substituting in the eq. 5.13 the identities given above (eq. 5.14) one can obtain a set of linear combinations of the principal stiffness, say U_1, U_2, U_3, U_4, U_5 and the integral of the trigonometric multiple angle W_1 and W_2 . It is a common practice use the integral of the trigonometric multiple angle in their normalized form respectively, W_1^* and W_2^* , where $W_i^* = \frac{12}{h^3} W_i$ and h is the laminate's thickness. Given the new formulation of the transformation eqns in terms of multiple angles, it is easy to

rewrite the terms of stiffness matrix reported in the equation 5.12 as follow

$$\begin{aligned}
 D_{11}^{(k)} &= \frac{h^3}{12} (U_1 + U_2 W_1^* + U_3 W_2^*) \\
 D_{12}^{(k)} &= \frac{h^3}{12} (U_4 - U_3 W_2^*) \\
 D_{22}^{(k)} &= \frac{h^3}{12} (U_1 - U_2 W_1^* + U_3 W_2^*) \\
 D_{66}^{(k)} &= \frac{h^3}{12} (U_5 - U_3 W_2^*)
 \end{aligned} \tag{5.15}$$

where

$$\begin{aligned}
 W_1^* &= \frac{8}{h^3} \sum_k^{N/2} \cos 2\vartheta^{(k)} (k^3 - (k-1)^3) \\
 W_2^* &= \frac{8}{h^3} \sum_k^{N/2} \cos 4\vartheta^{(k)} (k^3 - (k-1)^3)
 \end{aligned} \tag{5.16}$$

For a specified stacking position k the bending stiffness parameters $D_{ij}^{(k)}$ depends only on the trigonometric functions of ply orientation $\vartheta^{(k)}$ (equations 5.15, 5.16). Moreover, is straightforward observe that the overall bending stiffness parameters D_{ij} can be expressed as sum of $D_{ij}^{(k)}$. It follows that, for an assigned stacking position k , the fiber orientation ϑ^k is the only design variable in the optimization of flexural stiffness parameters.

The problem of maximizing the buckling load can be seen as the maximization of the flexural stiffness parameters (see eqns. 5.8 and 5.9) thus, as follows form eqns. 5.15 and 5.16, a combinatorial maximization problem. In view of the fact that the total number of plies, as well as the number of plies for each orientation, are assigned, the problem is also constrained.

5.3.1 Objective function

The objective of the optimization is to maximize the buckling loads of composite layered panels subject to technological constraints. Following Liu *et al* [151], the objective function is defined as a combination of fitness function and penalty functions. The fitness function is the buckling load factor λ (equation 5.11). An example of panel subjected to combined load is depicted in Figure 5.5. Penalty functions are defined to avoid matrix cracking and to guarantee that the number

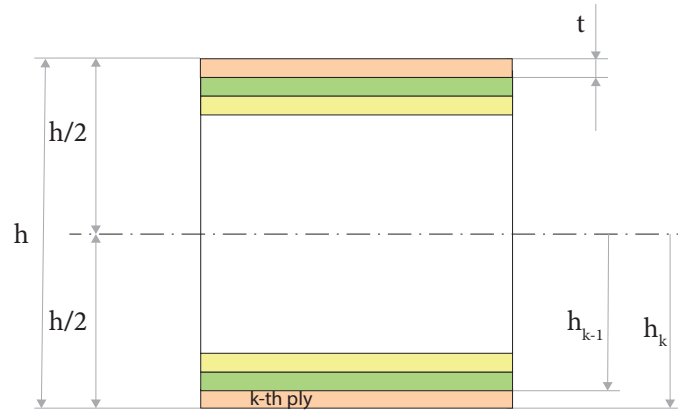


Fig. 5.4 Example of the stacking sequence of laminate plates.

of plies for each orientation is the one given as constraint to cope with blending requirements (Table 5.1). The objective function is therefore defined as follow

$$\varphi = \frac{\lambda}{P_{contiguity}} r^2 \quad (5.17)$$

where $P_{contiguity}$ is the penalty function to cope with matrix cracking and r is the penalty for violation of blending requirements. The stacking rule commonly used to cope with matrix cracking requirements consists in avoiding that more than four plies with same orientation are stacked together. In this work the $P_{contiguity}$ is defined as follow

$$P_{contiguity} = \begin{cases} 1 & N_{cont_{\vartheta}} < 5 \\ \prod_{\vartheta=0,90} 2(N_{cont_{\vartheta}} - 3) & N_{cont_{\vartheta}} \geq 5 \end{cases} \quad (5.18)$$

where $N_{cont_{\vartheta}}$ is the number of plies with same orientation ϑ stacked together. It is important to point out that, when the contiguity penalty is considered, many sub-optimal solutions exist. The extinction should enhance the performance of the algorithm in finding the global optima. For this reason, extinction is allowed only when the contiguity constraint is considered.

In Liu *et al* [151], the penalty for matrix cracking, say contiguity constraint, is $P_{cont}^{N_{cont}}$ where the penalty parameter P_{cont} is set to 1.05. while N_{cont} is the total number of same-orientation contiguous plies in excess of four same orientation.

Jing and co-workers [154] used *swap*'s operator to obtain the global optimal sequence of the laminate and two other operators, namely *delete* and *insert*, to deal with

continuity constraints. Both ([151] and [154]) have than introduced a repair strategy to deal with the contiguity constraint. In contrast, we preferred to have a more strict penalty function with respect of those of [151] instead of implement a repair strategy. Let us consider the case in which 5 plies with the same orientation are stacked together. In this case our $P_{contiguity}$ would be 4, while the one of [151] is 1.2763. So our penalty will lower the objective function more than three times with respect to that used by Liu and his colleagues. In the same way, if the number of contiguous plies is 6, our penalty function is about 4.48 times greater than those reported in [151] and so on. In other words, we preferred to penalize more the stacking sequence that violates the contiguity constraint instead to have a repair strategy. From our view point, a strict penalty function is closer to what happen in nature and aims to replicate the natural selection.

Penalty used for blending r is the same defined in [151], thus:

$$r = \prod_{\vartheta=0,\pm 45,90} r_{\vartheta} \quad (5.19)$$

with

$$r_{\vartheta} = \begin{cases} \frac{n_{\vartheta}+1}{n_{\vartheta_g}+1} & \text{if } n_{\vartheta} < n_{\vartheta_g} \\ 1 & \text{if } n_{\vartheta} = n_{\vartheta_g} \\ \frac{n_{\vartheta_g}+1}{n_{\vartheta}+1} & \text{if } n_{\vartheta} > n_{\vartheta_g} \end{cases}$$

where n_{ϑ_g} is the given number of plies for each orientation listed, case by case, in Table 5.1 while n_{ϑ} is the actual number of plies for each orientation.

5.3.2 Results

In this section we aim to show the efficiency and reliability of the proposed algorithm in optimizing the stacking sequence of composite structures. To relate the reliability and the efficiency of the algorithm we introduced the cost-effectiveness parameter, ξ . In view of comparing our results, we extended the calculation of the cost-effectiveness parameter also to the GAs reported in [151] and to the PS algorithm reported in [154]. Without loss in generality, the developed algorithm is validated by means of standard test cases, reported in [151].

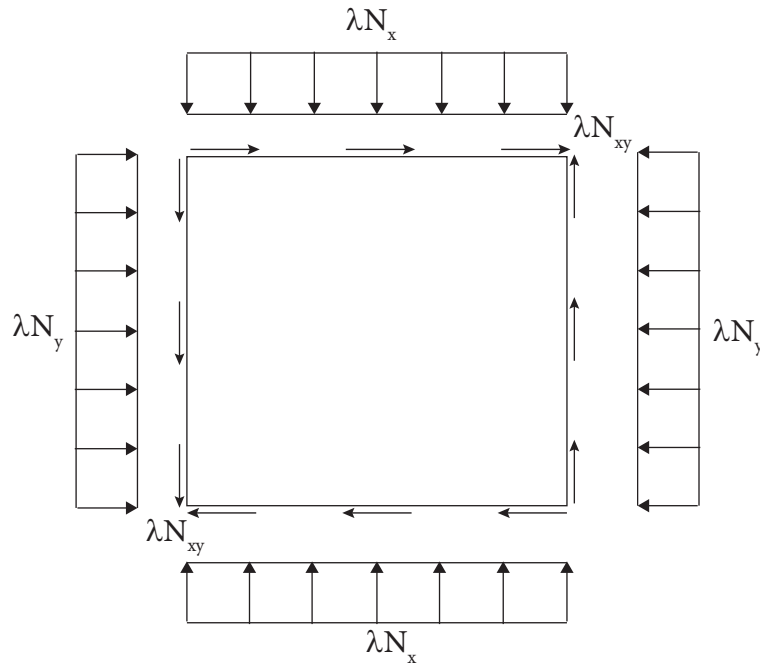


Fig. 5.5 Example panel subjected to combined loads.

The square panel ($a=b=609.6\text{mm}$) made by composite (graphite/epoxy) material is symmetric, balanced and simply supported along the edges. The physical properties of graphite/epoxy material used in this work are listed in Table 5.2. Eight different load configurations are analyzed, as listed in Table 5.1. The optimization objective is maximizing the overall buckling load factor for a given number of plies, N_{Total} . The set of allowable orientation is $0^\circ, \pm 45^\circ, 90^\circ$. In addition, the number of plies for each orientation n_{ϑ_g} is fixed. Stacking rules are defined by means of penalty functions.

Because of symmetry and due to the fact that plies at 0° and 90° are stacked in pairs, only one quarter of the laminate is considered in the encoded space. For each load configuration the optimization is performed without and with contiguity constraint. The optimized stacking sequences, as well as the buckling load factors, are reported in Table 5.5. To evaluate reliability and efficiency of the proposed algorithm, for every load configuration, 100 runs are performed. Results reported in Table 5.6 and Table 5.7 are therefore averaged over 100 attempts.

Table 5.5 Optimized stacking sequence from GA

Case	Stacking sequence without and with contiguity constraint	λ
1	$[(\pm 45)_{18}/(90_2)_9/(0_2)_9]_S$	0.9484
	$[(\pm 45)_{18}/(90_2)_2/0_2/(90_2)_2/(0_2)_2/90_2/(0_2)_2/90_2/0_2]_S$	0.9483
2	$[(\pm 45)_{17}/(90_2)_8/(0_2)_8]_S$	0.9486
	$[(\pm 45)_{17}/(90_2)_2/0_2/(90_2)_2/0_2/90_2/0_2/90_2/(0_2)_2/90_2/(0_2)_2/90_2/0_2]_S$	0.9483
3	$[(\pm 45)_{15}/(90_2)_7/(0_2)_7]_S$	0.9102
	$[(\pm 45)_{15}/(90_2)_2/0_2/90_2/0_2/90_2/(0_2)_2/90_2/0_2/90_2/0_2/90_2/0_2]_S$	0.9097
4	$[(\pm 45)_{12}/(90_2)_6/(0_2)_6]_S$	0.8715
	$[(\pm 45)_{12}/(90_2)_2/0_2/90_2/0_2/90_2/(0_2)_2/90_2/0_2/90_2/0_2]_S$	0.8705
5	$[(\pm 45)_8/(90_2)_4/(0_2)_4]_S$	0.7809
	$[(\pm 45)_8/(90_2)_2/0_2/90_2/(0_2)_2/90_2/0_2]_S$	0.7756
6	$[(\pm 45)_{16}/(90_2)_8/(0_2)_8]_S$	0.7809
	$[(\pm 45)_{16}/(90_2)_2/0_2/90_2/0_2/(90_2)_2/(0_2)_2/90_2/(0_2)_2/90_2/(0_2)_2/90_2]_S$	0.7740
7	$[(\pm 45)_8/(90_2)_{13}/(0_2)_9]_S$	1.6246
	$90_2/(\pm 45)_2/(90_2)_2/(\pm 45)_2/(90_2)_2/(\pm 45)_2/\pm 45/90_2/\pm 45/90_2/0_2/90_2/(0_2)_2/90_2/(0_2)_2/90_2/(0_2)_2/90_2/(0_2)_2]_S$	1.6153
8	$[(\pm 45)_7/(90_2)_{15}/(0_2)_{13}]_S$	1.1026
	$[(90_2)_2/(\pm 45)_3/90_2/\pm 45/(90_2)_2/(\pm 45)_2/90_2/\pm 45/90_2/\pm 45/90_2/0_2/90_2/(0_2)_2/90_2/(0_2)_2/90_2/(0_2)_2/90_2/(0_2)_2]_S$	1.1022

Table 5.6 reports the number of iteration required to achieve the convergence for the five algorithms herein compared. From Table 5.6 follows that the proposed algorithm outperforms others GAs, as well as PS, in term of computational efficiency when contiguity constraint is ignored. The reliability given by Stud^P GA is higher than those of GAs and equal to that of the PS. It must be noted that in our work we considered as reliable only the solutions that differ no more than 0.5% to the optimal solution, in agreement with what have been done in [151]. While Jing *et al* [154] considered as reliable all the runs that return a buckling load equal or higher to the optimum. Table 5.7 shows how overall performances of the Stud^P GA are better than the other GAs as well as the PS also when the contiguity constrain is activated.

Table 5.7 shows that

- the contemporary presence of $P_{contiguity}$ and extinction, slows the convergence rate;
- the buckling load factor decreases when $P_{contiguity}$ is activated, as reported in Table 5.5.

These results are in agreement with those reported in [151, 154].

Because of convergence criterion 1, the number of iterations required by the Stud^P GA for load configurations 4 and 5, with and without contiguity constraint, is always higher than that of PS. For the same reason SGA outperforms, in terms of efficiency, the Stud^P GA for load cases 5 and 8 with contiguity penalty, even though SGA's reliability is lower those of the proposed algorithm. In section 5.2.5 we wrote

Table 5.6 Comparison of computational efficiency between Stud^P GA, PS and other three GAs without contiguity constraint (SGA = standard GA, PMX = partially mapped crossover, GR = gene rank).

Load case	Number of evaluations required for				
	99% reliability		80% reliability		
	Stud ^P GA	PS	SGA	PMX	GR
1	156 (56)	256	10432	1328	1184
2	151 (51)	226	8600	1224	856
3	139 (39)	196	5216	1024	776
4	131 (31)	139	3304	824	608
5	114 (14)	63	1672	560	408
6	145 (45)	207	5112	848	480
7	211 (111)	570	2176	336	360
8	153 (53)	316	5024	840	296

that the standard approach to calculate reliability is letting the algorithm run for a fixed number of iteration, generally large, and check at which iteration arose the convergence. In view of that, ignoring the stopping criterion 1, for each of the cases considered, we can state that the convergence was achieved 100 iterations before. We report in Table 5.6 and Table 5.7 both values. The number of iterations without the stopping criterion 1 are reported between brackets.

Generally speaking Stud^P GA outperforms the other algorithms taken as a reference in this work. To highlight the validity of the proposed algorithm we compare its cost-effectiveness with those of PS and SGA, PMX and GR (Table 5.8). The most important result that arises from Table 5.8 is that, in terms of cost-effectiveness, the Stud^PGA performs better than PS as well as other GAs for all the cases considered if one ignore the stopping criterion 1 (results between brackets in Table 5.8). Vice versa, if one takes into account the stopping criterion 1, the PS has a better cost-effectiveness for load cases 4 and 5. Overall the algorithm is reliable and efficient and will be used to address also the other optimization problems presented in this chapter.

Table 5.7 Comparison of computational efficiency between Stud^P GA, PS and other three GA with contiguity constraint (SGA = standard GA, PMX = partially mapped crossover, GR = gene rank).

Load case	Number of evaluations required for				
	99% reliability		80% reliability		
	Stud ^P GA	PS	SGA	PMX	GR
1	226 (126)	262	672	792	456
2	221 (121)	232	536	792	400
3	186 (86)	203	368	658	352
4	164 (64)	143	224	496	304
5	146 (46)	65	80	272	184
6	168 (68)	211	400	552	416
7	275 (175)	579	3512	336	288
8	221 (121)	333	48	696	352

Table 5.8 Comparison of the cost-effectiveness between Stud^P GA, PS and other three GA with contiguity constraint (SGA = standard GA, PMX = partially mapped crossover, GR = gene rank).

Load case	Number of evaluations required for				
	Stud ^P GA	PS	SGA	PMX	GR
1	0.438 (0.786)	0.378	0.119	0.101	0.175
2	0.447 (0.818)	0.427	0.149	0.101	0.200
3	0.532 (1.151)	0.488	0.217	0.122	0.227
4	0.604 (1.547)	0.692	0.357	0.161	0.263
5	0.678 (2.152)	1.523	1.000	0.294	0.435
6	0.589 (1.456)	0.469	0.200	0.145	0.192
7	0.360 (0.566)	0.171	0.023	0.238	0.278
8	0.448 (4.714)	0.297	1.667	0.115	0.227

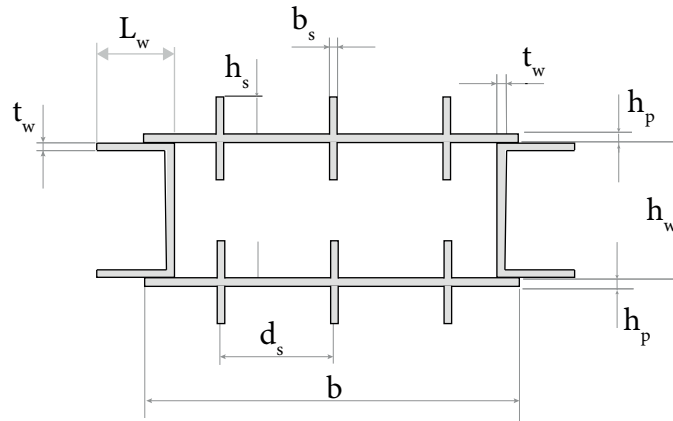


Fig. 5.6 Exemplification of the beam's cross section considered in [125].

5.4 Linear static optimization of unitized beam

In this section is performed the optimization of a unitized box beam. The box beam has the geometry shown in Figure 5.6. The beam under study is the same considered in [125, 160]. For the interest of clarity, the geometric characteristics of the box-beam are listed in Table 5.9. Three different load cases are considered: (a) concentrated tip load, (b) uniform distributed load and (c) triangular load. The first load considered herein is the same as in [125, 160]. The resultant load is the same for all the load configurations selected. The optimization is meant to investigate the effect that the load distribution has on the stiffeners path.

Table 5.9 Geometric features of the wing box under study.

Stiffeners' width	b_s	3 mm
Stiffeners' spacing	d_s	10 mm
Stiffeners' height	h_s	4 mm
Number of stiffeners	n_s	6
Plate's skin thickness	h_p	2 mm
Beam's length	L	1100 mm
Spar caps length	L_w	20 mm
Spar height	h_w	40 mm
Spar's thickness	t_w	2 mm

It is worth noting that, when idealized beam model are adopted, the optimization of the unitized beam comprises also the following steps

- Evaluation of the equivalent properties of the stiffened panel once the geometry of the stiffeners is assigned, and
- calculation of the equivalent beam properties;

The flowchart which exemplifies the steps to follow for calculating the beam stiffnesses is reported in Figure 5.7.

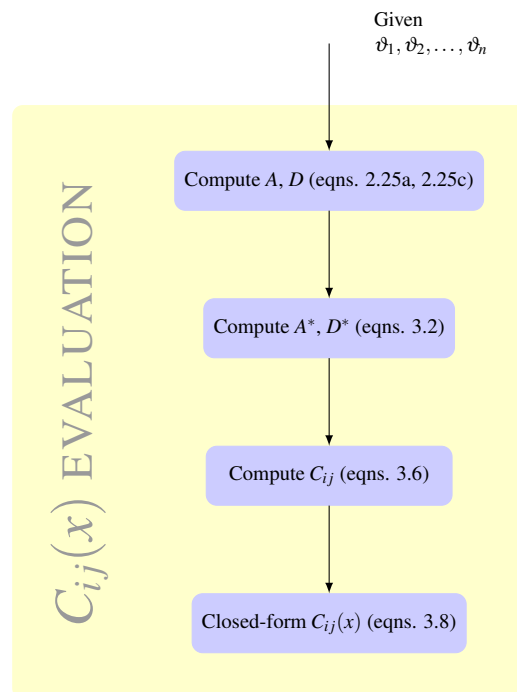


Fig. 5.7 Flowchart for the evaluation of the beam's stiffnesses.

Aiming at identifying the stiffeners topology which maximize the bending-torsion coupling, Cestino and Frulla [125] used an idealized beam model; they performed a parametric analysis instead of optimizing the beam and considered straight but oriented stiffeners. It is worth noting that, while the calculation of the beam cross sectional properties is the same adopted herein (see eqns. 3.6), the model adopted in [125] to calculate the equivalent properties of the stiffened panels is different, as already discussed in chapter 2. Cestino and Frulla [125] performed

also an experimental study to validate their model. We will use the results of such experiment to validate the model presented in this work.

Cestino *et al* [160] performed the topology optimization of the same beam, subjected to tip concentrated load, by means of Altair OptiStructTM. The topology optimization was performed by means of the SIMP method (Solid Isotropic Material with Penalization [161]). The objective of the optimization was maximizing the bending-torsion coupling provided that the constraints on minimum tip rotation and maximum tip deflection were fulfilled.

5.4.1 Problem formulation

The topology optimization problem, for the three load cases considered, are formulated such that the design variables are the stiffeners' orientations at prescribed control points. All the other geometric parameters are fixed (see Table 5.9). The functional to be maximized is the strain energy (compliance), the optimization problem can be formulated as follows

$$\mathbf{max} \quad \frac{1}{2} \int_0^L \left(\frac{M_y^2 G J_t}{G J_t E I_2 - k^2} \right) dx \quad (5.20)$$

$$\text{subject to: } \mathbf{K} \mathbf{u} = \mathbf{q}$$

$$\vartheta_1^{i+1} = \vartheta_2^i$$

$$-45^\circ \leq \vartheta_i \leq 45^\circ$$

$$\varphi_{tip} \geq \varphi_0$$

$$w_{tip} \leq w_0$$

where \mathbf{u} is the vector of the generalized displacement $\mathbf{u} = [\rho_x \ \rho_y \ \rho_z]^T$, \mathbf{K} is the stiffness matrix, ϑ_i is the angle of orientation of the stiffeners at the i -th control point, and $\mathbf{q} = [M_t \ M_{flap} \ M_{lag}]^T$ is the generalized force vector. The stiffness matrix

is given as follow

$$\mathbf{K} = \begin{bmatrix} GJ_t & K & 0 \\ k & EI_2 & 0 \\ 0 & 0 & EI_3 \end{bmatrix}$$

In this case, following Cestino *et al* [125, 160], planar deformations are considered (i.e. $\rho_z = 0$) therefore the stiffness matrix given above becomes

$$\mathbf{K} = \begin{bmatrix} GJ_t & K \\ k & EI_2 \end{bmatrix}$$

It is worth noting that the topology optimization problem, written as in eq. 5.20, assumes the form of a constrained combinatorial optimization. Indeed, recalling the eqns 3.6, the stiffness properties can be written as

$$\begin{aligned} GJ_t &= GJ_t(x, A_{66}^*, D_{66}^*, b, h_w, \Omega) \\ K &= K(x, A_{16}^*, A_{66}^*, D_{16}^*, b, h_w, \Omega) \\ EI_2 &= EI_2(x, A_{11}^*, A_{16}^*, A_{66}^*, D_{11}^*, b, h_w, \Omega) \end{aligned}$$

where the reduced matrix A^* , D^* can be derived from the complete matrix of the equivalent panels A , D by means of the eqns. 3.2. Recalling that, for a given panel, the membrane and bending matrices are given as

$$\begin{aligned} A &= A(x, \vartheta_1, \vartheta_2, h_s, h_p, b_s, n_s, E, G, k_y, k_z) \\ D &= D(x, \vartheta_1, \vartheta_2, h_s, h_p, b_s, n_s, E, G, k_y, k_z) \end{aligned}$$

Being all the other geometric parameters fixed, the membrane and bending matrices A and D depend only on the stiffeners' orientations and on the spatial coordinate x , as shown in chapter 2. It follows that the beam stiffnesses become only function of the stiffeners' orientations at the control points and of the spatial coordinate x .

$$\begin{aligned} GJ_t &= GJ_t(x, \vartheta_1, \vartheta_2, \dots, \vartheta_n) \\ K &= K(x, \vartheta_1, \vartheta_2, \dots, \vartheta_n) \\ EI_2 &= EI_2(x, \vartheta_1, \vartheta_2, \dots, \vartheta_n) \end{aligned}$$

It is worth noting that, regardless of the model adopted, being this variable stiffness or constant stiffness, the design variables are the orientations of the stiffeners at the

control points. Indeed, recalling that the spatial variation of the stiffeners orientation is governed by eqn. 2.1, it follows that the orientation in any point of the structure is known once the orientations at the control points are known. Thus, the spatial coordinate x is the independent variable rather than a design variable. It has been

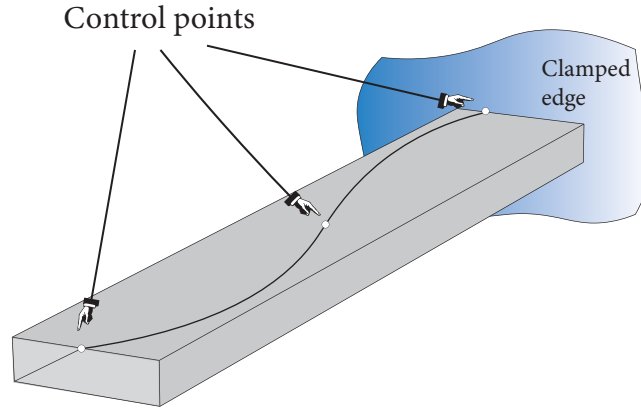


Fig. 5.8 Exemplification of a clamped free beam with control-points distributed span-wise.

hence shown that, regardless the beam's model adopted, the topology optimization problem becomes a combinatorial optimization, as for the buckling optimization problem.

The beam tip displacement and rotation are calculated by means of the Principle of Virtual Work (PVW), as follow

$$w = \int_0^L M^a(x)M^b(x)\Gamma_1(x)dx \quad (5.24a)$$

$$\varphi = \int_0^L M^a(x)M_t^b(x)\Gamma_2(x)dx \quad (5.24b)$$

where

$$\Gamma_1(x) = \frac{GJ_t(x)}{EI_2(x)GJ_t(x) - K^2(x)} \text{ and} \quad (5.24c)$$

$$\Gamma_2(x) = -\frac{K}{EI_2(x)GJ_t(x) - K^2(x)} \quad (5.24d)$$

The moment M^b is the bending moment due to a unit dummy load applied at the beam tip and M_t^b is a unit dummy torque applied at the beam tip. The constraints on beam tip deflection and rotation have been adjoined to the objective function by means of lagrangian multipliers, i.e. we used Lagrangian relaxation to restate the

problem as follow

$$\mathbf{max} \quad \frac{1}{2\lambda_\varphi|\varphi - \varphi_0|\lambda_w|w - w_0|} \int_0^L \left(\frac{M_y^2 G J_t}{G J_t E I_2 - k^2} \right) dx \quad (5.25)$$

subject to: $\mathbf{Ku} = \mathbf{q}$

$$\vartheta_1^{i+1} = \vartheta_2^i$$

$$-45^\circ \leq \vartheta_i \leq 45^\circ$$

In this way, tuning the two lagrangian weights λ_w and λ_φ one have that two amongst the three constraints are relaxed through the introduction of the augmented objective function given in eqn. 5.25. In the following, two control points will be used, as in Cestino [125]. The two control points are located at the beam root and tip respectively.

5.4.2 Results and discussion

The optimization is carried out by means of the Stud^p GA. A stress parameter η of 0.4 and a probability of extinction of 0.8 have been selected as for the cases of buckling loads maximization presented in the previous section. Standard mutations as those listed above are used; the cross over probability is set to 1. The allowable orientations range from $\vartheta = -45^\circ$ to $\vartheta = 45^\circ$ with a set space of 2.5° . For all the optimization performed herein, contrary to the optimization of the previous section, a population of 20 chromosome is used. Indeed, it is worth noting that the cardinality of the problem in hand is orders of magnitude less than the that of the buckling loads maximization hence is worthed to decrease the number of individuals within the population. Investigating the effect of the population size on to the performances of algorithm is out of the scope of the present optimization, one may refer for example to [162–164] for major details.

The box beam under study is made by Al 6060 Aluminum alloy ($E = 58000$ MPa, $\nu = 0.33$ and $\rho = 2780$ kg/m³). With reference to Fig. 5.6, all the other geometrical parameters, i.e. aft and fore panels thicknesses t_w , plate's skin thickness h_p , stiffeners width b_s and height h_s , cross sectional width b and height of the shear webs h_w are all fixed. In the interest of clarity, the corresponding values are listed in Table 5.9. As

mentioned above, three static cases are considered, namely: (a) tip concentrated load, (b) uniform distributed load and (c) triangular load. For all the cases considered, only a transverse load q_w is applied. The load is applied at the cross-sectional centroid which, being the beam symmetric, coincides with the beam axis. The following pairs of tip displacements w_0 and rotations φ_0 are given for the three problems in hand, namely: concentrated load $\{14 \text{ mm}, 0.287^\circ\}$, uniformly distributed load $\{4.6 \text{ mm}, 0.08^\circ\}$ and triangular load $\{3.3 \text{ mm}, 0.06^\circ\}$. For the case of concentrated load, the constraints on tip deflection and rotation are the same adopted in [160].

The first load case is the same used in Cestino [125, 160] considered herein as benchmark to validate the mathematical model derived. The beam is clamped at one end and subjected to a concentrated load $F = 41.37 \text{ kg}$ applied with an offset of $e = 40 \text{ mm}$ with respect to the beam tip. In Figure 5.9 is reported the comparison between the stiffnesses predicted with the present model and those obtained as in [125]; it is worth noting that in Figure 5.9 only straight stiffeners ($\vartheta_1 = \vartheta_2$) are considered, consistently with [125]. A small deviation with respect to the stiffnesses computed as in [125] is appreciable; the deviation is due to the model adopted to calculate the bending stiffnesses. It is worth nothing that, in this case, the stiffeners' height is comparable with that of the skin plate therefore the aforementioned discrepancy is small, as already discussed in chapter 2 for sub-stiffened structures.

Figure 5.10 reports the bending displacement and the rotation of the beam measured at the beam's tip. Different models, namely: (a) solid FE mode, (b) theoretical derivation as in Cestino [125], (c) experiment and (d) present derivation for the case of straight stiffeners oriented at 25° are compared against each other. The results reported in Figure 5.10 are obtained applying different loads, as it was done in the experiment performed by Cestino and Frulla. It should not surprise that the tip rotation obtained with the present model (red diamond in Figure 5.10) is closer to that obtained experimentally, in fact the torsional stiffness GJ_t is proportional to the D_{66}^* coefficient which, as discussed previously, is more accurate in the present model than that used in [125]; moreover, the coupling terms K computed with the two models are coincident, since the stiffeners are straight (see Figure 5.9). Indeed, looking at eqn 3.6b, the coupling coefficient for straight stiffeners is only function of the membrane coefficients since D_{16} and hence D_{16}^* are zero. It is also worth noting that all the models adopted match closely to each other. According to the results reported in Figures 5.9 and 5.10, the present model underestimates the deflection

(overestimates the bending stiffness), contrary to what expected. However, it is worth mentioning that the discrepancy is of the order of 0.5% and it is mainly due to the fact that either the manufactured model and the solid FE model have, in some portion of the beam, for manufacturing reasons, 5 stiffeners rather than 6.

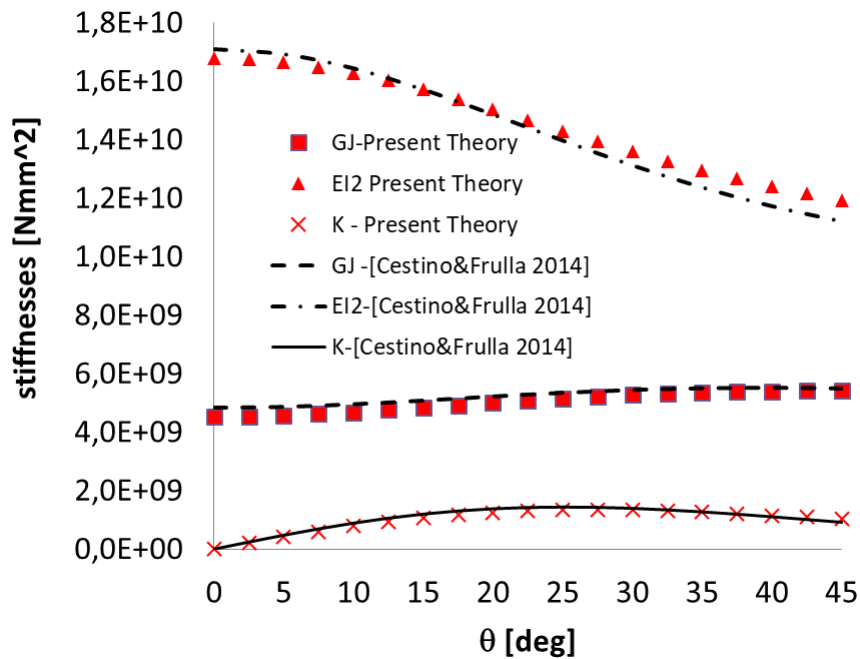


Fig. 5.9 Comparison of the stiffnesses obtained with the presented model and the model adopted in [125] considering straight stiffeners $\vartheta_1 = \vartheta_2$.

For the interest of clarity, in Figure 5.11 is reported the experimental setup used by Cestino and Frulla [125].

Although the model presented herein and in [125] are found in good agreement, the optimization yields a slightly different results in terms of optimal stiffeners topology. Indeed the optimal solution identified by means of the Stud^P GA yields to straight stiffeners oriented at 27.5° , rather than 25° as in [125]. In order to explain this result, is worth while noting that the value obtained with the Stud^P GA is that which yields the maximum coupling term K . This result has also been qualitatively confirmed in [160] where a thick plate was used as an initial guess and the topology optimization was performed using the SIMP algorithm. The topology synthesized by the SIMP algorithm, depicted in Figure 5.12, resembles that obtained with the present method. In this case, starting form a thick plate, the SIMP algorithm removes the

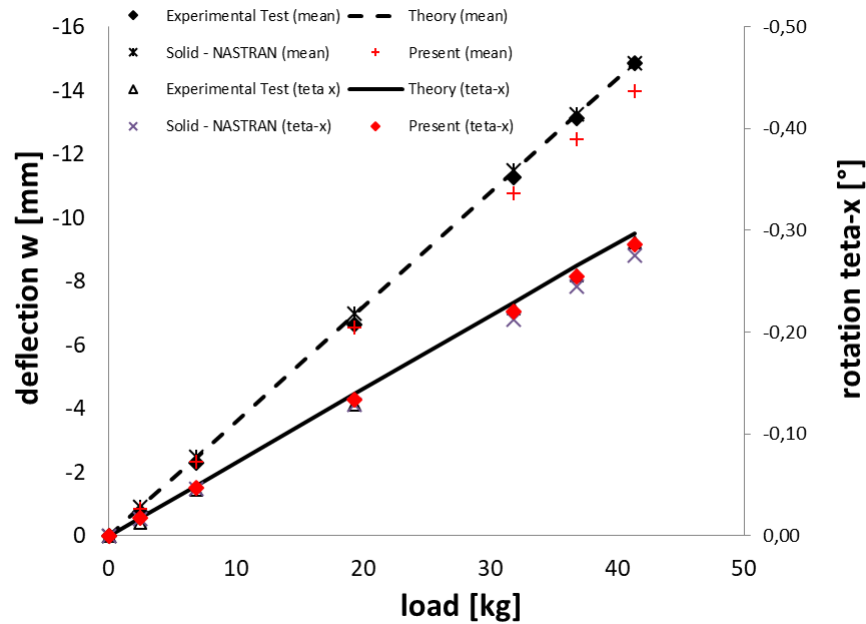


Fig. 5.10 Comparison of the mean tip displacement and tip rotation obtained with different models and experiments.

material until the strain energy is maximum, and the pair of maximum tip deflection and minimum tip rotation as given above are met ($\{14 \text{ mm}, 0.287^\circ\}$).

It is worth mentioning that the topology of the stiffeners obtained in [160] slightly changes from one stiffener to another, as shown in Figure 5.12; this result cannot be obtained with the present model since it is presumed that all the stiffeners have exactly the same topology. Moreover, one should also consider that the model adopted herein is an idealized model so the effect of stress concentration at tip and root of the beam cannot be represented. The local effects may influence locally the topology of the stiffeners leading to small variation of the stiffeners' orientation. It is also worth noting that, the shape of the stiffeners in the present model is fixed, particularly only blade stiffeners were considered, while, comparing with the results obtained in [160], it can be noted that the stiffeners synthesized by the SIMP algorithm resemble a L or Z shape (Figure 5.13). Notwithstanding the aforementioned differences, the two optimizations yields results that are qualitatively in good agreement.

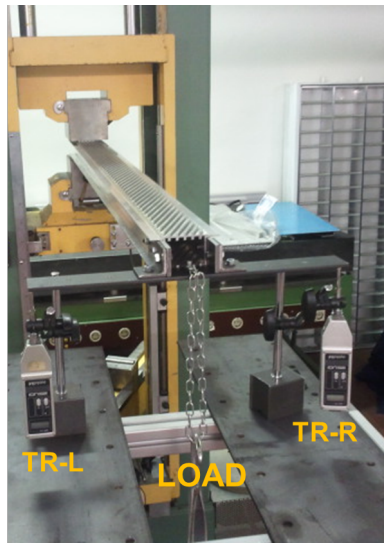


Fig. 5.11 Experimental setup for the first load case with straight stiffeners oriented at 25° .

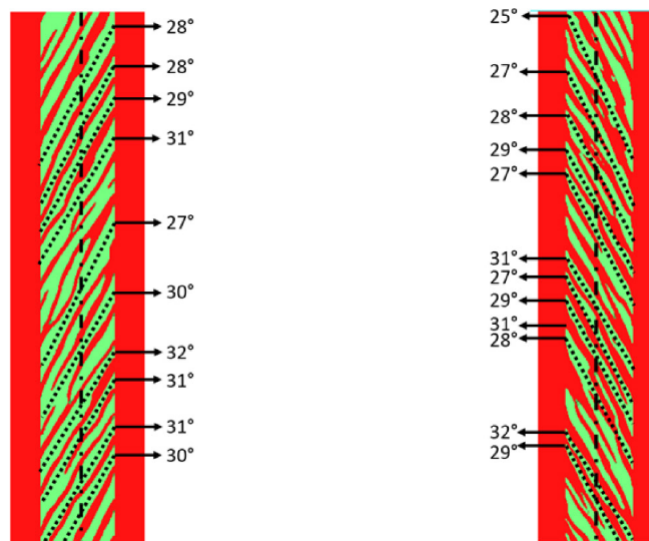


Fig. 5.12 Optimized stiffeners topology obtained with Altair OptiStruct (published with permission [160])

The beam tip deflection and rotation for the different load cases considered are listed in Table 5.10. The last column of Table 5.10 exemplifies the optimized topology for the stiffeners path.

Examining the case of uniformly distributed load, the optimization leads to curved stiffeners with $\vartheta_1 = 20^\circ$ and $\vartheta_2 = 22.5^\circ$. It is seen that the problem is multi-

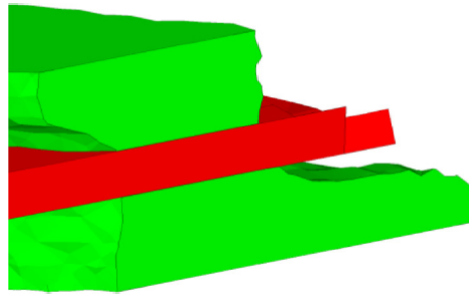
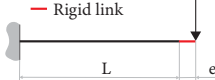

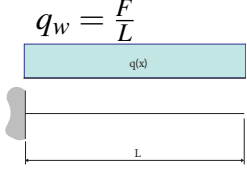

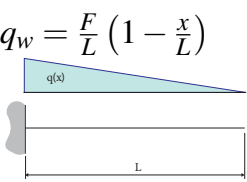
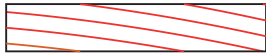


Fig. 5.13 Detailed view of the stiffeners cross section as obtained in [160] (published with permission)

Table 5.10 Results of the topology optimization for the static cases.

Load	$\vartheta_1[deg]$	$w[mm]$	$\phi[deg]$	Topology ⁱ
$q_w = \delta(L+e)F$ 	$\vartheta_1 = 27.5$ $\vartheta_2 = 27.5$	-13.89	-0.29	
$q_w = \frac{F}{L}$ 	$\vartheta_1 = 20$ $\vartheta_2 = 22.5$	-4.654	-0.081	
$q_w = \frac{F}{L} \left(1 - \frac{x}{L}\right)$ 	$\vartheta_1 = 5$ $\vartheta_2 = 12.5$	-2.195	-0.064	

ⁱ The beams are drawn out of scale.

modal, particularly, since the homogenized model have been considered herein, the solution $\vartheta_1 = 20^\circ$ and $\vartheta_2 = 22.5^\circ$ is equivalent to the solution $\vartheta_1 = 22.5^\circ$ and $\vartheta_2 = 20^\circ$. The same behavior has been observed for the case of triangular distributed load, in this case the optimum orientations are $\vartheta_1 = 5^\circ$ and $\vartheta_2 = 12.5^\circ$.

In this two cases, since the optimization lead to curved stiffeners, it is worth to perform the optimization with the variable stiffness model rather than the homogenized model. The reason is twofold: (a) investigating if the two beam's models lead to the same optimal solution irrespective of the beam model adopted (homogenized model vs variable stiffness model) and (b) understanding if the problem is still multi-modal also for the case of variable stiffness, i.e. if the solution ϑ_1, ϑ_2 is equivalent to ϑ_2, ϑ_1 . In order to account for the stiffness variability we need to evaluate the closed form equation for each of the beam's stiffnesses, namely EI_2 , GJ_t and K . This task is performed as explained in chapter 3, hence using a curve fitting method with a polynomial basis. It is seen that odd polynomials (cubic or quintic) are best suited for this purpose. The procedural steps to calculate the variable stiffness properties has been previously discussed and it is exemplified in Figure 5.7.

Performing the optimization for the load case 2, allowing the beam to have variable stiffness, it is seen that the optimized topology is again $\vartheta_1 = 20^\circ$, $\vartheta_2 = 22.5^\circ$. In this case it has been noted that the solution $\vartheta_1 = 20^\circ$, $\vartheta_2 = 22.5^\circ$ is no more equivalent to the solution $\vartheta_1 = 22.5^\circ$, $\vartheta_2 = 20^\circ$, hence the problem is no more multi-modal if one considers the variable stiffness model. The solution $\vartheta_1 = 20^\circ$, $\vartheta_2 = 22.5^\circ$ is the one that respect all the constraints and maximize the strain energy indeed, while the strain energy is higher for the second solution ($\vartheta_1 = 22.5^\circ$, $\vartheta_2 = 20^\circ$), the constraint on the maximum tip displacement is violated. This is possible because of the augmented objective function defined in eqn. 5.25. In this case it can be concluded that the homogenized model and the variable stiffness model give the same optimal topology; however, the deflection and rotation computed using the homogenized model differ from that of the variable stiffness model. In Table 5.11, are reported the results of the optimization obtained using the two models. For the sake of completeness we reported also the solution obtained with the variable stiffness model with ($\vartheta_1 = 22.5^\circ$, $\vartheta_2 = 20^\circ$). From Table 5.11, it can be noted that the solution $\vartheta_1 = 20^\circ$, $\vartheta_2 = 22.5^\circ$ obtained with the variable stiffness model respects all the constraints. In Figure 5.14 are reported the normalized trends of the stiffnesses with respect to the normalized abscissa \hat{x} for the case of $\vartheta_1 = 20^\circ$, $\vartheta_2 = 22.5^\circ$.

The same behavior discussed above has been also seen for the load case 3, i.e. triangular distributed load. Allowing the beam to have variable stiffness, it is seen that the optimized topology is again $\vartheta_1 = 5^\circ$, $\vartheta_2 = 12.5^\circ$. In this case it has been noted that the solution $\vartheta_1 = 12.5^\circ$, $\vartheta_2 = 5^\circ$ is no more equivalent to the solution $\vartheta_1 = 5^\circ$, $\vartheta_2 = 12.5^\circ$, hence the problem is no more multi-modal if one considers the

Table 5.11 Comparison of the tip deflection and tip rotation obtained with the different models for different topologies for the case of uniformly distributed load.

Model	ϑ_1	ϑ_2	w	φ
	[deg]	[deg]	mm	[deg]
Opt. Homogenized	20	22.5	4.65	-0.082
	22.5	20	4.65	-0.082
Opt. Var. Stiff.	20	22.5	4.62	-0.081
Non opt. Var. Stiff.	22.5	20	4.69	-0.083

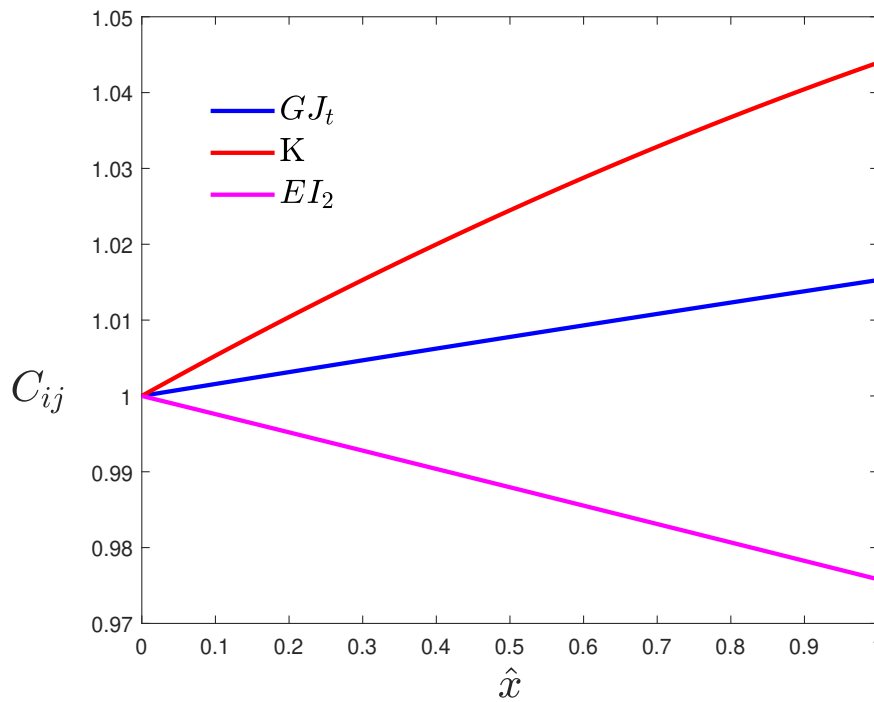


Fig. 5.14 Normalized optimum beam stiffness for the case of uniformly distributed load. The stiffness are normalized with respect to their value at the root.

variable stiffness model. In this case, contrary to the load case 2, we have seen that neither the variable stiffness nor the homogenized stiffness model strictly respect the optimization constraint of the maximum deflection ($w_0 \leq 2.2$). However, due to relaxation a near optimum solution has been identified, which is the solution with $\vartheta_1 = 5^\circ$, $\vartheta_2 = 12.5^\circ$. In Table 5.12 are reported the beam tip deflection and rotation

Table 5.12 Comparison of the tip deflection and tip rotation obtained with the different models for different topologies for the case of triangular load.

Model	ϑ_1	ϑ_2	w	φ
	[deg]	[deg]	mm	[deg]
Opt. Homogenized	5	12.5	2.215	-0.063
	12.5	5	2.215	-0.063
Opt. Var. Stiff.	5	12.5	2.206	-0.052
Non opt. Var. Stiff.	12.5	20	2.224	-0.075

obtained with the different models. For the sake of completeness, we reported also the solution obtained with the variable stiffness model with ($\vartheta_1 = 12.5^\circ$, $\vartheta_2 = 5^\circ$). The results obtained in this case, confirm that the variable stiffness model is more accurate than the homogenized model and that the problem is not multi-modal. In Figure 5.15 are reported the normalized stiffnesses with respect to the nondimensional abscissa \hat{x} for the case of $\vartheta_1 = 5^\circ$, $\vartheta_2 = 12.5^\circ$.

For the interest of clarity is worth to remark that, the fact that the algorithm identifies near optimum solutions does not mean that the optimization algorithm itself fails. Indeed, we allowed for such near optimal solutions to be identified through the use of the Lagrangian's relaxation. If one aims to identify solutions that respect all the constraints one can either increase the Lagrangian's weights or enlarge the design space allowing for a narrower set space between the stiffeners orientation, for example halving the set space.

Comparing figures 5.14 and 5.15 follows that for the case of triangular load the increment of the K required to fulfill the optimization objective is remarkably higher, while the span-wise variation of GJ_t and EI_2 are comparable for the two cases analyzed. It should not surprise that the beam bending stiffness decreases since the bending moment decreases moving towards the beam tip. Contrary, the coupling and the torsional stiffness both increase for the two cases analyzed; this might seem incoherent with the objective of the optimization. To this end is worth noting that the optimization problem is nonlinear, due to the function Γ_1 and Γ_2 . However, engineering reasoning can be used to get some insights. The optimum solutions, once the load configuration is selected, are a trade-off between Γ_1 and Γ_2 . If we aim to minimize the bending deflection and maximize the tip rotation, we can roughly

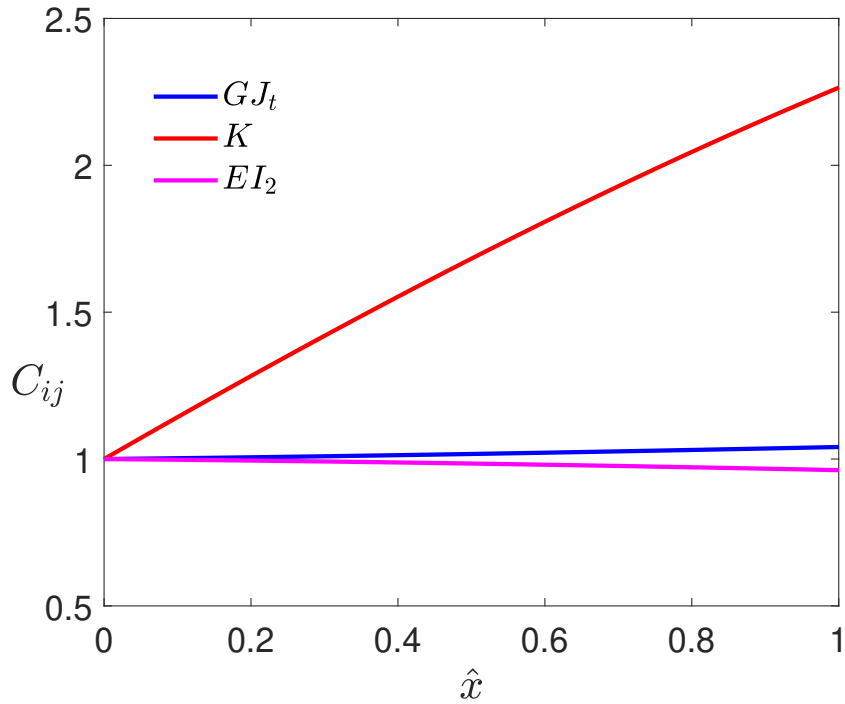


Fig. 5.15 Normalized optimum beam stiffness for the case of triangular load. The stiffness are normalized with respect to their value at the root.

say that we are aiming to minimize the function $\frac{w}{\varphi}$. With some algebraic steps, one have

$$\min \left(\frac{w}{\varphi} \right) \equiv \frac{\frac{GJ_t}{E I_2 G J_t - K^2}}{\frac{K}{E I_2 G J_t - K^2}} = \frac{GJ_t}{K} \quad (5.26)$$

which in turns shows that an higher increment on the coupling stiffness with respect to the torsional stiffness is required to met the objective of the optimization. The importance of this parameter was also pointed out in [125].

As a general conclusion, the section as highlighted the need for variable stiffness beam to get an accurate structural response.

5.5 Dynamic tailoring of HAR box-beam with curvilinear stiffeners

The configuration selected for the optimization is that of a typical High Altitude Long Endurance (HALE) aircraft, adopted by Cestino *et al* in [64]. The analysis is performed on to a scaled configuration suitable for a wind-tunnel test, rather than on the full scale model. The wing-box objective of the optimization is depicted for the interest of clarity in Figure 5.16. The properties of the constitutive material are given as follows: $E = 73GPa$, $\nu = 0.3$. The center of mass and the torsional center are coincident, $x_{CG} = x_c = 0$. The structural mass per unit length is $m_s = 1.095 \cdot 10^{-5} kg/mm$. The nonstructural mass is $m_{ns} = 1.095 \cdot 10^{-5} kg/mm$ while the inertia per unit length due to the non-structural mass is $3.4 \cdot 10^{-3} kgmm$.

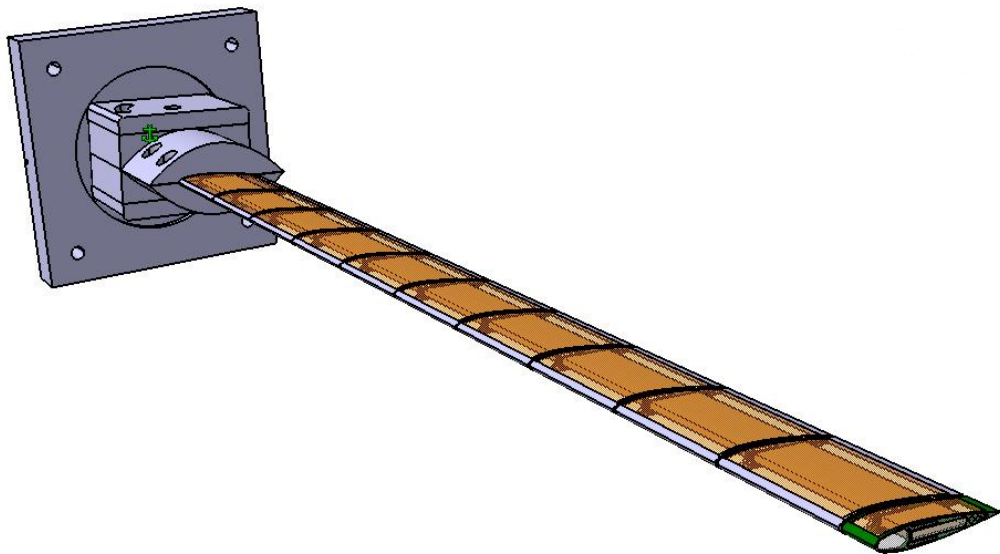


Fig. 5.16 Isometric view of the High Aspect Ratio wing considered herein for the analysis.

The wing-box has a rectangular cross section with $a = 20\text{mm}$, $b = 2.61\text{mm}$. The upper and lower panels thickness is $h_p = 0.2\text{mm}$ while the shear webs have a thickness t_w equal to 0.22 mm. The wing span is 522 mm. The model adopted herein differs from that used in [64] because considers stiffened panels for the upper and lower walls of the box-beam. Aiming at rewriting the topological problem in the form of combinatorial optimization, as in the previous section, we first need to establish a model with straight stiffeners oriented at zero which exhibits comparable value of the stiffnesses as that of the wing-box used in [64]. The model with the stiffeners oriented at zero will be henceforth referred to as benchmark model.

5.5.1 Identification of the benchmark model

This section is ment to identify the number of stiffeners required and their cross sectional dimensions such that the stiffened wing-box (benchmark model) exhibits the same (or approximately the same) stiffnesses of the scaled wing-box adopted by Cestino *et al* in [64]. We first perform a static assessment applying unit dummy load at the beam tip. In view of the selected geometry, i.e. stiffened upper and lower panels with straight stiffeners oriented at zero, the wing-box is decoupled ($K = 0$) and the stiffnesses are constant span-wise. It follows that the bending and torsional stiffness can be calculated with ease. It is seen that a wing-box with $n_s = 10$ sub-stiffeners having $h_s/h_p = 1.5$, $b_s = h_p$ approximates with a good agreement the wing-box considered in Cestino *et al* [64]. In Figures 5.17-5.19 are reported the static deflections/rotation of the model considered herein. The value of the stiffnesses are found in agreement with those reported in Cestino *et al* in [64] with negligible differences. For the sake of comparison, the resulting stiffnesses of the model are reported in Table 5.13 along with the stiffnesses of the wing box given in Cestino *et al* in [64].

The assessment of the benchmark model procedes performing the dynamic analysis and comparing the natural frequencies of the wing-box given in [64] with that obtained with the stiffened wing-box considered herein. It is seen that the wing-box model presented herein has comparable natural frequencies with that given in Cestino *et al* [64], as shown in Table 5.14.

A uniform distributed load q has been applied to the structure; particularly, the distributed load is given as $q = 1/2\rho V^2 cC_{l_\alpha} \alpha$ where, $\rho = 1.225\text{kg}/\text{m}^3$ is the air

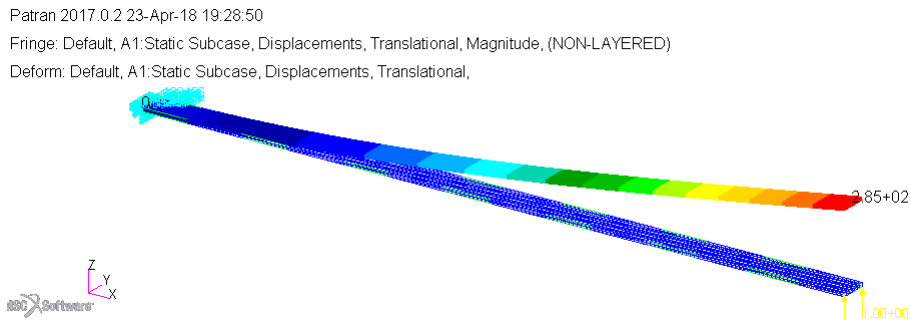


Fig. 5.17 Static assessment of the edgewise stiffness for the benchmark wing-box.

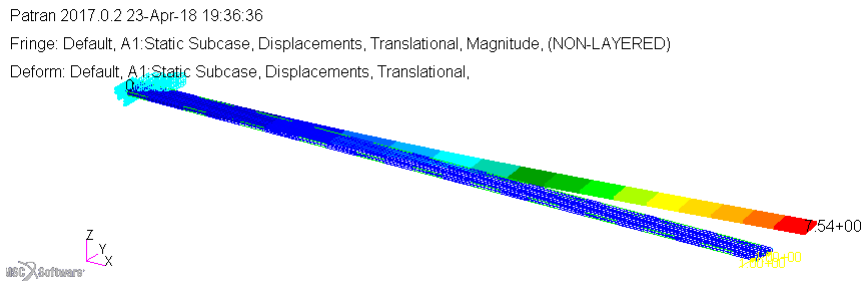


Fig. 5.18 Static assessment of the flat-wise stiffness for the benchmark wing-box.

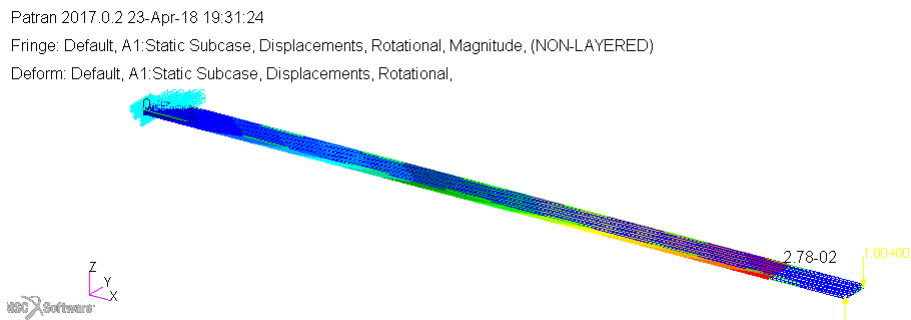


Fig. 5.19 Static assessment of the torsional stiffness for the benchmark wing-box.

density, V is the flight speed ($V = 20m/s$), c is the mean aerodynamic chord ($c =$), $C_{l\alpha} = 2\pi$ and $\alpha = 1.1^\circ$. A nonlinear analysis has been performed to evaluate the frequencies of the deformed structure. In Figure 5.20 is reported the nonlinear static deformation of the wing box. It is seen that also the frequencies of the deformed configuration are found in good agreement with those given in [64], as shown in

Table 5.13 Comparison of the wing box stiffnesses between the benchmark model established herein and that given in Cestino *et al* in [64].

Model	EI_2	EI_3	GJ_t	K
	$[Nmm^2]$	$[Nmm^2]$	$[Nmm^2]$	$[Nmm^2]$
Present	$3.33 \cdot 10^5$	$1.26 \cdot 10^7$	$3.75 \cdot 10^5$	0
Ref [64]	$3.41 \cdot 10^5$	$1.27 \cdot 10^7$	$3.41 \cdot 10^5$	0

Table 5.14 Linear and nonlinear frequencies [Hz] of the benchmark problem ($\vartheta_1 = 0^\circ$, $\vartheta_2 = 0^\circ$).

#f	Linear	Nonlinear
1	7.67	5.70
2	47.55	38.9
3	48.14	44.59
4	126.55	111.73
5	130.60	122.55

Table 5.14. The first three mode shapes of the deformed configuration are reported in Figures 5.21, 5.22 and 5.23.

Comparing the results obtained for the static and dynamic assessments, it can be concluded that the benchmark model has been established. Henceforth, all the design parameter will remain fixed and only the stiffeners' orientations will change aiming at decreasing the difference between the frequency of the linear system in the undeformed and deformed configuration.

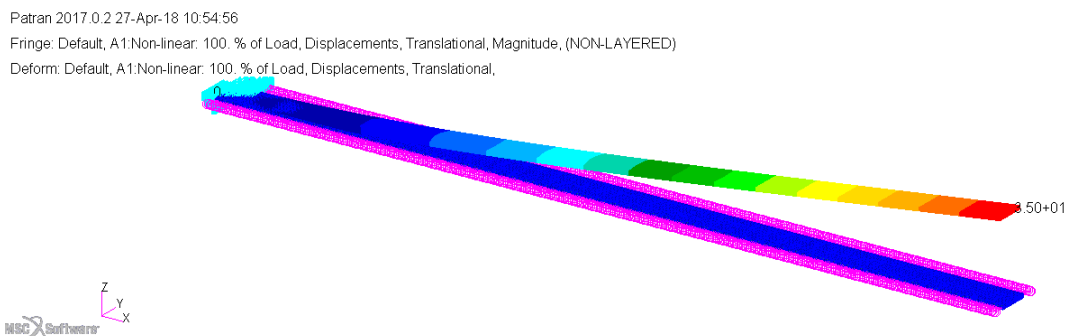


Fig. 5.20 Nonlinear static deformation of the benchmark box-beam

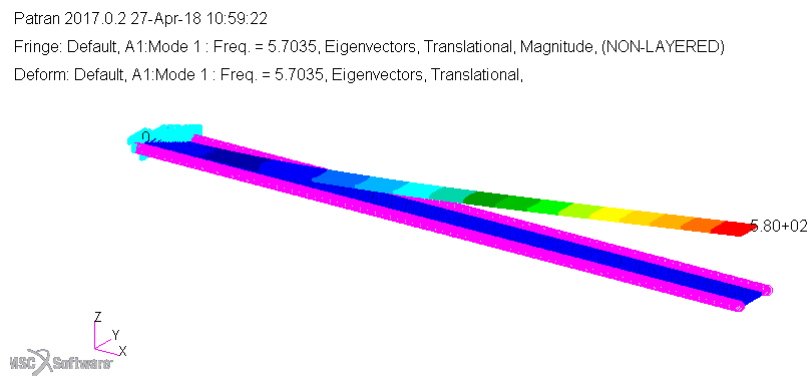


Fig. 5.21 First nonlinear mode shape of the wing box.

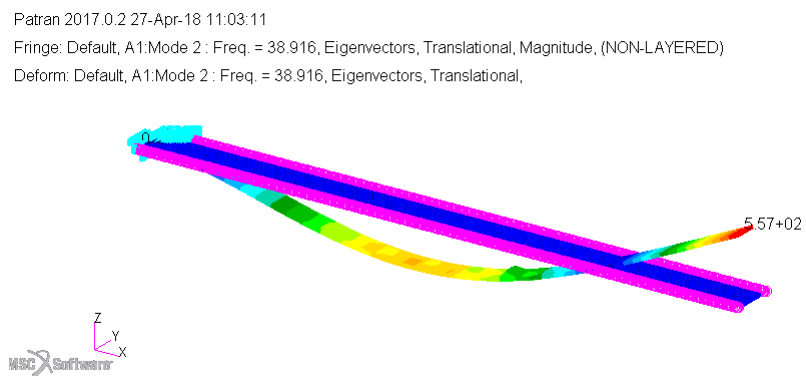


Fig. 5.22 Second nonlinear mode shape of the wing box.

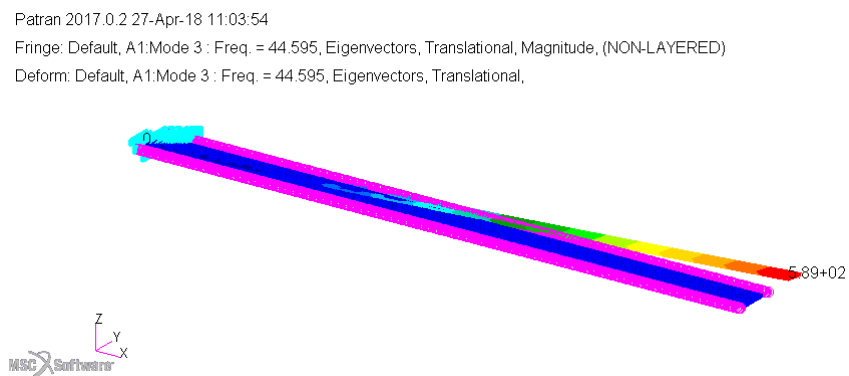


Fig. 5.23 Third nonlinear mode shape of the wing box.

5.6 Formulation of the optimization problem

The optimization problem can be formulated as follows

$$\begin{aligned}
 \mathbf{max} \quad & \sum_i \|\omega_i - \hat{\omega}_i\| & (5.27) \\
 \text{subject to:} \quad & [-\omega^2 \mathbf{M} + \mathbf{K}] \mathbf{u} = \vec{0} \\
 & [-\hat{\omega}^2 \hat{\mathbf{M}} + \hat{\mathbf{K}}] \hat{\mathbf{u}} = \vec{0} \\
 & \vartheta_1^{i+1} = \vartheta_2^i \\
 & -45^\circ \leq \vartheta_i \leq 45^\circ \\
 & w_{tip} \leq \frac{b}{10}
 \end{aligned}$$

where ω and $\hat{\omega}$ are respectively the frequencies of the undeformed and deformed configuration, M and K are the mass and stiffness matrices, b is the wing-box span; the quantities indicated with hat are those of the configuration linearized around the deformed state. Also in this case, as highlighted in Section 5.4, the optimization problem, written as in eqn. 5.27 is in the form of combinatorial optimization. It is worth mentioning that in the following we consider the structural mass being uniformly distributed, the reason is two fold: (a) in chapter 2 we have shown that the effect of mass variability is negligible and a good approximation can be achieved considering a uniform distributed mass and, (b) the inertia due to the nonstructural mass, for the wing-box considered herein, is the dominant component.

In this case, the optimization is performed by means of finite element analysis. The beam is modeled with CQUAD4 elements. The non-structural masses are attached with an offset to the aft and fore wing spars through rigid elements (RBE2). The beam has 522 element edgewise and 10 flatwise. The equivalent variable stiffness plate properties are calculated within the in-house Matlab code. The upper and lower panels are modeled as thick plates (MAT2) as in chapter 2. In this case however, only membrane and bending behavior are considered while, in view of the results of chapter 2, the shear behavior is neglected. The Stud^P GA has been used to perform the optimization. A population size of 20 chromosome is used. All the other relevant parameters for the Stud^P GA remains unchanged with respect to the optimization performed for the static cases considered in Section 5.4. Once the optimum solution has been identified, the results obtained by means of the FEA are compared against those obtained using the reduced order model derived in chapter 3. For the purpose

Table 5.15 Linear and nonlinear frequencies [Hz] of the optimized wing box ($\vartheta_1 = 0^\circ$, $\vartheta_2 = 10^\circ$).

#f	Linear	Nonlinear	
		FEA	ROM
1	7.67	5.79	5.81
2	47.55	39.6	39.9
3	48.16	44.86	45.1
4	126.59	113.79	114.3
5	130.60	122.00	124.6

of this comparison, 5 modes are used for the approximation as in eqn. , namely, two flatwise modes, two edgewise modes and one torsional mode. In view of the results and discussions of the previous section (Sec. 5.4), here we used only the variable stiffness beam model.

5.6.1 Optimization with two control points

In the first case study there are only two control points, namely at $X = 0$ and $x = L$. The algorithm converges within few iterations to the optimum values, namely $\vartheta_1 = 0^\circ$, $\vartheta_2 = 10^\circ$. The nonlinear static deflection of the optimum solution is shown in Figure 5.24. The value of the static deformation is $w_{NL}^{opt} = mm$. The resulting natural frequencies of the undeformed and deformed configurations respectively are reported in Table 5.15. In the fourth column of Table 5.15 are reported the frequencies of the deformed configuration obtained with the second order variable stiffness model described in chapter 3. It is worth noting that for the first three frequencies are found in good agreement with that of the FEA, while for the fourth and fifth frequencies the discrepancy with the frequencies calculate by FEA is higher. The reason could be that higher modes, not included in the basis function, may interact with the fourth and fifth frequencies leading the approximation to be less accurate. To achieve better approximation the number of basis functions used should be increased.

Comparing the frequencies of the undeformed and deformed configuration for the optimized solution it is worth noting the following

- a small deviation of the linear frequencies of the optimized configuration with respect to the benchmark model is found
- except for the case of the fifth frequency, all the other frequencies are higher for the optimized wing-box compared with that of the benchmark model.

Although the increase of the natural frequencies is not such that the frequencies of the deformed and undeformed configuration coincides, it can be concluded that in this case allowing the stiffeners to be oriented has a certain benefit on the tailorability of the structural response. It should not surprise that the optimization has synthesized moderately curved stiffeners, indeed this behavior was also observed in [64], for the NASA Common Research Model (CRM).

The first three mode shapes are depicted in Figures 5.25 5.26 and 5.27. Particularly, it is seen that the third mode is a lag-torsion coupled mode. This type of behavior was also observed by Cestino *et al.* [64] for the wing-box they analyzed.



Fig. 5.24 Nonlinear static deformation for the optimized wing box with two control points ($\vartheta_1 = 0^\circ$, $\vartheta_2 = 10^\circ$).

5.6.2 Optimization with three control points

The second case study considers the same benchmark model, in this case however there are three control points placed at $x=0$, $x=256$ mm and $x=522$ mm. Also in this case the algorithm converges within few iterations to an optimum solutions having the value of the fitness function $f(\vartheta_1, \vartheta_2) =$. The orientations at the control points are given as follows: $\vartheta_1 = -2.5, x = 0$, $\vartheta_2 = 5, x = 0.5b$ and $\vartheta_3 = 12.5, x = b$.

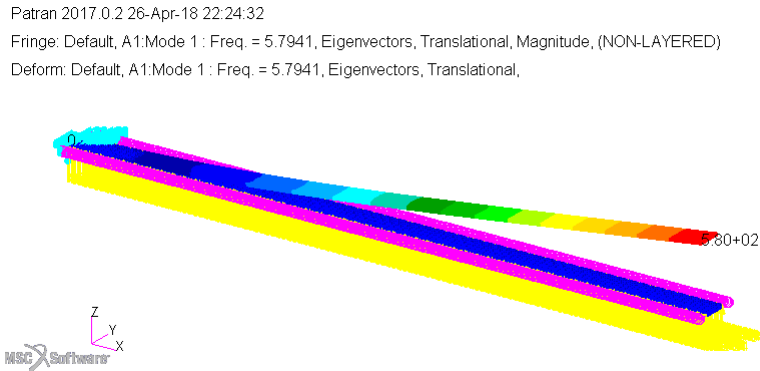


Fig. 5.25 First nonlinear mode shape of the optimized wing box with two control points ($\vartheta_1 = 0^\circ$, $\vartheta_2 = 10^\circ$).

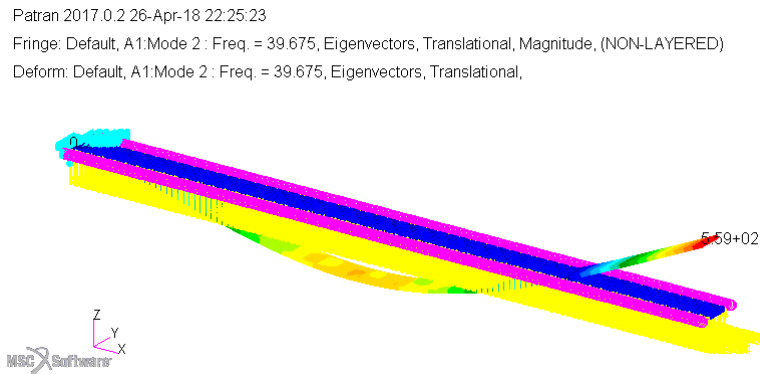


Fig. 5.26 Second nonlinear mode shape of the wing box with two control points ($\vartheta_1 = 0^\circ$, $\vartheta_2 = 10^\circ$).

Despite some differences, the two solutions are found in good agreement. The nonlinear static deformation of the optimized solution, for the case of three control points is depicted in Figure 5.28. The linear and nonlinear natural frequencies of the optimized wing.box are reported in Table 5.16. The nonlinear mode shapes are illustrated in Figures 5.29,5.30 and 5.31. Also in this case a lag-torsion coupling is observed.

In this case, the natural frequencies of the deformed configuration are higher than that of the benchmark model highlighting the beneficial effect of the dynamic tailoring. Comparing the results reported in Table 5.16 with that given in Table 5.15 it follows that the results obtained with three control points outperforms that of the case of the control points. This result could have been somehow predicted, indeed

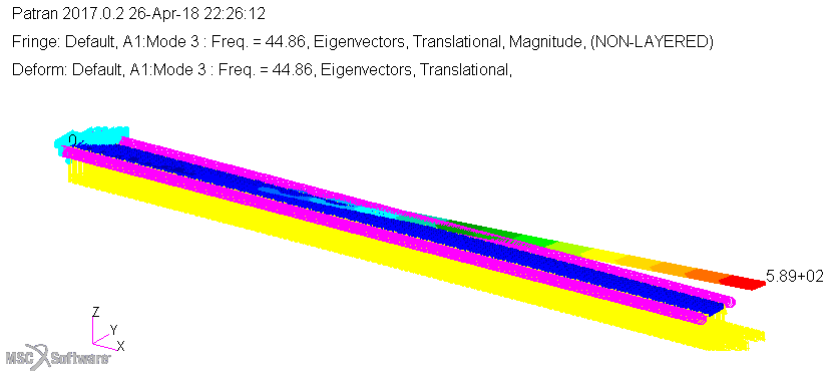


Fig. 5.27 Third nonlinear mode shape of the wing box with two control points ($\vartheta_1 = 0^\circ$, $\vartheta_2 = 10^\circ$).

Table 5.16 Linear and nonlinear frequencies [Hz] of the optimized wing box ($\vartheta_1 = -2.5^\circ$, $\vartheta_2 = 5^\circ$, $\vartheta_3 = 12.5^\circ$).

#f	Linear	Nonlinear	
		FEA	ROM
1	7.67	5.81	5.84
2	47.55	39.86	39.91
3	48.16	44.92	44.94
4	126.59	114.31	114.56
5	130.61	121.82	123.6

increasing the number of control points increase the cardinality of the problem and hence results in a wider search space. Also in this case, the frequencies determined with the reduced order model using as basis functions two modes for the flatwise and edgewise displacement, and one for the torsional displacement, leads to a good approximation of the frequencies determined via FEA. The discrepancy increase with the increase of the frequencies highlighting the need for an increased number of basis functions.

It is worth noting that the optimum values of the objective functions are close to each other and hence, the solution obtained with three control points can be considered as a near optimal solution. It is important point out also that the solution obtained with three control points it could have been found also with two control points. Indeed, being the variation of the stiffeners orientations linear in the independent variables x (see eqn.), and being the total variation of the orientation

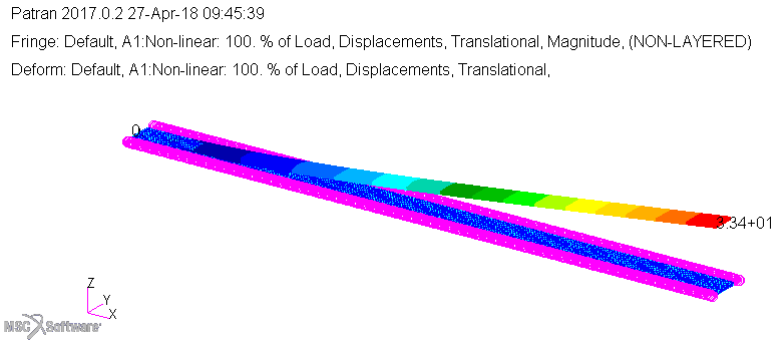


Fig. 5.28 Nonlinear static deformation for the optimized wing box with three control points ($\vartheta_1 = -2.5^\circ$, $\vartheta_2 = 5^\circ$, $\vartheta_3 = 12.5^\circ$).

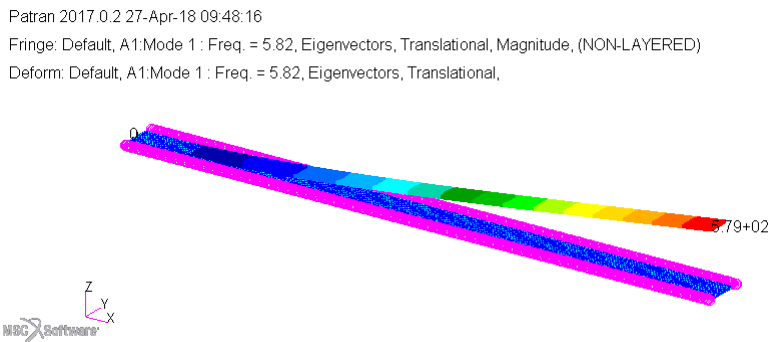


Fig. 5.29 First nonlinear mode shape of the optimized wing box with three control points ($\vartheta_1 = -2.5^\circ$, $\vartheta_2 = 5^\circ$, $\vartheta_3 = 12.5^\circ$).

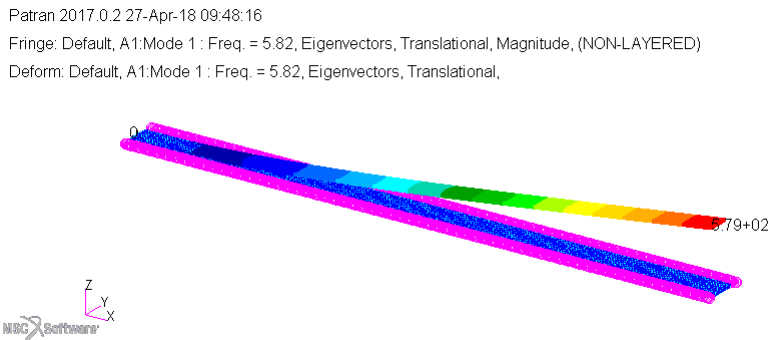


Fig. 5.30 Second nonlinear mode shape of the wing box with three control points ($\vartheta_1 = -2.5^\circ$, $\vartheta_2 = 5^\circ$, $\vartheta_3 = 12.5^\circ$).

in the case of three control points equal to 15° , follows that $\Delta\vartheta/2 = 7.5$ and hence

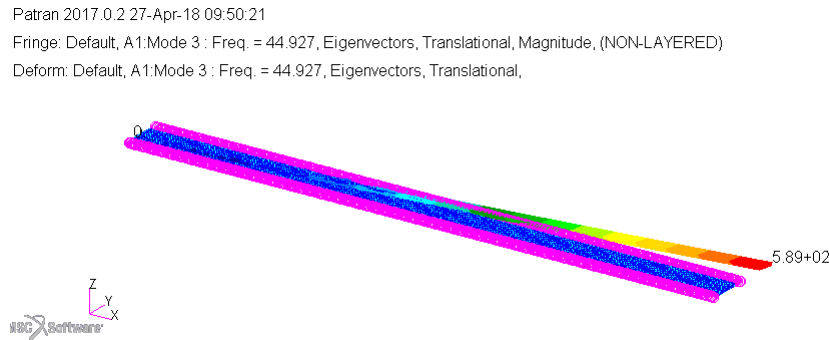


Fig. 5.31 Third nonlinear mode shape of the wing box with three control points ($\vartheta_1 = -2.5^\circ$, $\vartheta_2 = 5^\circ$, $\vartheta_3 = 12.5^\circ$).

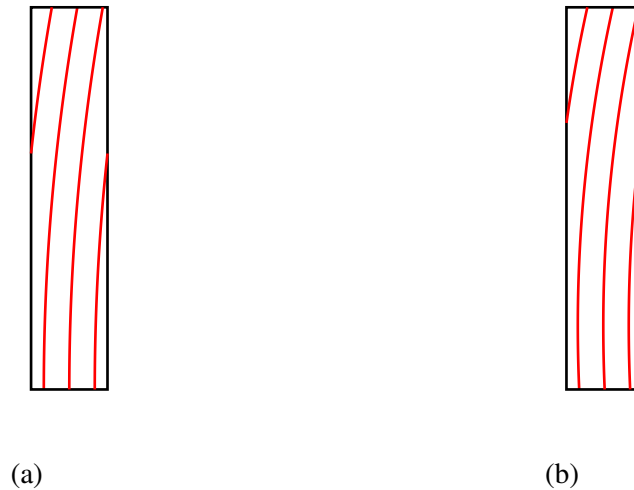


Fig. 5.32 Exemplification of the stiffeners geometries synthesized with (a) 2 and (b) 3 control points.

$\vartheta(x = L/2) = 5$, which in turn is equal to the value of ϑ_2 identified by the algorithm for the case of three control points.

It is also possible, despite only two case of optimization are performed, identify some trends. The results confirm what has been observed by Jutte and Stanford [55] for the Common Research Model of future transport aircraft. Indeed, moderately curved stiffeners are necessary to tailor the structural response and indeed are preferred by the optimization with respect to the straight ones. Moreover, as noted by Jutte and Stanford [55] it is seen that the optimum solutions has the stiffeners which led towards the leading edge of the wing. However, contrary to [34], it is

noted herein that at the wing tip the stiffeners are oriented in the direction of the trailing edge of the wing. As discussed by Stanford, having the stiffeners that lead toward the leading edge is advantageous for postponing the occurrence of the flutter. Flutter is not considered in this preliminary analysis. Aiming at minimizing the set space between the linear and nonlinear frequencies, and being the latter influenced by the amount of the nonlinear static deflection, the algorithm tries implicitly to reduce the static deformations. As a consequence, the point in which the maximum flap stiffness is located is shifted forward with respect to the root. The reason for not having the stiffeners parallel and oriented at zero, which would have guaranteed the maximum flap rigidity, is due to the coupling that arises when nonlinear geometrical deformations arise.

From Figure 5.33 to 5.36 are reported respectively the beam stiffnesses GJ_t , K , EI_2 , EI_3 with respect to the non-dimensional abscissa \hat{x} for the optimized solutions with two and three control points. The beam stiffnesses have been normalized with respect to their maximum value. As can be seen from Figure 5.33- 5.36, for the two optimized configurations all the stiffness components match closely all over the span, indeed only few percentage variation is seen between the stiffness obtained with the two control points and that with three control points model. It can be noted that for the two optimized solutions the edgewise stiffness EI_2 decreases span-wise, meaning that when the beam undergoes nonlinear deformations, not necessarily increasing the edgewise rigidity can lead to a decrease of the static deflection and hence to an increased set space among the linear and nonlinear frequencies. The increase or decrease of the nonlinear static deformations is instead a combination of all the stiffness component, as expected. Qualitatively the same conclusions drawn in Section 5.4 can be drawn herein. Indeed it is worth noting that the optimization yields higher values of the coupling and torsional stiffnesses at the beam's tip. Moreover, also in this case the increase of the coupling term K is remarkably higher compared against that of the torsional stiffness GJ_t .

5.7 Conclusions

In this chapter it has been introduced a revised version of the Stud GA with the aim of improving the algorithm efficiency without penalizing its reliability. The tuning parameters of the algorithm, originally introduced herein, have been identified and

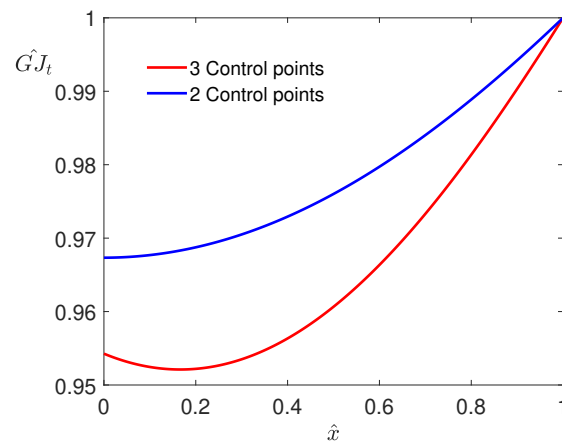


Fig. 5.33 Comparison of the torsional stiffness distribution with respect to the normalized abscissa for the case of 2 and 3 control points.

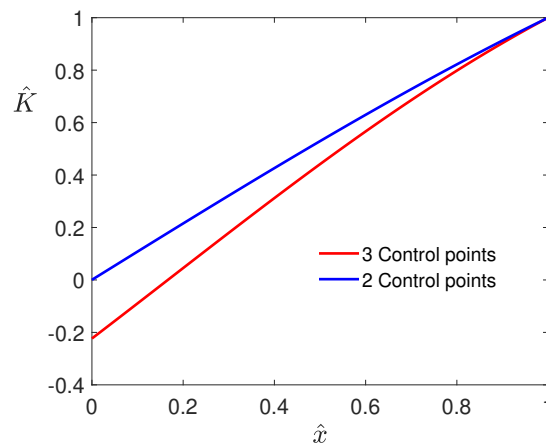


Fig. 5.34 Comparison of the coupling stiffness distribution with respect to the normalized abscissa for the case of 2 and 3 control points.

discussed. It has been shown that, contrary to what was known, a higher extinction rate can lower the performance of the algorithm. The algorithm has been tested considering benchmark constrained combinatorial problems for composite layered structures. The performances of the algorithm have been compared against those of other algorithms available in the open literature. It has been demonstrated that the Stud^P GA outperform the other heuristic methods for all the cases considered.

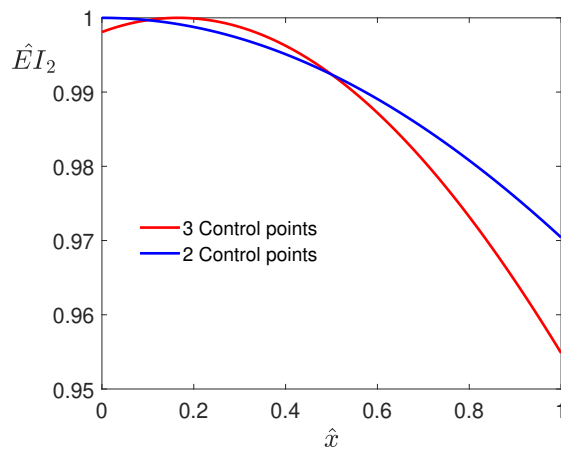


Fig. 5.35 Comparison of the edge-wise stiffness distribution with respect to the normalized abscissa for the case of 2 and 3 control points.

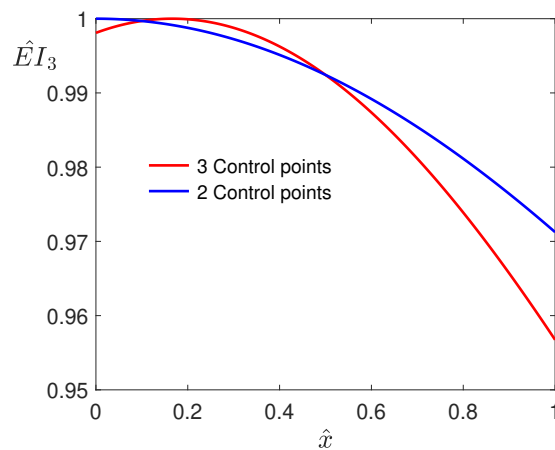


Fig. 5.36 Comparison of the flat-wise stiffness distribution with respect to the normalized abscissa for the case of 2 and 3 control points.

Particularly, with respect to other three GAs, the algorithm presented herein is also more reliable (99% against 80% of the SGA, PMX, GR).

The optimization algorithm has been then used to optimize two thin-walled box beams with curvilinear stiffeners. The topology optimization problem has been rewritten as a constrained combinatorial problem, where the design variables were the orientation of the stiffeners in a set of control points, assigned *a priori*.

In the first case, the optimization aims at attaining a desirable static performance, i.e. maximizing the bending-torsion coupling while ensuring a minimum tip deflection. Three different load cases were considered. For the case of tip concentrated load, the results obtained are found in agreement with that available in the open literature. It has been shown that a trade-off between torsional and coupling stiffness is necessary to ensure a desired coupled behavior.

In the last optimization problem addressed, the objective of the optimization was to reduce the set space among the linear and nonlinear frequencies. Particularly, the first five frequencies have been considered herein. The optimization has been carried out considering two and three control points. A population of 20 individuals has been used, with probability of mutation of 0.1 and probability of crossover of 1. Preliminary results obtained shows that the set space between the nonlinear frequencies can be effectively broaden through the use of moderately curved stiffeners. It can be concluded that the introduction of curvilinear stiffeners, and more in general variable stiffness properties, open up a variety of possible solutions to tailor the static and dynamic structural responses, as already highlighted in [34, 165, 166]. The results of the optimization obtained via FEA are compared against those obtained with the reduced order model presented in chapter 3. It has been noted that, for the wing-box under study, the approximation with 2 flatwise modes, 2 edgewise modes and one torsional mode yield to a good approximation of the first three frequencies. The discrepancy with respect to the frequencies determined through FEA increases if one considers higher frequencies highlighting the need to increase the number of basis functions. It has been hence shown that reduced order beam model can faithfully represent the behavior of complex structure, contrary to what stated in [36].

Chapter 6

Topology synthesis of planar ground structures

Some of the contents pertaining the optimization of Ground Structures have been previously published in

Danzi, F., Gibert, J. M., Cestino, E. and Frulla, G. "*Topology Synthesis of Planar Ground Structures for Energy Harvesting Applications*". Proc. of SPIE Smart Structures+Nondestructive Evaluation and Health Monitoring (SS/NDE), Portland, Oregon (USA), 25-29 March 2017 <https://doi.org/10.1117/12.2257351>

Danzi, F., Gibert, J. M., Frulla, G. and Cestino, E. "*Graph-based element removal method for topology synthesis of beam based ground structures*". STRUCTURAL AND MULTIDISCIPLINARY OPTIMIZATION. Volume 57, Issue 4, pp. 1809–1813, ISSN 1615-1488, <https://doi.org/10.1007/s00158-017-1818-x>

6.1 Introduction and motivation

In this chapter we formulate and solve the optimization of a planar Ground Structure (GS) aiming at identify solutions that exhibit commensurate frequencies. Having noted that the vast majority of Homogenization Design Method (HDM) leads to truss-like structures, in the following, we parameterize the design domain using the Ground Structure method. In order to synthesize meaningful, i.e. manufacturable, structure we conceived a double filtering scheme described below.

The Graph-based Element Removal Method (GERM) presented herein has been also applied for the topology synthesis of compliant mechanisms. However, the results pertaining the optimization of compliant mechanisms have not been included in this chapter and are summarized in Appendix D.

6.2 Topology optimization

According to Howell [167], structural optimization can be classified as follow: a) size optimization, b) shape optimization and c) topology optimization. Among the three categories, topology optimization offers the largest design space therefore is considered as the most general optimization problem. Numerical methods for topology optimization can be roughly classified as: a) Homogenization Design Method (HDM) and b) Ground Structure Method.

HDM is a truly continuum-based optimization where the design domain can be seen as a micro structural arrangement of voids and material. HDM has been applied to a broad range of problems including, but not limited to, compliant mechanism design problems [168, 169], multiple constraints problems [170] and optimal design of vibration based energy harvesters [171–174].

On the other hand, topological optimization of truss or ground structures is generally limited to the optimization of size variables, i.e. cross sections or beams' length. Much less effort have be done to truly topological variables, such as, the pattern of connection of members. Despite the most general form of a discrete structure can be described also by configuration variables which, for truss structures, are the nodal coordinates, we chose to keep the nodal coordinates fixed. Owing the complexity of simultaneous optimization of geometry, topology and cross-section, this is a common choice in structural layout optimization. The ground structure method has been historically used for the design of bridges and civil structures [175–177] and recently adopted for the synthesis of compliant mechanisms [178].

Topological and geometrical variables define the structural layout. It is well recognized that the structural layout can greatly affect the mechanical behavior of the structure. In general in fact, potential savings affected by shape optimization are more significant than those given by a fixed-shape structure. Indeed, mathematically, fixing *a priori* the structural shape means limiting the research area on a subset V_C

of the possible solutions V , $V_C \subset V$. Moreover, in most of the cases, some further constraint additionally limit the design space. For example, in the specific case of the optimization of the dynamic response, the frequency's bandwidth is generally defined *a priori* [79, 179]. It is worth noting that mathematically this further constraint limits the design subset to V_D , where $V_D \subset V_C \subset V$.

It is in view of the above mentioned restrictions, we chose to state the optimization problem in its non-dimensional form to maintain as large as possible the design set and use highly connected ground structures to seek for innovative configurations. Particularly, the GS allows to have members that are generally oriented rather than be adjoined at 0° or 90° . This will be shown to be crucial to identify novel solutions to the problem in hand.

6.3 Ground structure

The ground structure (GS) method was first proposed by Dorn to solve the Michell problem [180]. It provides an efficient means to identify near-optimal solutions for topologies of trusses, and later was extended to compliant mechanisms,[178]. The ground structure can be defined as a highly connected truss/beam structure which presents a fixed number of nodes in a given domain $\Omega \in \mathbb{R}^n$; this work is restricted to planar ground structures, i.e. $n = 2$. An example of the GS used in this chapter is depicted in Figure 6.1. Arguably the major drawback of the GS method is that it can lead to complex designs that can be difficult to realize physically.

The classic ground structure approach consists of letting the members' cross sections vary between the upper and lower bound and then removing members which have the cross section equal or closer to the lower bound, simplifying the complexity of the optimized topology. The complexity in the design and manufacturability arises from the high number of members in the synthesized topology. Moreover, in structural optimization problems there may be multiple optimal solutions. Sved and Ginos [181], noted that one must search all perfect structures obtained omitting members is necessary to ensure that a global minimum is reached. Researchers ([182–185, 177, 186, 187]) have proposed different methods to handle design complexity during the optimization or in post-processing. To the author's knowledge, the first conceiving a graph parameterization for a ground structure were Giger and Ermanni [188], subsequently adopted also by Sauter [189–191]. Instead of classic genotype

for evolutionary optimization, they defined a graph-based genotype, where each gene in the parametrization have the following information:

1. A unique identifier that is assigned to each node.
2. Nodal coordinates that is stored with the identifier.
3. A boolean parameter that is used to determine whether the node can be moved during the optimization process or not.
4. Two unique identifiers that are assigned to a members' nodes.
5. The cross-sectional area of each node is stored, since they considered variable thickness beams.

In this work, we adopt a similar graph based parametrization of the design domain.

6.3.1 Parameterization of the design domain

Aiming at identify solution that exhibit commensurable bending frequencies, we parameterize our design domain Ω using beam-based GS. However, the latter choice is not self-explanatory because GS can have different parameterization, and different level of connectivity, therefore some assumptions have to be made to define uniquely the cardinality of the problem. The parameterization we chose is based on the following assumptions

1. The line segments of connecting nodes must be contained in the design domain Ω , i.e. Ω is a convex set.
2. Beams may intersect but they cannot repeat in the parameterization.
3. Only beams with the shortest connection between nodes are admissible in the parameterization.
4. A beams' intersections does not generate additional nodes; that is, beams that cross are able to slide past each other.

With reference to Figure 6.1b, assumption 3 implies that node 1, 5 and 9 are connected by two members, i.e. the beam from node 1 to 5 and the beam from node 5 to

9. Beams 5-1 and 9-5 do not exist because of assumption 2. According to the assumptions listed above, a ground structure with $M \times N$ nodes has the following number of beams

$$n_{beams} = \binom{MN}{2} - \left[M \sum_{i=3}^N (i-2) + N \sum_{j=3}^M (j-2) + 2 \sum_{k=2}^Q (N-k)(M-k) \right] \quad (6.1)$$

where $Q = \min(N-1, M-1)$, $\binom{MN}{2}$ is the number of beam of the full connected graph, i.e. the one obtained neglecting all the assumptions 1 to 3. Equation 6.1 defines the cardinality of the problem that one would have considering the full connected GS, i.e the one with all the members retained in the design.

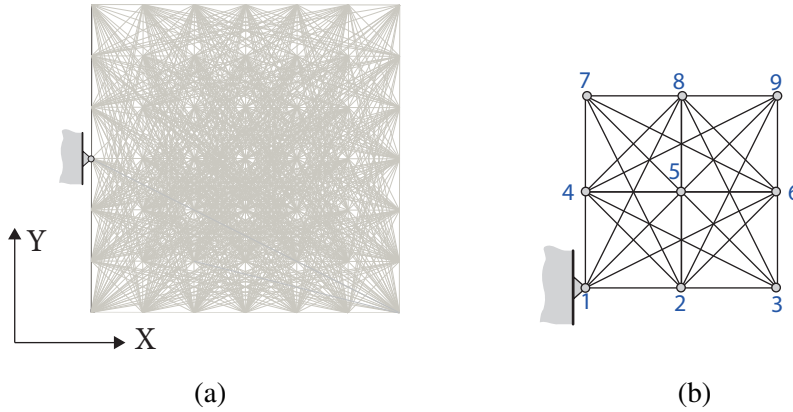


Fig. 6.1 Example of a Ground Structure with 7×7 nodes and 856 members, clamped in the center node along the Y side (Figure 6.1a), and a 3×3 GS clamped in node 1 (Figure 6.1b).

6.4 Graph Based Element Removal Method

The Graph-based Element Removal Method (GERM) is based on the observation that regardless of the level of connectivity specified in a GS parameterization, the GS is an undirected graph, $G(V, E)$, where $V = \{v_1, v_2, \dots, v_n\}$ with $|V| = n$ is a set of vertexes (nodes) connected by a set of edges (members) $E = \{e_1, e_2, \dots, e_m\}$ with $|E| = m < n$ and where $|\cdot|$ defines the cardinality of the set ([192]). The GERM algorithm is a double filtering scheme consisting of

1. *threshold limit removal*, i.e., removing members whose cross sectional areas are under a lower bound;

2. *graph based search and cut*, i.e., removing any elements that is not reachable from a specified root node(s).

Particularly, the need of having a double filtering scheme will be highlighted subsequently. The cross sectional dimensions, for each of the member in the parameterization, are given according to the following equation

$$x_i = x_l + \frac{x_u - x_l}{2^s} k \quad (6.2)$$

being k the cross sectional parameter and x_u, x_l the upper and lower limits for the cross sectional dimensions. The cross sectional parameter k is an integer, $0 \leq k \leq 2^s - 1$, represented using a binary encoding and s is the size of the binary vector. The limits x_u and x_l are adaptive and may either increase or decrease during the optimization according to the previously identified optimum topology. The original connectivity matrix is frozen once the $M \times N$ GS is selected. This allow us to define uniquely the cardinality of the genotype, according to equation 6.1.

Contrary to Giger and Ermanni and related works [188–191], the genotype we defined has only one data per gene, i.e. the cross sectional parameter k . It follows that the dimension of the genotype coincides with the cardinality of the GS (n_{beams}) according to equation 6.1. The reason for having a condensed genotype, in terms of information retained for each member, with respect to the one used by Giger and Ermanni [188], arises from the way we tackled the topology optimization and deserves some discussion.

First and foremost, we chose to fix the nodal position at the beginning of the optimization, this allows us to define uniquely the node positions and the elements length. Moreover, having chosen to have a genotype with a cardinality equals to the number of beams in the parameterization, the label of the "active" members is uniquely identified since coincides with the position of the gene in the genotype. Herein, with "active" members we mean those members that pass the two filtering schemes. Finally, since the GS is also fixed at the beginning of the optimization, also the original connectivity matrix is fixed and therefore we don't need to store the node's identifier for each beam. Indeed, the node identifier are the elements of the original connectivity matrix contained at the $i - th$ column, being i the number of that particular beam into the parameterization (or equivalently the edges of the graph or the position of the gene in the genotype). In other words, all the information are

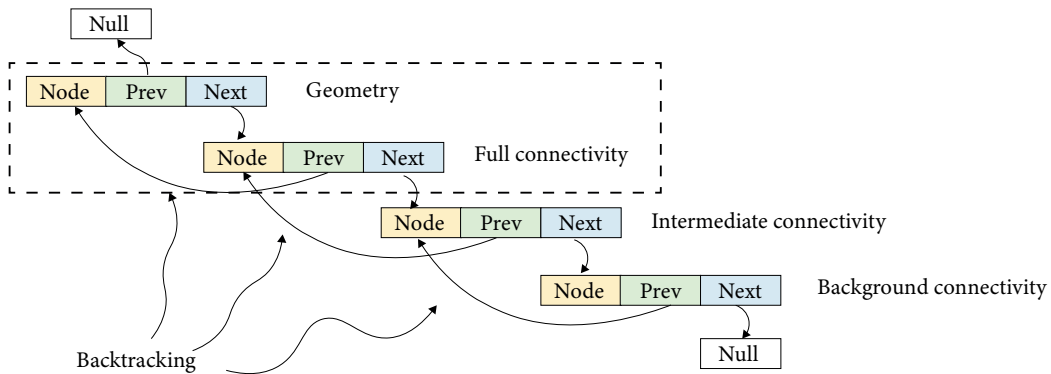


Fig. 6.2 Exemplification of the doubly linked list implemented in the optimization algorithm to recover all the information need to construct the Finite Element Model. All the data enclosed between the dashed line are frozen within the optimization and are only used to reconstruct the geometry of the synthesized structure.

retained considering the graph as a set of doubly linked lists. An exemplification of the data storage strategy is depicted in Figure 6.2. It is worth mention that Figure 6.2 uses the classic definition of a doubly linked list used in computer science. In this sense node stands for a data pointer which points from one list ("PREV") to another ("NEXT").

The effect of the application of GERM onto a 3×3 GS is instead illustrated in Figure 6.3. The concatenated lists, hereafter referred to as intermediate and background connectivity, will be described concurrently with the two filtering schemes.

6.4.1 Threshold Limit Removal

The first filtering scheme removes all the members that have the width (or equivalently height)¹ lower than a threshold limit, τ . This task is usually performed *a posteriori* on the optimized structure; conversely, in our Element Removal Method (ERM), as in [188–191], it is performed within the optimization by defining the threshold limit for the cross sections. Similar to [177], members with a cross section, x_i^2 , under the threshold limit are removed from the structure. The threshold limit is an input of the ERM and is given as fraction of the maximum cross sectional width (height). Being the latter updated at each iteration, or at least whenever a new

¹In our case we considered square cross sections

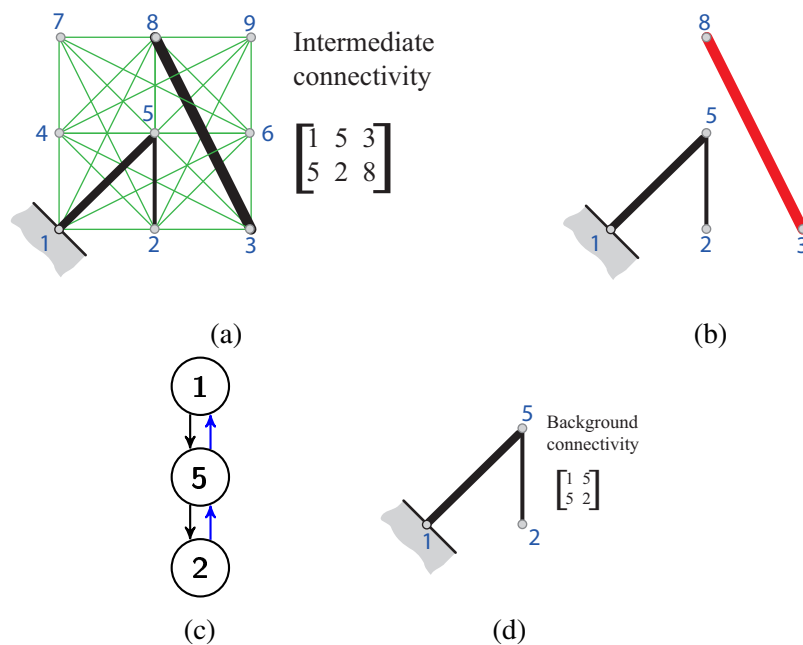


Fig. 6.3 Effect of GERM on the ground structure: **(6.3a)** shows a generic solution after one iteration of optimization, all the members in green are under the threshold limit ($|V| = 9$, $|E| = 28$); **(6.3b)** the first filtering scheme, the member in red is the resulting bouncing structure ($|V_1| = 5$, $|E_1| = 3$); **(6.3c)** DFS performed on the filtered topology starting from the constrained node to seek for bouncing (unconnected) structures; and **(6.3d)** optimized topology, ($|V_2| = 3$, $|E_2| = 2$).

optimum solution is identified, it follows that the ERM is adaptive and the threshold limit varies during the optimization. The TLR (Threshold Limit Removal) can be written as

$$TLR(\mathbf{x}, \tau, i) = \begin{cases} 1 & \text{if } \frac{x_i}{\max(\mathbf{x}^j)} < \tau, \quad 0 < \tau < 1, \\ 0 & \text{otherwise.} \end{cases} \quad (6.3)$$

where $\max(\mathbf{x}^j)$ is the thickness of the j -th member of the structure (genotype). It is worth noting that the TLR does not operate directly onto the genotype, but on an intermediate connectivity matrix IEN_{IM} , i.e. a revised connectivity which contains only those members with cross sectional dimension higher than the threshold limit. It is also worth mentioning that being the GERM coupled with a Genetic Algorithm (GA), i.e. with a population based algorithm, within the population there could be solutions with remarkably different thicknesses. This allows us to navigate the entire design domain avoiding to be stuck in a particular area. In other words, through the definition of TLR we enhance the exploration capability of the algorithm maintaining a certain level of diversity of the population.

The initial removal of elements after each iteration of the optimization requires an intermediate connectivity matrix, henceforth referred to as IEN_{IM} , which contains only the members with cross sectional dimensions higher than the threshold limit. The filtered structure will have new set of nodes (V_1) and members (E_1) so that $|V_1| \leq |V|$ and $|E_1| \leq |E|$, thus IEN_{IM} is $2 \times |E_1|$ matrix, for truss or beam based ground structures. The removal of elements leads to unconnected or floating structures within the design, as shown in Figure 6.4, that in turn leads to singular stiffness and mass matrices. Particularly, in Figure 6.4a we report the case of one bouncing structure laying between node 6 and 8 while, in Figure 6.4b is illustrated the case of two bouncing structures resulting after one iteration in the optimization. In order to eliminate the bouncing structure from the topology and hence eliminate any source of singularity within the code, we conceived the second filtering scheme.

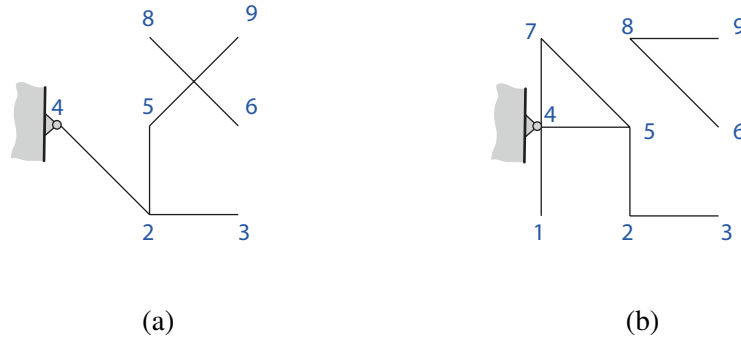


Fig. 6.4 Examples of resonators synthesized to have 1:2 frequency ratio. Structures (a) and (b) were synthesized from 3x3 ground structure (GS). It is important notice that structure (a) has one bouncing member, i.e. the beam between nodes 6 and 8. Structures (b) has two bouncing members, that is beams enclosed between nodes 6-8 and 8-9 respectively.

6.4.2 Graph Based Search and Cut

The second filtering scheme begins with a graph search. A depth first search (DFS)² is performed to identify and eliminate the floating structures from a given design. The DFS is performed on the adjacency matrix \mathbf{A} of the GS (or equivalently of the graph G). The adjacency matrix, $\mathbf{A}(G)$ is a $|V_1| \times |V_1|$ matrix whose elements are defined as

$$a_{i,j} = \begin{cases} 1 & \text{if } i, j \in E_1, \\ 0 & \text{otherwise.} \end{cases} \quad (6.4)$$

The adjacency matrix is updated at each iteration using the intermediate connectivity, and is based on the topology after the first filtering. The DFS starts with a discovery phase from the root node/vertex and explores, as far as possible, along each branch before "backtracking". The root node in our case is the node where the structure is clamped. The DFS can output several arrays depending on the implementation. In the GERM, the relevant array is a vector \mathbf{d} ($1 \times |V_1|$ vector); its elements contain either the discrete time of a node's discovery or -1 if the node cannot be reached from the target node and is identified as a vertex of a floating structure. The result of the second filter is a second set of nodes (V_2) and members (E_2). The cardinality of the new

²GERM could also be implemented with a breath first search (BFS) since the algorithm only requires identifying reachable nodes based on our vertex/root node. Algorithms for both the DFS and BFS are found in [193].

sets satisfies $|V_2| \leq |V_1|$ and $|E_2| \leq |E_1|$. This leads to a $2 \times |E_2|$ matrix background connectivity matrix, IEN_{BG} . It should be noted that the graph-representation of the GS allows the following:

- permits to identify all the unconnected members, i.e. members that have been removed after the TRL and/or bouncing structure, and
- allows to handle the intermediate and background connectivity matrix as a adjacency matrix.

```

Input:  $\tau$ ,  $IEN_{Full}$ (original connectivity),  $\mathbf{x}^0$ , target.node(s)
1 Initialization:  $remove = []$ ,  $IEN_{IM} = []$ 
   /* Threshold Limit Removal */
2 for  $i:=1$  to All members do
3   | if  $x(i) \leq \tau_{x_{max}}$  then
4   |   | Add:  $i$  to  $remove$ 
5   | end
6 end
7  $IEN_{IM} = IEN_{Full}(\sim remove)$ 
   /* Graph Based Search and Cut */
   /* Write adjacency matrix,  $A$  */
8  $A=0$ 
9 for  $i:=1$  to All nodes do
10  | if  $i == any(IEN_{IM}(1,:))$  then
11  |   | Assign:  $CurrentNode = i$ 
12  |   | Assign:  $NearNode = IEN_{IM}(2,i)$ 
13  |   | Construct:  $A(NearNode, CurrentNode)=1$ ,
14  |   |  $A(CurrentNode, NearNode)=1$ 
15  | end
16 end
17  $IEN_{IM} = IEN_{Full}(\sim remove)$ 
18 Perform DFS on  $A$ ,  $d = DFS(A, target)$ 
19 Remove bouncing members  $d$  from  $IEN_{IM}$ 
Output:  $IEN_{BG}$ 

```

GERM: pseudocode

In the interest of clarity, we report the pseudo-code of the GERM algorithm. Figure 6.3 presents a pictorial overview of one iteration in the algorithm. Figure 6.3a shows a solution after one iteration of optimization, members in the lower bound are in green and the root node is node 1. After the threshold limit removal, Figure

6.3b, there is a floating structure, i.e. the members between node 3 and 8. The DFS searches along all reachable nodes from the root node (Figure 6.3c) and returns the structure in Figure 6.3d. All the intermediate operations are performed on the intermediate connectivity during the first filtering scheme and onto the background connectivity during the graph search and cut. Finally the finite element matrices are constructed based on the background connectivity. All the other necessary data to construct the finite element matrices, such as nodes' position and elements' length, are recovered backtracking from the genotype.

It is important to point out that one of the main difficulties in topology optimization of trusses and frames is that the globally optimal solution cannot be obtained if unnecessary members are completely removed from the ground structure, indeed some members may be reused after removal at intermediate steps. In the developed method the members are removed from the real structure that is represented using the background connectivity. This allows us to perform the FEA with only the active numbers within a particular design. In addition, it improves the computational efficiency. In fact, the linear system to solve has a cardinality of $3V_2 \times 3V_2$. However, all the genetic operators, i.e. cross over and mutation, are applied to the original ground structure that contains all the members and related data (nodes location, cross sectional dimensions, lengths and so on). This allows the reuse of elements in the successive generation.

6.5 Case Study: Optimization of planar resonators

Many MEMS based resonators, exploit the nonlinear phenomena known as internal resonances³. One condition necessary for an internal resonance is for the system to have modal frequencies as a ratio, e.g., 1:2 or 1:3. The topology of the resonator is one dominant factor in determining whether a given modal ratio can occur. A common geometric configuration of resonators exhibiting this integer ratio of modal frequencies are L-shaped structures. L-shaped resonators have been of interest to the dynamics community for several decades [88–91].

³Internal resonance in a system exist when there are strong nonlinear interactions resulting in an energy exchange between different modes of vibration when the system is excited.

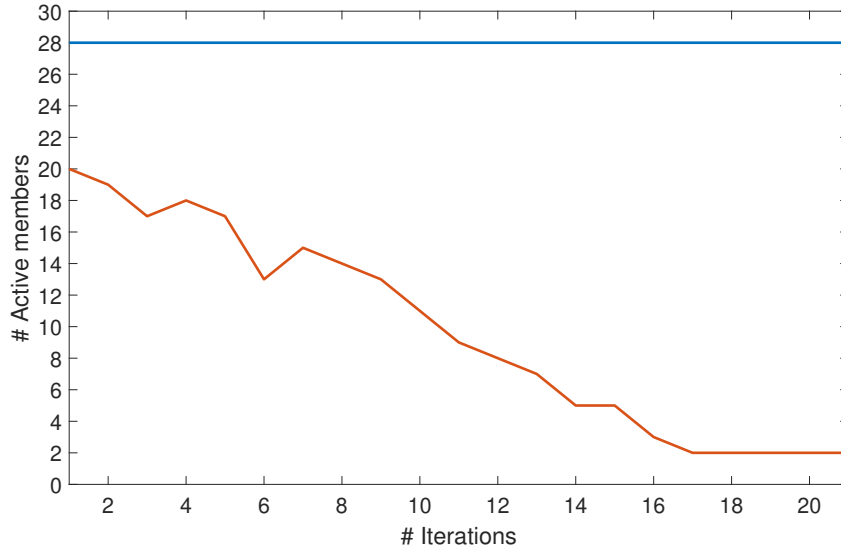


Fig. 6.5 Number of active members of the optimum solution during the optimization. It can be noted that the number of members does not decrease monotonically therefore the algorithm allows the reuse of element previously removed.

Previous efforts in synthesizing these resonators were restricted to consider members orthogonal to each other, [79]. In determining the topology of resonators we pose the problem as minimization problem using an augmented objective function, [194], with only one equality constraint. The optimization problem is hence formulated as follow

$$\min_{x^i} : \left\{ \underbrace{n_b \left[\sum_{j=1}^{j-1} \left(\eta - \frac{\omega_j}{\omega_1} \right)^2 + \frac{1}{\bar{\epsilon}_{xx} \epsilon_{xx}} \right]}_{\text{objective}} \right\} + \underbrace{w_\gamma \left(\gamma - \frac{V^*}{V_g} \right)^2}_{\text{adjoint constraint}}, \quad (6.5)$$

$$\text{subject to: } [-\omega^2 \mathbf{M} + \mathbf{K}] \mathbf{u} = \vec{0}.$$

where x_i are the sections width/height (design variables, square sections are considered), $j-1$ is the number of commensurate frequencies sought, $j = 2$ if one commensurate frequency is sought or $j = 2, 3$ if two commensurate frequencies are sought, n_b is the number of beams in the structure, η is the targeted frequencies ratio, ω are the bending frequencies, ϵ_{xx} and $\bar{\epsilon}_{xx}$ are respectively the maximum and the average bending strain in the GS, γ is the targeted volume ratio, w_γ is the weight for the volume constraint. The term V^*/V_g , is the ratio between the actual volume

V^* and the volume of the guess structure V_g , finally γ is the targeted volume ratio. \mathbf{M} and \mathbf{K} are the global mass and stiffness matrices, ω is the modal frequency, \mathbf{u} is the eigenvector containing the modal displacements at a node. Since square cross sections are considered, the area moment of inertia are evaluated as $1/12x_i^4$.

The GERM algorithm is implemented in Matlab. It operates on a fully connected GS whose members are Euler-Bernoulli beams⁴, with square cross sections and 3-degrees of freedom per node. The stiffness and mass matrices of the element used are written in the non-dimensional form and their representation is given in the subsequent section. The optimization is performed using an in-house genetic algorithm (GA). The cross sections width (design variables) are represented by binary encoding; we use populations of 20 chromosomes, fitness proportionate selection, single cross over and probability of mutation of 10%.

The GERM algorithm is applied after each iteration of the GA to evaluate the specified objective function. Since GERM retains the original connectivity of the structure, in the next iteration the non zeros design variables are applied to the parent whose elements have not been removed. All the genetic operators are applied to the original connectivity, the reason is twofold: (1) in this way there is no need to handle the changes of active members within the particular solutions therefore the chromosomes maintain the same dimension, (2) members with lower-bound value of variable that were removed may reappear by mutation to a larger value or crossover with another solution with larger value. The initial population is chosen at random while the dimension of the ground structure, i.e. the number of nodes M and N is given as input.

Figure 6.6, reports solutions for resonators with two and three commensurate frequencies. The target node is designated as the fix node at the joint and is constrained in all 3-degrees of freedom. In Figure 6.6a the algorithm recovers an L -shaped beam as one solution, with $\omega_2/\omega_1 = 2$ using, 3×3 full GS. However, the solution depends on the initial GS as shown in Figure 6.6b. Perhaps the example that best illustrates the GERM algorithm's ability to filter a design is the 7×7 full GS and the resulting V -shaped beam in Figure 6.6c. The original GS has 856 members and GERM leads to a solution with 2 members. Figure 7.9b, shows the optimized topology of a resonator with 3 commensurable frequencies

⁴Beam elements were chosen to avoid the loss of global equilibrium found in GSs composed of trusses.

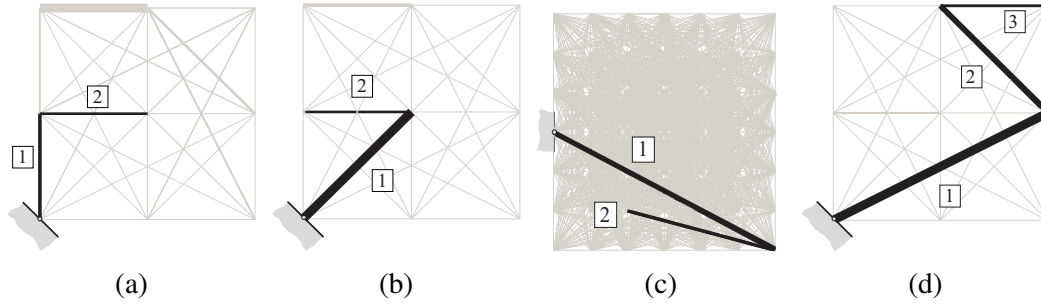


Fig. 6.6 Optimized topology for planar resonators: **(6.6a)** 3×3 full GS with $\omega_2/\omega_1 = 2$; **(6.6b)** 3×3 full GS with $\omega_2/\omega_1 = 2$; **(6.6c)** 7×7 full GS with $\omega_2/\omega_1 = 2$; and **(7.9b)** 3×3 full GS $\omega_2/\omega_1 = 2$ and $\omega_3/\omega_1 = 3$. All initial GS are generated at random. The optimized dimensions of the members of the optimized structure are: **(6.6a)** $h_2/h_1 = 0.70$, $L_2/L_1 = 1.0$; **(6.6b)** $h_2/h_1 = 0.24$, $L_2/L_1 = 0.71$; **(6.6c)** $h_2/h_1 = 0.68$, $L_2/L_1 = 0.61$; and **(7.9b)** $h_2/h_1 = 0.61$, $h_3/h_1 = 0.32$, $L_2/L_1 = 0.63$, $L_3/L_1 = 0.45$. The threshold limit is set to $\tau = 0.20$.

Figure 6.7 provides an expanded view of the results of solving Eqn. 6.5 by showing the optimal topology of a base excited structure with integer modal frequency ratios. The first column in Figure 6.7 shows target frequency ratios, the second columns presents the optimized topology, the final column show the first two/three mode shapes. Examining Figure 6.7 brings to the forefront several observations

1. In designing resonators where the first two modes occur at integer ratio of two, the algorithm recovers the L shaped structure, Figure 6.7 (a);
2. The L shaped design is not unique; a resonator that has its members in a 45° angle between each other also has a 1:2 ratio of the first two modal frequencies, Figure 6.7 (b). We will refer to resonators similar topologies as a V-shaped;
3. It is possible to design resonators that have multiple integer modal frequency ratios, Figure 6.7 (c), (d), and (e), are resonators with integer frequencies ratios of 1:2 between the first and second modal frequencies, and 1:3 between the first and third modal frequencies. Figure 6.7 (d) shows the optimal topology for a resonator with integer frequencies ratios of 1:2 between the first and second modal frequencies, and 1:4 between the first and third modal frequencies.
4. Only in certain cases does the algorithm consider orthogonal members in the optimal topology to achieve modal frequencies that have integer ratios;

5. Penalizing the number of members in the structure, has the result that total numbers of members in the resonator is equal to the number of commensurate frequencies.

Note that the present discussion does not consider the amplitude of the response at each modal frequency. However, it clearly shows the importance of the relative orientation of the structural members on the modal frequencies of the resonator. It is important note that other researchers have noted the importance of the angle of on the modal frequencies of the structures however, they have been limited to predicting natural frequencies of folding wings [195–197]. Furthermore, allowing the members to be attached at an arbitrary angle expands the possible design space for planar resonator. We will explore the nature of this design space and linear behavior of resonators that occupy this space in the next chapter.

6.6 Summary and conclusions

A novel ERM has been conceived to address the topology optimization of ground structures. The ERM proposed herein uses a double filtering scheme to simplify the topology of a truss-like structure getting rid of the unnecessary beams. Moreover, the double filtering scheme allows to build non-singular mass and stiffness matrices otherwise possible because of bouncing structures. The ERM has been shown to provide optimum topologies for both compliant mechanisms and resonators.

Specifically, in determining the optimum topology of resonators the discrete optimization problem has been formulated in its non-dimensional form to eliminate the constraints on the frequency bandwidth. Furthermore, an augmented objective function has been defined to formulate the problem in its unconstrained form gaining in terms of computational efficiency. The ERM coupled with a standard genetic algorithm has been proven to be effective to optimize the topology of ground structure which exhibit commensurate frequencies.

Previous efforts at designing these type of resonators have constrained the relative orientation of the members to be inline or perpendicular to each other. The topological optimization problem implies that the relative orientation of the member plays an important role in determining the frequency characteristics of the structure and that the number of commensurate frequencies is dependent on the number of

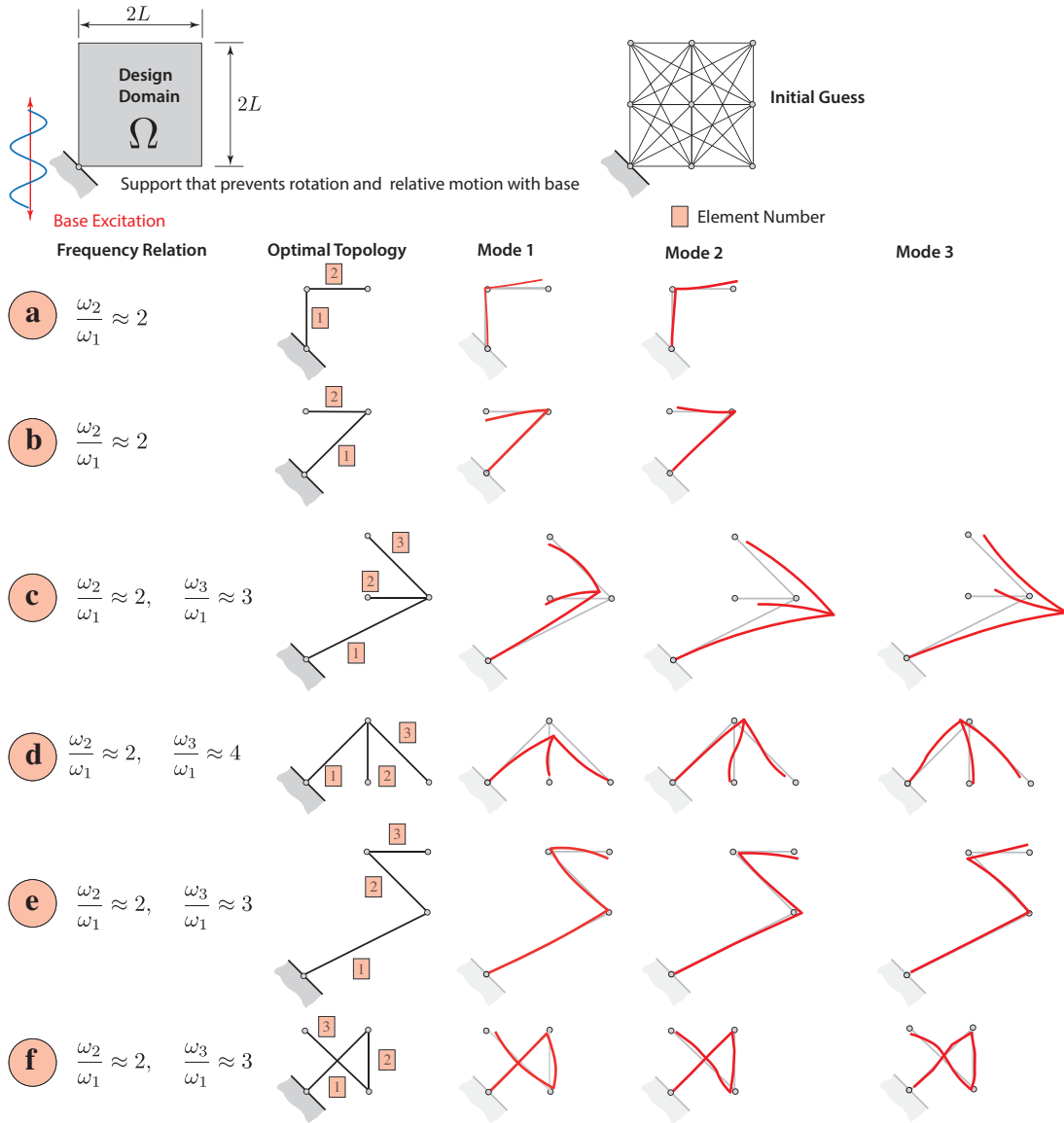


Fig. 6.7 Example of optimized topologies: a) and b) have one integer frequency ratios, $\omega_2/\omega_1 \approx 2$; c), d), f) have two integer frequency ratio, $\omega_2/\omega_1 \approx 2, \omega_3/\omega_1 \approx 3$. The resonator in d) has the two frequencies ratios such that $\omega_2/\omega_1 \approx 2, \omega_3/\omega_1 \approx 4$. The figure shows that the number of members is one less the number of integer frequencies ratio sought or equal to the number of the commensurable frequencies.

members in the structure. Examining the results obtained one may conclude the following:

1. A 2-DOF systems can be designed to have the first two frequencies that occur at an integer ratio based on the topology of the resonator.
2. In all the optimum topologies the fixed member is thicker than the secondary member.
3. The algorithm always finds N distinct elements of the structure corresponding to the integer frequency ratio.
4. The L-shaped beam is not the solely solution to have commensurate frequencies having 1:2 ratio. In fact, it is not the preferred orientation obtained by the optimization routine. The algorithm prefers angled orientation, or "V-shape" structure.

In conclusion, we observe that regardless of the type of elements dealt with, whether they are beams or rods of a ground structure, or shells of a 2D continuum, or even solid elements in a 3D structure, the connectivity matrix of finite elements can always be rewritten in terms of adjacency matrix of a graph. Therefore, the GERM has the potential to be applied to a wide range of topology synthesis problems with only minor changes with respect to the form presented herein.

Aiming at further investigate the dependency of the angle between the members and the correlation between the number of commensurate frequencies to the number of members of which the structure is composed, in the next chapter it is derived the analytical and the reduced order model for a multi-members structure.

Chapter 7

Analytical and semi-analytical model for multi-member structures

Part of the derivation presented in this chapter has been previously published in The Journal of Sound and Vibration and in the SPIE SS/NDE Conference Proceedings. The full citation is provided below

Danzi, F., Gibert, J. M., Frulla, G. and Cestino, E. "*Generalized topology for resonators having N commensurate harmonics*". JOURNAL OF SOUND AND VIBRATION. Volume 419, 2018, pp 585-603, ISSN 0022-460X, <https://doi.org/10.1016/j.jsv.2017.10.001>.

Danzi, F. and Gibert, J. M. "*Exact dynamics of an angle-shaped resonator for energy scavenging applications*". Proc. of SPIE Smart Structures and Materials + Nondestructive Evaluation and Health Monitoring, 2018, Denver, Colorado (USA), 5-8 March 2018, <https://doi.org/10.1117/12.2296642>.

Danzi, F., Gibert, J. M., Cestino, E. and Frulla, G. "*Topology Synthesis of Planar Ground Structures for Energy Harvesting Applications*". Proc. of SPIE Smart Structures+Nondestructive Evaluation and Health Monitoring (SS/NDE), Portland, Oregon (USA), 25-29 March 2017, <https://doi.org/10.1117/12.2257351>.

7.1 Introduction

Influenced by the results obtained with the topological synthesis presented in the previous chapter, we develop herein the analytical and semi-analytical model of a multi-member structure with members adjoined to each other at a folding angle φ .

Section 7.2 presents the derivation of the equations of motion and the analytical solution for the case of a V-shaped structure, i.e. an angle-shaped structure with two members adjoined to an angle φ . Consistent with the results presented in the previous chapter, the structure is clamped at one edge and free on the other side. The governing equation and the boundary conditions are derived by taking the variation of the Hamiltonian. The resulting boundary value problem is solved analytically giving rise to the characteristic equation of the system.

In Section 7.3, we present the derivation of the semi-analytical model for a fixed-free, multi-member structure, having N beams. The equations of motion are derived by means of the Euler-Lagrange equation and then solved by means of the Rayleigh-Ritz method. A root-finding algorithm is used to identify solutions having commensurate frequencies. Solutions for two and three members structures, namely V-, Y- and Z- shaped resonators, are presented. The dynamic of the V-shaped resonator is analyzed in depth. The effect of the folding angle φ on to the frequency response function to harmonic base excitation is investigated; the sensitivity of the solution to the position of the center of gravity of the entire system is shown through a parametric study.

Section 7.4 presents the universal design map for the one-to-two, V-shape resonators. The latter are design maps which allow for fast design of resonators once the dimensions and frequency of a prismatic cantilever beam are known.

7.2 Formulation of the Governing Equations

This section focuses on the dynamics of the angled structure having two members adjoined at an angle φ as shown in Figure 7.1.

7.2.1 Equation of motion of angle-shaped resonator having two members adjoined at an angle φ

The problem is analyzed by having a global $\mathbf{X} - \mathbf{Y}$ coordinate system that describes the overall motion of the resonator. A local $\mathbf{x}_1 - \mathbf{y}_1$ coordinate system is oriented along the first beam's undeformed position and the coordinate system $\mathbf{x}_2 - \mathbf{y}_2$ is fixed along the second beams undeformed position. The local coordinate systems have

unit vectors \mathbf{i} , \mathbf{j} , and \mathbf{i}' , \mathbf{j}' , respectively. The symbols x_1 and x_2 denote position along each beam's length and $w_1(x_1, t)$ and $w_2(x_2, t)$ represent the transverse displacement of the first and second beam's in their respective local reference frame.

Utilizing kinematics and neglecting nonlinear terms, the velocity at an arbitrary point along the first and second beam can be written as

$$\mathbf{v}_{p1} = \dot{w}_1(x_1, t) \mathbf{j} \quad \text{and} \quad \mathbf{v}_{p2} = \dot{w}_1(L_1, t) \mathbf{j} + \dot{w}_2(x_2, t) \mathbf{j}' + x_2 \frac{\partial \dot{w}_1(L_1, t)}{\partial x_1} \mathbf{j}'. \quad (7.1)$$

The unit vectors from each local coordinate system are related by the following transformation

$$\begin{pmatrix} \mathbf{i}' \\ \mathbf{j}' \end{pmatrix} = \begin{bmatrix} \cos \varphi & \sin \varphi \\ -\sin \varphi & \cos \varphi \end{bmatrix} \begin{pmatrix} \mathbf{i} \\ \mathbf{j} \end{pmatrix}. \quad (7.2)$$

Utilizing Hamilton's Extended Principle the action integral H can be written as

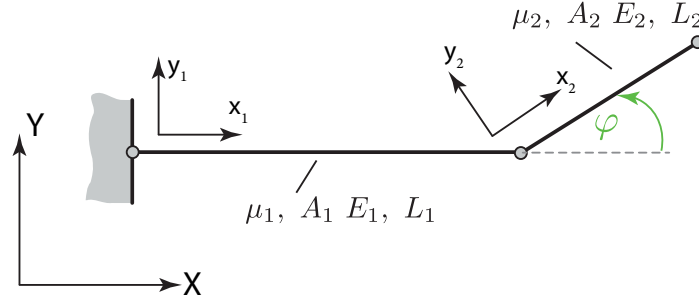


Fig. 7.1 Schematic of Angle-shaped resonator composed of two prismatic beams having a folding angle φ .

$$\begin{aligned} H = \int_{t_1}^{t_2} \mathcal{L} dt = \int_{t_1}^{t_2} \left\{ \int_0^{L_1} \left\{ \frac{1}{2} \mu_1 \mathbf{v}_{p1} \cdot \mathbf{v}_{p1} - \frac{1}{2} E_1 I_1 \left(\frac{\partial^2 w_1}{\partial x_1^2} \right)^2 \right\} dx_1 \right. \\ \left. + \int_0^{L_2} \left\{ \frac{1}{2} \mu_2 \mathbf{v}_{p2} \cdot \mathbf{v}_{p2} - \frac{1}{2} E_2 I_2 \left(\frac{\partial^2 w_2}{\partial x_2^2} \right)^2 \right\} dx_2 \right\} dt, \quad (7.3) \end{aligned}$$

where \mathcal{L} is the Lagrangian, defined as $\mathcal{L} = T - U$, where T and U are the kinetic and potential energy respectively. Utilizing Hamilton's Extended Principle the Lagrangian assumes the following form

$$\delta H = \int_{t_1}^{t_2} \delta \mathcal{L} dt = \int_{t_1}^{t_2} (\delta T - \delta U) dt = 0, \quad (7.4)$$

where the virtual changes of the kinetic energy can be written as

$$\begin{aligned} \delta T = & \int_0^{L_1} \mu_1 \dot{w}_1 \delta \dot{w}_1 dx_1 + \\ & \int_0^{L_2} \mu_2 \left[\dot{w}_1 \Big|_{L_1} + \dot{w}_2 \cos \varphi + x_2 \frac{\partial \dot{w}_1}{\partial x_1} \Big|_{L_1} \cos \varphi \right] \delta \dot{w}_1 \Big|_{L_1} dx_2 + \\ & \int_0^{L_2} \mu_2 \left[x_2^2 \left(\frac{\partial \dot{w}_1}{\partial x_1} \right) \Big|_{L_1} + x_2 \dot{w}_2 + x_2 \dot{w}_1 \Big|_{L_1} \cos \varphi \right] \frac{\partial \dot{w}_1}{\partial x_1} \Big|_{L_1} dx_2 + \\ & \int_0^{L_2} \mu_2 \left[\dot{w}_2 + x_2 \left(\frac{\partial \dot{w}_1}{\partial x_1} \right) \Big|_{L_1} + \dot{w}_1 \Big|_{L_1} \cos \varphi \right] \delta \dot{w}_2 dx_2. \end{aligned} \quad (7.5)$$

Integrating by parts in time yields

$$\begin{aligned} \int_{t_1}^{t_2} \delta T dt = & \int_0^{L_1} \left[- \int_{t_1}^{t_2} \mu_1 \ddot{w}_1 \delta w_1 dt + \mu_1 \dot{w}_1 \delta w_1 \Big|_{t_1}^{t_2} \right] dx_1 + \\ & \int_0^{L_2} \left[- \int_{t_1}^{t_2} \mu_2 \left[\ddot{w}_1 \Big|_{L_1} + \ddot{w}_2 \cos \varphi + x_2 \frac{\partial \ddot{w}_1}{\partial x_1} \Big|_{L_1} \cos \varphi \right] \delta w_1 \Big|_{L_1} dt \right] dx_2 + \\ & \int_0^{L_2} \left[- \int_{t_1}^{t_2} \mu_2 \left[x_2^2 \left(\frac{\partial \dot{w}_1}{\partial x_1} \right) \Big|_{L_1} + x_2 \dot{w}_2 + x_2 \dot{w}_1 \Big|_{L_1} \cos \varphi \right] \frac{\partial w_1}{\partial x_1} \Big|_{L_1} dt \right] dx_2 + \\ & \int_0^{L_2} \left[- \int_{t_1}^{t_2} \mu_2 \left[\ddot{w}_2 + x_2 \left(\frac{\partial \ddot{w}_1}{\partial x_1} \right) \Big|_{L_1} + \ddot{w}_1 \Big|_{L_1} \cos \varphi \right] \delta w_2 dt \right] dx_2 + \\ & \int_0^{L_2} \mu_2 \left[\dot{w}_1 \Big|_{L_1} + \dot{w}_2 \cos \varphi + x_2 \frac{\partial \dot{w}_1}{\partial x_1} \Big|_{L_1} \cos \varphi \right] \delta w_1 \Big|_{L_1} \Big|_{t_1}^{t_2} dx_2 + \\ & \int_0^{L_2} \mu_2 \left[x_2^2 \left(\frac{\partial \dot{w}_1}{\partial x_1} \right) \Big|_{L_1} + x_2 \dot{w}_2 + x_2 \dot{w}_1 \Big|_{L_1} \cos \varphi \right] \frac{\partial w_1}{\partial x_1} \Big|_{L_1} \Big|_{t_1}^{t_2} dx_2 + \\ & \int_0^{L_2} \mu_2 \left[\dot{w}_2 + x_2 \left(\frac{\partial \dot{w}_1}{\partial x_1} \right) \Big|_{L_1} + \dot{w}_1 \Big|_{L_1} \cos \varphi \right] \delta w_2 \Big|_{t_1}^{t_2} dx_2. \end{aligned} \quad (7.6)$$

The virtual change in the potential energy can be written as

$$\delta U = \frac{1}{2} \sum_{i=1}^2 \int_0^{L_i} E_i I_i \left(\frac{\partial^2 w_i}{\partial x_i^2} \right) \delta \left(\frac{\partial^2 w_i}{\partial x_i^2} \right) dx_i, \quad (7.7)$$

$$= \sum_{i=1}^2 E_i I_i \left(\frac{\partial^2 w_i}{\partial x_i^2} \right) \delta \left(\frac{\partial w_i}{\partial x_i} \right) \Big|_0^{L_i} - \sum_{i=1}^2 \int_0^{L_i} \frac{\partial}{\partial x_i} \left(E_i I_i \left(\frac{\partial^2 w_i}{\partial x_i^2} \right) \delta \left(\frac{\partial w_i}{\partial x_i} \right) \right) dx_i. \quad (7.8)$$

The third term of Eqn. (7.8) can be integrated by parts to yield

$$\begin{aligned} \sum_{i=1}^2 \int_0^{L_i} \frac{\partial}{\partial x_i} \left(E_i I_i \left(\frac{\partial^2 w_i}{\partial x_i^2} \right) \right) \delta \left(\frac{\partial w_i}{\partial x_i} \right) dx_i = & \sum_{i=1}^2 \frac{\partial}{\partial x_i} \left(E_i I_i \left(\frac{\partial^2 w_i}{\partial x_i^2} \right) \right) \delta w_i \Big|_0^{L_i} \\ & - \sum_{i=1}^2 \int_0^{L_i} \frac{\partial^2}{\partial x_i^2} \left(E_i I_i \left(\frac{\partial^2 w_i}{\partial x_i^2} \right) \right) \delta w_i dx_i. \end{aligned} \quad (7.9)$$

The total variation of the potential energy can be written as

$$\begin{aligned} \delta U = & \sum_{i=1}^2 E_i I_i \left(\frac{\partial^2 w_i}{\partial x_i^2} \right) \delta \left(\frac{\partial w_i}{\partial x_i} \right) \Big|_0^{L_i} - \sum_{i=1}^2 \frac{\partial}{\partial x_i} \left(E_i I_i \left(\frac{\partial^2 w_i}{\partial x_i^2} \right) \right) \delta w_i \Big|_0^{L_i} \\ & + \sum_{i=1}^2 \int_0^{L_i} \frac{\partial^2}{\partial x_i^2} \left(E_i I_i \left(\frac{\partial^2 w_i}{\partial x_i^2} \right) \right) \delta w_i dx_i. \end{aligned} \quad (7.10)$$

The dot products of the velocities as reported in equation leads to the following expressions

$$\begin{aligned} \mathbf{v}_{p1} \cdot \mathbf{v}_{p1} = & \dot{w}_1^2, \quad \text{and} \\ \mathbf{v}_{p2} \cdot \mathbf{v}_{p2} = & \dot{w}_2^2 + \dot{w}_1^2 \Big|_{L_1} + x_2^2 \frac{\partial \dot{w}_1}{\partial x_1} \Big|_{L_1} + 2x_2 \dot{w}_2 \frac{\partial \dot{w}_1}{\partial x_1} \Big|_{L_1} + 2\dot{w}_2 \dot{w}_1 \Big|_{L_1} \cos \varphi \\ & + 2x_2 \frac{\partial \dot{w}_1}{\partial x_1} \Big|_{L_1} \dot{w}_1 \Big|_{L_1} \cos \varphi. \end{aligned}$$

The symbols μ_1 and μ_2 are the mass density per unit length of the first and second beams, respectively. The terms $E_1 I_1$ and $E_2 I_2$ represent each beam's rigidity, where E_i is the modulus of elasticity and I_i is the area moment of inertia of each beam. Next, taking the variations in both w_1 and w_2 leaves the following

$$\begin{aligned} \delta H = & \int_{t_1}^{t_2} \left(\int_0^{L_1} -\mu_1 \ddot{w}_1 \delta w_1 dx_1 - \int_0^{L_2} \mu_2 \left[\dot{A}_1 \delta w_1 \Big|_{L_1} + \dot{A}_2 \frac{\partial}{\partial x_1} \delta w_1 \Big|_{L_1} + \dot{A}_3 \delta w_2 \right] dx_2 \right. \\ & - \int_0^{L_1} \frac{\partial^2}{\partial x_1^2} \left(E_1 I_1 \frac{\partial^2 w_1}{\partial x_1^2} \right) \delta w_1 dx_1 - \int_0^{L_2} \frac{\partial^2}{\partial x_2^2} \left(E_2 I_2 \frac{\partial^2 w_2}{\partial x_2^2} \right) \delta w_2 dx_2 \\ & - E_1 I_1 \frac{\partial^2 w_1}{\partial x_1^2} \frac{\partial}{\partial x_1} \delta w_1 \Big|_0^{L_1} - E_2 I_2 \frac{\partial^2 w_2}{\partial x_2^2} \frac{\partial}{\partial x_2} \delta w_2 \Big|_0^{L_2} + \frac{\partial}{\partial x_1} \left(E_1 I_1 \frac{\partial^2 w_1}{\partial x_1^2} \right) \delta w_1 \Big|_0^{L_1} \\ & \left. + \frac{\partial}{\partial x_2} \left(E_2 I_2 \frac{\partial^2 w_2}{\partial x_2^2} \right) \delta w_2 \Big|_0^{L_2} \right) dt = 0, \end{aligned} \quad (7.11)$$

where the constants \dot{A}_1 , \dot{A}_2 , \dot{A}_3 can be written as

$$\begin{aligned} \dot{A}_1 = & \dot{w}_1 \Big|_{L_1} + \dot{w}_2 \cos \varphi + x_2 \frac{\partial \dot{w}_1}{\partial x_1} \Big|_{L_1} \cos \varphi, \quad \dot{A}_2 = x_2^2 \frac{\partial \dot{w}_1}{\partial x_1} \Big|_{L_1} + x_2 \dot{w}_2 + x_2 \dot{w}_1 \Big|_{L_1}, \quad \text{and} \\ \dot{A}_3 = & \dot{w}_2^* + x_2 \frac{\partial \dot{w}_1}{\partial x_1} \Big|_{L_1} + \dot{w}_1 \Big|_{L_1} \cos \varphi. \end{aligned}$$

Gathering like virtual displacements leads to the following governing equations

$$E_1 I_1 \frac{\partial^4 w_1}{\partial x_1^4} + \mu_1 \dot{w}_1 = 0, \quad (7.12)$$

$$E_2 I_2 \frac{\partial^4 w_2}{\partial x_2^4} + \mu_2 \left(\ddot{w}_2^* + x_2 \frac{\partial \dot{w}_1}{\partial x_1} \Big|_{L_1} + \dot{w}_1 \Big|_{L_1} \cos \varphi \right) = 0. \quad (7.13)$$

The associated geometric and forced boundary conditions are

$$w_1(0,t) = \frac{\partial w_1}{\partial x_1}(0,t) = 0, \quad w_2(0,t) = \frac{\partial w_2}{\partial x_2}(0,t) = 0, \quad \text{and} \quad (7.14)$$

$$E_2 I_2 \frac{\partial^2 w_2}{\partial x_2^2}(L_2,t) = 0, \quad \frac{\partial}{\partial x_2} \left(E_2 I_2 \frac{\partial^2 w_2}{\partial x_2^2}(L_2,t) \right) = 0. \quad (7.15)$$

Finally, continuity of the shear and moments at the interface between the two beams can be written as

$$\begin{aligned} \int_0^{L_2} \mu_2 \left(\ddot{w}_1 \Big|_{L_1} + \ddot{w}_2 \cos \varphi + x_2 \frac{\partial \ddot{w}_1}{\partial x_1} \Big|_{L_1} \cos \varphi \right) dx_2 &= \frac{\partial}{\partial x_1} \left(E_1 I_1 \frac{\partial^2 w_1}{\partial x_1^2} \right) \Big|_{L_1}, \quad \text{and} \\ \int_0^{L_2} \mu_2 \left(\ddot{w}_2 + x_2 \frac{\partial \ddot{w}_1}{\partial x_1} \Big|_{L_1} + \ddot{w}_1 \Big|_{L_1} \cos \varphi \right) x_2 dx_2 &= -E_1 I_1 \frac{\partial^2 w_1}{\partial x_1^2} \Big|_{L_1}. \end{aligned} \quad (7.16a)$$

It is worth noting that when $\varphi = \pi/2$, the equations reduce to the governing equations of the L -shaped beam given by Bang [198].

7.2.2 Characteristic equation

In order to derive the characteristic equation, the Fourier method or separation of variables is used to decompose the displacements as a spatial function multiplied by unknown temporal coordinate

$$w_1(x_1,t) = W_1(x_1)T_1(t) \quad \text{and} \quad w_2(x_2,t) = W_2(x_2)T_2(t). \quad (7.17)$$

Substituting the definition of $w_1(x_1,t)$ in Eqn.(7.17) into Eqn.(7.12) leads to the following

$$E_1 I_1 W_1''''(x_1)T_1(t) + \mu_1 W_1(x_1)\ddot{T}_1(t) = 0,$$

which can rearranged as

$$\frac{\ddot{T}_1(t)}{T_1(t)} = -\frac{E_1 I_1 W_1''''(x_1)}{\mu_1 W_1(x_1)} = -\omega^2. \quad (7.18)$$

the prime denotes the derivative with respect to the spatial coordinate. Solutions to Eqn.(7.18) is given as

$$W_1(x_1) = C_1 \sin \gamma_1 x_1 + C_2 \cos \gamma_1 x_1 + C_3 \sinh \gamma_1 x_1 + C_4 \cosh \gamma_1 x_1, \quad (7.19)$$

where $\gamma_1^4 = \omega^2 \mu_1 / E_1 I_1$. Applying the geometric boundary conditions for $W_1(x_1)$

$$W_1(0) = C_2 + C_4 = 0, \quad \text{and} \quad W_1'(0) = \gamma_1 (C_1 + C_3) = 0. \quad (7.20)$$

Therefore, Eqn. (7.19) can be written as

$$W_1(x_1) = C_1 (\sin \gamma_1 x_1 - \sinh \gamma_1 x_1) + C_2 (\cos \gamma_1 x_1 - \cosh \gamma_1 x_1). \quad (7.21)$$

Likewise, Eqn. (7.13) can be written as

$$E_2 I_2 W_2''''(x_2) T_2(t) + \mu_2 [W_2(x_2) \ddot{T}_2(t) + x_2 W_1'(L_1) \ddot{T}_1(t) + W_1(L_1) \ddot{T}_1(t) \cos \varphi] = 0. \quad (7.22)$$

In order for Eqn. (7.22) to be valid at any arbitrary time t , $T_1(t) = T_2(t)$; Eqn. (7.22) then reduces to

$$E_2 I_2 W_2''''(x_2) - \omega^2 \mu_2 [W_2(x_2) + x_2 W_1'(L_1) + W_1(L_1) \cos \varphi] = 0. \quad (7.23)$$

The solution to Eqn. (7.23) can be written as

$$W_2(x_2) = D_1 \sin \gamma_2 x_2 + D_2 \cos \gamma_2 x_2 + D_3 \sinh \gamma_2 x_2 + D_4 \cosh \gamma_2 x_2 - W_1'(L_1) x_2 - W_1(L_1) \cos \varphi, \quad (7.24)$$

where $\gamma_2^4 = \omega^2 \mu_2 / E_2 I_2$. It is worth noting that the equation above presents the complementary solution, i.e. the solution to the homogeneous equation, plus the particular solution. The latter has been obtained by means of the method of undetermined coefficients, assuming $W_{2p}(x_2) = Ax_2 + B$. Substituting Eqn. (7.24) into the boundary conditions yields

$$W_2(0) = D_2 + D_4 + W_1(L_1) \cos \varphi = 0, \quad (7.25a)$$

$$\begin{aligned} W_2'(0) &= \gamma_2 (D_1 + D_3) + W_1'(L_1) x_2 = \\ &= \gamma_2 (D_1 + D_3) - \gamma_1 C_1 (\cos \gamma_1 L_1 - \cosh \gamma_1 L_1) + \gamma_1 C_2 (\sin \gamma_1 L_1 + \sinh \gamma_1 L_1). \end{aligned} \quad (7.25b)$$

Hence, Eqn. (7.24) can be rewritten as

$$\begin{aligned} W_2(x_2) &= D_1 \sin \gamma_2 x_2 + D_2 (\cos \gamma_2 x_2 - \cosh \gamma_2 x_2) + D_3 \sinh \gamma_2 x_2 + \\ &\quad - W_1'(L_1) x_2 + W_1(L_1) \cos \varphi (1 - \cosh \gamma_1 x_1). \end{aligned} \quad (7.26)$$

Substituting the second of Eqn. (7.17) into Eqn.(7.15) and Eqn.(7.16a) leads to

$$E_2 I_2 W_2''(L_2) = 0, \quad \text{and} \quad E_2 I_2 W_2'''(L_2) = 0, \quad (7.27a,b)$$

$$-\omega^2 \int_0^{L_2} \mu_2 (W_1(L_1) \cos \varphi + W_2 + W'(L_1) \cos \varphi) = E_1 I_1 W_1'''(L_1), \quad (7.27c)$$

$$-\omega^2 \int_0^{L_2} \mu_2 [W_2 + x_2 W_1'(L_1) + W_1(L_1) \cos \varphi] x_2 dx_2 = -E_1 I_1 W_1''(L_1). \quad (7.27d)$$

Substituting Eqns. (7.21) and (7.26) into the Eqns. defined (7.27) and adjoining Eqn. (7.25b) lead to the following algebraic system

$$\begin{bmatrix} A_{11} & A_{12} & A_{13} & A_{14} & A_{15} \\ A_{21} & A_{22} & A_{23} & A_{24} & A_{25} \\ A_{31} & A_{32} & A_{33} & A_{34} & A_{35} \\ A_{41} & A_{42} & A_{43} & A_{44} & A_{45} \\ A_{51} & A_{52} & A_{53} & 0 & A_{55} \end{bmatrix} \begin{Bmatrix} C_1 \\ C_2 \\ D_1 \\ D_2 \\ D_3 \end{Bmatrix} = \begin{Bmatrix} 0 \\ 0 \\ 0 \\ 0 \\ 0 \end{Bmatrix}, \quad (7.28)$$

The determinant of the coefficients matrix A gives the characteristic equation. The expression of the coefficients A_{ij} are reported below.

$$A_{11} = -E_1 I_1 \gamma_1^3 [\cos(\gamma_1 L_1) + \cosh(\gamma_1 L_1)] + m_2 \omega^2 \cos^2 \varphi [-\sin(\gamma_1 L_1) + \sinh(\gamma_1 L_1)] - m_2 \omega^2 (\sinh(\gamma_1 L_1) - \sin(\gamma_1 L_1)) + \frac{\rho_2}{\gamma_2} \omega^2 \cos^2 \varphi \sinh(\gamma_2 L_2) [\sin(\gamma_1 L_1) - (\sinh(\gamma_1 L_1))], \quad (7.29a)$$

$$A_{12} = E_1 I_1 \gamma_1^3 [\sin(\gamma_1 L_1) - \sinh(\gamma_1 L_1)] + m_2 \omega^2 [\cos(\gamma_1 L_1) - \cosh(\gamma_1 L_1)] (1 - \cos^2 \varphi) + \frac{\rho_2}{\gamma_2} \omega^2 \cos^2 \varphi \sinh(\gamma_2 L_2) [\cos(\gamma_1 L_1) - \cosh(\gamma_1 L_1)], \quad (7.29b)$$

$$A_{13} = \frac{\rho_2}{\gamma_2} \omega^2 \cos \varphi [1 - \cos(\gamma_2 L_2)], \quad (7.29c)$$

$$A_{14} = \frac{\rho_2}{\gamma_2} \omega^2 \cos \varphi [\sin(\gamma_2 L_2) - \sinh(\gamma_2 L_2)], \quad (7.29d)$$

$$A_{15} = -\frac{\rho_2}{\gamma_2} \omega^2 \cos \varphi [1 - \cosh(\gamma_2 L_2)], \quad (7.29e)$$

$$A_{21} = \cos \varphi [\cosh(\gamma_2 L_2) \sin(\gamma_1 L_1) - \cosh(\gamma_2 L_2) \sinh(\gamma_1 L_1)], \quad (7.29f)$$

$$A_{22} = \cos \varphi [\cos(\gamma_1 L_1) \cosh(\gamma_2 L_2) - \cosh(\gamma_1 L_1) \cosh(\gamma_2 L_2)], \quad (7.29g)$$

$$A_{23} = -\sin(\gamma_2 L_2), \quad (7.29h)$$

$$A_{24} = -\cos(\gamma_2 L_2) - \cosh(\gamma_2 L_2), \quad (7.29i)$$

$$A_{25} = \sinh(\gamma_2 L_2), \quad (7.29j)$$

$$A_{31} = \cos \varphi [\sin(\gamma_1 L_1) \sinh(\gamma_2 L_2) - \sinh(\gamma_1 L_1) \sinh(\gamma_2 L_2)], \quad (7.29k)$$

$$A_{32} = \cos \varphi [\cos(\gamma_1 L_1) \sinh(\gamma_2 L_2) - \cosh(\gamma_1 L_1) \sinh(\gamma_2 L_2)], \quad (7.29l)$$

$$A_{33} = \cos(\gamma_2 L_2), \quad (7.29m)$$

$$A_{34} = \sin(\gamma_2 L_2) - \sinh(\gamma_2 L_2), \quad (7.29n)$$

$$A_{35} = \cosh(\gamma_2 L_2), \quad (7.29o)$$

$$A_{41} = \frac{\mu_2 \omega^2}{\gamma_2^2} \cos \varphi \left\{ \sin(\gamma_1 L_1) [1 - \cosh(\gamma_2 L_2)] - \sinh(\gamma_1 L_1) [1 - \cosh(\gamma_2 L_2)] \right\} + E_1 I_1 \gamma_1^2 [\sin(\gamma_1 L_1) + \sinh(\gamma_1 L_1)] + \frac{\mu_2 \omega^2 L_2}{\gamma_2} \cos \varphi \sinh(\gamma_2 L_2) [\sin(\gamma_1 L_1) - \sinh(\gamma_1 L_1)], \quad (7.29p)$$

$$A_{42} = \frac{\mu_2 \omega^2}{\gamma_2^2} \cos \varphi \left\{ \cos(\gamma_1 L_1) \left[1 - \cosh(\gamma_2 L_2) \right] - \cosh(\gamma_1 L_1) \left[1 - \cosh(\gamma_2 L_2) \right] \right\} + E_1 I_1 \gamma_1^2 \left[\cos(\gamma_1 L_1) + \cosh(\gamma_1 L_1) \right] + \frac{\mu_2 \omega^2 L_2}{\gamma_2} \cos \varphi \sinh(\gamma_2 L_2) \left[\cos(\gamma_1 L_1) - \cosh(\gamma_1 L_1) \right], \quad (7.29q)$$

$$A_{43} = -\frac{\mu_2 \omega^2 L_2}{\gamma_2} \cos(\gamma_2 L_2) + \frac{\mu_2 \omega^2}{\gamma_2^2} \sin(\gamma_2 L_2), \quad (7.29r)$$

$$A_{44} = \frac{\mu_2 \omega^2}{\gamma_2^2} \left[\cos(\gamma_2 L_2) + \cosh(\gamma_2 L_2) - 2 \right] + \frac{\mu_2 \omega^2 L_2}{\gamma_2} \left[\sin(\gamma_2 L_2) - \sinh(\gamma_2 L_2) \right], \quad (7.29s)$$

$$A_{45} = \frac{\mu_2 \omega^2 L_2 \cosh(\gamma_2 L_2)}{\gamma_2} - \frac{\mu_2 \omega^2 \sinh(\gamma_2 L_2)}{\gamma_2^2} \quad (7.29t)$$

$$A_{51} = \gamma_1 \cosh(\gamma_1 L_1) - \gamma_1 \cos(\gamma_1 L_1), \quad (7.29u)$$

$$A_{52} = \gamma_1 \sin(\gamma_1 L_1) + \gamma_1 \sinh(\gamma_1 L_1), \quad (7.29v)$$

$$A_{35} = \gamma_2, \quad (7.29w)$$

$$A_{55} = \gamma_2. \quad (7.29x)$$

Examining the the L -shaped structure when $\varphi = \pi/2$, the characteristic equation coincides with the one given by Gürgöze [199]. Moreover, after some algebraic manipulations, the frequencies equation when $\varphi = 0$ reduce to that of a straight beam, i.e. $1 + \cos(\gamma L) \cosh(\gamma L)$.

7.2.3 Validation of the analytical model

In this section we aim at validating our analytical model against results already available in the open literature. Particularly, the frequencies obtained for the L -shaped structure presented by Gürgöze [199] and of a straight beam are compared to the present analysis. In the latter case, we considered a cantilevered structure divided into two equal members. The numerical parameters for the two structures are reported in Table 7.1. In both cases, the roots of the frequencies equation are obtained using Wolfram Mathematica[®]. Solutions for the L -shaped beam reported in Table 7.2 agree with those given by Gürgöze [199]; solutions for the straight beam reported in the last row of Table 7.2; both are found to be in agreement with the analytical solutions.¹

¹The solutions for the straight beam are given by $f = k^2 \sqrt{\frac{EI}{\rho AL^4}}$, where ρ is the density in kg/m³, $L = L_1 + L_2$ and $k=1.8751, 4.694, 7.855, 10.995, 14.135, 17.279$ and 20.4203 .

Table 7.1 Parameters for the two validation structures.

Structure	L_1 m	L_2 m	μ_1 kg/m	μ_2 kg/m	φ deg	$E_1 I_1$ Nm ²	$E_2 I_2$ Nm ²
<i>L</i>	4.249	2.215	0.0045	0.0060	90	0.0267	0.0147
Straight	0.210	0.210	0.0694	0.0694	0	0.5512	0.5512

Table 7.2 Bending frequencies [rad/s] for the straight and *L*-shaped structures.

Structure	ω_1	ω_2	ω_3	ω_4	ω_5	ω_6	ω_7
Gürgöze [199]	0.2247	0.7940	2.6814	5.7715	8.0768	14.6665	18.5553
Present <i>L</i> -shaped	0.2247	0.7940	2.6814	5.7715	8.0768	14.6665	18.5553
Straight	56.1891	352.131	985.978	1932.12	3193.94	4771.19	6663.89
Present straight	56.1891	352.131	985.978	1932.12	3193.94	4771.19	6663.89

7.3 Generalized Reduced Order Model

Let us consider the multi-member beam structure shown in Fig. 7.2. Following Haddow et al. [89], we assume a polynomial admissible function of undetermined constants based on the equilibrium equation of each member in the absence of external loading. The polynomials are then substituted into the associated boundary and continuity conditions, yielding an overdetermined system in determining the unknown constants. The free variables in this system become the generalized coordinates. Writing the admissible functions in terms of the free variables and substituting into the Lagrangian of the system results in the equations of motion of the system.

7.3.1 Determining the Admissible Functions

Figure 7.2 shows a cantilevered truss structure composed of N beams that are prismatic, homogeneous and isotropic. The generalized structure can have f free boundary nodes and θ internal nodes. We denote the set of free boundary and internal nodes as F and Θ , respectively. Particularly, in Figure 7.2 there are 2 free nodes (i.e. nodes 4 and 5), while the nodes 2 and 3 are internal nodes. Let ξ_i be the local axial coordinate, w_i^* the bending displacement in the local $\xi_i - \eta_i$ reference frame. Finally, L_i denotes the length of the i -th beam. The governing equations for the vertical

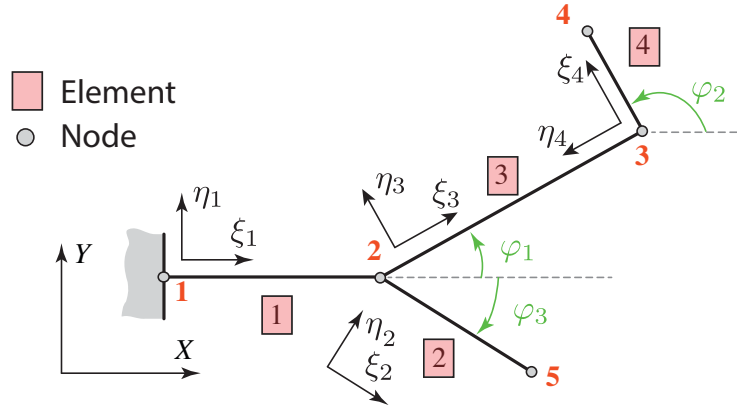


Fig. 7.2 Generalized model representing a 4-DOF structure with $N = 4$ elements, $F = 2$ free nodes, and $\theta = 2$ internal nodes.

displacements can be written, in the local coordinate system, as follows

$$\frac{\partial^4 w_i^*}{\partial \xi_i^4} = 0 \quad \text{for } 0 \leq \xi_i \leq L_i.$$

Solutions to the fourth order differential equations are third order polynomials that can be written in the following form:

$$w_i^*(\xi_i, t) = a_{0,i} + a_{1,i}\xi_i + a_{2,i}\xi_i^2 + a_{3,i}\xi_i^3, \quad (7.30)$$

where $i = 1, 2, \dots, N$ indicates the i^{th} beam. The $4N$ constants $a_{j,i}$, are the unknown generalized coordinates of the beams. The generalized boundary conditions can be written as follows:

$$w_i^*(0, t) = 0, \quad \frac{\partial w_i^*}{\partial \xi_i}(0, t) = 0, \quad (7.31a)$$

$$E_f I_f \frac{\partial^2 w_f^*}{\partial \xi_f^2}(L_f, t) = 0, \quad \text{and} \quad (7.31b)$$

$$E_{\beta_-} I_{\beta_-} \frac{\partial^2 w_{\beta_-}^*}{\partial \xi_{\beta_-}^2}(L_{\beta_-}, t) = \sum_{\beta_+} E_{\beta_+} I_{\beta_+} \frac{\partial^2 w_{\beta_+}^*}{\partial \xi_{\beta_+}^2}(0, t). \quad (7.31c)$$

where E and I are the Young's modulus and the area moment of inertia respectively while β , denotes all the beams that share an internal node θ . Particularly, we denote with β_- the member that has the reference system pointing towards the node θ , all the other members are denoted with β_+ , as shown Figure 7.3. Let us denote with p and q respectively the first and second node of each member in the local reference system. Note that in Figure 7.3 the node q_i of the i^{th} beam is also an internal node.

Now considering the generalized problem one can write: 1) F zero moment equations for each free node; 2) N equations as each beam was clamped in $\xi_i = 0$, that is Eqn. (7.31a) and 3) $N - F$ equilibrium equations in each internal node. In total, the equations governing the motion of the resonators has $4N$ unknowns and $F + 2N + (N - F) = 3N$ constraint equations. Thus the equations of motion of the system can be written as a function of N free variables, that are the generalized coordinates and assume the following form:

$$a_{0,i} = a_{1,i} = 0, \quad (7.32a)$$

$$a_{2,i} = \frac{E_{\beta_-} I_{\beta_-} (a_{2,\beta_-} + 3a_{3,\beta_-} L_{\beta_-})}{E_i I_i} - \sum \frac{E_{\beta_+} I_{\beta_+} a_{2,\beta_+}}{E_i I_i}, \quad (7.32b)$$

$$\text{where } \beta_+ := \{\text{members} | p_{\beta_+} = q_i\},$$

$$a_{3,i} = \begin{cases} \text{unknown} & \text{if } p, q \in \Theta, \\ -\frac{a_{2,i}}{3L_i} & \text{if } p \in \Theta, q \in F. \end{cases} \quad (7.32c)$$

Once the displacement field has been parameterized in terms of the free variables, the equations of motion can be obtained by means of the Euler-Lagrange equation:

$$\frac{d}{dt} \left(\frac{\partial \mathcal{L}}{\partial \dot{q}_i} \right) - \frac{\partial \mathcal{L}}{\partial q_i} = 0, \quad (7.33)$$

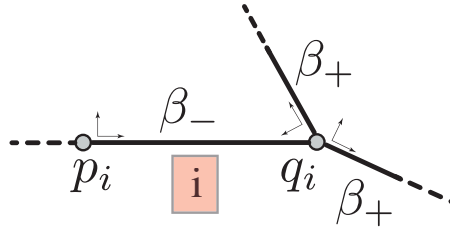


Fig. 7.3 Detail of an internal node β of the structure.

where, \mathcal{L} is the Lagrangian defined as $T - U$, where T and U are as above the kinetic and the potential energy of the system. The energies can be written as:

$$T = \frac{1}{2} \sum_i^N \int_0^{L_i} \mu_i \dot{v}_i^2 d\xi_i, \quad \text{and} \quad U = \frac{1}{2} \sum_{i=1}^N (E_i I_i) \int_0^{L_i} \left(\frac{\partial^2 w_i^*}{\partial \xi_i^2} \right)^2 d\xi_i,$$

$\mu_i = \rho_i A_i$ are the mass per unit length of the beams and v_j are the absolute velocities with respect to the global $\mathbf{X} - \mathbf{Y}$ coordinate system. It must be noted that the potential energy is written with respect to the local reference system. While, the kinetic energy of the structure, is written in the global reference system. The generalized kinetic

energy expression assumes the following form:

$$T_i = \frac{1}{2} \int_0^{L_i} \mu_i (\dot{w}_i^2 + \dot{u}_i^2) d\xi_2, \quad (7.34)$$

where

$$\begin{aligned} \dot{w}_1(\xi_1) &= \dot{w}_1^* + \dot{w}_B, \\ \dot{w}_i(\xi_i) &= \left(\dot{w}_i^* + \xi_i \sum_{j=1} \dot{w}_{j,\xi_j|L_j} \right) \cos(\varphi_i) + \dot{w}_{i-1|L_{i-1}}, \\ \dot{u}_i(\xi_i) &= \left(\dot{w}_i^* + \xi_i \sum_{j=1} \dot{w}_{j,\xi_j|L_j} \right) \sin(\varphi_i) + \dot{u}_{i-1|L_{i-1}}. \end{aligned} \quad (7.35)$$

where \dot{w}_1^* and \dot{w}_B denote respectively the vertical velocity of the first member and the base velocity, \dot{w}_i^* is the transverse velocity in the local reference of the i -th member, the summation is extended to all the beam members (j) from the clamped edge to the node p of the i^{th} beam, $\dot{w}_{i-1|L_{i-1}}$ and $\dot{u}_{i-1|L_{i-1}}$ are the absolute velocities of the structure in p_i and finally, the term $\dot{w}_{j,\xi_j|L_j}$ is the angular velocity in p_i . The latter term ensures the continuity of the curvature between two contiguous beams and it is the result of having assumed $a_{1,i} = 0$.

The equation of motion in matrix form can be written as follows:

$$[\mathbf{M}] \{\ddot{\mathbf{a}}\} + [\mathbf{K}] \{\mathbf{a}\} = \{\mathbf{f}\}, \quad (7.36)$$

where $[\mathbf{M}]$ and $[\mathbf{K}] \in \mathbb{R}^{N \times N}$ are the mass and stiffness matrices, respectively, and $\{\mathbf{a}\} \in \mathbb{R}^N$ is the vector of the generalized coordinates; the dot indicates the time derivatives. Finally, $\{\mathbf{f}\} \in \mathbb{R}^N$ are the generalized forces. The associate eigenvalue problem assume the following form:

$$[\mathbf{K} - \Omega^2 \mathbf{M}] \{\mathbf{A}\} = \{\mathbf{0}\}, \quad (7.37)$$

where $\omega_i^2 = \omega_i^2(E_j, \rho_j, h_j, b_j, L_j, \varphi_j) \quad j = 1 \dots N$, are the eigenvalues of the system associated to the eq. (7.37). Note that for the modal frequencies to be integer multiples, they must also be commensurable:

$$c_1 \omega_1 + c_2 \omega_2 + \dots + c_N \omega_N = 0, \quad \text{where } c_i \in \mathbb{Z} \quad (7.38)$$

where $\omega_i^2 = \omega_i^2(E_j, \rho_j, h_j, b_j, L_j, \varphi_j) \quad j = 1 \dots N$, are the eigenvalues of the homogeneous system associated to the eq. (7.40), i.e. the square of the natural frequencies. Each beam has six sets of design parameters, namely, the beam's density ρ_i , the Young modulus E_i , the cross section dimensions b_i and h_i , the beam's length L_i and the angle of orientation of each beam with respect to the global reference frame φ_i .

Table 7.3 Geometric and Material Properties for N-DOF Resonators

Resonator's properties	
Length, L_1 (mm)	150.00
Thickness, h_1 (mm)	10.00
Young's Modulus, E_1 (GPa)	73.00
Density, ρ_1 (kg/m ³)	2780.00

In general the solutions to the eq. (7.38) are a hyper-surface S , which can be defined as the set

$$S \in \mathbb{R}^{6N} = \left\{ \omega(E_j, \rho_j, h_j, b_j, L_j, \varphi_j) \in \mathbb{R}^{6N+1} \mid \sum_i^N c_i \omega_i(E_j, \rho_j, h_j, b_j, L_j, \varphi_j) = 0, \quad j = 1 \dots N, \quad c_i \in \mathbb{Z} \right\}. \quad (7.39)$$

Hereafter, the analysis is accomplished by restricting the material parameters and the geometry of the cross section, i.e. ρ and E are fixed and equal for each beam, and each beam has a square cross section. These constraints reduce the total of number of parameters to $4N$.

Next, we examine the design space by utilizing a root finding algorithm to identify all the possible solutions to the Eqn. (7.38). It should be noted that design space has two constraints that can be imposed to prevent unrealistic designs, i.e., the angle between two contiguous beams can never equal 180° and $h/L > 1/10$. The first constraint prevents the structure from folding back on itself and the second prevents violation of the Euler-Bernoulli beam assumption. These unfeasible solutions are discarded in the envelopes reported in the following sections.

Frequency response of the resonator

In determining, the linear frequency response we assume a base excitation of the form, $\ddot{w}_b(t) = Ge^{i\Omega t}$ and the response is of the form $\mathbf{a} = \mathbf{A}e^{i\Omega t}$, subsequently the force vector becomes $\mathbf{f} = \mathbf{F}e^{i\Omega t}$. The equations of motion can then be written in the form

$$[\mathbf{K} - \Omega^2 \mathbf{M}] \{\mathbf{A}\} = \{\mathbf{F}\}, \quad (7.40)$$

The response can be recovered using the relations in eqns. (7.32) a)-c), and the displacement field in Eqn. (7.30). Finally, in examining the design space for the resonators we specify the first member with the properties shown in Table 7.3.

7.3.2 Case $N = 2$: V-shaped resonator

Consider the 2-DOF system shown in Figure 7.4. In this case the resonator has

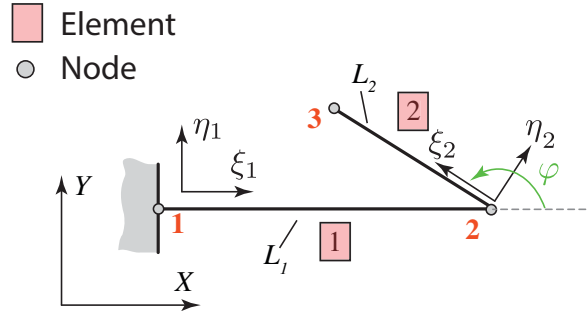


Fig. 7.4 V-shaped resonator with a 2-DOF structure with $N = 2$ elements, $F = 1$ free nodes, and $\theta = 1$ internal nodes.

eight design parameters. In order to highlight the importance of the member's relative orientation, we set L_1, h_1, b_1, E , and ρ_1 as the fixed set of parameters. While, $\hat{l} = L_2/L_1, \hat{h} = h_2/h_1 = b_2/b_1$, and φ are the design variables whose effects we analyze. The set of boundary conditions in Eqn.(7.31) becomes:

$$w_1^*(0, t) = 0, \quad \frac{\partial w_1^*}{\partial \xi_1}(0, t) = 0, \quad w_2^*(0, t) = 0, \quad \frac{\partial w_2^*}{\partial \xi_2}(0, t) = 0, \quad (7.41a)$$

$$E_2 I_2 \frac{\partial^2 w_2^*}{\partial \xi_2^2}(L_2, t) = 0, \quad \text{and} \quad E_1 I_1 \frac{\partial^2 w_1}{\partial \xi_1^2}(L_1, t) = E_2 I_2 \frac{\partial^2 w_2^*}{\partial \xi_2^2}(0, t). \quad (7.41b)$$

Substituting the Eqns. in (7.30) into the Eqns. in (7.41b) yields the following

$$a_{0,j} = a_{1,j} = 0, \quad \text{for } j = 1, 2 \quad (7.42a)$$

$$a_{2,2} = \frac{E_1 I_1}{E_2 I_2} (a_{2,1} + 3a_{3,1} L_1), \quad \text{and} \quad (7.42b)$$

$$a_{3,2} = -\frac{a_{2,2}}{3L_2}. \quad (7.42c)$$

which agree with the equations in (7.32). The motion of the system is described by two generalized coordinates $a_{2,1}$ and $a_{3,1}$.

The expression of the potential energy is trivial and therefore omitted. The kinetic

energy T can be written as:

$$T = \frac{1}{2} \int_0^{L_1} \mu_1 \dot{w}_1^2 d\xi_1 + \frac{1}{2} \int_0^{L_2} \mu_2 (\dot{w}_2^2 + \dot{u}_2^2) d\xi_2, \quad (7.43)$$

where

$$\begin{aligned} \dot{w}_1 &= \dot{w}_1^* + \dot{w}_B(t), \\ \dot{w}_2 &= \dot{w}_2^* \cos(\varphi) + \dot{w}_{1,\xi_1|L_1} \xi_2 \cos(\varphi) + \dot{w}_{1|L_1}, \\ \dot{u}_2 &= \dot{w}_2^* \sin(\varphi) + \dot{w}_{1,\xi_1|L_1} \xi_2 \sin(\varphi). \end{aligned} \quad (7.44)$$

The square of the natural frequencies are the eigenvalues of the system reported in Eqn. (7.37). The eigenvalues are:

$$\omega_{1,2}^2 = \frac{n_{11} + n_{12} \pm \sqrt{(n_{11} - n_{22})^2 + n_{12}n_{21}}}{2\Delta},$$

where

$$\begin{aligned} n_{11} &= k_{11}m_{22} - k_{12}m_{12}, & n_{12} &= k_{12}m_{22} - k_{22}m_{12}, \\ n_{21} &= k_{12}m_{11} - k_{11}m_{21}, & n_{22} &= k_{22}m_{11} - k_{12}m_{21}, \\ \Delta &= m_{11}m_{22} - m_{12}^2. \end{aligned}$$

The stiffness matrix for the Rayleigh of the V -shaped resonator approximation are written as

$$\begin{aligned} \hat{k}_{11} &= \frac{4L_2E_1^2I_1^2}{3E_2I_2} + 4L_1E_1I_1, \\ \hat{k}_{12} &= \frac{4L_2E_1^2I_1^2L_1}{E_2I_2} + 6E_1I_1L_1^2 = \hat{k}_{21}, \\ \hat{k}_{22} &= \frac{12L_2E_1^2I_1^2L_1^2}{E_2I_2} + 12E_1I_1L_1^3. \end{aligned}$$

Likewise, the mass matrix is given as

$$\begin{aligned} \hat{m}_{11} &= \frac{A_1L_1^5\rho_1}{5} + \frac{4A_2L_1^2L_2^3\rho_2}{3} + \frac{11A_2E_1^2I_1^2L_2^5\rho_2}{105E_2^2I_2^2} + \frac{11A_2E_1I_1L_1L_2^4\rho_2}{15E_2I_2} + \\ &\quad + \frac{A_2E_1I_1L_1^2L_2^3\rho_2 \cos(\varphi)}{2E_2I_2} + A_2L_1^4L_2\rho_2 + 2A_2L_1^3L_2^2\rho_2 \cos(\varphi), \\ \hat{m}_{12} &= \frac{A_1L_1^6\rho_1}{6} + \frac{5A_2L_1^4L_2^2\rho_2 \cos(\varphi)}{2} + \frac{33A_2E_1I_1L_1^2L_2^4\rho_2}{20E_2I_2} + \frac{11A_2E_1^2I_1^2L_1L_2^5\rho_2}{35E_2^2I_2^2} + \\ &\quad + \frac{A_2E_1I_1L_1^3L_2^3\rho_2 \cos(\varphi)}{E_2I_2} + A_2L_1^5L_2\rho_2 + 2A_2L_1^3L_2^3\rho_2 = \hat{m}_{21}, \\ \hat{m}_{22} &= \frac{A_1L_1^7\rho_1}{7} + \frac{33A_2E_1^2I_1^2L_1^2L_2^5\rho_2}{35E_2^2I_2^2} + \frac{33A_2E_1I_1L_1^3L_2^4\rho_2}{10E_2I_2} + \frac{3A_2E_1I_1L_1^4L_2^3\rho_2 \cos(\varphi)}{2E_2I_2} + \end{aligned}$$

$$+ A_2 L_1^6 L_2 \rho_2 + 3 A_2 L_1^4 L_2^3 \rho_2 + 3 A_2 L_1^5 L_2^2 \rho_2 \cos(\varphi).$$

And finally the expression of the generalized forces assume the following form

$$\begin{aligned} \hat{f}_1 &= \left(\frac{1}{3} \rho_1 A_1 L_1^3 + \left(\frac{\rho_2 A_2 L_2 (4 E_2 I_2 L_1^2 + L_2 (4 E_2 I_2 L_1 + E_1 I_1 L_2) \cos(\varphi))}{4 E_2 I_2} \right) \right) \ddot{w}_B(t), \\ \hat{f}_2 &= \left(\frac{\rho_1 A_1 L_1 E_2 I_2 L_1^3 + \rho_2 A_2 L_2 (4 E_2 I_2 L_1^2 + 3 L_2 (2 E_2 I_2 L_1 + E_1 I_1 L_2) \cos(\varphi))}{4 E_2 I_2} \right) \ddot{w}_B(t). \end{aligned}$$

In this case, to have commensurable frequencies one must have:

$$\Lambda = \frac{\omega_2}{\omega_1} = c, \quad \text{where } c \in \mathbb{Z} \quad (7.46)$$

Plugging the solution of the eigenvalue problem into Eq. (7.46) leads to the equation $\Lambda(\hat{h}, \hat{l}, \varphi) = c$. This equation is the general form of the level curve of a family of hyper-surfaces S , $S \in \mathbb{R}^4$. Solutions to the Eq. (7.46) are obtained by means of a root-finding algorithm. We report solutions to the Eqn. (7.46), in the form of level surfaces (3D) and level sets (2D), respectively. The solutions reported are referred to $c = 2$.

In order to find the solutions by means of the bisection method, we solve for the optimal \hat{l} over a range of φ and \hat{h} . At a fixed φ and \hat{h} , the equation $\Lambda(\hat{h}, \hat{l}, \varphi)$ is quadratic in \hat{l} . Particularly, there are two families of solution hereafter referred as outer $\hat{l} \geq 1$, i.e., the second beam is longer than the fixed beam, and inner curve $\hat{l} \leq 1$, the second beam is shorter than the fixed beam, respectively.

Figure 7.5 plots the solution by restricting the design domain by letting $\hat{h} = 1$ and having φ vary so that $0 \leq \varphi < 2\pi$. The resulting curve is closed and bound by points that resemble saddle node bifurcations. Two solutions coexist in the region $115^\circ \lesssim \varphi \lesssim 245^\circ$ and are annihilated for angles outside this region. Note there is good agreement with the present semi-analytical model indicated by the dashed line, with a finite element analysis that has 10 elements per member indicated by the orange line.

The solution forms a surface by letting \hat{h} vary so that $0.5 \leq \hat{h} \leq 2$ and $0 \leq \varphi < 2\pi$. Considering solutions that lie between 0° and 180° and splitting the surface on the bifurcation line (red) yields the plot in Fig. 7.6 a) and b) in the form of inner and outer level surfaces. The green line indicates the L -shaped beams envelope. For sake of clarity, the inner and outer level surfaces are reported separately. Figure 7.6 shows that increasing the ratio \hat{h} the set of possible folding angles, to have commensurable

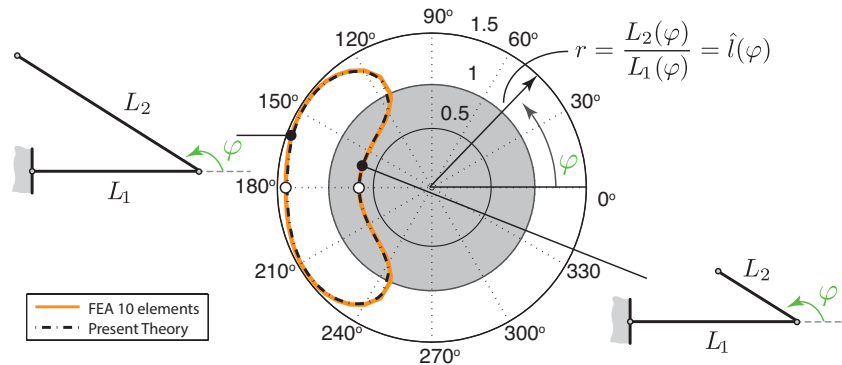


Fig. 7.5 Bifurcation envelopes obtained through FEA (10 elements per member) and with the present semi-analytical model for $\omega_2/\omega_1 = 2$ as a function of φ for $\hat{h} = 1$. Solutions in white region are for $\hat{l}(\varphi) > 1$, and solutions in gray region for are for $\hat{l}(\varphi) < 1$.

frequencies, decreases. This can be explained by realizing that the system is sensitive to the position the center of gravity. Figure 7.7 plots the normalized distance of the CG from the fixed end for the 1:2 resonator with $\hat{h} = 0.5$. The inner envelope has a bigger design space, $62^\circ \leq \hat{h} < 180^\circ$ with respect to the outer envelope nonetheless it exhibits only 8% variation of the CG distance; meanwhile, the outer envelopes, has almost 16% of variation despite having a smaller design space. This motivates also why the surface exhibits the bifurcation mentioned before between the inner and outer envelope when \hat{h} increases.

Figure 7.8 plots the frequency response function of a V-shaped resonator $\omega_2/\omega_1 = 2$ at $u_2(L_2)$ and $\hat{h} = 0.5$. The contours of the FRF are projected on the folding angle-frequency space. Note just as in the surface plot in Fig. 7.6 there are two length ratios that give commensurate frequencies there also two corresponding FRF's, i.e., Fig. 7.6 a) for $\hat{l} < 1$, and Fig. 7.6 b) for $\hat{l} > 1$. The solid lines indicate individual FRF's are folding angles of 75° , 90° , 100° , 120° , and 150° . The plots of the FRF assume modal damping of the $\zeta = 0.01$ for all modes.

Note for $\hat{l} < 1$ the response at the first modal frequencies is greater than the response at the second modal frequencies for all allowable folding angles. However, if $\hat{l} > 1$ the maximum response at the modal frequencies depends on the folding angles. This may be advantageous in designing MEMS bases sensors that rely on the second modal frequency of the resonator [76, 200].

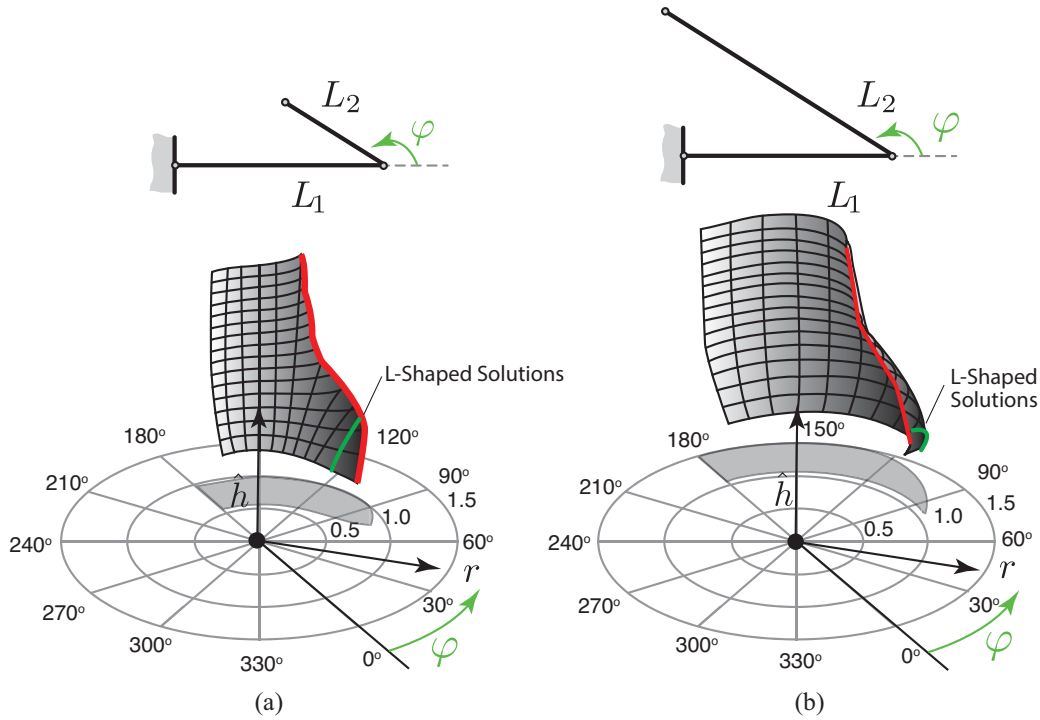


Fig. 7.6 Contour plots for (a) $\hat{l} < 1$ and (b) $\hat{l} > 1$ with $\omega_2/\omega_1 = 2$ as a function of φ . The envelopes are obtained considering square cross sections with various $\hat{h} = h_2/h_1$.

7.3.3 Case $N = 3$: Y-shaped resonator

Figures 7.9 a) and b) show the topology of the Y and Z resonators, respectively. Using the process outlined the Y and Z resonators are 3-DOF structures and have 12 design parameters. The set of boundary conditions in Eqn. (7.31) for the case of the Y -shaped structure can be written as:

$$\begin{aligned}
 w_1(0,t) &= 0, & \frac{\partial w_1}{\partial \xi_1}(0,t) &= 0, \\
 w_2^*(0,t) &= 0, & \frac{\partial w_2^*}{\partial \xi_2}(0,t) &= 0, \\
 w_3^*(0,t) &= 0, & \frac{\partial w_3^*}{\partial \xi_3}(0,t) &= 0, \\
 E_2 I_2 \frac{\partial^2 w_2^*}{\partial \xi_2^2}(L_2,t) &= 0, \\
 E_3 I_3 \frac{\partial^2 w_3^*}{\partial \xi_3^2}(L_3,t) &= 0, \quad \text{and} \\
 E_1 I_1 \frac{\partial^2 w_1}{\partial \xi_1^2}(L_1,t) &= E_2 I_2 \frac{\partial^2 w_2^*}{\partial \xi_2^2}(0,t) + E_3 I_3 \frac{\partial^2 w_3^*}{\partial \xi_3^2}(0,t).
 \end{aligned} \tag{7.47}$$

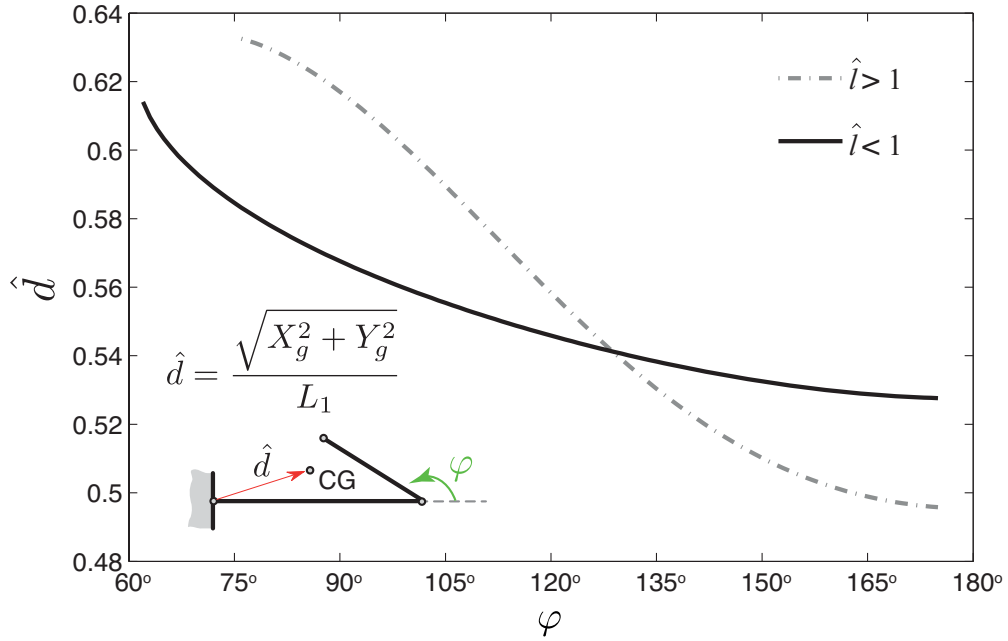


Fig. 7.7 Nondimensional distance of the center of gravity, \hat{d} , from the fixed end. The distance from the fixed end to the CG changes with respect to the folding angle φ for a family of resonators where $\omega_2/\omega_1 = 2$ with $\hat{h} = 0.5$. The outer envelope exhibits an higher variation of the normalized distance of the CG from the fixed end despite the design space, in term of folding angle φ , is smaller compared with that of the inner envelope.

Substituting the Eqns. in (7.47) into the Eqns. in (7.30) leads to:

$$a_{0,j} = a_{1,j} = 0, \quad \text{for } j = 1, 2, 3 \quad (7.48a)$$

$$a_{2,3} = \frac{E_1 I_1 (a_{2,1} + 3a_{3,1} L_1) - E_2 I_2 a_{2,2}}{E_3 I_3}, \quad (7.48b)$$

$$a_{3,2} = -\frac{a_{2,2}}{3L_2}, \quad (7.48c)$$

$$a_{3,3} = -\frac{a_{2,3}}{3L_3}. \quad (7.48d)$$

The motion of the system is described by three generalized coordinates, i.e., $a_{2,1}$, $a_{3,1}$ and $a_{2,2}$.

The kinetic energy T can be written as:

$$T = \frac{1}{2} \int_0^{L_1} \mu_1 \dot{w}_1^2 d\xi_1 + \frac{1}{2} \int_0^{L_2} \mu_2 (\dot{w}_2^2 + \dot{u}_2^2) d\xi_2 + \frac{1}{2} \int_0^{L_3} \mu_3 (\dot{w}_3^2 + \dot{u}_3^2) d\xi_3, \quad (7.49)$$

$$(7.50)$$

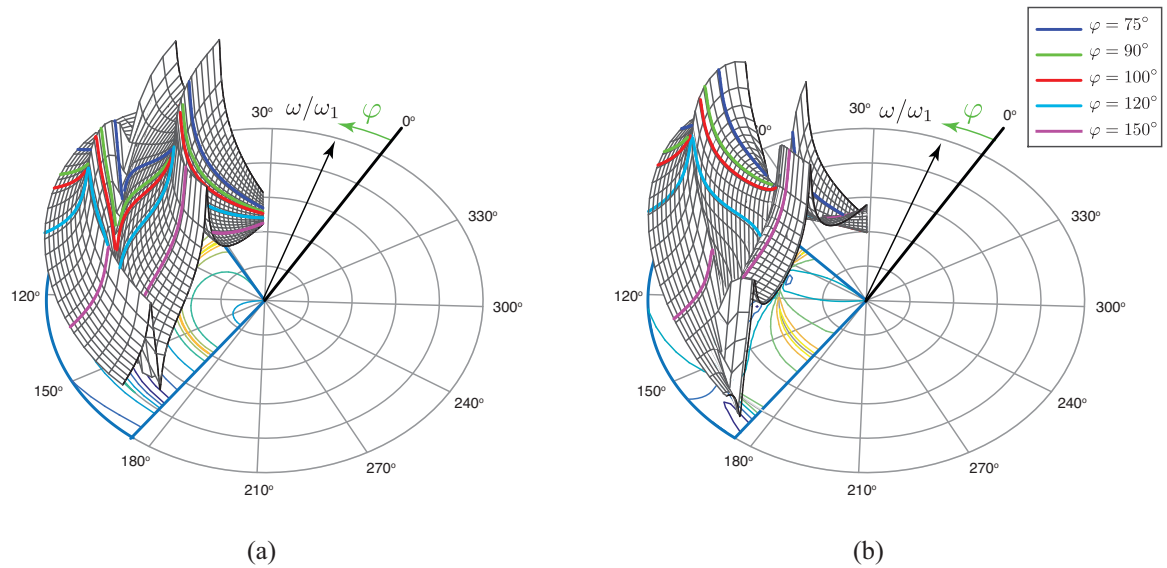


Fig. 7.8 Polar surface plot of FRFs at $u_2(L_2)$ due to a base excitation for a V-shaped resonator with respect to folding angle φ for $\hat{h} = 0.5$ that have 1:2 commensurate frequencies, contours of the FRF are projected on the polar domain: a) FRF for commensurate frequencies for $\hat{l} < 1$, solutions exist approximately ranging from 62° to 175° , b) FRF for commensurate frequencies for $\hat{l} > 1$, solutions exist for angles approximately ranging from 76° to 175° . The plots assume equal modal damping of $\zeta = 0.01$.

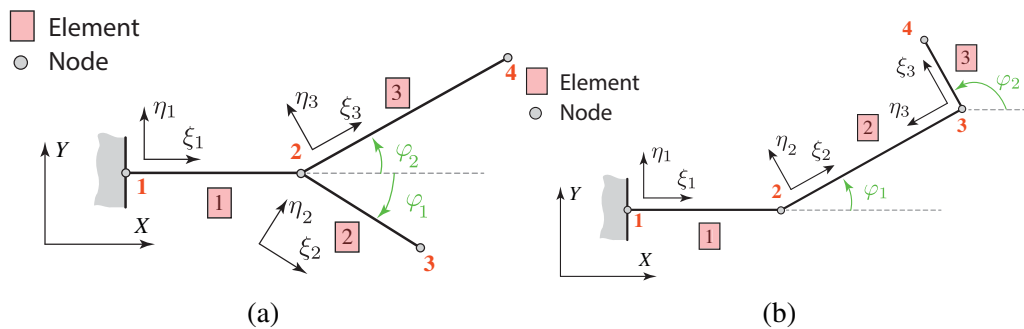


Fig. 7.9 Topology of Y and Z shaped resonators: a) Y- shaped resonator with a 3-DOF structure with $N = 3$ elements, $F = 2$ free nodes, and $\theta = 1$ internal nodes, and b) Z- shaped resonator with a 3-DOF structure with $N = 3$ elements, $F = 1$ free nodes, and $\theta = 2$ internal nodes.

where

$$\dot{w}_1 = \dot{w}_i^* + \dot{w}_B, \quad (7.51)$$

$$\dot{w}_2 = \dot{w}_2^* \cos(\varphi_1) + \dot{w}_{1,\xi_1|L_1} \xi_2 \cos(\varphi_1) + \dot{w}_{1|L_1}, \quad (7.52)$$

$$\dot{u}_2 = \dot{w}_2^* \sin(\varphi_1) + \dot{w}_{1,\xi_1|L_1} \xi_2 \sin(\varphi_1), \quad (7.53)$$

$$\dot{w}_3 = \dot{w}_3^* \cos(\varphi_2) + \dot{w}_{1,\xi_1|L_1} \xi_3 \cos(\varphi_2) + \dot{w}_{1|L_1}, \quad (7.54)$$

$$\dot{u}_3 = \dot{w}_3^* \sin(\varphi_2) + \dot{w}_{1,\xi_1|L_1} \xi_3 \sin(\varphi_2). \quad (7.55)$$

The squares of the modal frequencies are the eigenvalues of the system in Eqn. (7.40.) The coefficients of the stiffness and mass matrix for the *Y*-Shaped resonator are reported in Appendix C.1. Appendix C.1 also provides the expression of the generalized forces given a generic base excitation.

7.3.4 Case $N = 3$: **Z-shaped resonator**

Following the same approach, the BC's for the *Z*-shaped structure, have the following form:

$$\begin{aligned} w_1(0,t) = 0, \quad \frac{\partial w_1}{\partial \xi_1}(0,t) = 0, \\ w_2^*(0,t) = 0, \quad \frac{\partial w_2^*}{\partial \xi_2}(0,t) = 0, \\ w_3^*(0,t) = 0, \quad \frac{\partial w_3^*}{\partial \xi_3}(0,t) = 0, \end{aligned} \quad (7.56)$$

$$E_3 I_3 \frac{\partial^2 w_3^*}{\partial \xi_3^2}(L_3,t) = 0, \quad E_1 I_1 \frac{\partial^2 w_1}{\partial \xi_1^2}(L_1,t) = E_2 I_2 \frac{\partial^2 w_2^*}{\partial \xi_2^2}(0,t),$$

$$\text{and } E_2 I_2 \frac{\partial^2 w_2^*}{\partial \xi_2^2}(L_2,t) = E_3 I_3 \frac{\partial^2 w_3^*}{\partial \xi_3^2}(0,t)$$

that yields the following:

$$a_{2,2} = \frac{E_1 I_1 (a_{2,1} + 3a_{3,1} L_1)}{E_2 I_2}, \quad (7.57a)$$

$$a_{2,3} = \frac{E_2 I_2 (a_{2,2} + 3a_{3,2} L_2)}{E_3 I_3}, \quad (7.57b)$$

$$a_{3,3} = -\frac{a_{2,3}}{3L_3}. \quad (7.57c)$$

The generalized coordinate are $a_{2,1}$, $a_{3,1}$ and $a_{2,2}$. The expression of the kinetic energy T is:

$$T = \frac{1}{2} \int_0^{L_1} \mu_1 \dot{w}_1^2 d\xi_1 + \frac{1}{2} \int_0^{L_2} \mu_2 (\dot{w}_2^2 + \dot{u}_2^2) d\xi_2 + \frac{1}{2} \int_0^{L_3} \mu_3 (\dot{w}_3^2 + \dot{u}_3^2) d\xi_3, \quad (7.58)$$

where

$$\begin{aligned}
 \dot{w}_1(\xi_1) &= \dot{w}_i^* + \dot{w}_B, \\
 \dot{w}_2 &= \dot{w}_2^* \cos(\varphi_1) + \dot{w}_{1,\xi_1|L_1} \xi_2 \cos(\varphi_1) + \dot{w}_{1|L_1}, \\
 \dot{u}_2 &= \dot{w}_2^* \sin(\varphi_1) + \dot{w}_{1,\xi_1|L_1} \xi_2 \sin(\varphi_1), \\
 \dot{w}_3 &= \dot{w}_3^* \cos(\varphi_2) + (\dot{w}_{1,\xi_1|L_1} + \dot{w}_{2,\xi_2|L_2}) \xi_3 \cos(\varphi_2) + \dot{w}_{2|L_2}, \\
 \dot{u}_2 &= \dot{w}_2^* \sin(\varphi_2) + (\dot{w}_{1,\xi_1|L_1} + \dot{w}_{2,\xi_2|L_2}) \xi_3 \sin(\varphi_2) + \dot{u}_{2,\xi_2|L_2}.
 \end{aligned}
 \tag{7.59}$$

The expression of the stiffness and mass matrix, as well as those of the generalized forces, for the Z-shaped structure are reported in Appendix C.2.

Qualitatively the same conclusions drawn for the V-shaped resonator can be extended to these two families of resonators presented in this section. However, for sake of brevity we report in Tables 7.4 and 7.5 some of the possible solutions and the corresponding non-dimensional ratios. Note that by varying the folding angles allows the design of resonators with various topologies that have modal frequencies with $\omega_2/\omega_1 = 2$ and $\omega_3/\omega_1 = 3$.

Table 7.4 Non-dimensional ratios for Y-shaped resonators with $\omega_2/\omega_1 = 2$ and $\omega_3/\omega_1 = 3$ resonances. It is assumed that the resonators have square cross sections and are made by the same material.

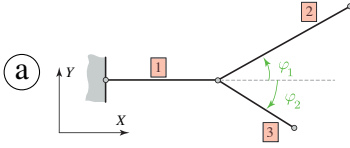
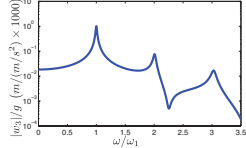
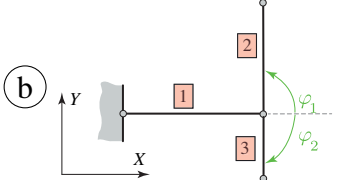
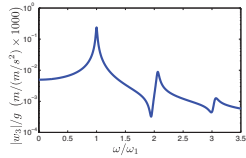
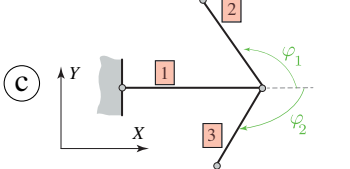
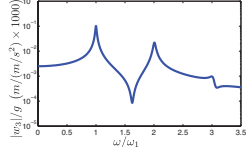
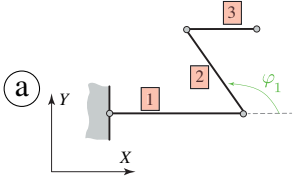
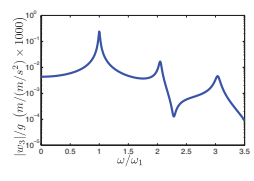
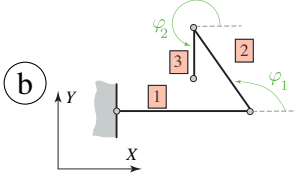
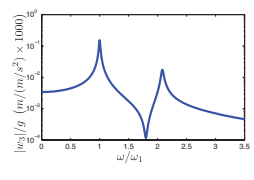
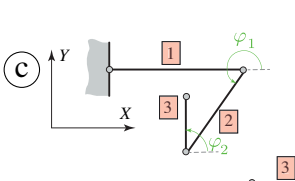
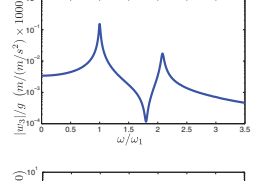
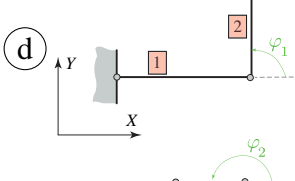
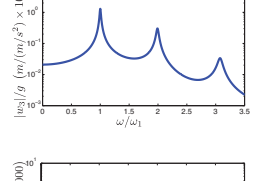
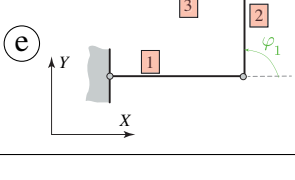
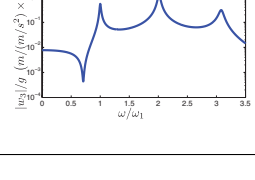
Topology	\hat{h}_i	\hat{l}_i	φ	FRF
	$\hat{h}_1 = 1.00$ $\hat{h}_2 = 0.53$ $\hat{h}_3 = 0.50$	$\hat{l}_1 = 1.00$ $\hat{l}_2 = 0.90$ $\hat{l}_3 = 0.75$	$\varphi_1 = 45^\circ$ $\varphi_2 = -45^\circ$	
	$\hat{h}_1 = 1.00$ $\hat{h}_2 = 0.50$ $\hat{h}_3 = 0.50$	$\hat{l}_1 = 1.00$ $\hat{l}_2 = 0.62$ $\hat{l}_3 = 0.50$	$\varphi_1 = 90^\circ$ $\varphi_2 = -90^\circ$	
	$\hat{h}_1 = 1.00$ $\hat{h}_2 = 0.50$ $\hat{h}_3 = 0.45$	$\hat{l}_1 = 1.00$ $\hat{l}_2 = 0.55$ $\hat{l}_3 = 0.43$	$\varphi_1 = 135^\circ$ $\varphi_2 = 225^\circ$	

Table 7.5 Non-dimensional ratios for Z-shaped resonators with $\omega_2/\omega_1 = 2$ and $\omega_3/\omega_1 = 3$. The resonators have square cross sections and each member is composed of the same material.

Topology	\hat{h}_i	\hat{l}_i	φ	FRF
	$\hat{h}_1 = 1.00$ $\hat{h}_2 = 0.50$ $\hat{h}_3 = 0.35$	$\hat{l}_1 = 1.00$ $\hat{l}_2 = 0.44$ $\hat{l}_3 = 0.36$	$\varphi_1 = 135^\circ$ $\varphi_2 = 0^\circ$	
	$\hat{h}_1 = 1.00$ $\hat{h}_2 = 0.60$ $\hat{h}_3 = 0.35$	$\hat{l}_1 = 1.00$ $\hat{l}_2 = 0.55$ $\hat{l}_3 = 0.39$	$\varphi_1 = 110^\circ$ $\varphi_2 = 270^\circ$	
	$\hat{h}_1 = 1.00$ $\hat{h}_2 = 0.60$ $\hat{h}_3 = 0.35$	$\hat{l}_1 = 1.00$ $\hat{l}_2 = 0.55$ $\hat{l}_3 = 0.39$	$\varphi_1 = 250^\circ$ $\varphi_2 = 90^\circ$	
	$\hat{h}_1 = 1.00$ $\hat{h}_2 = 0.61$ $\hat{h}_3 = 0.38$	$\hat{l}_1 = 1.00$ $\hat{l}_2 = 0.54$ $\hat{l}_3 = 0.75$	$\varphi_1 = 90^\circ$ $\varphi_2 = 0^\circ$	
	$\hat{h}_1 = 1.00$ $\hat{h}_2 = 0.91$ $\hat{h}_3 = 0.41$	$\hat{l}_1 = 1.00$ $\hat{l}_2 = 1.20$ $\hat{l}_3 = 0.83$	$\varphi_1 = 90^\circ$ $\varphi_2 = 180^\circ$	

7.4 Design charts for the V-shaped resonator

In the spirit of this work, this section presents the design chart for the V-shaped resonators. Furthermore, the folding angle φ plays the role of packing (or unpacking) the mass and increasing (or decreasing) the stiffness of the structure while maintaining the frequencies in a given integer ratio. The effect of the folding angle φ on the frequency is shown in Figures 7.10 and 7.11. The frequencies are normalized with respect to those of a cantilevered beam having the dimension of the first member of the resonator. The normalized bending frequencies $\tilde{\omega}$ is the ratio between the first bending frequency of the resonator and the first bending frequency of the cantilever beam. The non-dimensional frequency are the dotted curves meanwhile the solid line are the non-dimensional lengths \hat{l} . Provided that the

non-dimensional ratios are maintained, Figures 7.10 and 7.11 are universal charts useful to design one-to-two resonators with square cross sections. It must be noticed that the presence of the second member allows the following advantages: (a) the first bending frequencies of the resonator is lower than the cantilevered beam counterpart; (b) the resonator has exactly two commensurate frequencies, equal to the number of members. While the main focus is on designing resonators with commensurate frequencies vary the orientation of the members in a given volume allows for design of energy harvesting devices for low frequency applications [96].

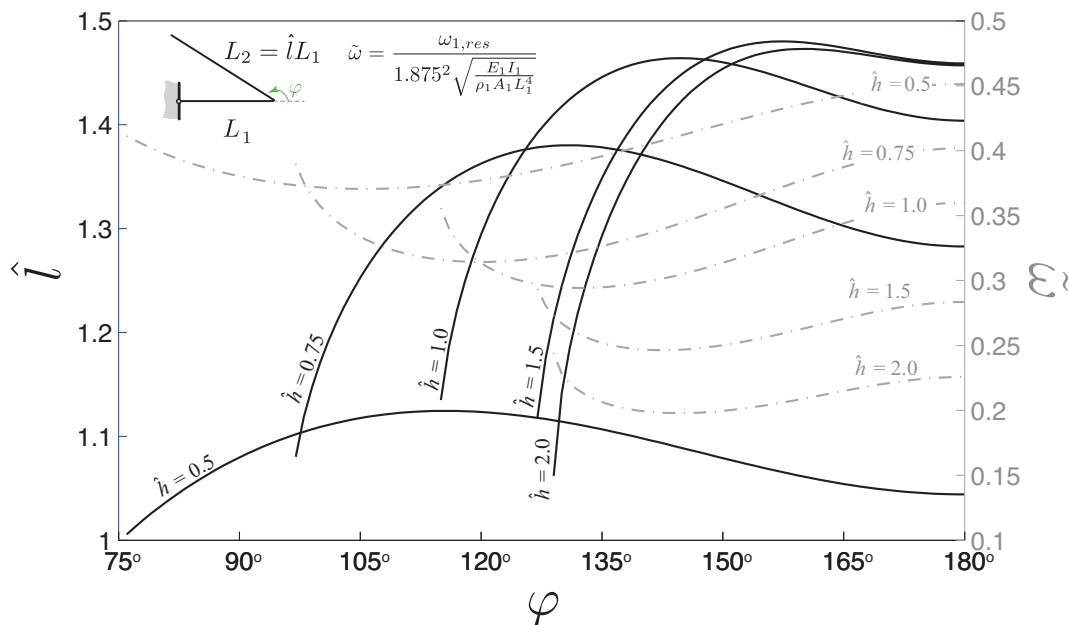


Fig. 7.10 Design chart for $\omega_2/\omega_1 = 2$ resonator with square cross sections. Curves are solutions $\tilde{\omega}(\varphi, \hat{h}, \hat{l})$ from the outer envelope for different \hat{h} . The dotted lines are the nondimensional bending frequencies; the solid lines are the nondimensional length \hat{l} . Note also that beside the advantage of having two commensurable frequencies, the first bending frequency of the resonator ranges between 0.45 and 0.2 of the cantilevered beam counterpart.

In the interest of clarity herein is reported an example of resonator sizing using the design chart illustrated above. Let us consider the case of a cantilever beam having the following dimensions $a = b = 10$ mm and $L = 150$ mm. The beam is made by an aluminum alloy having the following properties: Young’s modulus $E = 73$ GPa, Poisson’s ratio $\nu = 0.3$ and density $\rho = 2780$ kg/m³. The first two bending frequencies are respectively $f_1 = 188$ Hz and $f_2 = 1176$ Hz. Let us suppose that we are interested at designing a resonator having about 40% of reduction of the first bending frequencies with respect to the cantilever beam and with the second frequency commensurate in a ratio one-to-two and suppose that the thickness ratio should be $\hat{h} = 0.75$. Let us draw a line starting from the right hand side of the design

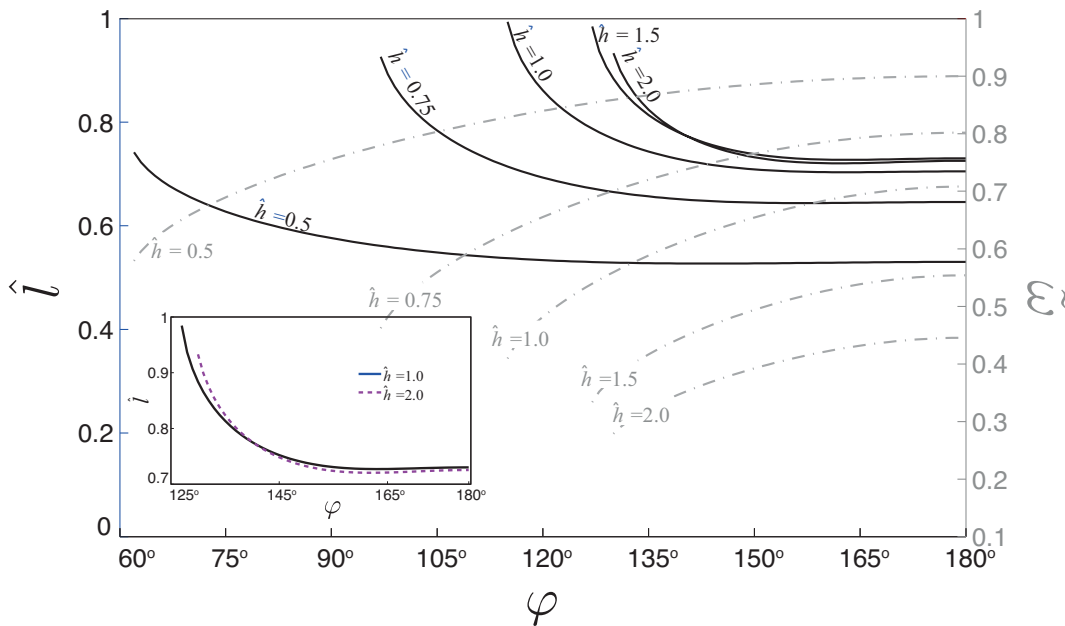


Fig. 7.11 Design chart for $\omega_2/\omega_1 = 2$ resonator with a square cross section. The figure reports solutions $\tilde{\omega}(\varphi, \hat{h}, \hat{l})$ from the inner envelope for different \hat{h} . The dotted lines are the non-dimensional bending frequencies; the solid lines are the nondimensional length \hat{l} . The design map allows the rapid design of resonator once the geometry of the first element is fixed. The inset shows a zoomed view of the two envelopes with $\hat{h} = 1.5$ and $\hat{h} = 2.0$ respectively. Note also that beside the advantage of having two commensurable frequencies, the first bending frequency of the resonator can be adjusted to be lower than its cantilevered counterpart in the range of 28% to 90%.

map at $\hat{\omega} = 0.6$. We cross the line of $\hat{h} = 0.75$ at $\varphi = 111^\circ$. Now that the angle has been identified, the value of \hat{l} is identified moving along the direction of the green arrow reported in Figure 7.12 until one cross the solid black line at $\hat{h} = 0.75$. The value of \hat{l} is therefore identified and it is $\hat{l} = 0.73$. Substituting this value into the reduced order model yields the following frequencies: $f_1 = 114.5\text{Hz}$ and $f_2 = 229.1\text{Hz}$. The two bending are therefore in a ratio 2.0013 and are in the range of frequencies sought.

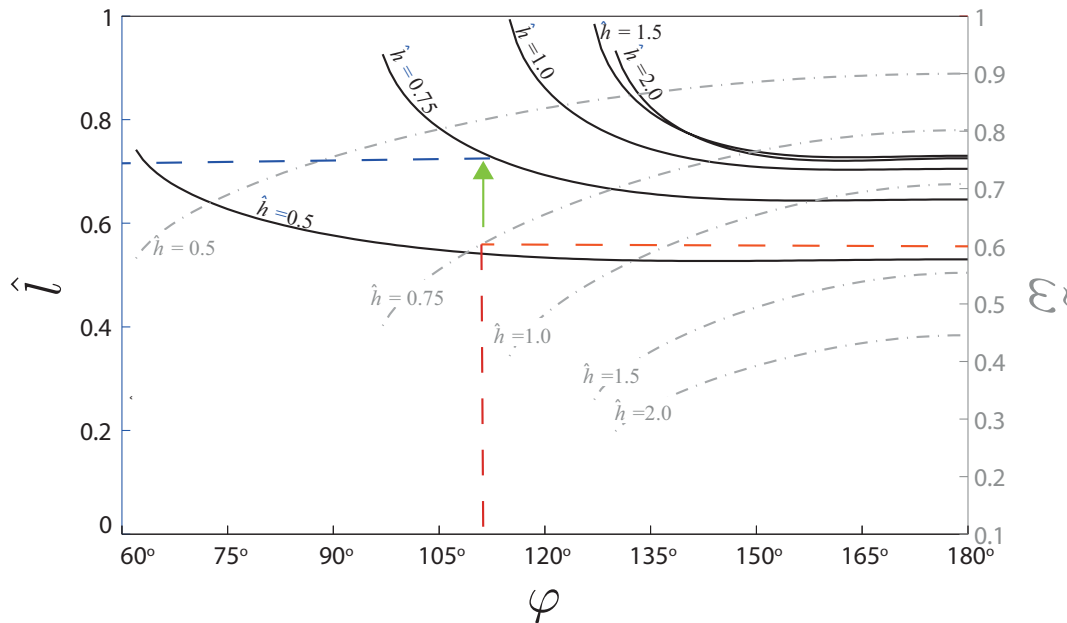


Fig. 7.12 Exemplification of the usage of the universal chart to design a resonator in a ratio one-to-two.

7.5 Summary and conclusion

In this chapter, the equations of motion of a multi-member angle-shaped resonator have been derived. The equations are then specialized for the case of a two members and three members structure. The equation are then parametrically solved using a root finding algorithm to identify solutions which exhibit commensurate frequencies in the ratio one-to-two for the V-shaped and 1:2 ,1:3 for the three members resonator. For the case of the V-shaped resonator, it is seen that solutions are quadratic in the parameter \hat{l} , meaning that in general two solutions exists. However, in some cases, only one solution exists, in this case the locus of solutions (hyper-surface) presents a sort of bifurcation. A discussion on the physic behind the bifurcation phenomena seen for the solutions is provided, particularly on the effect of

the position of the overall center of gravity of the system to the solution identified. It is shown how solution belonging to the outer envelope affect more the overall CG position. The analytical solution for the frequencies equation of the V-shaped resonator has been derived. The reduced order model and the analytical model have been validated through a comparative study against finite elements. It has been shown that a rule of thumb holds, i.e. the number of commensurate frequencies equals the number of the members composing the structure. Moreover, it has been shown that higher frequencies with respect to the ones sought have a certain set space and are not commensurate, meaning that the system can effectively be modeled as a N-DOF system. Universal design chart have been provided, to help sizing the resonator at a glance.

Chapter 8

Electro-mechanical model for the V-shaped resonators

Part of the derivation presented in this chapter has been previously published in the SPIE SS/NDE Conference Proceedings. The full citation is provided below

Danzi, F. and Gibert, J. M. "*Exact dynamics of an angle-shaped resonator for energy scavenging applications*". Proc. of SPIE Smart Structures and Materials + Nondestructive Evaluation and Health Monitoring, 2018, Denver, Colorado (USA), 5-8 March 2018, <https://doi.org/10.1117/12.2296642>.

8.1 Introduction

This chapter presents the derivation of the linear electro-mechanical equation of motion for the angle-shaped resonators. The electro-mechanical equation of motion are obtained by means of the extended Hamiltonian principle and then solved using a Rayleigh-Ritz approach to obtain the discretized electromechanical equations.¹ Following Haddow *et al* [89] and consistently with the derivation presented in the previous chapter, we assumed a polynomial admissible function of undetermined constants based on the equilibrium equation of each member in the absence of external loading. The electro-mechanical model accounts for the

¹The Rayleigh-Ritz approach leads to the same discretized equations of motion of the assumed mode approach, as discussed in Meirovitch [201]. Indeed the two methods are closely related despite the first begins with the spatial discretization of the eigenvalue problem while the second is concerned with the spatial discretization of the boundary-value problem.

presence of a unimorph layer of Polyvinylidene fluoride (PVDF) attached to the first member for a length l_p starting from the root.

Once the model is established, the performance of the resonator when subjected to multiple harmonic excitations are investigated. Excitation with different energy content in the two harmonics are considered. The investigation considers also for the presence of a phase excitation α among the two harmonics. A metric defined as in [202] is used to investigate the sensitivity of the harvester to the phase excitation. The performances of five resonators at different folding angle φ are compared. The resonators are designed such that they have the same bending frequencies. The design procedure to arrive to the dimensional parameters of the resonators under study is summarized in section 8.2. Particularly, three resonators are taken from the inner envelope, i.e. for those locus of solutions in which $L_2 < L_1$ (or equivalently $\hat{l} < 1$) while the other two solutions are from the outer envelope, namely $\hat{l} > 1$.

Among the possible non-transient excitations suitable for energy harvesting from vibrations, we focus on excitations containing a dominant harmonic component and multiple subharmonics and/or super harmonics [203]. These signals can have substantial amount of energy contained in their fundamental frequency component and smaller amounts of energy in their sub and super harmonic components. These spectrums are seen in many rotary machines such as: helicopter rotors, car engines, wind turbines etc. Figure 8.1 shows the power spectrum from a dc motor illustrating this phenomena [204]. The vibrations are measured in three directions. In all directions the dominant energy content lies at approximately 50 Hz, while the higher order components contain a significantly smaller amount of energy.

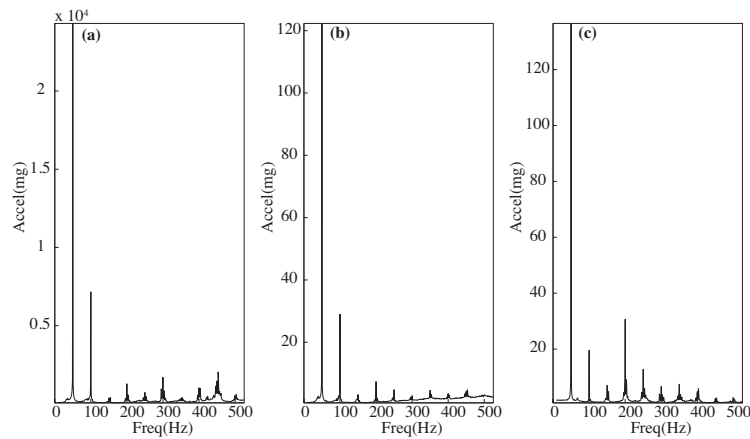


Fig. 8.1 Accelerometer measurements from a Ward Leonard DC generator: (a) x -axis, (b) y -axis, and (c) z -axis. Data was downloaded from the EH Network Data Repository (<http://eh-network.org/data>).

Energy can be extracted from this source of excitation using: a harvester that is parametrically excited [203, 205, 206]², array of fixed frequency vibration energy harvesters each one tuned at the frequency of interest, or a single harvester designed to operate at two modal frequencies [208–212]. In this analysis the modal frequencies are restricted to be integer multiples of the dominant harmonic in the excitation, particularly herein are considered the case of one-to-two frequency's ratio.

8.2 Resonator Design

In elucidating the effect of folding angle we seek resonators that have the same bending frequencies. However, designing resonators that have the same modal frequencies with different configurations is not a trivial task. The process begins by arbitrarily picking five solutions from the design envelope of planar resonator reported in Figure 8.2. As it has been already discussed in the previous chapter, the solutions to the frequency equation of the reduced order model that exhibit commensurate frequencies are hyper-surfaces S , $S \in \mathbb{R}^{12}$ [213]. Assuming that the two members are made of the same material, fixing the orientation of the first beam, the width b of the both beams, and defining the non dimensional ratios $\hat{l} = L_2/L_1, \hat{h} = h_2/h_1$, solutions to the frequencies equations collapse in dimensionality to a surface \bar{S} , $\bar{S} \in \mathbb{R}^3$. This surface allows one to design the resonators based on the thickness ratio, the folding angles and the length ratios. Further, constraining the thickness parameter (\hat{h}) to a fixed value, solutions to the frequencies equation become a planar curve \mathcal{C} , i.e. $\mathcal{C} \in \mathbb{R}^2$. Figure 8.2 presents the design curve, \mathcal{C} , for the 1:2 angle-shaped resonators as a function of the length ratio \hat{l} and the folding angle φ when the thickness ratio is $\hat{h} = 0.5$. Those solutions are obtained for rectangular cross sections; the width of the beam members is fixed and it is $b = 12mm$. Markers placed on Fig. 8.2 indicate the folding angle and lengths of the five configurations selected. As can be seen From Figure 8.2, at φ equal to 80° corresponds only one solution, namely that of the inner surface. Contrary at $\varphi = 90^\circ$ and $\varphi = 120^\circ$ solutions are found on both the inner and outer envelope. Table 8.1 reports the nondimensional ratios, folding angles and the first bending frequencies for the resonators corresponding to these configurations. Henceforth, the resonators are named as V_{80} , L^i , V_{120}^i , L^o , V_{120}^o according to the folding angle φ , the apex stands for solution from the inner

²Parametrically excited systems are characterized by differential equations with time varying coefficients. In nonparametric excitations a large amplitude response is only present when the frequency of excitation is close to the linear natural frequency. Conversely, parametric excitations produce a large amplitude response even if the excitation frequency is away from the linear natural frequency. [207]

Table 8.1 Non-dimensional ratios for the different resonators and first bending frequency [Hz]. The solutions are obtained using a root finding algorithm to have commensurable frequencies in a ratio 1:2 using the reduced order model. [194]

Resonator	\hat{h}	\hat{l}	$\varphi[deg]$	f_1	f_2
V_{80}	0.5	0.8019	80	16.86	33.72
L^i	0.5	0.6646	90	20.79	41.58
L^o	0.5	1.0778	90	12.07	24.14
V_{120}^i	0.5	0.5621	120	25.84	51.68
V_{120}^o	0.5	1.1967	120	11.23	22.46

i and outer o envelope respectively. Table 8.2 lists the dimensions and properties of these resonators.

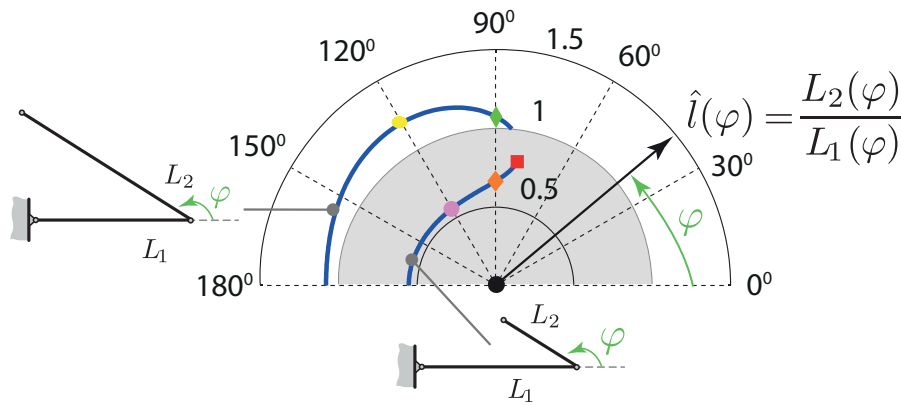


Fig. 8.2 Polar representation of the solution having 1:2 frequency ratio as a function of the folding angle φ , $\hat{h} = 0.5$. The envelope is obtained considering rectangular cross sections for a fixed beams width (b). Solutions in the white region are for $\hat{l}(\varphi) > 1$, solutions in gray region are for $\hat{l}(\varphi) < 1$. The markers indicate the five resonators considered for the sake of comparison.

Now that the configurations are chosen, we note that constraining the geometry of the first beam and the thickness ratio between beams leads to structures that exhibit different bending frequencies, as reported in Table 8.1. In all configurations the ratio of modal frequencies remains 1:2; however, the frequencies increase with an increase in the folding angle for the case of the inner envelope while, for solutions of the outer envelope the bending frequencies decrease when the angle increase. In order to have five resonators with the same bending

Table 8.2 Configuration parameters for the angled resonators.

h_1	h_2	b	μ_1	μ_2	$E_1 I_1$	$E_2 I_2$
mm	mm	mm	kg/m	kg/m	Nm ²	Nm ²
2	1	12	0.0694	0.0694	0.5512	0.0689

frequencies, the structures are resized according to the following scaling equation

$$l_{1_{scaled}} = l_1 \sqrt{\frac{f}{f_{V_{80}}}}. \quad (8.1)$$

It is worth noticing from Eqn. (8.1) that the frequencies of the V_{80} resonator has been considered as the reference value. The scaled length of the L^i , V_{120}^i , L^o , V_{120}^o of the first members of the resonator considered are listed in Table 8.3. For the sake of completeness, Table 8.3 reports also the bending frequencies obtained after the scaling. Notice that the non-dimensional ratios listed in Table 8.1 still hold and the dimensions of the second beam can be easily determined. Having noted that the frequencies of the structure are sensitive to the dimensions of the member as well as to the folding angle, three among the five resonators considered herein were cut out from an aluminum rectangular plate using a water jet cutter (WJC). Indeed, the WJC has the following advantages: high precision at sharp corner at the joining of the two members, (b) no heat-affected zone are present.

In Table 8.4 are reported the bending frequencies obtained by means of the analytical model and the reduced order model presented in the previous chapter along with those obtained with a finite element analysis (FEA) and, finally, for the solutions of the inner envelope, with experiments. The solutions from each analysis agrees with each other and, where present, with the experiments. Figure 8.3 reports the mode shapes of the five resonators considered herein. Additionally, the mode shapes obtained with the analytical solution, the reduced order model and the FEA match closely. Particularly, the results pertaining the FEA were obtained employing 100 elements per member. For the sake of comparison we report herein the mode shapes obtained with the reduced order model, Fig 8.3 and the FEA. Figure 8.4 illustrates the experimental setup used for the experiments. It is worth mention the following: a) the third bending frequency has a set space from the first two and, b) neither the third nor the higher order frequencies are commensurate. This allow to handle the system as a two degree of freedom system. In particular, the third bending frequency are given as follow: 149.12Hz for the V_{80}^i resonator, 175.70Hz and 126.70 for the inner and outer L-shaped resonator respectively, finally for the V_{120} the third bending frequency is 126.00Hz for the inner solution and 112.36Hz for the outer solution. It is

Table 8.3 Scaled design: first beam length, and first two modal frequencies.

Resonator	L_1^{ii}	f_1 [Hz]	f_2 [Hz]
V_{80}^i	210.0	16.86	33.72
L^i	233.2	16.86	33.72
L^o	177.7	16.86	33.72
V_{120}^i	260.0	16.86	33.72
V_{120}^o	171.4	16.86	33.72

ⁱⁱ L_1 is scaled to have the same bending frequencies of the V_{80} resonator, 1:2 configurations are obtained using a root finding algorithm detailed in Danzi et al[194].

also noted, thanks to the FEA that the resonators have a torsional frequency in between the second and the third bending frequency. Particularly, the torsional frequency varies between 35.75Hz for the L^o resonator and 50.1Hz for the V_{120}^i resonator. In view of the above observations, the use of the reduced order model derived in the previous section, to study the performance of the harvesters, is justified.

Table 8.4 Natural frequencies [Hz] of the angle-shaped resonators under study.

Resonator	Analytical		FEA ⁱ		ROM		Experimental	
	f_1	f_2	f_1	f_2	f_1	f_2	f_1	f_2
V_{80}^i	16.79	33.26	16.84	33.18	16.86	33.72	17.0	33.8
L^i	16.82	33.11	16.84	33.18	16.86	33.72	16.77	33.70
L^o	16.82	33.11	16.71	33.50	16.86	33.72	-	-
V_{120}^i	16.80	33.19	16.80	33.22	16.86	33.72	17.0	34.0
V_{120}^o	16.80	33.19	16.80	33.22	16.86	33.72	-	-

ⁱ 10^2 elements per member

8.3 Electro-mechanical equation of motion

The governing equation for the coupled electro-mechanical system is obtained by means of the extended Hamiltonian principle, that is

$$\int_{t_1}^{t_2} \mathcal{L} dt = \int_{t_1}^{t_2} (T - V + W_{ie}) dt \quad (8.2)$$

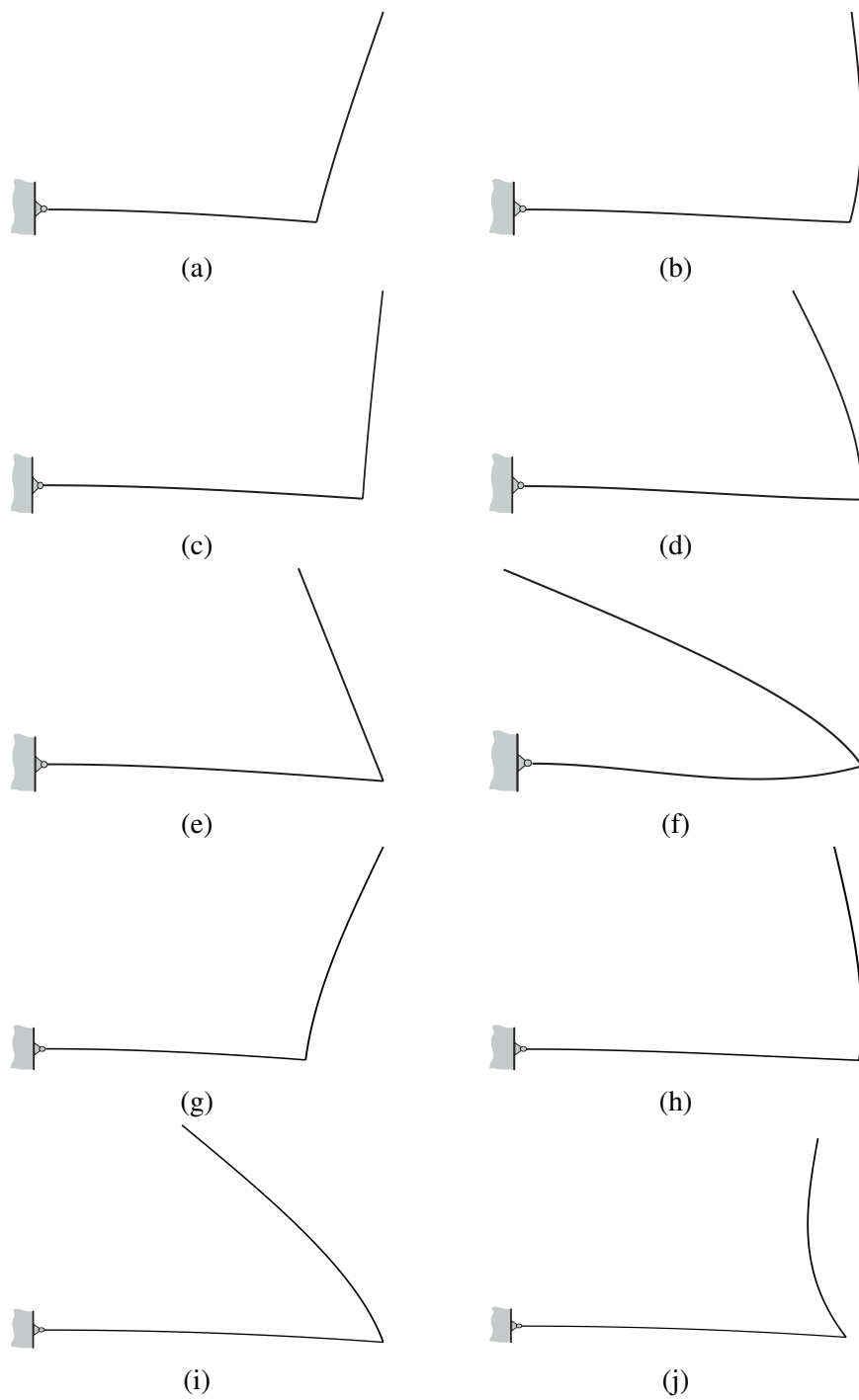


Fig. 8.3 First and second mode shape of the five resonators under study, drawn to scale: (a) and (b) V_{80}^i shaped resonator; (c) and (d) L^i shaped resonator; (e) and (f) V_{120}^i resonator, (g) and (h) L^o resonator and (i) and (j) V_{120}^o resonator

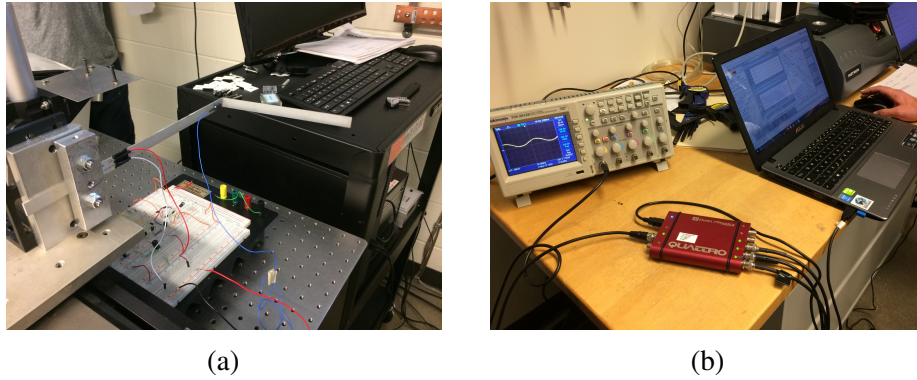


Fig. 8.4 Experimental setup: a) the V_{80} resonator mounted on the rigid support and connected to the base of the APS Dynamics ELECTRO-SEIS Shaker, b) the data acquisition system.

Table 8.5 Geometric and Material Properties of the PVDF

Young's Modulus, E_p	3000 MPa
Length, L_p	50 mm
Width, w_p	12 mm
Thickness, t_p	0.5 mm
Density, ρ_p	1700 kg/m ³
Piezoelectric strain constant, d_{31}	30 pC/N
Relative dielectric constant, ϵ_{33}/ϵ_0	12

where \mathcal{L} is the Lagrangian and T , V and W_{ie} are the kinetic energy, the total potential energy and the internal electrical energy, respectively. The expression of the kinetic and potential energy are modified with respect to those reported in the previous chapter to account for the presence of the piezoelectric layer laying on the first member for a length l_p . The electro-mechanical properties of the PVDF layer adopted in this analysis are listed in Table 8.5.

The internal electrical energy of the harvester can be expressed as follow

$$W_{ie} = \frac{1}{2} \int_V E_3 D_3 dV \quad (8.3)$$

where E_3 is the electric field in the y-direction and D_3 is the electric displacement in the y-direction. The Rayleigh approximation give rise to the following stiffness matrix coefficients

$$k_{11} = \frac{4L_2 E_1^2 I_1^2}{3E_2 I_2} + 4L_1 E_1 I_1, \quad (8.4)$$

$$k_{12} = \frac{4L_2E_1^2I_1^2L_1}{E_2I_2} + 6E_1I_1L_1^2 = k_{21}, \quad (8.5)$$

$$k_{13} = e_{31}bl_p(h_s + t_p) \quad (8.6)$$

$$k_{22} = \frac{12L_2E_1^2I_1^2L_1^2}{E_2I_2} + 12E_1I_1L_1^3, \quad (8.7)$$

$$k_{23} = \frac{3e_{31}bl_p^2(h_s + t_p)}{2} \quad (8.8)$$

$$k_{33} = 1/R. \quad (8.9)$$

Likewise, the expression of the mass matrix coefficient can be written as

$$m_{11} = \frac{A_1L_1^5\rho_1}{5} + \frac{4A_2L_1^2L_2^3\rho_2}{3} + \frac{11A_2E_1^2I_1^2L_2^5\rho_2}{105E_2^2I_2^2} + \frac{11A_2E_1I_1L_1L_2^4\rho_2}{15E_2I_2} + \frac{A_2E_1I_1L_1^2L_2^3\rho_2 \cos(\varphi)}{2E_2I_2} + A_2L_1^4L_2\rho_2 + 2A_2L_1^3L_2^2\rho_2 \cos(\varphi), \quad (8.10)$$

$$m_{12} = \frac{A_1L_1^6\rho_1}{6} + \frac{5A_2L_1^4L_2^2\rho_2 \cos(\varphi)}{2} + \frac{33A_2E_1I_1L_1^2L_2^4\rho_2}{20E_2I_2} + \frac{11A_2E_1^2I_1^2L_1L_2^5\rho_2}{35E_2^2I_2^2} + \frac{A_2E_1I_1L_1^3L_2^3\rho_2 \cos(\varphi)}{E_2I_2} + A_2L_1^5L_2\rho_2 + 2A_2L_1^3L_2^3\rho_2 =$$

$m_{21},$

$$m_{22} = \frac{A_1L_1^7\rho_1}{7} + \frac{33A_2E_1^2I_1^2L_1^2L_2^5\rho_2}{35E_2^2I_2^2} + \frac{33A_2E_1I_1L_1^3L_2^4\rho_2}{10E_2I_2} + \frac{3A_2E_1I_1L_1^4L_2^3\rho_2 \cos(\varphi)}{2E_2I_2} + A_2L_1^6L_2\rho_2 + 3A_2L_1^4L_2^3\rho_2 + 3A_2L_1^5L_2^2\rho_2 \cos(\varphi). \quad (8.12)$$

The electro-mechanical damping coefficient becomes

$$c_{31} = be_{31}l_p(h_s + t_p) \quad (8.13)$$

$$c_{32} = \frac{3be_{31}l_p^2(h_s + t_p)}{2} \quad (8.14)$$

$$c_{33} = -\frac{b\epsilon_{33}l_p}{tp} \quad (8.15)$$

It is worth notice that the complete damping matrix is obtained superimposing to the coefficients reported above, those obtained considering a proportional damping. In particular we assumed $\zeta = 0.1$, begin the latter the modal damping coefficient. The expression of the generalized force are given as follow

$$f_1 = \left[\frac{1}{3}\rho_1A_1L_1^3 + \frac{\rho_2A_2L_2(4E_2I_2L_1^2 + L_2(4E_2I_2L_1 + E_1I_1L_2)\cos(\varphi))}{4E_2I_2} + \frac{\rho_pA_p l_p^3}{3} \right] \ddot{w}_B(t), \quad (8.16)$$

$$f_2 = \left[\frac{1}{4} \rho_1 A_1 L_1^4 + \frac{\rho_2 A_2 L_2 (4E_2 I_2 L_1^3 + 3L_2 (2E_2 I_2 L_1^2 + E_1 I_1 L_1 L_2) \cos(\varphi))}{4E_2 I_2} + \frac{\rho_p A_p l_p^4}{4} \right] \ddot{w}_B(t). \quad (8.17)$$

A cursory inspection of Eqn. 8.16 allow one to speculate about the possible advantage offered by the angle-shaped resonator with respect to the L-shaped resonator. Indeed, it is worth noting that the term which multiply the $\cos \varphi$ become zero for the case of the L-shaped resonator.

8.4 Analysis of the performances

8.4.1 Identification of the optimal resistance

The comparison starts with the evaluation of the optimal resistance for each of the harvester selected. In the following analysis each harvester will work with its optimal resistance. The analysis is performed by parametrically changing the resistance between the upper and lower bounds and comparing the output the output power. Figure 8.5, reports the optimal resistances for the three resonators considered herein. It can be seen that the optimal resistance increase with the increasing of the folding angle. Only the resonator of the inner envelope are considered, because the resonator of the outer envelope are generally heavier and leads to a lower energy density.

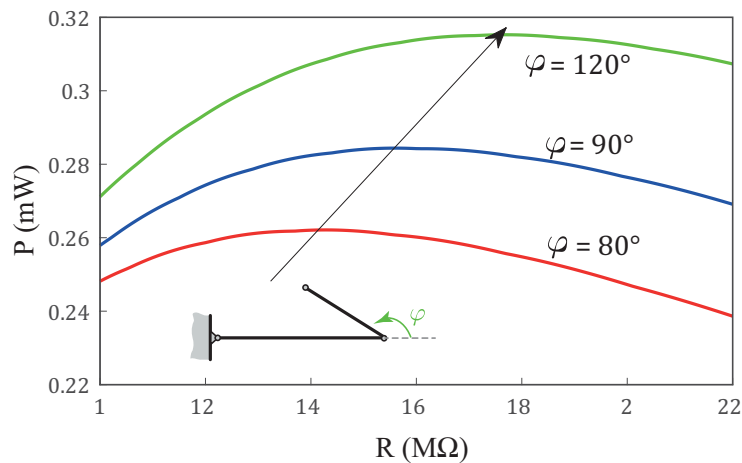


Fig. 8.5 Optimum resistance for the three angled resonators.

8.4.2 Performances of the resonator of the inner envelope

In the following we examine the power that can be scavenged from the harvesters when subjected to multiple harmonic excitations. Particularly, we focus on the following kind of excitation

$$\ddot{w}_b = \ddot{w}_{b_1} \cos(\omega t + \alpha) + \ddot{w}_{b_2} \cos(n\omega t) \quad (8.18)$$

where α is the phase difference between the two harmonic excitations, $n = 2$. Three cases of excitation are considered: a) $\ddot{w}_{b_1} = \ddot{w}_{b_2} = 0.1g$, b) $\ddot{w}_{b_1} = 0.1g$ and $\ddot{w}_{b_2} = 0.05g$ and c) $\ddot{w}_{b_1} = 0.05g$ and $\ddot{w}_{b_2} = 0.1g$. The instantaneous power scavenged is given as: $P(t) = V^2(t)/R$, where R is the leakage resistance while $V(t)$ is the instantaneous voltage. Consistently with the assumption of harmonic base excitation, $V(t)$ can be written as

$$V(t) = \frac{1}{2}V_0 \exp(j\omega t) + \frac{1}{2}\bar{V}_0 \exp(-j\omega t) = |V_\omega| \cos(\omega t + \vartheta) \quad (8.19)$$

where V_0 is $V_0 = V_{0R} + jV_{0I}$ and $\vartheta = \tan^{-1}(V_{0I}/V_{0R})$. In case of two base excitations with commensurate frequencies and phase shifting α among them, the Eq. 8.19 becomes

$$V(t) = |V_{\omega_1}| \cos(\omega_1 t + \vartheta_1 + \alpha) + |V_{\omega_2}| \cos(n\omega_1 t + \vartheta_2) \quad (8.20)$$

Since the system is linear one can use superposition to obtain the total voltage, eq. 8.20. In order to guarantee that the effect of nonlinearities is negligible we limited the base motion to low base acceleration. To investigate the effect of the phase shifting between the base excitations on the power harvested, we used the metric introduced in [202] defined as

$$\bar{P} = \frac{\max_t P(t, \alpha)}{\min_\alpha \max_t P(t, \alpha)} \quad (8.21)$$

referred in the following as the power normalized peak in time.

Figure 8.6 depicts the FRFs of the Voltage and of the Power density (power per unit mass) for each resonator. The resonators are subjected to a base excitation whose frequency is allowed to vary. As expected in all the plots one sees two resonant peaks occurring at a 1:2 frequency ratio. Additionally, Figure 8.6 illustrates that as the folding angle increases, the power per unit density harvested from the first harmonic component, i.e., the one with the frequency coincident with the first resonance of the structure, increase with respect to that scavenged from the second harmonic component. This leads to the observation that for folding angle greater than $\pi/2$ harvest more power from the primary component of the excitation. The latter observations also apply to the Voltage. In fact, the same conclusion can be drawn considering Figure 8.5. Indeed, if one draw a fictitious line at a fixed value of the

resistance in Figure 8.5, it can be seen that the resonators with higher folding angle ensure an higher output power. Figure 8.7 reports the power extracted over a cycle of oscillation. Also in this case, it appears from a cursory inspection of the curve reported in Figure 8.7 that the harvester having folding angle higher than $\pi/2$ is advantageous in terms of powered scavenged. Moreover, from Figure 8.7 one can notice that the variation of the power in time is limited if the second member is in the second quadrant ($\varphi > 90^\circ$). Examining the normalized power defined in Eqn.(8.21) for the three resonators considered herein are: $\bar{P}_{120} = 1.06$, $\bar{P}_{90} = 1.22$ and $\bar{P}_{80} = 1.30$. The latter results can be interpreted as the sensitivity of the harvester, at various folding angle φ , to the phase excitation. The lower the peak power in time the lower the sensitivity of the structure to the phase excitation.

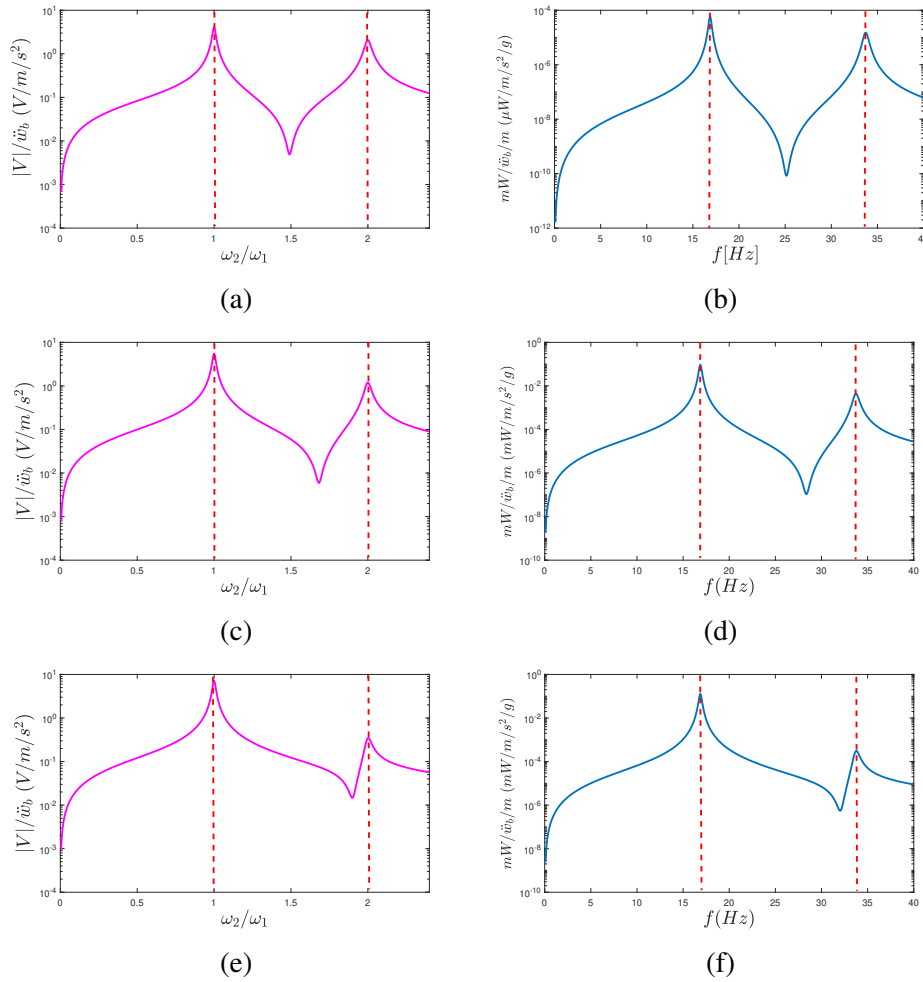
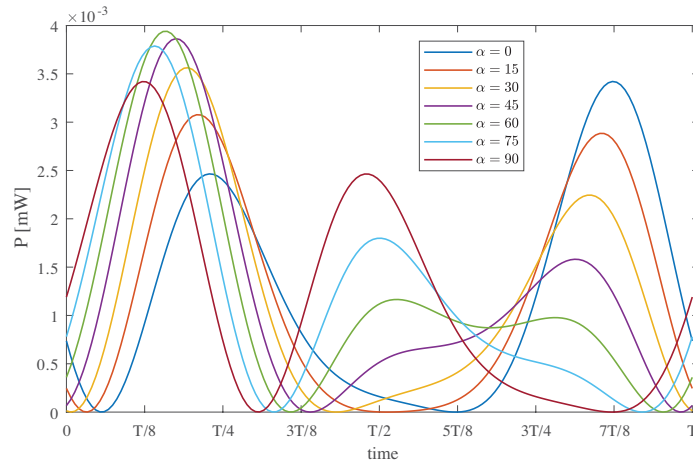
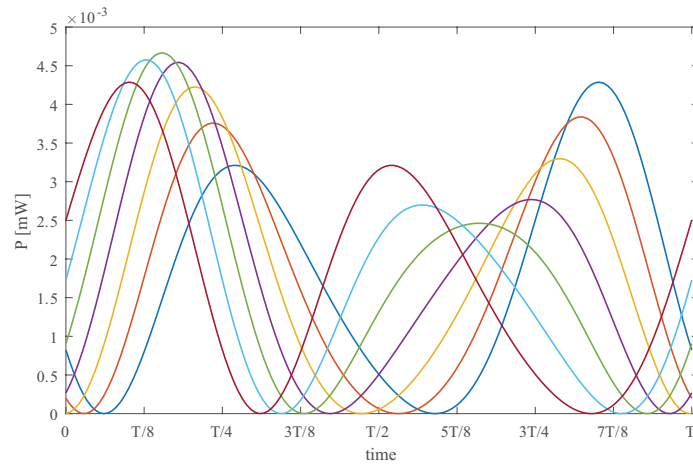


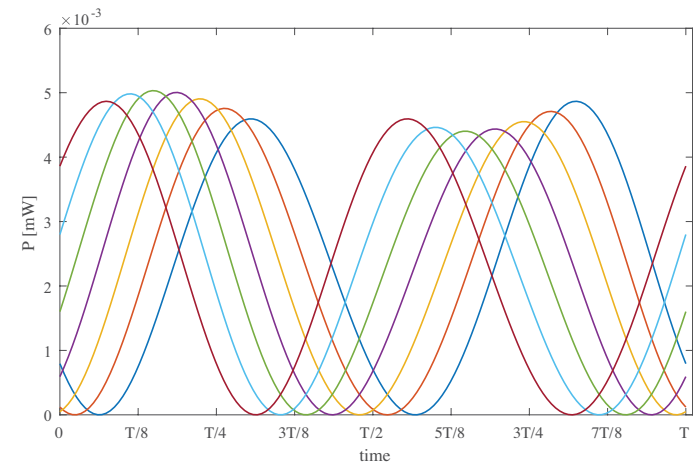
Fig. 8.6 FRF of Voltage(left) and of Power Density (right) for the three resonators under study, respectively from top to bottom V_{80} , L and V_{120} .



(a)



(b)



(c)

Fig. 8.7 Power harvested as a function of time over one cycle of oscillation: a) V_{80} resonator, b) L resonator, and c) V_{120} resonator.

In Figure 8.8 are reported the instantaneous voltage and power harvested in a cycle of oscillation. Figures 8.8a and 8.8b report the instantaneous voltage and power when the two harmonic have the same energy content, namely $0.1g$. In Figures 8.10c and 8.10d are depicted the instantaneous voltage and power when the energy content in the first harmonic is $0.1g$ while in the second harmonic is $0.05g$. Finally in Figures 8.10e and 8.10f are illustrated the instantaneous voltage and power when the second harmonic has an higher energy content, respectively $\ddot{w}_{b_1} = 0.05g$ and $\ddot{w}_{b_1} = 0.1g$. Comparing the instantaneous power reported in Figure 8.10d with respect to that of Figure 8.10f, it can be seen as the power harvested is more when the first harmonic has the higher energy content. Comparing the maximum attainable power in Figure 8.8, follows that a noticeable effect of the phase excitation can be seen: a) in the case of two frequencies with the same energy content or, b) when the second harmonic has an higher energy content with respect to the first excitation. A small variation of the power is seen when the second harmonic has a smaller energy content. This results is confirmed also looking at the peak power in time which, indeed is a measure of the sensitivity of the harvester to the base excitation. It is also worth noticing that the maximum attainable power for the different phase excitation present an antisymmetry with respect of the phase excitation. Particularly, looking at the curve with $\alpha = 0$ and $\alpha = \pi/2$ it can be noted that those are antisymmetric with respect to the half period of oscillation but the same peak power can be obtained. The same applies also to the pairs $\alpha = \pi/12$ and $\alpha = 11/12\pi$, $\alpha = \pi/6$ and $\alpha = 5\pi/6$ and so on. This can be explained with simple trigonometric reasoning looking at the equation 8.20. Moreover, in terms of power scavenged it can be noted that the case of excitation a) and b) are favorable while, when the second harmonic has an higher energy content the power attainable decrease considerably.

Next, are compared the performance of the L^i harvester. The same trends discussed above can also be observed in Figure 8.10, where are depicted the instantaneous voltage and power for the case of the L^i resonator for the three sources of excitation. The harvester is less sensitive to the phase excitation when the second harmonic component has the higher energy content. Comparing the Figures 8.8 and 8.10 follows that, under the same base excitation the V_{120}^i is advantageous with respect to the L^i in term of the power harvested. This can be explain because of the intrinsic coupling behavior that a general angle shaped structure has with respect to the L-shaped configuration, as it as been already pointed out by looking at the generalized force vectors. However, the L-shaped structure presents a smaller value of the peak power in time in all the cases analyzed, meaning that the L-shaped is less sensitive than the V_{120}^i to the phase excitation.

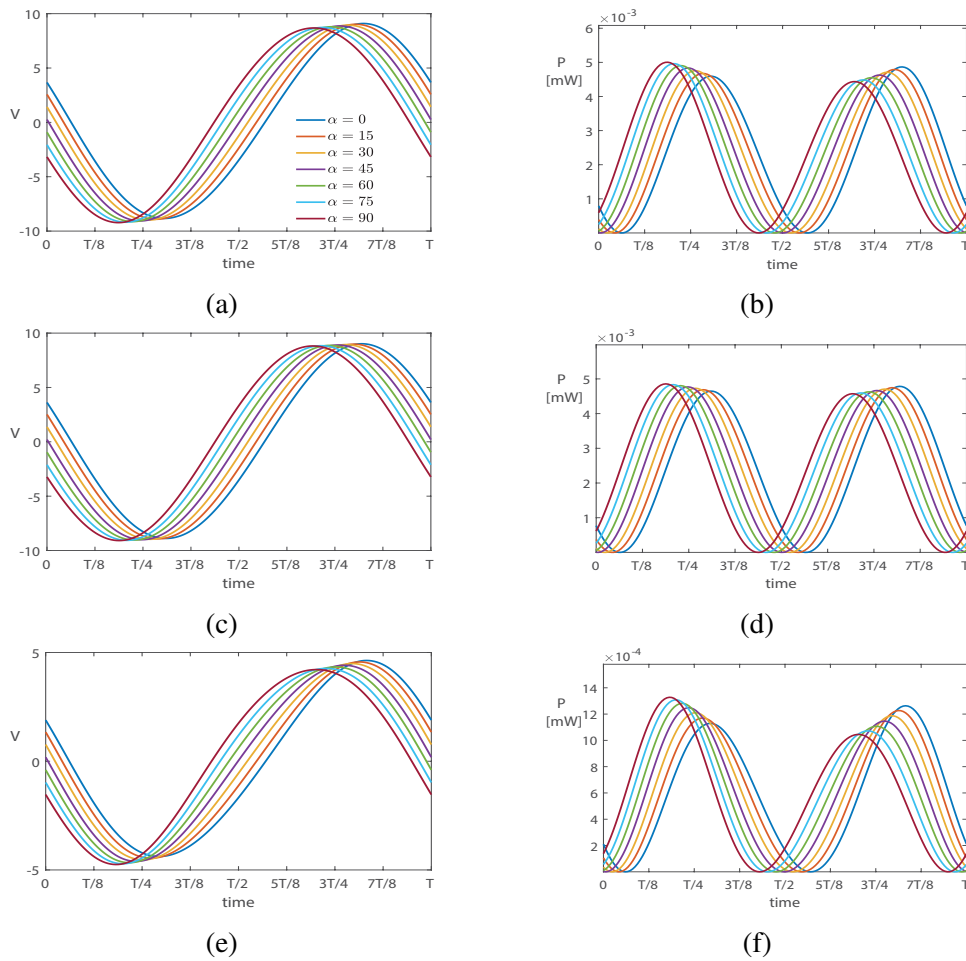


Fig. 8.8 Effect of the phase shifting angle α on the instantaneous voltage (Figures (a)-(c)-(e)) and instantaneous power (Figures (b)-(d)-(f)) produced by the V_{120}^i harvester subjected to double harmonics. Figures (a) and (b) are relative to the case of excitation with the same energy content. Figures (c) and (d) are those of excitation with $\ddot{w}_{b_1} = 0.1g$ and $\ddot{w}_{b_1} = 0.05g$. Finally Figures (e) and (f) are relative to the case with $\ddot{w}_{b_1} = 0.05g$ and $\ddot{w}_{b_1} = 0.1g$.

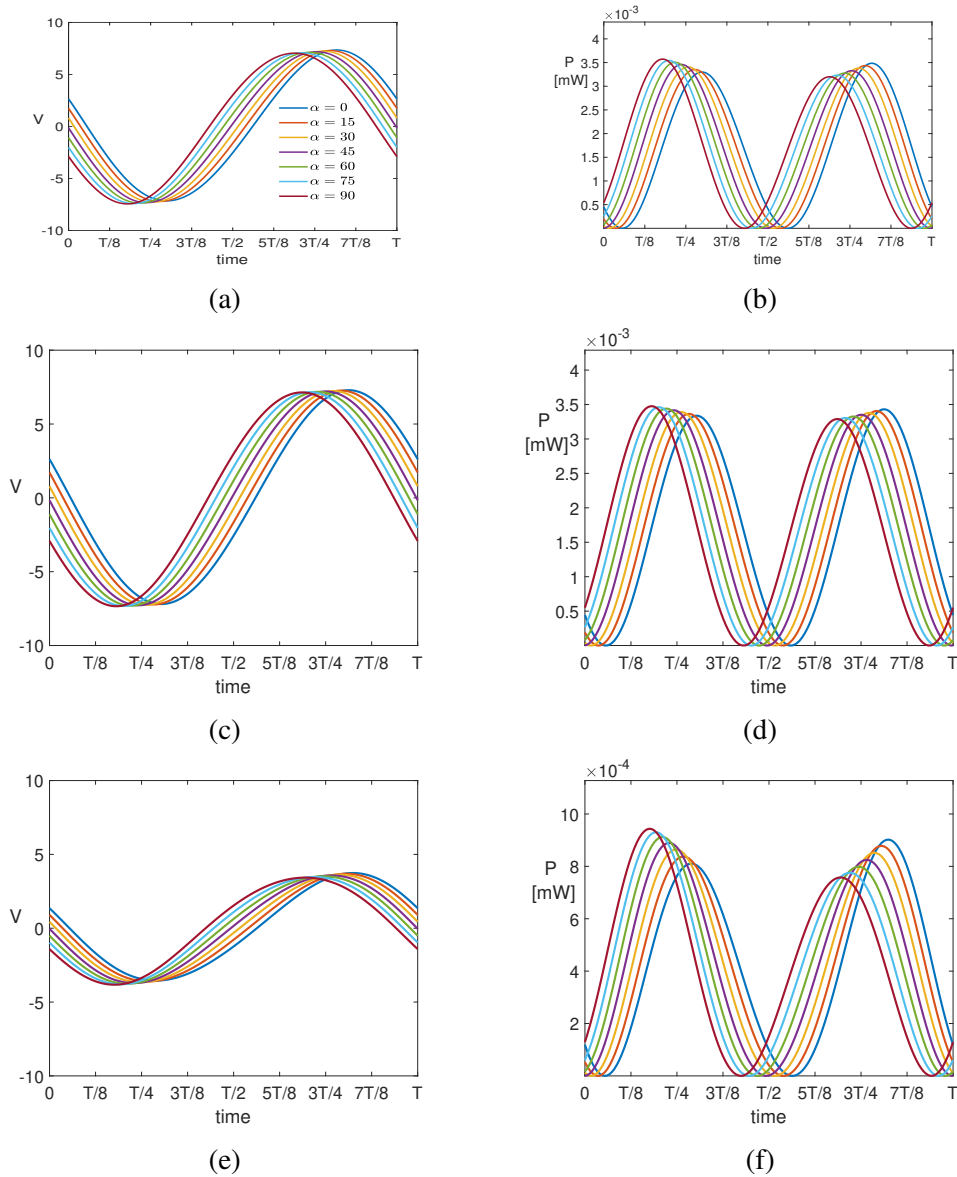


Fig. 8.9 Effect of the phase shifting angle α on the instantaneous voltage (Figures (a)-(c)-(e)) and instantaneous power (Figures Figures (b)-(d)-(f)) produced by the L^i harvester subjected to double harmonics. Figures (a) and (b) are relative to the case of excitation with the same energy content. Figures (c) and (d) are those of excitation with $\ddot{w}_{b_1} = 0.1g$ and $\ddot{w}_{b_1} = 0.05g$. Finally Figures (e) and (f) are relative to the case with $\ddot{w}_{b_1} = 0.05g$ and $\ddot{w}_{b_1} = 0.1g$.

8.5 Conclusions

In this chapter the electro-mechanical equation of motion of the angle-shaped resonator have been derived by means of extended Hamiltonian principle. For the sake of comparison, the

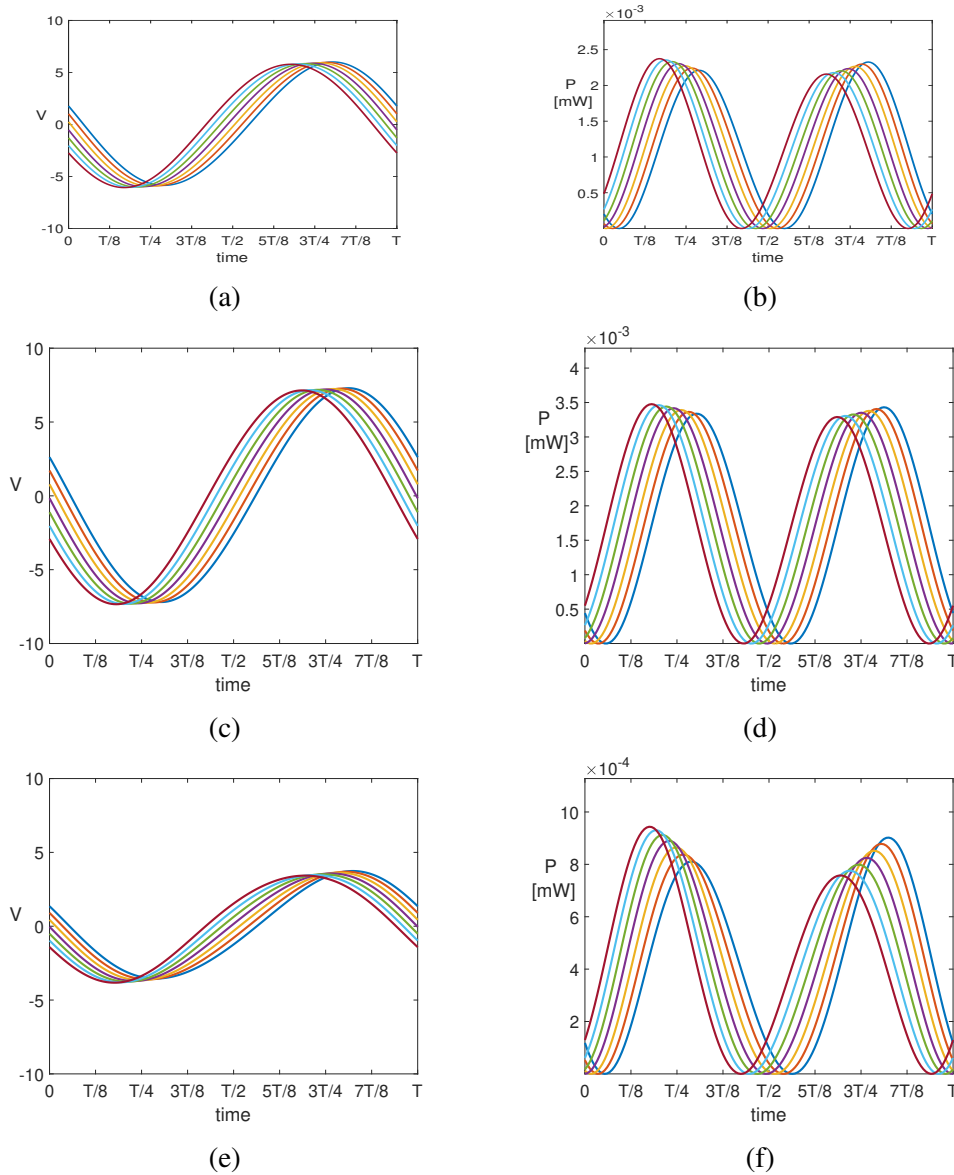


Fig. 8.10 Effect of the phase shifting angle α on the instantaneous voltage (Figures (a)-(c)-(e)) and instantaneous power (Figures (b)-(d)-(f)) produced by the V_{120}^i harvester subjected to double harmonics. Figures (a) and (b) are relative to the case of excitation with the same energy content. Figures (c) and (d) are those of excitation with $\ddot{w}_{b_1} = 0.1g$ and $\ddot{w}_{b_1} = 0.05g$. Finally Figures (e) and (f) are relative to the case with $\ddot{w}_{b_1} = 0.05g$ and $\ddot{w}_{b_1} = 0.1g$.

electro-mechanical equation are solved for three topologies arbitrarily selected among the possible solutions. It has been derived a scaling rule to desing the resonator such that they have the same bending frequencies. It has been shown that the folding angle plays a crucial role in determining the performances of the harvester. Particularly, it is seen that at different

folding angle correspond at different value of the optimal resistance. It is seen also that when the folding angle increase, the power density increases as well. Moreover, structures with folding angle higher than $\pi/2$ are less sensitive to the phase shift between the harmonic components of the excitation. Folding angles higher than $\pi/2$ are preferable when the energy content of the first harmonic is higher than those of the other harmonics.

Chapter 9

Summary and outlook

9.1 Contribution to knowledge

The major contributions of this work are summarized below.

Contribution 1 is the formulation of two-new equivalent plate models. The models provide insight into the attainable performance of curved stiffened structures based on their topology.

- Chapter 2 contains the derivation of the equivalent continuum layer models of curvilinear stiffened structures. The stiffeners were modeled as piecewise rectilinear members oriented at an angle ϑ with respect to the plate global reference frame. The derivation is a hybridization of the direct compatibility method and the energy equivalence method and uses two basic repetitive units for the purpose of smearing the strain energy density of the stiffened structure and hence derive an equivalent continuum model. It has been shown that, for curved stiffeners, the homogenization method give rise to full rank matrices. The effect of the curvature on to the equivalent properties has been investigated. Additionally, it has been shown that the method presented is valid for moderately curved stiffeners. A limit envelope has been provided. Using the method presented herein the effective engineering properties can be then calculated, allowing one to examine the effect of the transverse shear. A preliminary parametric study, performed on a plate having the aspect ratio $b/a = 1.6$ with 5 stiffeners, has shown that neglecting the effect of the transverse shear the error committed is of the order of few percent. The effect of the number of subdivisions of repetitive element has been investigated. It is seen that the method converges to the asymptotic values of the stiffnesses using few subdivisions of the repetitive element. The homogenization method has been assessed through a comparison of the buckling loads and natural

frequencies of simply supported panels. It has been shown that the equivalent continuum model which consider the stiffness variability is more accurate than the constant stiffness model. It has also been shown that, at least for the case investigated in chapter two, the effect of the variability of the mass is negligible when compared with that of the variability of the stiffness.

Contribution 2 is the development of a low fidelity reduced order model that can qualitatively predict the behavior of coupled structures with variable stiffnesses.

- In Chapter 3 the equations of motion of a second order nonlinear flexural-flexural-torsional beam has been derived. It has been shown that, having considered the variable properties yields up to thirty terms more in the system of governing equations. As a result the design domain has been enlarged resulting in a greater *tailorability* of the structural response.
- The reduced order model has been used to optimize the topology of the stiffeners of tow unitized box beams. In the first case, the objective of the optimization was to maximize the strain energy while maintaining the tip deflection bounded and ensuring a minimum tip rotation. Three different load cases were analyzed. The results presented agree with those obtained with a commercial code where the optimization was carried out using the SIMP algorithm in combination with a Finite Element Analysis. Results were found in agreement also with experiments. The second optimization problem aimed at decoupling the mode shapes of a scaled wing model of a High Altitude aircraft. The objective of the optimization was having the frequencies of the deformed structure as close as possible to the undeformed wing. It has been shown that moderately curved stiffeners can beneficial affect the behavior of the wing box. It has been demonstrated that the reduced order model presented herein, having few degrees of freedom and a limited number of design variables, is able to qualitatively predict the structural response of variable stiffness beam in presence of structural couplings;

Contribution 3 is the development of an invariant-based scaling for predicting the performances of anisotropic structures.

- The theoretical framework for scaling of anisotropic structure has been briefly summarized in Chapter 4 and the steps to apply the scaling procedure have been explained. A preliminary analysis has been performed on a High Aspect Ratio box-beam showing that, taking advantage of the objective properties for tensors, it is possible to predict the performances of a given structure when one varies the constitutive material, provided

that a reference solution is known. The scaled results are found in good agreement with those evaluated numerically. Other examples pertaining trace-based scaling have been reported; particularly, it has been shown that buckling loads and post-buckling deflections can be scaled consistently once a reference solution is known. The scaling procedure is envisaged to be useful within preliminary design stages and could potentially replace cumbersome material selection optimization.

Contribution 4 is the development of a novel population based optimization algorithm has been introduced to overcome the low convergence rate of GAs and improve the exploration capabilities.

- In Chapter 4 a novel optimization method, derived from the Stud GA, has been presented. The optimization method emulates the concept of linebreeding and outcrossing, used in breeding farm, to improve the exploration and exploitation capabilities of the algorithm. The optimization method adopts two parameters, namely the probability of extinction and the stress parameter, to enhance the performance of the algorithm. A parametric study has been performed aiming at identify the correct tuning parameters, particularly it has been shown that a lower probability of extinction is sufficient to enhance the exploration capability of the algorithm, in contrast with the common practice of having extinction at each iteration. The Stud^P GA algorithm has been tested on benchmark problems for buckling loads maximization of composite flat panels. It has been shown that the algorithm outperforms other heuristics as well as the permutation search (PS) algorithm on the same set of problems.

Contribution 5 is the development of systematic framework to design planar resonators for desired set of modal characteristics.

- The synthesis of planar resonator has been preliminary addressed as topology optimization of Ground Structures aiming at gaining useful insight on the design. The optimization aimed at identify structure having commensurate frequencies. It has been shown that, despite the level of complexity of the initial ground structure, the topology synthesis yields structure with few members. Particularly, in the case of two commensurate frequencies, in any integer ratio, the algorithm recovered a two members structure; while, for the case of three commensurate structure the algorithm identifies structures having three members. The optimization algorithm was able to recover, among the solutions identified, the L-shaped beam. However, the latter was not the preferable solution. In most of the cases the algorithm preferred a structure having members oriented at an angle φ ;

- In Chapter 6, aiming at investigating the effect of the folding angle onto the frequencies of the resonators, the analytical solution for the case of the angle-shaped resonators along with a generalized reduced order model were derived. It has been shown that the solution to the problem of having commensurate frequencies are hyper-surface belonging to \mathbb{R}^{6N} , being N the number of members of the structure. The reduced order model has been then specialized to the case of two and three members, or equivalently to the case of two and three commensurate frequencies. Three planar configurations for the resonators were identified, namely the V, Y and Z-shaped resonators. An in-depth study of the V-shaped resonator has been presented. Particularly, the cardinality of the problem has been reduced assuming fixed some parameters and the 3D and 2D envelopes were provided. It has been shown that solutions are quadratic in the length parameter and that the 3D envelope exhibits a sort of bifurcation in the design domain, i.e. for certain angle solutions exist in the inner envelope only. It is seen that solution of the outer envelope are more sensitive to the variation of the position of the center of gravity, this motivates the bifurcation phenomenon. Universal design charts were provided. The latter being useful to design resonators knowing the dimension and frequencies of a cantilever beam. An examples of design based on the universal chart was provided. Universal design chart are the answer to the query of identify a systematic way/method to design resonators;
- Chapter 7 presents the derivation of the equation of motion of the electro-mechanical V-shaped resonator. Three topologies of the resonator were selected aiming at investigating the effect of the folding angle on to the energy harvested. The resonators were designed such that the first two bending frequencies for the different topologies coincide. Moreover all the resonators were operated at their optimal resistance. Indeed, it has been shown that at different folding angle corresponds a different optimal resistance. It has been shown that when the folding angle increase, the power density increases as well. Moreover, structures with folding angle higher than $\pi/2$ are less sensitive to the phase shifting between the harmonic components of the excitation. Folding angles higher than $\pi/2$ are preferable when the energy content of the first harmonic is higher than those of the other harmonic(s), which is a common situation for vibration due to rotary machines.

Contribution 6 is the formulation of a novel filtering scheme for topology synthesis of planar ground structures.

- Chapter 5 presented a novel topology synthesis method based on a double filtering scheme for the topology optimization of ground structures. The double filtering scheme has been conceived based on the observation that regardless of the level of

connectivity in the ground structure, the GS is a graph i.e. a connection of nodes by means of arch. Using standard graph exploration algorithm it has been possible to navigate the structure and identify those members that were unconnected to the rest of the structure. The unconnected structure arises from the first filtering scheme which instead removes members with a cross section less than a threshold limit. The algorithm has been proven to be effective in synthesizing planar resonators and compliant structures

9.2 Outlook

Based on the premise that having a set space between torsional and bending frequencies postpones the occurrence of aeroelastic instabilities, the analysis reported in this thesis are limited to the study of the nonlinear dynamic response of unitized box beam. A natural extension of the work will consider an unsteady aerodynamic model coupled to the beam model in order to investigate the effect of the stiffeners' topology on to the flutter speed of HAR wings. Moreover, beam's rotation angular velocity can be included to model, for example, helicopters' blades and wind turbines. Higher order nonlinearities can be included in the model to account for larger deformations. The model can also be adopted in a two-level optimization strategy where at the local level the aim is to maximize the buckling loads and or minimizing the post-buckling deflection while, at the global level the model can be adopted to calculate flutter speed, wing deflection and so forth.

Because of the enlarged design space, variable stiffness structures, represent a promising options for designing of compliant structures to achieve shape adaptation. Other coupling terms, herein neglected, can have beneficial effect on to the structural response.

Invariant-based failure criterion, such as Omni-circle, have been already defined and can be used in combination with trace-based scaling for optimization purposes to allow for effective ways of designing anisotropic structures.

Resonator studies in this work are limited to the linear analysis. A research is on-going to study the nonlinear dynamic behavior of the angle-shaped resonators. It is known that broad-band energy harvesting capability can be achieved exploiting nonlinearities. Indeed one of the drawback of linear energy harvester which operates at their resonance is the narrow range of applicability. The effect of the folding angle on to the frequency bandwidth, is under investigation. The dynamics of multi-member resonators is an interesting research area that deserves dedicated studies.

Looking at the global picture and framing together the two problems addressed in this work, it is also worth mentioning the following:

- The mode shapes of the V-shaped structure can be used as a modal basis to study dihedral wing, in contrast to the usual modal basis used, i.e. the mode shapes of the cantilever beam.
- So far, resonators have been studied for applications to small scales. A solution which would be worthwhile to study, for energy harvesting purposes, is a resonating wing which exploits ambient vibrations induced, for example, by gusts. Indeed, multiple integer frequencies may arise from the folding angle (dihedral angle in the usual aeronautic jargon) as well as variable stiffness properties or a combination of the two.

References

- [1] Walter Lacarbonara. Obituary: Professor ali h. nayfeh 21 december 1933–27 march 2017. *Journal of Sound and Vibration*, 400, 04 2017.
- [2] B.A. Rocca, S. Preidikman, M.L. Verstraete, and D.T. Mook. Influence of spanwise twisting and bending on lift generation in mav-like flapping wings. *Journal of Aerospace Engineering*, 30(1), 2017.
- [3] T. Fitzgerald, M. Valdez, S. Preidikman, and B. Balachandran. Thin, flapping wings: Structural models and fluid-structure interactions. 2010.
- [4] SUZANNE SMITH, Balakumar Balachandran, and ALI NAYFEH. Nonlinear interactions and the hubble space telescope. In *Astrodynamics Conference*, page 4617, 1992.
- [5] Samuel C. Stanton, Clark C. McGehee, and Brian P. Mann. Reversible hysteresis for broadband magnetopiezoelastic energy harvesting. *Applied Physics Letters*, 95(17):174103, 2009.
- [6] A. F. Arrieta, P. Hagedorn, A. Erturk, and D. J. Inman. A piezoelectric bistable plate for nonlinear broadband energy harvesting. *Applied Physics Letters*, 97(10):104102, 2010.
- [7] A. Erturk, J. Hoffmann, and D. J. Inman. A piezomagnetoelastic structure for broadband vibration energy harvesting. *Applied Physics Letters*, 94(25), 2009.
- [8] DX Cao, S Leadenham, and A Erturk. Internal resonance for nonlinear vibration energy harvesting. *The European Physical Journal Special Topics*, 224(14-15):2867–2880, 2015.
- [9] RL Harne, A Sun, and KW Wang. Leveraging nonlinear saturation-based phenomena in an l-shaped vibration energy harvesting system. *Journal of Sound and Vibration*, 363:517–531, 2016.
- [10] A. F. Arrieta, S. A. Neild, and D. J. Wagg. Nonlinear dynamic response and modeling of a bi-stable composite plate for applications to adaptive structures. *Nonlinear Dynamics*, 58(1):259, Feb 2009.
- [11] A.F. Arrieta, D.J. Wagg, and S.A. Neild. Dynamic snap-through for morphing of bi-stable composite plates. *Journal of Intelligent Material Systems and Structures*, 22(2):103–112, 2011.

- [12] A. F. Arrieta, O. Bilgen, M. I. Friswell, and P. Hagedorn. Passive load alleviation bi-stable morphing concept. *AIP Advances*, 2(3):032118, 2012.
- [13] F. Runkel, A. Reber, G. Molinari, A.F. Arrieta, and P. Ermanni. Passive twisting of composite beam structures by elastic instabilities. *Composite Structures*, 147:274–285, 2016.
- [14] Federico Roizner and Moti Karpel. Parametric flutter margin method for aeroservoelastic stability analysis. *AIAA Journal*, 56(3):1011–1022, Dec 2017.
- [15] Federico Roizner, Moti Karpel, Robert Carrese, Nishit Joseph, and Pier Marzocca. *Parametric Flutter Margin Analysis with CFD-Based Aerodynamics*. AIAA SciTech Forum. American Institute of Aeronautics and Astronautics, Jan 2018. 0.
- [16] Cassaro; Mario, Manuela Battipede, Piero Gili, and Pier Marzocca. An unconventional adaptive flutter suppression actuation system: From modeling to experimentation. *Journal of Intelligent Material Systems and Structures*, 28(8):1089–1101, 2017.
- [17] Mario Cassaro, Manuela Battipede, Pier Marzocca, E Cestino, and Aman Behal. L1 adaptive flutter suppression control strategy for highly flexible structure. *SAE International Journal of Aerospace*, 6:693–702, 07 2013.
- [18] Xuan Liu, David Furrer, Jared Kusters, and Jack Holmes. Vision 2040: A roadmap for integrated, multiscale modeling and simulation of materials and systems, 2018.
- [19] Wei Xiong and Gregory B. Olson. Integrated computational materials design for high-performance alloys. *MRS Bulletin*, 40(12):1035–1044, 2015.
- [20] Alden Dima, Sunil Bhaskarla, Chandler Becker, Mary Brady, Carelyn Campbell, Philippe Dessauw, Robert Hanisch, Ursula Kattner, Kenneth Kroenlein, Marcus Newrock, Adele Peskin, Raymond Plante, Sheng-Yen Li, Pierre-François Rigodiat, Guillaume Sousa Amaral, Zachary Trautt, Xavier Schmitt, James Warren, and Sharief Youssef. Informatics infrastructure for the materials genome initiative. *JOM*, 68(8):2053–2064, Aug 2016.
- [21] R.L. Bisplinghoff and H. Ashley. *Principles of Aeroelasticity*. Dover Books on Engineering Series. Dover Publications, 2002.
- [22] G. Frulla, E. Cestino, and P. Marzocca. Critical behaviour of slender wing configurations. *Proceedings of the Institution of Mechanical Engineers, Part G: Journal of Aerospace Engineering*, 224(5):587–600, 2010.
- [23] G. Frulla, E. Cestino, C. Bruni, and P. Marzocca. Considerations on beam-wise structural models used for aeroelastic analysis of slender wings. In *10th AIRTEC INTERNATIONAL Congress*, November 2015.
- [24] Mary I. Frecker. Recent advances in optimization of smart structures and actuators. *Journal of Intelligent Material Systems and Structures*, 14(4-5):207–216, 2003.
- [25] H. Zhu, P. Wang, and Z. Fan. Evolutionary design optimization of mems: A brief review. In *2010 IEEE International Conference on Industrial Technology*, pages 1683–1687, March 2010.

- [26] Astitva Tripathi and Anil K. Bajaj. Design for 1:2 internal resonances in in-plane vibrations of plates with hyperelastic materials. Number 55997, page V008T13A028, 2013.
- [27] Gerhard Venter. *Review of Optimization Techniques*. American Cancer Society, 2010.
- [28] Amir Hossein Gandom, Xin-She Yang, Siamak Talatahari, and Amir Hossein Alavi. *Metaheuristic applications in structures and infrastructures*. Elsevier, 2013.
- [29] Xin-She Yang. Metaheuristic optimization: Algorithm analysis and open problems. In Panos M. Pardalos and Steffen Rebennack, editors, *Experimental Algorithms*, pages 21–32, Berlin, Heidelberg, 2011. Springer Berlin Heidelberg.
- [30] D. H. Wolpert and W. G. Macready. No free lunch theorems for optimization. *IEEE Transactions on Evolutionary Computation*, 1(1):67–82, Apr 1997.
- [31] M. H. Shirk, T. J. Hertz, and T. A. Weisshaar. Aeroelastic tailoring - theory, practice, and promise. *Journal of Aircraft*, 23(1):6–18, Jan 1986.
- [32] M. Munk. Propeller containing diagonally disposed fibrous material. Technical Report U.S. Patent 2,484,308,1111, October 1949.
- [33] T. Weisshaar. *Aircraft Aeroelastic Design and Analysis*. 1995.
- [34] C. V. Jutte and B. K. Stanford. Aeroelastic tailoring of transport aircraft wings: State-of-the-art and potential enabling technologies. Technical Report NASA/TM–2014-218252, April 2014.
- [35] T. Weisshaar, C. Nam, and A. Batista-Rodriguez. Aeroelastic tailoring for improved uav performance. In *AIAA Structures, Structural Dynamics, and Materials Conference*, April 1998.
- [36] Paolo Gasbarri, Leonardo D. Chiwiacowsky, and Haroldo F. de Campos Velho. A hybrid multilevel approach for aeroelastic optimization of composite wing-box. *Structural and Multidisciplinary Optimization*, 39(6):607, Aug 2009.
- [37] W. J. Larson and L. K. Pranke. McGraw-Hill, 1999.
- [38] L. Librescu and O. Song. On the static aeroelastic tailoring of composite aircraft swept wings modelled as thin-walled beam structures. *Composites Engineering*, 2(5-7):497–512, 1992.
- [39] L. Librescu, L. Meirovitch, and O. Song. Refined structural modeling for enhancing vibrational and aeroelastic characteristics of composite aircraft wing. *Recherche Aerospaciale*, pages 23–35, 1996.
- [40] A. Chattopadhyay, S Zhang, and R. Jha. Structural and aeroelastic analysis of composite wing box sections using higher-order laminate theory. In *In Proceedings of the 37th Structures, Structural Dynamics, and Materials Conference*, April 1996.
- [41] Carlos Cesnik, Dewey Hodges, and Mayuresh Patil. Aeroelastic analysis of composite wings. Structures, Structural Dynamics, and Materials and Co-located Conferences. American Institute of Aeronautics and Astronautics, Apr 1996. 0.

- [42] Mayuresh Patil. Aeroelastic tailoring of composite box beams. Aerospace Sciences Meetings. American Institute of Aeronautics and Astronautics, Jan 1997. 0.
- [43] Mayuresh Patil, Dewey Hodges, and Carlos Cesnik. Nonlinear aeroelastic analysis of aircraft with high-aspect-ratio wings. Structures, Structural Dynamics, and Materials and Co-located Conferences. American Institute of Aeronautics and Astronautics, Apr 1998. 0.
- [44] M. Patil. *Nonlinear Aeroelastic Analysis, Flight Dynamics, and Control of a Complete Aircraft*. PhD thesis, Georgia Institute of Technology, 1999.
- [45] Reza Koohi, Hossein Shahverdi, and Hassan Haddadpour. Nonlinear aeroelastic analysis of a composite wing by finite element method. *Composite Structures*, 113:118 – 126, 2014.
- [46] Zhiqiang Wan, Bocheng Zhang, Ziliang Du, and Chao Yang. Aeroelastic two-level optimization for preliminary design of wing structures considering robust constraints. *Chinese Journal of Aeronautics*, 27(2):259 – 265, 2014.
- [47] Davide Locatelli, Sameer B. Mulani, and Rakesh K. Kapania. Wing-box weight optimization using curvilinear spars and ribs (sparibs). *Journal of Aircraft*, 48(5):1671–1684, Sep 2011.
- [48] Gustavo Gonzalez Lozano, Ashutosh Tiwari, Christopherr Turne, and Simon Astwood. A review on design for manufacture of variable stiffness composite laminates. *Proceedings of the Institution of Mechanical Engineers, Part B: Journal of Engineering Manufacture*, 230(6):981–992, 2016.
- [49] Pedro Ribeiro, Hamed Akhavan, Andrzej Teter, and Jerzy Warmiński. A review on the mechanical behaviour of curvilinear fibre composite laminated panels. *Journal of Composite Materials*, 48(22):2761–2777, 2014.
- [50] Z Gurdal, B. F. Tatting, and K. C. Wu. Variable stiffness composite panels: Effects of stiffness variation on the in-plane and buckling response. *Composites Part A: Applied Science and Manufacturing*, 39(5):911–922, 2008.
- [51] Chauncey Wu, Zafer Gurdal, and James Starnes. *Structural Response of Compression-Loaded, Tow-Placed, Variable Stiffness Panels*. Structures, Structural Dynamics, and Materials and Co-located Conferences. American Institute of Aeronautics and Astronautics, Apr 2002. 0.
- [52] Gangadharan Raju, Zhangming Wu, Simon White, and Paul M. Weaver. Optimal postbuckling design of variable angle tow composite plates. *AIAA Journal*, pages 1–17, Apr 2018.
- [53] Zhangming Wu, Gangadharan Raju, and Paul M Weaver. Optimization of postbuckling behaviour of variable thickness composite panels with variable angle tows: Towards “buckle-free” design concept. *International Journal of Solids and Structures*, 132-133:66 – 79, 2018.
- [54] Xiaodong Chen, Zhangming Wu, Guojun Nie, and Paul Weaver. Buckling analysis of variable angle tow composite plates with a through-the-width or an embedded rectangular delamination. *International Journal of Solids and Structures*, 138:166 – 180, 2018.

- [55] Christine V. Jutte, Bret Stanford, Carol D. Wieseman, and James B. Moore. Aeroelastic tailoring of the nasa common research model via novel material and structural configurations. AIAA SciTech Forum. American Institute of Aeronautics and Astronautics, Jan 2014. 0.
- [56] Steven P. Doyle. Aeroelastic optimization of wing structure using curvilinear spars and ribs (sparibs) and sparibmorph. In *58th AIAA/ASCE/AHS/ASC Structures, Structural Dynamics, and Materials Conference*, AIAA SciTech Forum. American Institute of Aeronautics and Astronautics, Jan 2017. 0.
- [57] Bret Stanford and Christine Jutte, Jun 2016. 0.
- [58] Andrew Pye. Materials optimization - the key to product profitability. *Materials & Design*, 2(1):7 – 14, 1980.
- [59] Laura Florez and Daniel Castro-Lacouture. Optimization model for sustainable materials selection using objective and subjective factors. *Materials & Design*, 46:310 – 321, 2013.
- [60] Novita Sakundarini, Zahari Taha, Salwa Hanim Abdul-Rashid, and Raja Ariffin Raja Ghazila. Optimal multi-material selection for lightweight design of automotive body assembly incorporating recyclability. *Materials & Design*, 50:846 – 857, 2013.
- [61] Ali Jahan and Kevin L. Edwards. A state-of-the-art survey on the influence of normalization techniques in ranking: Improving the materials selection process in engineering design. *Materials & Design (1980-2015)*, 65:335 – 342, 2015.
- [62] N. Zehnder and P. Ermanni. A methodology for the global optimization of laminated composite structures. *Composite Structures*, 72(3):311 – 320, 2006.
- [63] M.F. Ashby. *Materials Selection in Mechanical Design*. Butterworth-Heinemann, 1999.
- [64] E. Cestino, G. Frulla, E. Perotto, and P. Marzocca. Experimental slender wing model design by the application of aeroelastic scaling laws. *Journal of Aerospace Engineering*, 27(1):112–120, 2014.
- [65] S. M. Arnold, D. Cebon, and M. Ashby. *Materials Selection for Aerospace Systems*. NASA/TM—2012-217411. National Aeronautics and Space Administration, Glenn Research Center, Cleveland, Ohio 44135, 2012.
- [66] Luyun Chen and Yufang Zhang. A study on the application of material selection optimization approach for structural-acoustic optimization. *Materials & Design (1980-2015)*, 52:207 – 213, 2013.
- [67] Huda Zainul and Edi Prasetyo. Materials selection in design of structures and engines of supersonic aircrafts: A review. *Materials & Design*, 46:552 – 560, 2013.
- [68] R.L. Bisplinghoff, H. Ashley, and R.L. Halfman. *Aeroelasticity*. Dover Books on Aeronautical Engineering Series. Dover Publications, 1996.
- [69] Zhiqiang Wan and Carlos E. S. Cesnik. Geometrically nonlinear aeroelastic scaling for very flexible aircraft. *AIAA Journal*, 52(10):2251–2260, Jul 2014.

- [70] Vanessa L. Bond, Robert A. Canfield, Afzal Suleman, and Maxwell Blair. Aeroelastic scaling of a joined wing for nonlinear geometric stiffness. *AIAA Journal*, 50(3):513–522, Mar 2012.
- [71] H. C. Nathanson, W. E. Newell, R. A. Wickstrom, and J. R. Davis. The resonant gate transistor. *IEEE Transactions on Electron Devices*, 14(3):117–133, March 1967.
- [72] Ashwin Vyas, Dimitrios Peroulis, and Anil K Bajaj. A microresonator design based on nonlinear 1: 2 internal resonance in flexural structural modes. *Journal of Microelectromechanical Systems*, 18(3):744–762, 2009.
- [73] Zhimiao Yan and Muhammad R Hajj. Energy harvesting from an autoparametric vibration absorber. *Smart Materials and Structures*, 24(11):115012, 2015.
- [74] Ningning Zhou, Alice Agogino, and Kristofer S. J. Pister. Automated design synthesis for micro-electro-mechanical systems (mems), 2002.
- [75] Raffi Kamalian, Alice M. Agogino, and Hideyuki Takagi. The role of constraints and human interaction in evolving mems designs: Microresonator case study, 2004.
- [76] Bongwon Jeong, Chris Pettit, Sajith Dharmasena, Hohyun Keum, Joohyung Lee, Jungkyu Kim, Seok Kim, D Michael McFarland, Lawrence A Bergman, Alexander F Vakakis, et al. Utilizing intentional internal resonance to achieve multi-harmonic atomic force microscopy. *Nanotechnology*, 27(12):125501, 2016.
- [77] Onur Avci, Osama Abdeljaber, Serkan Kiranyaz, and Daniel Inman. Vibration suppression in metastructures using zigzag inserts optimized by genetic algorithms. In *Shock & Vibration, Aircraft/Aerospace, Energy Harvesting, Acoustics & Optics, Volume 9*, pages 275–283. Springer, 2017.
- [78] Suguang Dou and Jakob Søndergaard Jensen. Optimization of hardening/softening behavior of plane frame structures using nonlinear normal modes. *Computers & Structures*, 164:63–74, 2016.
- [79] Astiva Tripathi and Anil K. Bajaj. Computational synthesis for nonlinear dynamics based design of planar resonant structures. *Journal Vibration and Acoustics*, 135(5):051031–051031–13, 2013.
- [80] Dmitri Tcherniak. Topology optimization of resonating structures using simp method. *International Journal for Numerical Methods in Engineering*, 54(11):1605–1622, 2002.
- [81] Bin Zheng, Ching-Jui Chang, and Hae Chang Gea. Topology optimization of energy harvesting devices using piezoelectric materials. *Structural and Multidisciplinary Optimization*, 38(1):17–23, 2009.
- [82] Wei He, David Bindel, and Sanjay Govindjee. Topology optimization in micromechanical resonator design. *Optimization and Engineering*, 13(2):271–292, 2012.
- [83] Jiadong Deng, Katherine Rorschach, Evan Baker, Cheng Sun, and Wei Chen. Topology optimization and fabrication of low frequency vibration energy harvesting microdevices. *Smart Materials and Structures*, 24(2):025005, 2014.

- [84] Suguang Dou, B Scott Strachan, Steven W Shaw, and Jakob S Jensen. Structural optimization for nonlinear dynamic response. *Phil. Trans. R. Soc. A*, 373(2051):20140408, 2015.
- [85] Tamal Mukherjee and Gary K. Fedder. Hierarchical mixed-domain circuit simulation, synthesis and extraction methodology for mems. *Journal of VLSI signal processing systems for signal, image and video technology*, 21(3):233–249, Jul 1999.
- [86] Manish Agarwal, Jonathan Cagan, and George Stiny. A micro language: Generating mems resonators by using a coupled form — function shape grammar. *Environment and Planning B: Planning and Design*, 27(4):615–626, 2000.
- [87] R. Kamalian and A. M. Agogino. Improving evolutionary synthesis of mems through fabrication and testing feedback. In *2005 IEEE International Conference on Systems, Man and Cybernetics*, volume 2, pages 1908–1913 Vol. 2, Oct 2005.
- [88] JW Roberts and MP Cartmell. Forced vibration of a beam system with autoparametric coupling effects. *Strain*, 20(3):123–131, 1984.
- [89] AG Haddow, ADS Barr, and DT Mook. Theoretical and experimental study of modal interaction in a two-degree-of-freedom structure. *Journal of Sound and Vibration*, 97(3):451–473, 1984.
- [90] MP Cartmell and JW Roberts. Simultaneous combination resonances in a parametrically excited cantilever beam. *Strain*, 23(3):117–126, 1987.
- [91] B Balachandran and AH Nayfeh. Nonlinear motions of beam-mass structure. *Nonlinear Dynamics*, 1(1):39–61, 1990.
- [92] Li-Qun Chen, Wen-An Jiang, Meghashyam Panyam, and Mohammed F Daqaq. A broadband internally resonant vibratory energy harvester. *Journal of Vibration and Acoustics*, 138(6):061007, 2016.
- [93] I Mehdipour, F Braghin, N Lecis, and C Galassi. Analytical modeling and experimental verification of a s-shaped vibration energy harvester. volume Volume 2: Modeling, Simulation and Control; Bio-Inspired Smart Materials and Systems; Energy Harvesting, page V002T07A006, 2016.
- [94] In-Ho Kim, SeungSeop Jin, Seon-Jun Jang, and Hyung-Jo Jung. A performance-enhanced energy harvester for low frequency vibration utilizing a corrugated cantilevered beam. *Smart Materials and Structures*, 23(3):037002, 2014.
- [95] M. Amin Karami and Daniel J. Inman. Electromechanical modeling of the low-frequency zigzag micro-energy harvester. *Journal of Intelligent Material Systems and Structures*, 22(3):271–282, 2011.
- [96] Shengxi Zhou, Weijia Chen, Mohammad H Malakooti, Junyi Cao, and Daniel J Inman. Design and modeling of a flexible longitudinal zigzag structure for enhanced vibration energy harvesting. *Journal of Intelligent Material Systems and Structures*, 0(0):1045389X16645862, 0.
- [97] Jiadong Deng, Katherine Rorschach, Evan Baker, Cheng Sun, and Wei Chen. Topology optimization and fabrication of low frequency vibration energy harvesting microdevices. *Smart Materials and Structures*, 24(2):025005, 2015.

- [98] M.P. Nemeth. *A Treatise on Equivalent-plate Stiffnesses for Stiffened Laminated-composite Plates and Plate-like Lattices*. NASA technical paper. National Aeronautics and Space Administration, Langley Research Center, 2011.
- [99] M. T. Huber. Die grundlagen einer rationellen berechnung der kruezwise beweheten eisenbetonplatten. *Zeitschrift des Oesterreichischen Ingenieur und Architekten-Vereines*, 66:557–564, 1914.
- [100] M. T. Huber. Die theorie der kreuzweise bewehrten eisenbeton-platte nebst anwendungen auf mehrere bautechnisch wichtige aufgabenuiber rechteckige platten. *Bauingenieur*, 4:354–360 and 392–395, 1923.
- [101] W. Flugge. Die stabilitat der kreiszylinderschale. *Ingenieur-Archiv*, 3:463–506, 1932.
- [102] C. B. Smith, T. B. Heebink, and C. B. Norris. The effective stiffness of a stiffener attached to a flat plywood plate. Technical Report 1557, U. S. Department of Agriculture, Forest Products Laboratory, September 1946.
- [103] A. Pfluger. Zum beulproblcm der anisotropen rechteckplatte. *Ingenieur-Archiv*, 16:111–120, 1947.
- [104] A. Gomza and P Seide. Minimum-weight design of simply supported transversely stiffened plates under compression. Technical Report NACA TN 1710, 1948.
- [105] S. U. Benscoter and R. H. MacNeal. Equivalent plate theory for a straight multicell wing. Technical Report NACA TN 2786, 1952.
- [106] N. F. Dow, C. Libove, and R. E. Hubka. Formulas for the elastic constants of plates with integral waffle-like stiffening. Technical Report NACA Rep. 1195, 1953.
- [107] R. F. Crawford and C. Libove. Shearing effectiveness of integral stiffening. Technical Report NACA TN 3443, 1955.
- [108] W. H. Hoppmann. Bending of orthogonally stiffened plates. *Journal of Applied Mechanics*, pages 267–27, June 1955.
- [109] W. H. Hoppmann. Elastic compliances of orthogonally stiffened plates. In *Proceedings of the Society of Experimental Stress Analysis*, volume 14, pages 137–144, 1956.
- [110] Jr Huffington, N. J. Theoretical determination of rigidity properties of orthogonally stiffened plates. *Journal of Applied Mechanics*, pages 15–20, March 1956.
- [111] K. Heki and T. Saka. Stress analysis of lattice plates as anisotropic continuum plates. In *IASS Pacific Symposium - Part II on Tension Structures and Space Frames*, October 1971.
- [112] C. J. Won. Stiffened plates with arbitrary oblique stiffeners. *International Journal of Solids and Structures*, 26:779–799, 1990.
- [113] G. I. Pshenichnov. A theory of latticed plates and shells. *Series on Advances in Mathematics for Applied Sciences*, 5, 1993.

- [114] N. Jaunky, N. F. Knight, Jr., and D. R. Ambur. Formulation of an improved smeared stiffener theory for buckling analysis of grid-stiffened composite panels. Technical Report NASA TM 110162, 1995.
- [115] H.J. Chen and S. W. Tsai. Analysis and optimum design of composite grid structures. *Journal of Composite Materials*, 30(4):503–534, 1996.
- [116] D. Slinchenko and V. E. Verijenko. Structural analysis of composite lattice shells of revolution on the basis of smearing stiffness. *Composite Structures*, 54:341–348, 2001.
- [117] Rakesh Kapania, Jing Li, and Hitesh Kapoor. Optimal design of unitized panels with curvilinear stiffeners. Aviation Technology, Integration, and Operations (ATIO) Conferences. American Institute of Aeronautics and Astronautics, Sep 2005. 0.
- [118] Pankaj Joshi, Sameer Mulani, Rakesh Kapania, and Yung Shin. Optimal design of unitized structures with curvilinear stiffeners using response surface methodology. Structures, Structural Dynamics, and Materials and Co-located Conferences. American Institute of Aeronautics and Astronautics, Apr 2008. 0.
- [119] Ali Yeilaghi Tamijani and Rakesh K. Kapania. Vibration analysis of curvilinearly-stiffened functionally graded plate using element free galerkin method. *Mechanics of Advanced Materials and Structures*, 19(1-3):100–108, 2012.
- [120] Dan Wang and Mostafa M. Abdalla. Global and local buckling analysis of grid-stiffened composite panels. *Composite Structures*, 119:767 – 776, 2015.
- [121] Bret Stanford, Christine Jutte, and Carol D. Wieseman. Trim and structural optimization of subsonic transport wings using nonconventional aeroelastic tailoring. *AIAA Journal*, 54:1–17, 10 2015.
- [122] Wei Zhao and Rakesh K. Kapania. Buckling analysis of unitized curvilinearly stiffened composite panels. *Composite Structures*, 135:365 – 382, 2016.
- [123] J. Reddy. *Mechanics of Laminated Composite Plates and Shells*. Taylor & Francis Group. CRC Press, 2003.
- [124] C. T. Wang. *Applied Elasticity*. Mcgraw Hill, 1953.
- [125] Enrico Cestino and Giacomo Frulla. Analysis of slender thin-walled anisotropic box-beams including local stiffness and coupling effects. *Aircraft Engineering and Aerospace Technology*, 86(4):345–355, 2014.
- [126] Robert M. Jones. *Mechanics of Composite Materials*. Taylor & Francis, 1998.
- [127] Yeong-Bin Yang and Shyh-Rong Kuo. Effect of curvature on stability of curved beams. *Journal of Structural Engineering*, 113(6):1185–1202, 1987.
- [128] W. Lacarbonara. *Nonlinear Structural Mechanics: Theory, Dynamical Phenomena and Modeling*. Springer US, 2013.
- [129] Victor Berdichevsky, Erian Armanios, and Ashraf Badir. Theory of anisotropic thin-walled closed-cross-section beams. *Composites Engineering*, 2(5):411 – 432, 1992. Use of Composites in Rotorcraft and Smart Structures.

- [130] Erian A. Armanios and Ashraf M. Badir. Free vibration analysis of anisotropic thin-walled closed-section beams. *AIAA Journal*, 33(10):1905–1910, Oct 1995.
- [131] G. Frulla and E. Cestino. Flutter analysis of a high aspect ratio composite wing test-model. In *AIRTEC 5th International Conference—Supply on the Wings*, November 2010.
- [132] G. Frulla and E. Cestino. Structural analysis of slender composite thin-walled box-beam for aeroelastic applications. In *AIRTEC 6th International Conference – Supply on the Wings*, November 2011.
- [133] E. Cestino and G. Frulla. Critical aeroelastic behaviour of slender composite wings in an incompressible flow. In J.M. Davis, editor, *Composite Materials in Engineering Structures*, chapter 8, pages 313–339. Nova Science Publishers, Inc., 2010.
- [134] M. R. M. Crespo da Silva and C. C. Glynn. Nonlinear flexural-flexural-torsional dynamics of inextensional beams. i. equations of motion. *Journal of Structural Mechanics*, 6(4):437–448, 1978.
- [135] P. Frank Pai. Three kinematic representations for modeling of highly flexible beams and their applications. *International Journal of Solids and Structures*, 48(19):2764 – 2777, 2011.
- [136] A. H. Nayfeh and F. P. Pai. *Linear and Nonlinear Structural Mechanics*. Wiley Interscience, 2004.
- [137] Claudia Bruni. *ANALYSIS OF SLENDER PIEZOELECTRIC WING CONFIGURATIONS FOR ENERGY HARVESTING: AEROELASTIC MODELING AND EXPERIMENTAL COMPARISONS*. PhD thesis, Politecnico di Torino, 2016.
- [138] S.W. Tsai and N.J. Pagano. *Invariant Properties of Composite Materials*. AIR FORCE MATERIALS LAB WRIGHT-PATTERSON AFB OHIO, Defense Technical Information Center, 1968.
- [139] T. C. T. TING. Invariants of anisotropic elastic constants. *The Quarterly Journal of Mechanics and Applied Mathematics*, 40(3):431–448, 1987.
- [140] Sangwook Sihn Stephen W. Tsai and Jose Daniel D. Melo. Trace-based stiffness for a universal design of carbon-fiber reinforced composite structures. *Composites Science and Technology*, 118:23 – 30, 2015.
- [141] Stephen W. Tsai and Jose Daniel D. Melo. A unit circle failure criterion for carbon fiber reinforced polymer composites. *Composites Science and Technology*, 123:71 – 78, 2016.
- [142] Jose Daniel D. Melo, Jing Bi, and Stephen W. Tsai. A novel invariant-based design approach to carbon fiber reinforced laminates. *Composite Structures*, 159:44 – 52, 2017.
- [143] Stephen W. Tsai and Jose Daniel D. Melo. An invariant-based theory of composites. *Composites Science and Technology*, 100:237 – 243, 2014.

- [144] Francesco Danzi, Giacomo Frulla, and Giulio Romeo. An invariant-based performance-oriented procedure for preliminary design of composite structures. *Aircraft Engineering and Aerospace Technology*, 90(3):532–541, 2018.
- [145] Sung Kyu Ha and Jr Carlos Alberto Cimini. Theory and validation of the master ply concept for invariant-based stiffness of composites. *Journal of Composite Materials*, 52(12):1699–1708, 2018.
- [146] Giulio Romeo and Giacomo Frulla. Post-buckling behaviour of graphite/epoxy stiffened panels with initial imperfections subjected to eccentric biaxial compression loading. *International Journal of Non-Linear Mechanics*, 32(6):1017 – 1033, 1997.
- [147] P.P Friedmann. Aeroelastic scaling for rotary-wing aircraft with applications. *Journal of Fluids and Structures*, 19(5):635 – 650, 2004. Aeroelasticity.
- [148] G. Frulla. Aeroelastic behaviour of a solar-powered high-altitude long endurance unmanned air vehicle (hale-uav) slender wing. *Proceedings of the Institution of Mechanical Engineers, Part G: Journal of Aerospace Engineering*, 218(3):179–188, 2004.
- [149] Wael Khatib and PeterJ. Fleming. The stud ga: A mini revolution? In Agoston. Eiben, Thomas Bäck, Marc Schoenauer, and Hans Paul Schwefel, editors, *Parallel Problem Solving from Nature – PPSN V*, volume 1498 of *Lecture Notes in Computer Science*, pages 683–691. Springer Berlin Heidelberg, 1998.
- [150] Amy Samuels, Joan B. Silk, and Peter S. Rodman. Changes in the dominance rank and reproductive behaviour of male bonnet macaques (*macaca radiata*). *Animal Behaviour*, 32(4):994 – 1003, 1984.
- [151] Boyang Liu, Raphael T. Haftka, Mehmet A. Akgún, and Akira Todoroki. Permutation genetic algorithm for stacking sequence design of composite laminates. *Computer Methods in Applied Mechanics and Engineering*, 186(2–4):357 – 372, 2000.
- [152] Giovanni Squillero and Alberto Tonda. Divergence of character and premature convergence: A survey of methodologies for promoting diversity in evolutionary optimization. *Information Sciences*, page In press, 2015.
- [153] Garrison W. Greenwood, Gary B. Fogel, and Manuel Ciobanu. Emphasizing extinction in evolutionary programming. In *In Proceedings of the Congress of Evolutionary Computation*, pages 666–671, 1999.
- [154] Z. Jing, X. Fan, and Q. Sun. Stacking sequence optimization of composite laminates for maximum buckling load using permutation search algorithm. *Composite Structures*, 121:225–236, 2015.
- [155] Stanley Gotshall and Bart Rylander. Optimal population size and the genetic algorithm. In *Proceedings On Genetic And Evolutionary Computation Conference*, 2000.
- [156] David E. Goldberg and Robert Lingle, Jr. Alleles loci and the traveling salesman problem. In *Proceedings of the 1st International Conference on Genetic Algorithms*, pages 154–159, Hillsdale, NJ, USA, 1985. L. Erlbaum Associates Inc.

- [157] R.M. Jones. *Mechanics Of Composite Materials*. Materials Science and Engineering Series. Taylor & Francis, 1998.
- [158] James M. Whitney. *Structural analysis of laminated anisotropic plates*. Technomic Publishing Co. Inc., 1987.
- [159] S. W. Tsai. *Composite Design*. Think Composites, 1988.
- [160] E. Cestino, G. Frulla, R. Duella, P. Piana, F. Pennella, and F. Danzi. Application of structural topology optimization to couple thin-walled stiffened box-beams. In *Proc SAE 2017 AeroTech Congress& Exhibition*, Fort Worth (TX), United States, 2017.
- [161] M. P. Bendsøe. Optimal shape design as a material distribution problem. *Structural optimization*, 1(4):193–202, Dec 1989.
- [162] M. O. Odetayo. Optimal population size for genetic algorithms: an investigation. In *IEEE Colloquium on Genetic Algorithms for Control Systems Engineering*, pages 2/1–2/4, May 1993.
- [163] J. Arabas, Z. Michalewicz, and J. Mulawka. Gavaps-a genetic algorithm with varying population size. In *Proceedings of the First IEEE Conference on Evolutionary Computation. IEEE World Congress on Computational Intelligence*, volume 1, pages 73–78, Jun 1994.
- [164] R. Mallipeddi and P. N. Suganthan. Empirical study on the effect of population size on differential evolution algorithm. In *2008 IEEE Congress on Evolutionary Computation (IEEE World Congress on Computational Intelligence)*, pages 3663–3670, June 2008.
- [165] Bret Stanford and Peter Dunning. Optimal topology of aircraft rib and spar structures under aeroelastic loads. *Journal of Aircraft*, 52:1298–1311, 09 2014.
- [166] Bret K. Stanford and Peter D. Dunning. Optimal topology of aircraft rib and spar structures under aeroelastic loads. *Journal of Aircraft*, 52(4):1298–1311, Sep 2014.
- [167] Larry L. Howell. *Compliant Mechanisms*. John Wiley & Sons, 2001.
- [168] Joo Jinyong, Kota Sridhar, and Kikuchi Noboru. Topological synthesis of compliant mechanisms using linear beam elements. *Mechanics of Structures and Machines*, 28(4):245–280, 2000.
- [169] Lu Kerr-Jia and Kota Sridhar. Design of compliant mechanisms for morphing structural shapes. *Journal of Intelligent Material Systems and Structures*, 14(6):379–391, 2003.
- [170] Jfang Tao and Papalambros Panos Y. Optimal structural topology design using the homogenization method with multiple constraints. *Engineering Optimization*, 27(2):87–108, 1996.
- [171] E. C. Nelli Silva, J. S. Ono Fonseca, F. Montero de Espinosa, A. T. Crumm, G. A. Brady, J. W. Halloran, and N. Kikuchi. Design of piezocomposite materials and piezoelectric transducers using topology optimization—part i, 1999.
- [172] E.C. Nelli Silva, S. Nishiwaki, and N. Kikuchi. Design of piezocomposite materials and piezoelectric transducers using topology optimization—part ii, 1999.

- [173] E.C. Nelli Silva and N. Kikuchi. Design of piezocomposite materials and piezoelectric transducers using topology optimization— part iii. *Archives of Computational Methods in Engineering*, 6:305–329, 1999.
- [174] B. Zheng, C.J. Chang, and H.C. Gea. Topology optimization of energy harvesting devices using piezoelectric materials. *Struct Multidisc Optim*, 38:17–23, 2009.
- [175] G. I. N. Rozvany. A critical review of established methods of structural topology optimization. *Structural and Multidisciplinary Optimization*, 37(3):217–237, Jan 2009.
- [176] L. H. Weng, Y.-C. Guo, X.-W. Shi, and X. Q. Chen. An overview on defected ground structure. *Progress In Electromagnetics Research B*, 7:173–189, 2008.
- [177] Xiaojia Zhang, Adeildo S. Ramos, and Glaucio H. Paulino. Material nonlinear topology optimization using the ground structure method with a discrete filtering scheme. *Structural and Multidisciplinary Optimization*, 55(6):2045–2072, 2017.
- [178] Hong Zhou and Kwun-Lon Ting. Topological synthesis of compliant mechanisms using spanning tree theory. *Journal of Mechanical Design*, 127(4):753–759, 2005.
- [179] J.H. Zhu, F. He, T. Liu, Qinglin Liu, and Yang Chong. Structural topology optimization under harmonic base acceleration excitations. *Structural Multidisciplinary Optimization*, 57:1061–1078, 2018.
- [180] W. S. Dorn, R. E. Gomory, and H. J. Greenberg. Automatic design of optimal structures. *Journal de Mecanique*, 3:25–52, 1964.
- [181] G. Sved and Z. Ginos. Structural optimization under multiple loading. *International Journal of Mechanical Sciences*, 10(10):803 – 805, 1968.
- [182] L. He and M. Gilbert. Rationalization of trusses generated via layout optimization. *Structural and Multidisciplinary Optimization*, 52(4):677–694, 2015.
- [183] Alireza Asadpoure, James K. Guest, and Lorenzo Valdevit. Incorporating fabrication cost into topology optimization of discrete structures and lattices. *Structural and Multidisciplinary Optimization*, 51(2):385–396, 2015.
- [184] Adeildo S Ramos Jr and Glaucio H Paulino. Filtering structures out of ground structures—a discrete filtering tool for structural design optimization. *Structural and Multidisciplinary Optimization*, 54(1):95–116, 2016.
- [185] André J. Torii, Rafael H. Lopez, and Leandro F. F. Miguel. Design complexity control in truss optimization. *Structural and Multidisciplinary Optimization*, 54(2):289–299, 2016.
- [186] Hazem Madah and Oded Amir. Truss optimization with buckling considerations using geometrically nonlinear beam modeling. *Computers & Structures*, 192:233 – 247, 2017.
- [187] Haichao An and Hai Huang. Topology and sizing optimization for frame structures with a two-level approximation method. *AIAA Journal*, 55, 2017.

- [188] M. Giger and P. Ermanni. Evolutionary truss topology optimization using a graph-based parameterization concept. *Structural and Multidisciplinary Optimization*, 32:313–326, 2006.
- [189] Michael Sauter. *A Graph-based Optimization Method for the Design of Compliant Mechanisms and Structures*. PhD thesis, Swiss Federal Institute of Technology Zurich, 2008.
- [190] M. Sauter, T. Kern, and P. Ermanni. Final design interpretation of the complex-shaped beam optimizations for compliant mechanisms. In *2007 IEEE Congress on Evolutionary Computation*, pages 3930–3937, Sept 2007.
- [191] M. Sauter, G. Kress, M. Giger, and P. Ermanni. Complex-shaped beam element and graph-based optimization of compliant mechanisms. *Structural Multidisciplinary Optimization*, 36:429–442, 2008.
- [192] Glaucio H Paulino, Ivan FM Menezes, Marcelo Gattass, and Subrata Mukherjee. Node and element resequencing using the laplacian of a finite element graph: part i: general concepts and algorithm. *International Journal for Numerical Methods in Engineering*, 37(9):1511–1530, 1994.
- [193] Thomas H Cormen. *Introduction to algorithms*. MIT press, 2009.
- [194] Francesco Danzi, James Gibert, Enrico Cestino, and Giacomo Frulla. Topology synthesis of planar ground structures for energy harvesting applications. volume 10164, pages 101641L–101641L–18, 2017.
- [195] W. Zhang, W. H. Hu, D. X. Cao, and M. H. Yao. Vibration frequencies and modes of a z-shaped beam with variable folding angles. *Journal of Vibration and Acoustics*, 138(4):041004–041004–7, May 2016.
- [196] Ivan Wang and Earl H. Dowell. Structural dynamics model of multisegmented folding wings: Theory and experiment. *Journal of Aircraft*, 48(6):2149–2160, Nov 2011.
- [197] Ivan Wang, S. Chad Gibbs, and Earl H. Dowell. Aeroelastic model of multisegmented folding wings: Theory and experiment. *Journal of Aircraft*, 49(3):911–921, May 2012.
- [198] Hyochoong Bang. Analytical solution for dynamic analysis of a flexible L-shaped structure. *Journal of Guidance, Control, and Dynamics*, 19(1):248–250, 1996.
- [199] Metin Gürgöze. Comment on analytical solution for dynamic analysis of a flexible l-shaped structure. *Journal of Guidance, Control, and Dynamics*, 21(2):359–359, Mar 1998.
- [200] Randi Potekin, Sajith Dharmasena, D Michael McFarland, Lawrence A Bergman, Alexander F Vakakis, and Hanna Cho. Cantilever dynamics in higher-harmonic atomic force microscopy for enhanced material characterization. *International Journal of Solids and Structures*, 110:332–339, 2017.
- [201] L. Meirovitch. *Analytical methods in vibrations*. Macmillan series in advanced mathematics and theoretical physics. Macmillan, 1967.

- [202] Wenhan Yu. Modeling and analysis of dual mass energy harvesting for excitations with multiple harmonics, 2015.
- [203] MF Daqaq and D Bode. Exploring the parametric amplification phenomenon for energy harvesting. *Proceedings of the Institution of Mechanical Engineers, Part I: Journal of Systems and Control Engineering*, 225(4):456–466, 2011.
- [204] The Energy Harvesting Network. Earthquake: Twitter users learned of tremors seconds before feeling them.
- [205] Yu Jia and Ashwin A Seshia. An auto-parametrically excited vibration energy harvester. *Sensors and Actuators A: Physical*, 220:69–75, 2014.
- [206] Matteo Scapolan, Maryam Ghandchi Tehrani, and Elvio Bonisoli. Energy harvesting using parametric resonant system due to time-varying damping. *Mechanical Systems and Signal Processing*, 79:149–165, 2016.
- [207] Ali H Nayfeh and Dean T Mook. *Nonlinear oscillations*. John Wiley & Sons, 2008.
- [208] Alper Erturk, Jamil M Renno, and Daniel J Inman. Modeling of piezoelectric energy harvesting from an l-shaped beam-mass structure with an application to uavs. *Journal of intelligent material systems and structures*, 20(5):529–544, 2009.
- [209] Wanlu Zhou, Gopinath Reddy Penamalli, and Lei Zuo. An efficient vibration energy harvester with a multi-mode dynamic magnifier. *Smart Materials and Structures*, 21(1):015014, 2011.
- [210] O Aldraihem and A Baz. Energy harvester with a dynamic magnifier. *Journal of Intelligent Material Systems and Structures*, 22(6):521–530, 2011.
- [211] Xiudong Tang and Lei Zuo. Enhanced vibration energy harvesting using dual-mass systems. *Journal of sound and vibration*, 330(21):5199–5209, 2011.
- [212] In-Ho Kim, Hyung-Jo Jung, Bo Mi Lee, and Seon-Jun Jang. Broadband energy-harvesting using a two degree-of-freedom vibrating body. *Applied Physics Letters*, 98(21):214102, 2011.
- [213] Francesco Danzi, James M. Gibert, Giacomo Frulla, and Enrico Cestino. Generalized topology for resonators having n commensurate harmonics. *Journal of Sound and Vibration*, -(-):-, 2018.
- [214] MI Frecker, GK Ananthasuresh, S Nishiwaki, N Kikuchi, and S Kota. Topological synthesis of compliant mechanisms using multi-criteria optimization. *Journal of mechanical design*, 119(2), 1997.

Appendix A

Typical HAR HALE wing box

A.1 Lay-up of the composite wing box used for scaling

The aircraft under study has a rectangular, untapered and unswept wing. The wingspan is 32 m and the MAC (Mean Aerodynamic Chord) is 1.41 m. The wing aspect ratio is $AR=22.7$. The aircraft under study is the same considered in Cestino *et al* [64]. The aircraft's operating altitude is 20 km (air density $\rho_z=0.088$ kg/m³). The aft and fore panels have a layup of $[0_2/\pm 45_2]_S$. The layup of the upper and fore panels is given in Table A.1.1. The wing box is divided in sections, the wing sections are labelled in alphabetic order starting with the section A at the wing root. Are the panels are symmetric.

Table A.1.1 Number of plies for the wing box used for scaling.

Load	$N_{<0,45,90>}$	N_{Total}
A1	(8, 9, 10)	72
A3	(5, 5, 5)	40
B1	(8, 8, 8)	64
B3	(5, 5, 5)	40
C1	(8, 8, 8)	64
C3	(5, 5, 5)	40
D1	(8, 8, 8)	64
D3	(5, 5, 5)	40
E1	(6, 7, 8)	56
E3	(2, 2, 2)	16
F1	(6, 7, 8)	56
F3	(2, 2, 2)	16
G1	(6, 7, 8)	56
G3	(2, 2, 2)	16
H1	(6, 6, 6)	48
H3	(2, 2, 2)	16
I1	(6, 6, 6)	48
I3	(2, 2, 2)	16
J1	(6, 6, 6)	48
J3	(2, 2, 2)	16
K1	(4, 5, 6)	40
K3	(2, 2, 2)	16
L1	(4, 5, 6)	4'
L3	(2, 2, 2)	16
M1	(4, 4, 4)	32
M3	(2, 2, 2)	16
N1	(4, 4, 4)	32
N3	(2, 2, 2)	16
O1	(4, 4, 4)	32
O3	(2, 2, 2)	16
P1	(4, 3, 2)	24
P3	(2, 2, 2)	16
Q1	(4, 3, 2)	24
Q3	(2, 2, 2)	16
R1	(2, 2, 2)	16
R3	(2, 2, 2)	16
S1	(0, 1, 2)	8
S3	(2, 2, 2)	16

Appendix B

Non-dimensional Euler-Bernoulli beam element

B.1 Derivation of the non-dimensional form of the Euler Bernoulli beam model

In chapter 6, we wrote that *a priori* assumptions and or constraints limits the design domain to be a subset of the design space. Aiming at identify generalized solutions which exhibit commensurate frequencies in a integer ratio, we formulate the optimization problem in its non-dimensional form. We have already seen in section 6.4.1, that the cross sectional dimensions are given as non-dimensional ratio. Consistently with that, we wrote the finite element matrices of a two nodes Euler Bernoulli beam, in the non-dimensional form.

Let us consider the two nodes finite element reported in Figure B.1.1. Let $\bar{w} = w/L_T$ and $\bar{u} = u/L_T$ the non-dimensional bending and axial displacement respectively and L_T a characteristic length of the structure; here we assumed L_T being the element length L^i . Let the non-dimensional time is $\tau = \omega_n t$, it follows:

$$\frac{d(\cdot)}{dt} = \frac{d(\cdot)}{d\tau} \frac{d\tau}{dt} = \omega_n \frac{d(\cdot)}{d\tau} \quad , \quad \frac{d^2(\cdot)}{dt^2} = \omega_n^2 \frac{d^2(\cdot)}{d\tau^2}$$

where ω_n is the bending natural frequency of the beam.

Considering the following set of non-dimensional parameters ($\alpha = A/A_T, \ell = L/L_T, h_r = h/h_{nom}, r = L/L_T, \ell_m = L_T/h_{nom}$), where the subscript T denotes characteristic length the

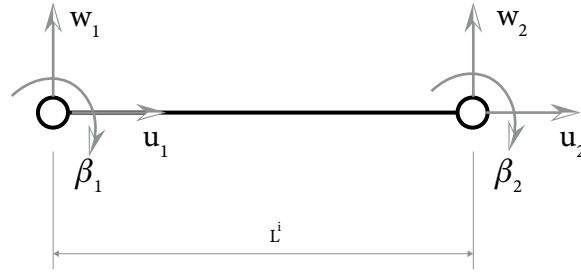


Fig. B.1.1 Exemplification of the two node, 6 degree of freedom finite element adopted in the present analysis

mass and stiffness matrices for rod and beam elements are

$$M_{rod} = \frac{\alpha r}{6} \begin{bmatrix} 2 & 1 \\ 1 & 2 \end{bmatrix}, \quad (B.1.1)$$

$$K_{rod} = 12\alpha\ell\ell_m^2 \begin{bmatrix} 1 & -1 \\ -1 & 1 \end{bmatrix}, \quad (B.1.2)$$

$$M_{beam} = \frac{\alpha r}{420} \begin{bmatrix} 156 & 22r & 54 & -13r \\ 22r & 4r^2 & 13r & -3r^2 \\ 54 & 13r & 156 & -22r \\ -13r & -3r^2 & -22r & 4r^2 \end{bmatrix}, \quad (B.1.3)$$

$$K_{beam} = \alpha h_r^2 \begin{bmatrix} 12\ell^3 & 6\ell^2 & -12\ell^3 & 6\ell^2 \\ 6\ell^2 & 4\ell & -6\ell^2 & 2\ell \\ -12\ell^3 & -6\ell^2 & 12\ell^3 & -6\ell^2 \\ 6\ell^2 & 2\ell & -6\ell^2 & 4\ell \end{bmatrix}. \quad (B.1.4)$$

Being $\{u_1, w_1, \beta_1, u_2, w_2, \beta_2\}^T$ the displacement vector, the complete mass and stiffness matrix for the element in hand assume the following structure:

$$\begin{bmatrix} \bullet & 0 & 0 & \bullet & 0 & 0 \\ 0 & \blacktriangle & \blacktriangle & 0 & \blacktriangle & \blacktriangle \\ 0 & \blacktriangle & \blacktriangle & 0 & \blacktriangle & \blacktriangle \\ \bullet & 0 & 0 & \bullet & 0 & 0 \\ 0 & \blacktriangle & \blacktriangle & 0 & \blacktriangle & \blacktriangle \\ 0 & \blacktriangle & \blacktriangle & 0 & \blacktriangle & \blacktriangle \end{bmatrix}$$

where \bullet are the components of the rod matrices while the \blacktriangle are the components of the beam matrices.

Appendix C

Coefficients of the stiffness and mass matrices

C.1 Case $p = 3$, Y-shaped resonator

The mass matrices for the Rayleigh approximation of the Y-shaped resonator are written as:

$$\begin{aligned}\hat{m}_{11} &= \frac{A_1 L_1^5 \rho_1}{5} + \frac{4A_2 L_1^2 L_2^3 \rho_2}{3} + \frac{4A_3 L_1^2 L_3^3 \rho_3}{3} + \\ &\quad \frac{11A_3 E_1^2 I_1^2 L_3^5 \rho_3}{105 E_3^2 I_3^2} + \frac{11A_3 E_1 I_1 L_1 L_3^4 \rho_3}{15 E_3 I_3} + \frac{A_3 E_1 I_1 L_1^2 L_3^3 \rho_3 \cos(\varphi_2)}{2 E_3 I_3} + \\ &\quad + A_2 L_1^4 L_2 \rho_2 + A_3 L_1^4 L_3 \rho_3 + 2A_2 L_1^3 L_2^2 \rho_2 \cos(\varphi_1) + 2A_3 L_1^3 L_3^2 \rho_3 \cos(\varphi_2), \\ \hat{m}_{12} &= \frac{A_1 L_1^6 \rho_1}{6} + \frac{5A_2 L_1^4 L_2^2 \rho_2 \cos(\varphi)}{2} + \frac{5A_3 L_1^4 L_3^2 \rho_3 \cos(\varphi_2)}{2} + \frac{33A_3 E_1 I_1 L_1^2 L_3^4 \rho_3}{20 E_3 I_3} + \frac{11A_3 E_1^2 I_1^2 L_1 L_3^5 \rho_3}{35 E_3^2 I_3^2} + \\ &\quad A_3 E_1 I_1 L_1^3 L_3^3 \rho_3 \cos(\varphi_2) E_3 I_3 + A_2 L_1^5 L_2 \rho_2 + A_3 L_1^5 L_3 \rho_3 + 2A_2 L_1^3 L_2^2 \rho_2 + 2A_3 L_1^3 L_3^2 \rho_3 = \hat{m}_{21}, \\ \hat{m}_{13} &= \frac{A_2 \rho_2 \cos(\varphi) L_1^2 L_2^3}{4} - \frac{A_3 E_2 I_2 L_3^3 \rho_3 \cos(\varphi_2) L_1^2}{4 E_3 I_3} + \frac{11A_2 \rho_2 L_1 L_2^4}{30} - \frac{11A_3 E_2 I_2 L_3^4 \rho_3 L_1}{30 E_3 I_3} - \\ &\quad \frac{11A_3 E_1 E_2 I_1 I_2 L_3^5 \rho_3}{105 E_3^2 I_3^2} = \hat{m}_{31}, \\ \hat{m}_{22} &= \frac{A_1 L_1^7 \rho_1}{7} + \frac{33A_3 E_1^2 I_1^2 L_1^2 L_3^5 \rho_3}{35 E_3^2 I_3^2} + \frac{33A_3 E_1 I_1 L_1^3 L_3^4 \rho_3}{10 E_3 I_3} + \frac{3A_3 E_1 I_1 L_1^4 L_3^3 \rho_3 \cos(\varphi_2)}{2 E_3 I_3} + A_2 L_1^6 L_2 \rho_2 + \\ &\quad A_3 L_1^6 L_3 \rho_3 + 3A_2 L_1^4 L_2^3 \rho_2 + 3A_3 L_1^4 L_3^3 \rho_3 + 3A_2 L_1^5 L_2^2 \rho_2 \cos(\varphi) + 3A_3 L_1^5 L_3^2 \rho_3 \cos(\varphi_2), \\ \hat{m}_{23} &= \frac{A_2 \rho_2 \cos(\varphi) L_1^3 L_2^3}{4} - \frac{A_3 E_2 I_2 L_3^3 \rho_3 \cos(\varphi_2) L_1^3}{4 E_3 I_3} + \frac{11A_2 \rho_2 L_1^2 L_2^4}{20} - \frac{11A_3 E_2 I_2 L_3^4 \rho_3 L_1^2}{20 E_3 I_3} - \\ &\quad \frac{11A_3 E_1 E_2 I_1 I_2 L_3^5 \rho_3 L_1}{35 E_3^2 I_3^2} = \hat{m}_{32},\end{aligned}$$

$$\hat{m}_{33} = \frac{11A_2L_2^5\rho_2}{105} + \frac{11A_3E_2^2I_2^2L_3^5\rho_3}{105E_3^2I_3^2}.$$

The stiffness matrices for the Rayleigh approximation of the Y-shaped resonator are written as:

$$\begin{aligned}\hat{k}_{11} &= \frac{4L_3E_1^2I_1^2}{3E_3I_3} + 4L_1E_1I_1, \\ \hat{k}_{12} &= \frac{4L_3E_1^2I_1^2L_1}{E_3I_3} + 6E_1I_1L_1^2 = \hat{k}_{21}, \\ \hat{k}_{13} &= -\frac{4E_1E_2I_1I_2L_3}{3E_3I_3} = \hat{k}_{31}, \\ \hat{k}_{22} &= \frac{12L_3E_1^2I_1^2L_1^2}{E_3I_3} + 12E_1I_1L_1^3, \\ \hat{k}_{23} &= -\frac{4E_1E_2I_1I_2L_1L_3}{E_3I_3} = \hat{k}_{32}, \\ \hat{k}_{33} &= \frac{4L_3E_2^2I_2^2}{3E_3I_3} + \frac{4L_2E_2I_2}{3}.\end{aligned}$$

The generalized forces of the Y-shaped resonator are written as:

$$\begin{aligned}\hat{f}_1 &= \left\{ \frac{L_3^2 \left[2A_3L_1\rho_3 \cos(\varphi_2) + \frac{A_3E_1I_1L_3\rho_3 \cos(\varphi_2)}{2E_3I_3} \right]}{2} + \frac{A_1L_1^3\rho_1}{3} +, \right. \\ &\quad \left. A_2L_1^2L_2\rho_2 + A_3L_1^2L_3\rho_3 + A_2L_1L_2^2\rho_2 \cos(\varphi) \right\} \ddot{w}_B(t), \\ \hat{f}_2 &= \left\{ \frac{L_3^2 \left[3A_3\rho_3 \cos(\varphi_2)L_1^2 + \frac{3A_3E_1I_1L_3\rho_3 \cos(\varphi_2)L_1}{2E_3I_3} \right]}{2} +, \right. \\ &\quad \left. \frac{A_1L_1^4\rho_1}{4} + \frac{3A_2L_1^2L_2^2\rho_2 \cos(\varphi)}{2} + A_2L_1^3L_2\rho_2 + A_3L_1^3L_3\rho_3 \right\} \ddot{w}_B(t), \\ \hat{f}_3 &= \left\{ \frac{A_2\rho_2 \cos(\varphi)L_2^3}{4} - \frac{A_3E_2I_2L_3^3\rho_3 \cos(\varphi_2)}{4E_3I_3} \right\} \ddot{w}_B(t).\end{aligned}$$

C.2 Case $p = 3$, Z-shaped resonator

The mass matrices for the Rayleigh approximation of the Z-shaped resonator are written as:

$$\begin{aligned}
\hat{m}_{11} = & \frac{A_1 L_1^5 \rho_1}{5} + \frac{4A_2 L_1^2 L_2^3 \rho_2}{3} + \frac{4A_3 L_1^2 L_3^3 \rho_3}{3} + \frac{A_2 E_1^2 I_1^2 L_2^5 \rho_2}{5E_2^2 I_2^2} + \frac{11A_3 E_1^2 I_1^2 L_3^5 \rho_3}{105E_3^2 I_3^2} + \frac{A_3 E_1^2 I_1^2 L_2^4 L_3 \rho_3}{E_2^2 I_2^2} + \\
& + \frac{4A_3 E_1^2 I_1^2 L_2^2 L_3^3 \rho_3}{3E_2^2 I_2^2} + \frac{A_2 E_1 I_1 L_1 L_2^4 \rho_2}{E_2 I_2} + \frac{11A_3 E_1 I_1 L_1 L_3^4 \rho_3}{15E_3 I_3} + \frac{2A_2 E_1 I_1 L_1^2 L_2^3 \rho_2 \cos(\varphi)}{3E_2 I_2} + \\
& + \frac{A_3 E_1 I_1 L_1^2 L_3^3 \rho_3 \cos(\varphi_2)}{2E_3 I_3} + \frac{8A_3 E_1 I_1 L_1 L_2 L_3^3 \rho_3}{3E_2 I_2} + \frac{4A_3 E_1 I_1 L_1 L_2^3 L_3 \rho_3}{E_2 I_2} + \frac{2A_3 E_1^2 I_1^2 L_2^3 L_3^3 \rho_3 \cos(\varphi - \varphi_2)}{E_2^2 I_2^2} + \\
& + \frac{A_3 E_1 I_1 L_1 L_2 L_3^3 \rho_3 \cos(\varphi - \varphi_2)}{E_3 I_3} + \frac{2A_3 E_1 I_1 L_1^2 L_2^2 L_3 \rho_3 \cos(\varphi)}{E_2 I_2} + \frac{2A_3 E_1 I_1 L_1^2 L_2^2 L_3^3 \rho_3 \cos(\varphi_2)}{E_2 I_2} + \\
& + \frac{6A_3 E_1 I_1 L_1 L_2^2 L_3^3 \rho_3 \cos(\varphi - \varphi_2)}{E_2 I_2} + \frac{11A_3 E_1^2 I_1^2 L_2 L_3^4 \rho_3}{15E_2 E_3 I_2 I_3} + \frac{A_3 E_1^2 I_1^2 L_2^2 L_3^3 \rho_3 \cos(\varphi - \varphi_2)}{2E_2 E_3 I_2 I_3} + \\
& + A_2 L_1^4 L_2 \rho_2 + A_3 L_1^4 L_3 \rho_3 + 2A_2 L_1^3 L_2^2 \rho_2 \cos(\varphi) + 2A_3 L_1^3 L_3^2 \rho_3 \cos(\varphi_2) + 4A_3 L_1^2 L_2^2 L_3 \rho_3 + \\
& + 4A_3 L_1^3 L_2 L_3 \rho_3 \cos(\varphi) + 4A_3 L_1^2 L_2 L_3^2 \rho_3 \cos(\varphi - \varphi_2), \\
\hat{m}_{12} = & \frac{A_1 L_1^6 \rho_1}{6} + \frac{5A_2 L_1^4 L_2^2 \rho_2 \cos(\varphi)}{2} + \frac{5A_3 L_1^4 L_3^2 \rho_3 \cos(\varphi_2)}{2} + \frac{9A_2 E_1 I_1 L_1^2 L_2^4 \rho_2}{4E_2 I_2} + \frac{33A_3 E_1 I_1 L_1^2 L_3^4 \rho_3}{20E_3 I_3} \\
& + \frac{3A_2 E_1^2 I_1^2 L_1 L_2^5 \rho_2}{5E_2^2 I_2^2} + \frac{11A_3 E_1^2 I_1^2 L_1 L_3^5 \rho_3}{35E_3^2 I_3^2} + \frac{4A_2 E_1 I_1 L_1^2 L_2^3 \rho_2 \cos(\varphi)}{3E_2 I_2} + \\
& + \frac{A_3 E_1 I_1 L_1^3 L_3^3 \rho_3 \cos(\varphi_2)}{E_3 I_3} + \frac{4A_3 E_1^2 I_1^2 L_1 L_2^2 L_3^3 \rho_3}{E_2^2 I_2^2} + \frac{6A_3 E_1 I_1 L_1^2 L_2 L_3^3 \rho_3}{E_2 I_2} + \frac{9A_3 E_1 I_1 L_1^2 L_2^2 L_3 \rho_3}{E_2 I_2} + \\
& + \frac{6A_3 E_1^2 I_1^2 L_1 L_2^2 L_3^3 \rho_3 \cos(\varphi - \varphi_2)}{E_2^2 I_2^2} + \frac{4A_3 E_1 I_1 L_1^3 L_2 L_3^3 \rho_3 \cos(\varphi)}{E_2 I_2} + \frac{4A_3 E_1 I_1 L_1^3 L_2 L_3^3 \rho_3 \cos(\varphi_2)}{E_2 I_2} + \\
& + \frac{3A_3 E_1^2 I_1^2 L_1 L_2^4 L_3 \rho_3}{E_2^2 I_2^2} + \frac{9A_3 E_1 I_1 L_1^2 L_2 L_3^3 \rho_3 \cos(\varphi - \varphi_2)}{4E_3 I_3} + \frac{27A_3 E_1 I_1 L_1^2 L_2^2 L_3^3 \rho_3 \cos(\varphi - \varphi_2)}{2E_2 I_2} + \\
& + \frac{11A_3 E_1^2 I_1^2 L_1 L_2 L_3^4 \rho_3}{5E_2 E_3 I_2 I_3} + \frac{3A_3 E_1^2 I_1^2 L_1 L_2^2 L_3^3 \rho_3 \cos(\varphi - \varphi_2)}{2E_2 E_3 I_2 I_3} + A_2 L_1^5 L_2 \rho_2 + A_3 L_1^5 L_3 \rho_3 + 2A_2 L_1^3 L_2^3 \rho_2 + \\
& + 2A_3 L_1^3 L_3^3 \rho_3 + 6A_3 L_1^3 L_2^2 L_3 \rho_3 + 5A_3 L_1^4 L_2 L_3 \rho_3 \cos(\varphi) + 6A_3 L_1^3 L_2 L_3^2 \rho_3 \cos(\varphi - \varphi_2) = \hat{m}_{21}, \\
\hat{m}_{13} = & \frac{2A_2 L_1 L_2^5 \rho_2}{5} + \frac{A_2 L_1^2 L_2^4 \rho_2 \cos(\varphi)}{4} + \frac{3A_3 L_1^2 L_2^2 L_3^3 \rho_3 \cos(\varphi_2)}{2} + \frac{A_2 E_1 I_1 L_2^6 \rho_2}{6E_2 I_2} + \frac{2A_3 E_1 I_1 L_2^3 L_3^3 \rho_3}{E_2 I_2} + \\
& + \frac{A_3 E_1 I_1 L_2^5 L_3 \rho_3}{E_2 I_2} + \frac{11A_3 E_2 I_2 L_1 L_2 L_3^4 \rho_3}{10E_3 I_3} + \frac{5A_3 E_1 I_1 L_2^4 L_3^3 \rho_3 \cos(\varphi - \varphi_2)}{2E_2 I_2} + \frac{A_3 E_1 I_1 L_2^3 L_3^3 \rho_3 \cos(\varphi - \varphi_2)}{E_3 I_3} + \\
& + \frac{3A_3 E_2 I_2 L_1^2 L_2^3 \rho_3 \cos(\varphi_2)}{4E_3 I_3} + \frac{11A_3 E_1 E_2 I_1 I_2 L_2 L_3^5 \rho_3}{35E_3^2 I_3^2} + \frac{3A_3 E_2 I_2 L_1 L_2^2 L_3^3 \rho_3 \cos(\varphi - \varphi_2)}{2E_3 I_3} + \\
& + 2A_3 L_1 L_2^4 L_3 \rho_3 + 2A_3 L_1 L_2^2 L_3^3 \rho_3 + A_3 L_1^2 L_2^3 L_3 \rho_3 \cos(\varphi) + 4A_3 L_1 L_2^3 L_3^2 \rho_3 \cos(\varphi - \varphi_2) + \frac{33A_3 E_1 I_1 L_2^2 L_3^4 \rho_3}{20E_3 I_3} \\
= & \hat{m}_{31},
\end{aligned}$$

$$\begin{aligned}
\hat{m}_{22} = & \frac{A_1 L_1^7 \rho_1}{7} + \frac{9A_2 E_1^2 I_1^2 L_1^2 L_2^5 \rho_2}{5E_2^2 I_2^2} + \frac{33A_3 E_1^2 I_1^2 L_1^2 L_3^5 \rho_3}{35E_3^2 I_3^2} + \frac{9A_2 E_1 I_1 L_1^3 L_2^4 \rho_2}{2E_2 I_2} + \frac{33A_3 E_1 I_1 L_1^3 L_3^4 \rho_3}{10E_3 I_3} + \\
& + \frac{3A_3 E_1 I_1 L_1^4 L_3^3 \rho_3 \cos(\varphi_2)}{2E_3 I_3} + \frac{9A_3 E_1^2 I_1^2 L_1^2 L_2^4 L_3 \rho_3}{E_2^2 I_2^2} + \frac{12A_3 E_1 I_1 L_1^3 L_2 L_3^3 \rho_3}{E_2 I_2} + \frac{18A_3 E_1 I_1 L_1^3 L_2^3 L_3 \rho_3}{E_2 I_2} + \\
& + \frac{12A_3 E_1^2 I_1^2 L_1^2 L_2^2 L_3^3 \rho_3}{E_2^2 I_2^2} + \frac{2A_2 E_1 I_1 L_1^4 L_2^3 \rho_2 \cos(\varphi)}{E_2 I_2} + \frac{6A_3 E_1 I_1 L_1^4 L_2^2 L_3 \rho_3 \cos(\varphi)}{E_2 I_2} + \\
& + \frac{6A_3 E_1 I_1 L_1^4 L_2 L_2^3 \rho_3 \cos(\varphi_2)}{E_2 I_2} + \frac{9A_3 E_1 I_1 L_1^3 L_2 L_2^3 \rho_3 \cos(\varphi - \varphi_2)}{2E_3 I_3} + \frac{18A_3 E_1^2 I_1^2 L_1^2 L_2^3 L_3^2 \rho_3 \cos(\varphi - \varphi_2)}{E_2^2 I_2^2} + \\
& + \frac{27A_3 E_1 I_1 L_1^3 L_2^2 L_3^2 \rho_3 \cos(\varphi - \varphi_2)}{E_2 I_2} + \frac{33A_3 E_1^2 I_1^2 L_1^2 L_2 L_3^4 \rho_3}{5E_2 E_3 I_2 I_3} + \frac{9A_3 E_1^2 I_1^2 L_1^2 L_2^3 L_3^3 \rho_3 \cos(\varphi - \varphi_2)}{2E_2 E_3 I_2 I_3} \\
& + A_2 L_1^6 L_2 \rho_2 + A_3 L_1^6 L_3 \rho_3 + 3A_2 L_1^4 L_2^3 \rho_2 + 3A_3 L_1^4 L_3^3 \rho_3 + 3A_2 L_1^5 L_2^2 \rho_2 \cos(\varphi) + 3A_3 L_1^5 L_3^2 \rho_3 \cos(\varphi_2) + \\
& + 9A_3 L_1^4 L_2^2 L_3 \rho_3 + 6A_3 L_1^5 L_2 L_3 \rho_3 \cos(\varphi) + 9A_3 L_1^4 L_2 L_3^2 \rho_3 \cos(\varphi - \varphi_2), \\
\hat{m}_{23} = & \frac{3A_2 L_1^2 L_2^5 \rho_2}{5} + \frac{A_2 L_1^3 L_2^4 \rho_2 \cos(\varphi)}{4} + \frac{3A_3 L_1^3 L_2^2 L_3^2 \rho_3 \cos(\varphi_2)}{2} + \frac{A_2 E_1 I_1 L_1 L_2^6 \rho_2}{2E_2 I_2} + \frac{3A_3 E_1 I_1 L_1 L_2^5 L_3 \rho_3}{E_2 I_2} + \\
& + \frac{6A_3 E_1 I_1 L_1 L_2^3 L_3^3 \rho_3}{E_2 I_2} + \frac{99A_3 E_1 I_1 L_1 L_2^2 L_3^4 \rho_3}{20E_3 I_3} + \frac{33A_3 E_2 I_2 L_1^2 L_2 L_3^4 \rho_3}{20E_3 I_3} + \frac{3A_3 E_2 I_2 L_1^3 L_2 L_3^3 \rho_3 \cos(\varphi_2)}{4E_3 I_3} \\
& + \frac{15A_3 E_1 I_1 L_1 L_2^4 L_3^2 \rho_3 \cos(\varphi - \varphi_2)}{2E_2 I_2} + \frac{3A_3 E_1 I_1 L_1 L_2^3 L_3^3 \rho_3 \cos(\varphi - \varphi_2)}{E_3 I_3} + \frac{9A_3 E_2 I_2 L_1^2 L_2^2 L_3^3 \rho_3 \cos(\varphi - \varphi_2)}{4E_3 I_3} \\
& + \frac{33A_3 E_1 E_2 I_1 I_2 L_1 L_2 L_3^5 \rho_3}{35E_3^2 I_3^2} + 3A_3 L_1^2 L_2^2 L_3^3 \rho_3 + 3A_3 L_1^2 L_2^4 L_3 \rho_3 + 6A_3 L_1^3 L_2^3 L_3^2 \rho_3 \cos(\varphi - \varphi_2) + \\
& + A_3 L_1^3 L_2^3 L_3 \rho_3 \cos(\varphi) = \hat{m}_{32}, \\
\hat{m}_{33} = & \frac{A_2 L_2^7 \rho_2}{7} + \frac{33A_3 E_2^2 I_2^2 L_2^2 L_3^5 \rho_3}{35E_3^2 I_3^2} + \frac{33A_3 E_2 I_2 L_2^3 L_3^4 \rho_3}{10E_3 I_3} + \frac{3A_3 E_2 I_2 L_2^4 L_3^3 \rho_3 \cos(\varphi - \varphi_2)}{2E_3 I_3} + A_3 L_2^6 L_3 \rho_3 + \\
& + 3A_3 L_2^4 L_3^3 \rho_3 + 3A_3 L_2^5 L_3^2 \rho_3 \cos(\varphi - \varphi_2).
\end{aligned}$$

The stiffness matrices for the Rayleigh approximation of the Z-shaped resonator are written as:

$$\begin{aligned}
\hat{k}_{11} &= \frac{4E_1^2 I_1^2 L_2}{E_2 I_2} + \frac{4E_1^2 I_1^2 L_3}{3E_3 I_3} + 4E_1 I_1 L_1, \\
\hat{k}_{12} &= \frac{(12E_1^2 I_1^2 L_1 L_2)}{E_2 I_2} + \frac{4E_1^2 I_1^2 L_1 L_3}{E_3 I_3} + 6E_1 I_1 L_1^2 = \hat{k}_{21}, \\
\hat{k}_{13} &= \frac{2E_1 I_1 L_2 (2E_2 I_2 L_3 + 3E_3 I_3 L_2)}{E_3 I_3} = \hat{k}_{31}, \\
\hat{k}_{22} &= \frac{36E_1^2 I_1^2 L_1^2 L_2}{E_2 I_2} + \frac{12E_1^2 I_1^2 L_1^2 L_3}{E_3 I_3} + 12E_1 I_1 L_1^3, \\
\hat{k}_{23} &= \frac{6E_1 I_1 L_1 L_2 (2E_2 I_2 L_3 + 3E_3 I_3 L_2)}{E_3 I_3} = \hat{k}_{32}, \\
\hat{k}_{33} &= \frac{12L_3 E_2^2 I_2^2 L_2^2}{E_3 I_3} + 12E_2 I_2 L_2^3.
\end{aligned}$$

The generalized forces of the Z-shaped resonator are written as:

$$\begin{aligned} \hat{f}_1 = & \left\{ \frac{L_2^2 \left[2A_2 L_1 \rho_2 \cos(\varphi) + \frac{2A_2 E_1 I_1 L_2 \rho_2 \cos(\varphi)}{3E_2 I_2} \right]}{2} + \right. \\ & \frac{L_3^2 \left[A_3 \rho_3 \cos(\varphi_2) \left(2L_1 + \frac{2E_1 I_1 L_2}{E_2 I_2} \right) + \frac{A_3 E_1 I_1 L_3 \rho_3 \cos(\varphi_2)}{2E_3 I_3} \right]}{2} + \\ & \left. + A_3 L_3 \rho_3 \left[L_1^2 + 2 \cos(\varphi) L_1 L_2 + \frac{E_1 I_1 \cos(\varphi) L_2^2}{E_2 I_2} \right] + \frac{A_1 L_1^3 \rho_1}{3} + A_2 L_1^2 L_2 \rho_2 \right\} \ddot{w}_B(t), \\ \hat{f}_2 = & \left\{ \frac{L_2^2 \left(3A_2 \rho_2 \cos(\varphi) L_1^2 + \frac{2A_2 E_1 I_1 L_2 \rho_2 \cos(\varphi) L_1}{E_2 I_2} \right)}{2} + \right. \\ & \frac{L_3^2 \left[A_3 \rho_3 \cos(\varphi_2) \left(3L_1^2 + \frac{6E_1 I_1 L_2 L_1}{E_2 I_2} \right) + \frac{3A_3 E_1 I_1 L_1 L_3 \rho_3 \cos(\varphi_2)}{2E_3 I_3} \right]}{2} \\ & \left. + A_3 L_3 \rho_3 \left[L_1^3 + 3 \cos(\varphi) L_1^2 L_2 + \frac{3E_1 I_1 \cos(\varphi) L_1 L_2^2}{E_2 I_2} \right] + \frac{A_1 L_1^4 \rho_1}{4} + A_2 L_1^3 L_2 \rho_2 \right\} \ddot{w}_B(t), \\ \hat{f}_3 = & \left\{ \frac{L_3^2 \left[3A_3 \rho_3 \cos(\varphi_2) L_2^2 + \frac{3A_3 E_2 I_2 L_3 \rho_3 \cos(\varphi_2) L_2}{2E_3 I_3} \right]}{2} + \frac{A_2 L_2^4 \rho_2 \cos(\varphi)}{4} + A_3 L_2^3 L_3 \rho_3 \cos(\varphi) \right\} \ddot{w}_B(t). \end{aligned}$$

Appendix D

Optimization of compliant mechanisms

It is well known that the design of compliant mechanisms poses unique challenges; the mechanism should be flexible to undergo a desired motion but rigid enough to maintain a load carrying capability. This problem can be addressed by defining a multi-criteria optimization, [214], where the functional to maximize is a combination of the two objectives. Similar to the previous section, we add the criteria to minimize the number of beams, n_b . The multi-criteria optimization problem can be formulated as follows:

$$\begin{aligned} \max_{x_i} : & \frac{1}{n_b} \left[\frac{\mathbf{v}_B^T \mathbf{K}_1 \mathbf{u}_A}{\mathbf{u}_B^T \mathbf{K}_2 \mathbf{u}_B} \right] = \frac{1}{n_b} \left[\frac{MPE}{SE} \right] \\ \text{subject to: } & \mathbf{K}_1 \mathbf{u}_A = \mathbf{f}_A, \quad \mathbf{K}_1 \mathbf{v}_B = \mathbf{f}_B, \\ & \mathbf{K}_2 \mathbf{u}_B = -\mathbf{f}_B, \quad V \leq V_0, \quad x_i \leq \tau \max(x), \end{aligned} \tag{D.0.1}$$

where \mathbf{f}_A is the nodal vector containing the load need for the flexibility of the structure, \mathbf{f}_b is the nodal force vector containing a dummy load in the direction of desired displacement and rigidity, Δ . The corresponding nodal displacements and global stiffness matrices for each load vector are: \mathbf{u}_A and \mathbf{u}_B , and \mathbf{K}_1 and \mathbf{K}_2 . The $MPE = \mathbf{v}_B^T \mathbf{K}_1 \mathbf{u}_A$ (Mutual Potential Energy) and $SE = \mathbf{u}_B^T \mathbf{K}_2 \mathbf{u}_B$ (Strain Energy) are the functionals for the mechanism design and structure design respectively; V and V_0 are respectively the mechanism volume and maximum allowable volume; x_i is the cross section width of each member of the mechanism; τ is the threshold limit. The goal is to maximize the displacement in B along a desired direction when the set of nodal forces f_A is applied in A .

D.1 Preliminary Numerical Results

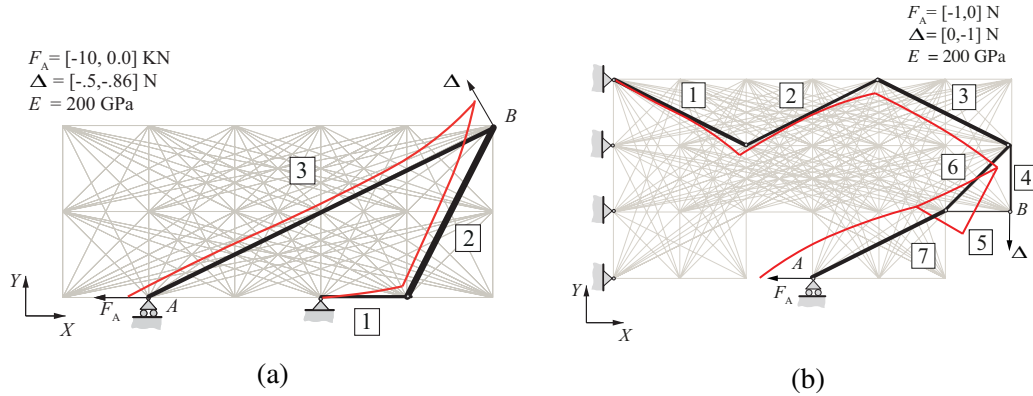


Fig. D.1.1 Starting structure and optimized topology for the compliant mechanisms: **(D.1.1a)** is the internal gripper and **(D.1.1b)** is the crimping mechanism. The non-dimensional ratio for the beams heights $h_2/h_1 = 1.59$, $h_3/h_1 = 1.12$ in the internal gripper. Similarly, the optimized heights of the beams are $h_2/h_1 = 0.45$, $h_3/h_1 = 1.0$, $h_4/h_1 = 0.86$, $h_5/h_1 = 0.8$, $h_6/h_1 = 0.45$, $h_7/h_1 = 1.0$ for the crimping mechanism. Structures in red are in their deformed positions. The threshold limit is set to $\tau = 0.25$ for the internal gripper, and $\tau = 0.35$ for the crimping mechanism.

Figures D.1.1a and D.1.1b presents two compliant mechanism designs: an internal gripper and a crimper. In both cases the target node is at A the location of the applied force. The DFS search is modified to ensure that only viable solutions are retained, i.e., they must have node B and at least one boundary node. Again, the GERM algorithms simplified the design from 109 to 3 members in the internal gripper and from 203 to 7 members in the crimper. Furthermore, in both designs the threshold limit has been adjusted to prevent overlapping elements. The results are in agreement with those found in literature ([214]).